THE UNIVERSITY *of* EDINBURGH

Thermo-Fluid Modelling of Electrical Generator Frames Under Forced Convection in an Oscillating Water Column Environment

Nisaar Ahmed

Doctor of Philosophy

The University of Edinburgh

March 2018

ABSTRACT

This PhD involved computational fluid dynamic simulations of finned generators cooling under forced convection in an oscillating water column environment. Various design changes to the upstream Wells turbine and its effect on the consequent cooling of the generator were investigated.

Simulations were run in steady-state to obtain an initial condition, thereafter, unsteady simulations revealed a steadying of heat transfer over the course of multiple blade rotation cycles. This justified the use of steady-state for the remaining simulations over a range of flow coefficients.

The results revealed that the heat transfer from the generator increased for tighter blade tip clearances, thicker blade profiles and greater turbine solidity. The heat transfer was found to increase with rising flow rate coefficient, which was adjusted by increasing the inlet velocity whilst maintaining the angular velocity of the turbine at a constant 2000 RPM. Additionally, the variation of turbine angular velocity at a fixed flow rate coefficient was investigated, the heat transfer was also found to increase with angular velocity, albeit by a far lesser extent.

The inclusion of the Wells turbine upstream of the generator was investigated initially and was found to increase heat transfer due to the resulting impingement of airflow across the generator. In all design scenarios in which the heat transfer increases, there is also an observed increase in the mass flow rate of air, radially, towards the generator.

DECLARATION

I declare that this thesis was composed by myself and the work contained therein is my own, except where explicitly stated otherwise in the text.

(Nisaar Ahmed)

ACKNOWLEDGEMENTS

This PhD began as a suggestion by my supervisor Professor Markus Mueller, during a meeting in which we were discussing the implications of some CFD results in my dissertation topic, as part of my 1-year MSc degree in Sustainable Energy Systems.

Since then, this work has given me a deep understanding of fluid mechanics and computational fluid dynamics, opened opportunities for secondments, and led to post-doc employment with the University of Edinburgh. I would like to take this opportunity to thank all the people who helped make this work possible.

My supervisor Markus Mueller, for seeing the potential in me during my MSc, convincing me that I would overcome any obstacles that may arise, and all his advice throughout the duration of this work.

Eddie Chong, my friend and colleague in the power-lab, who for the majority of the time was the only other PhD student grappling with the complexities of CFD.

Prashant Valluri, for his hours of CFD lectures, and the detailed advice he gave me whenever I visited his office.

Susan Tulley, for sharing her knowledge of CFD and turbulence with me over the years.

Tamas Jozsa, for a number of short but vital meetings I had with him after he first joined IES, after which I finally understood the approach of turbulence modelling.

The people who work in IT support, especially Michael Gordon and Kevin Tomlinson, who helped in installing Star-CCM+ across various super-clusters.

Finally, my parents, for their love, patience and support during this PhD and beyond.

TABLE OF CONTENTS

LIST OF FIGURES

LIST OF TABLES

LIST OF SYMBOLS

Roman

c_p	Specific heat (J/kgK)
d, D	Diameter (m), Drag (N)
ΔT	Temperature rise above ambient temperature (ºC or K)
E	Energy (J)
f	Value of interest
F	Force (N), Factor
g	Gravitational acceleration (m/s^2)
Gr	Rotational Grashof number (dimensionless)
h	Convection heat transfer coefficient (W/m^2K), Grid size
H	Wave height (m)
k	Turbulent kinetic energy (m^2/s^2), Thermal conductivity (W/mK)
L	Length (m), Lift (N)
$\dot{m}$	Mass flow rate (kg/s)
Ma	Mach number (dimensionless)
Nu	Nusselt number (dimensionless)
ΔP	Pressure drop (Pa)
Pr	Prandtl number (dimensionless)
P	Power (W), Perimeter (m)
p	Order of convergence
Q	Volumetric flow rate (m^3/s)
$\dot{Q}$	Heat transfer (W)
r	Local radius (m), Refinement ratio
R	Rotor radius (m), Thermal resistance (K/W)
S_{ij}	Strain-rate tensor (s^{-1})
t	Time (s)
T	Temperature (°C or K)
U	Axial flow velocity (m/s)
u	Velocity (m/s)
u^+	Dimensionless velocity (dimensionless)
u^*	Friction velocity (m/s)

V	Velocity (m/s)
W_{in}, W_{out}	Work transfer to and from a system (J)
x	Grid size or distance travelled
y	Normal distance from the wall (m)
y^+	Dimensionless wall distance (dimensionless)
z	Elevation above a reference plane (m)

Greek

α	Thermal diffusivity (m^2/s), Flow rate coefficient (dimensionless)
Δ	Finite difference
δ_{ij}	Kronecker delta function
ε	Turbulent dissipation rate (m^2/s^3), Emissivity (dimensionless)
ϵ	Relative difference (m)
η	Efficiency (dimensionless)
Γ	Inertia to body force ratio (dimensionless)
μ, μ_t	Dynamic viscosity and Turbulent viscosity
ν	Kinematic viscosity (m^2/s), Courant number
ω	Angular velocity (rad/s), Specific dissipation rate (s^{-1})
Φ	Dissipation function
ρ	Density (kg/m^3)
σ	Standard deviation
τ	Shear stress (Pa)
τ_{turb}	Reynolds stress tensor

Subscripts

cond	Conduction
conv	Convection
cr	Critical
f	Friction
h	Hub, Hydrodynamic
inf	Free-stream
i	Inner, Inlet
l	Laminar

∞	Fully developed flow
n	Normal
o	Outer, Outlet, Stagnation/Stationary
r	Rotational
rms	Root mean square
S	Safety
s	Surface
t	Turbulent, Thermal,
w	Wall

1.0 INTRODUCTION

During the oil crisis in the 1970's the possibility of harnessing energy from renewable resources became a serious consideration. However, as the oil industry recovered, and prices stabilised in the following decade attention towards renewable energy began to fade. Today with both the world population and the average level of industrialisation increasing, pressure to satisfy the rising global energy demand with cleaner "green" energy has escalated, renewing interest in alternative energy sources.

The end of the oil crisis and a consequent return of cheap oil effectively ended the drive towards renewable energy alternatives during that era. The considerable drop in oil prices in recent years is reminiscent of this scenario. However, renewable energy technologies are unlikely to suffer a repeat of what happened almost 50 years ago due to crucial changes that have occurred in the market.

Firstly, the level of installed capacity has grown rapidly in recent years, in terms of installed capacity around the globe, the value reached 161GW in 2016, a 10% increase from 2015 (REN21, 2017). At the end of 2016, renewables sources accounted for 24% of the global electricity production (IEA, 2017). The majority of this came from hydropower, 4% from wind and 1.5% from solar.

Secondly, historically, renewables were relatively expensive; however, the cost of generating renewable energy has plummeted in recent years, most especially in the solar and wind sector. For example, the cost of generating electricity by solar power is approximately 6 times cheaper than it was 10 years ago and is soon expected to be cheaper than fossil fuel power generation (WEF, 2016).

Finally, a large market has developed for energy storage technologies, the absence of which, in the past, was a major obstacle in realising a power grid supplied by renewables. Rather than the traditional pump-storage techniques, alternative methods include the use of various molten materials such as silicon, salt or graphite to store energy as heat, at temperatures reaching above 1400 degrees Celsius. This can later be used to generate and supply power to the grid as needed. The molten silicon in such thermal storage systems can be used indefinitely over a 20-year service life as compared to batteries which have a finite number of charge/discharge cycles. Thermal energy storage also has the added advantage of being much cheaper than conventional battery storage (Lewis, 2017).

Renewable energy has come to the forefront of innovative design and development in the last decade. By definition, renewable energy is sustainable and if implemented sensibly would certainly reduce global carbon dioxide emissions. Aside from the intermittency of any given renewable energy source, the major drawbacks in various renewables technologies can be summed up as follows:

- Large wind energy turbines can create both acoustic and visual disturbances for nearby residents.

- Solar energy technologies require very large surface areas to generate feasible levels of power.
- Coastal wave and tidal power installations can disturb natural habitats of marine life.

As renewable energy is generated locally, that is, within the country of consumption, it does not suffer from the security of supply issues that threaten other fuel sources. Renewable energy also provides new industry and new jobs. A report on employment in the German renewable energy industry (primarily wind) indicates a 164% increase in employment as the share of primary energy production from renewable energy increases from 3.6% to 21.5% (BMU, 2006).

The renewable energy resource of the UK, specifically Scotland is substantial. In the past the growth of renewable energy was focused mainly in the wind sector. The onshore wind resource has been estimated at over 50TWh/year (DTI, 2001) and the offshore resource would naturally be greater due to higher available wind-speeds. The other major renewable energy resource available is from the sea. Theoretical resources estimate of more than 69TWh/year for wave energy and 95TWh/year for tidal energy in UK waters were published in the Crown Estate's report of 2012. Wave power has remained relatively unexploited compared to wind power however as the technology to harness it becomes more commercially viable it is expected to become a significant source of energy.

1.1 Wave energy

Wave power is an extension of solar thermal energy and is generated mainly by the differential solar heating of the Earth's surface. When an air mass is heated, its pressure changes, and air flows down the pressure gradient, combined with the rotation of the Earth and continued solar heating these convective currents lead to the varying strengths of wind. Across a large body of water, the friction between the water surface and flowing air causes energy to be transferred from the wind to the water producing ripples and wavelets. These can grow to form large surface waves and swells depending on the extent of wind speed, the fetch length (the distance travelled by a consistent wind, blowing over the water surface), the duration of blowing and the water depth (Young, 1999). The waves have four defining characteristics: wave height from crest to trough, wave-length from crest to crest (or trough to trough), wave speed, and the direction of propagation. Other sources of wave generation include seismic events and gravity – in the form of tides. After formation waves can travel long distances with minimal losses of energy until impacting with the shore (Knowles, 1997).

The power in a wave is proportional to its period of motion (T) and the square of its amplitude (H) as shown in Equation 1.

$$P \propto H^2 T \tag{1}$$

Water waves travel into shallower water as they approach the shore and their power diminishes due to frictional coupling with the sea bed. Figure 1-1 shows how the resource increases (in the UK) away from the shore.

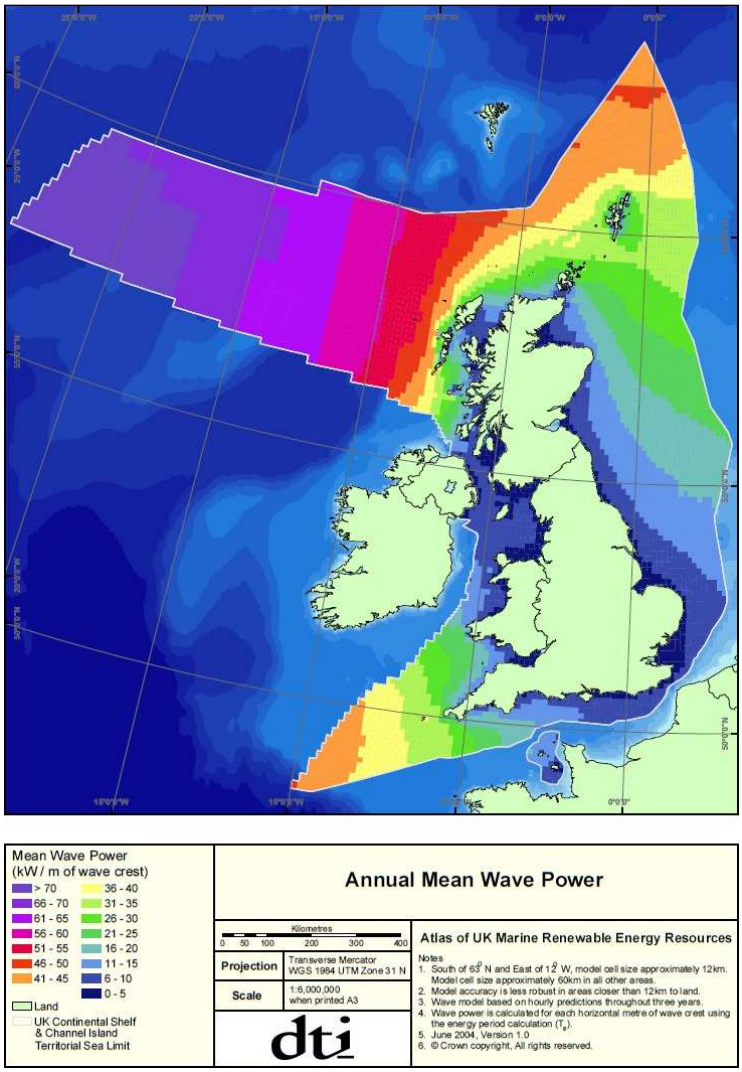

Figure 1-1: UK Wave Resource [DTI, 2004]

This would imply that wave power devices would be better placed well offshore to take advantage of the massive resource. However, developers are more interested in placing devices onshore or nearshore as they are easier to install, provide an easier electrical connection (less need for long cables) and are more accessible for maintenance. For these reasons, the financial costs of onshore/nearshore devices are overall lower than those of offshore devices. Shallow water regions tend to also help in the attenuation of extreme storm waves, which would otherwise prove a problem for the designer (Bryden, 2009).

Wave energy devices have been developed for over fifty years. Financial and political obstacles, together with a general lack of confidence from the public, (Waveplam, 2009) hindered the implementation of proven device concepts that have a high chance of becoming commercial sources

of electrical power. The design of a mechanical device to capture wave energy from the sea is a serious engineering problem. The proposed device should be able to derive useful energy from relatively calm seas with wave heights typically 1 to 5m high. It must also be able to survive the more aggressive sea conditions where the waves can exceed the range of 10-15m in height. The device should be reliable and therefore simple in operation. The rule of thumb is generally – the fewer moving parts the better.

Wave energy is by its nature is cyclical in the short term. Since every wave has a crest and trough the energy extracted would have a maximum and minimum over a single cycle. In the long-term wave energy is variable as the performance of shoreline devices are affected by the rise and fall of the semi-diurnal tides. The available wave energy can also differ between summer and winter as demonstrated in figure 1-2 below.

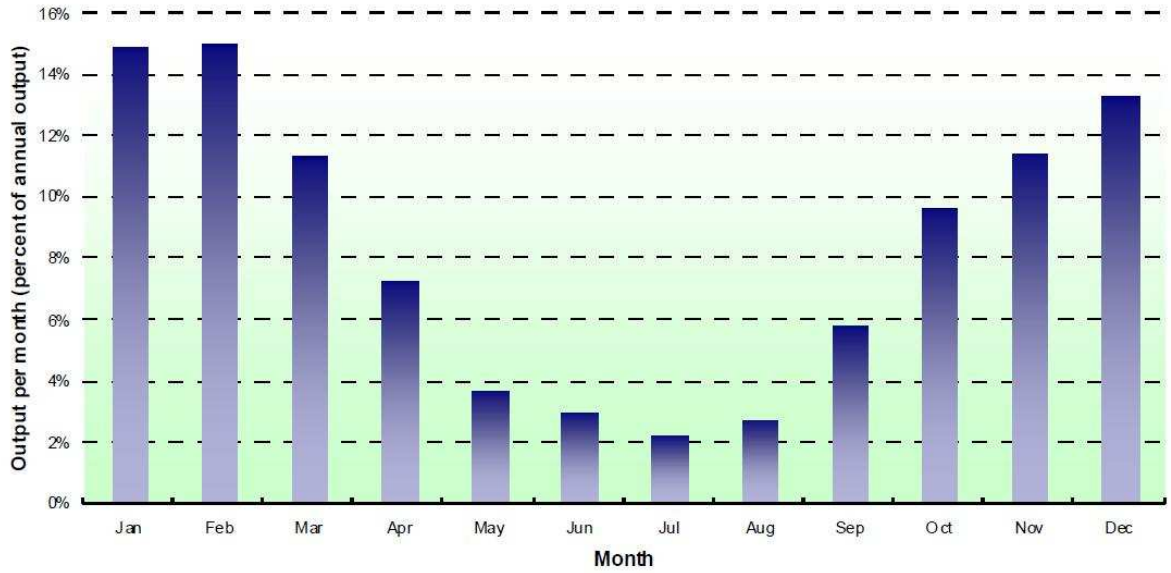

Figure 1-2: Monthly wave resource (as a percentage of annual totals) for sites in North East, North West and South West regions of the UK [Carbon Trust, 2005]

1.2 Wave energy devices

The differences in wave power over the year have implications for designing the energy converter with the right balance between power rating and capital cost. A power rating best suited for the winter months would lead to overall lower efficiency and hence wasted capital. On the other hand, a low rated converter would be significantly affected by the more powerful storm waves, which, though rare, would influence the proportion of time the converter is in a condition to operate thus preventing maximum revenues.

The basic principle for power generation in this field is for a wave energy device to be constrained such that the forces created by the waves can be usefully resisted by the energy converter. Wave

energy devices can be classified in three ways, firstly in terms of where they are situated, such as in the shallow waters along a shoreline or in the deeper waters further offshore. Secondly, in terms of their orientation to, and consequent interaction with, the incoming waves. Devices aligned perpendicular to the wave-front, to gradually absorb energy from the waves over a distance, are termed attenuators, whilst devices aligned parallel to the wave-front are termed terminators. Devices that can utilise energy in the waves arriving from any direction are termed point absorbers.

A final classification is related to the method of technology used to capture the wave energy, this includes the use of hydraulics in tethered buoyant and other relative motion devices often seen in deep water scenarios. Whilst the two principal technologies which appear particularly suited to coastal table wave energy developments are tapered channel systems and enclosed water column devices. Examples of such devices will be further discussed below.

A tethered buoyant device is essentially a free-floating object whose motion is restricted by a mooring system, which incorporates some form of hydraulic power extraction system. The workings of both a free and fixed generic point absorber buoy is shown in figure 1-3 below. The surge of water waves causes the buoys to move up and down relative to a heavy bottom plate. This motion powers a hydraulic pump in-between, which in turn rotates a generator to produce electricity. The mass of the heavy or "heave" plate need not even be large. For a plate of small mass, the additional weight of the water directly above the plate can be used to provide the necessary reaction force during motion. In the case of a fixed device, the plate is held to the ocean floor by a dead-weight, a technique often reserved for shallower waters.

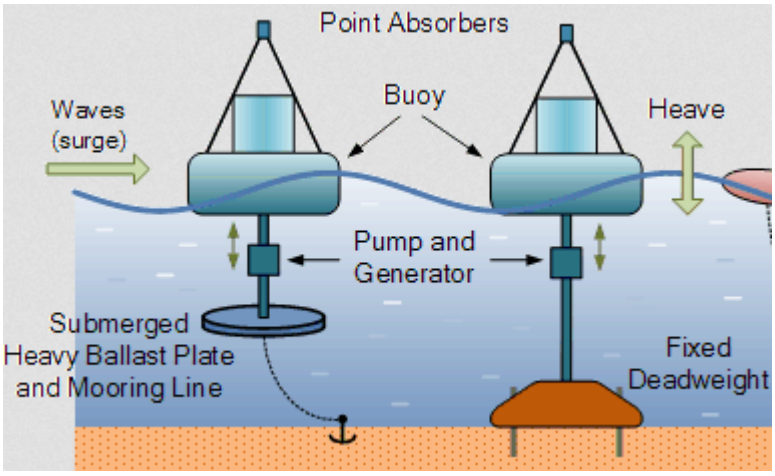

Figure 1-3: Heaving Buoy Energy Device [AET, 2015]

Hydraulics are also utilised in oscillating wave surge converters. The design essentially consists of a pendulum mounted on a pivoted joint which oscillates in response to the incoming water waves, which in-turn powers a hydraulic pump. An example of this device is the Pendulor, demonstrated in

figure 1-4, a rectangular box - open to the sea at one end. The action of the waves causes the pendulum flap, hinged above the opening, to swing back and forth.

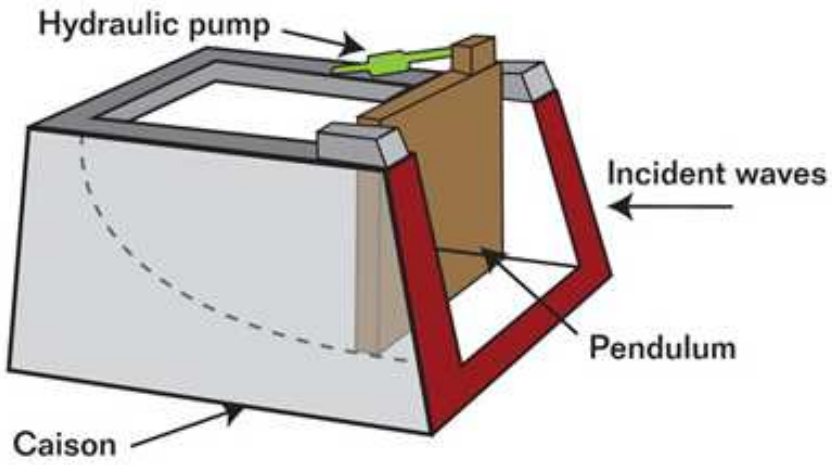

Figure 1-4: The Pendulor [Liptak, 2007]

Energy can be extracted from the sea via hydraulics that operate in response to the relative motion of different parts of an extended structure. Pelamis is an example of this; the device is composed of hollow, cylindrical sections linked by hinged joints. The sections are oriented towards the oncoming waves and move with respect to each other as the waves pass down their length. The hydraulic rams built into the joints of the device, drive electrical generators to produce power. The workings of the Pelamis device is shown in figure 1-5. There are challenges in using hydraulics, which need to be addressed. For example, the use of a viscous fluid, most often some kind of oil, could present an environmental risk should any leaking occur from faulty valves, seals or hoses. Secondly, given the high viscosity of the fluid involved, hydraulic systems require considerable energy to move any given component. With a large number of components in a hydraulic system reliability is a major challenge for the sector.

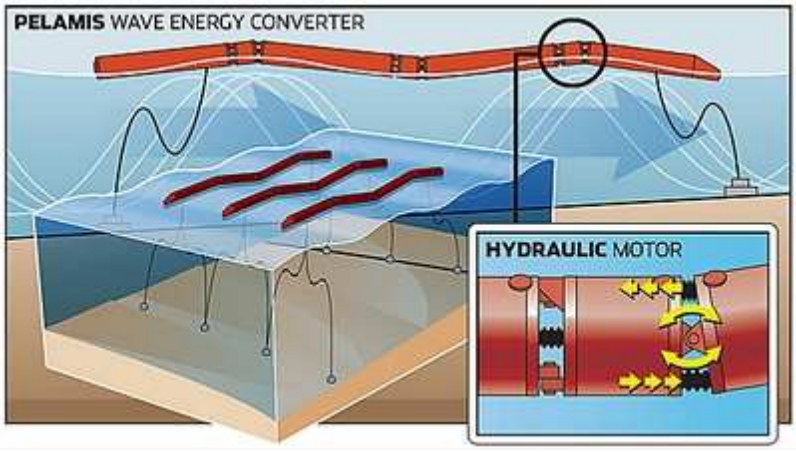

Figure 1-5: Pelamis wave energy converter [Toshichile, 2012]

The concept of a tapered channel is uniquely applicable to a coastal development. It consists of a narrowing channel with wall heights typically 3 to 5 meters higher than the mean sea level. The energy in the wave transports water from the wide end of the artificial channel up into an artificial pond; this is then drained back down to sea level through a low head water turbine as demonstrated in figure 1-6. The storage pond does allow for some energy storage against time when wave energy is not available. However, this concept is very sensitive to tidal sea changes and requires a very specific type of coastline to permit the easy construction of such a channel and storage pond. The requirements of a low tidal range and suitable coastline limit the world-wide implementation of this device. However, devices of similar design can be moored offshore, floating on the water surface and consequently unaffected by the incoming and outgoing tides.

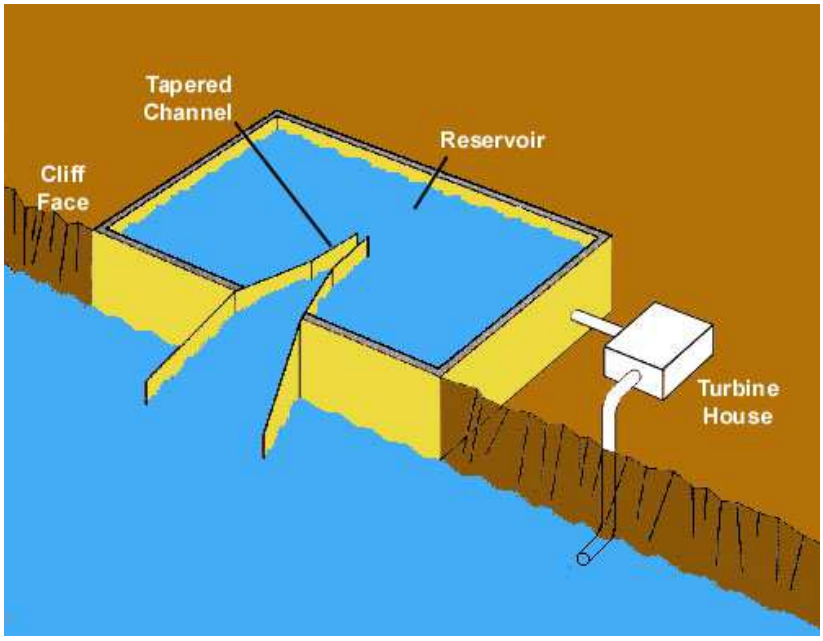

Figure 1-6: Concept of the tapered channel [TCWE, 2010]

The final device is an oscillating water column. The OWC consists of a partially submerged chamber enclosing water and air. At the rear of this chamber there is an exit hole allowing air to flow to the atmosphere via a turbine. As the waves impact the OWC, the water level in the chamber rises and falls, blowing out and drawing in the air past the turbine and powering a generator. A diagram demonstrating the design and operation of the OWC is shown in figure 1-7.

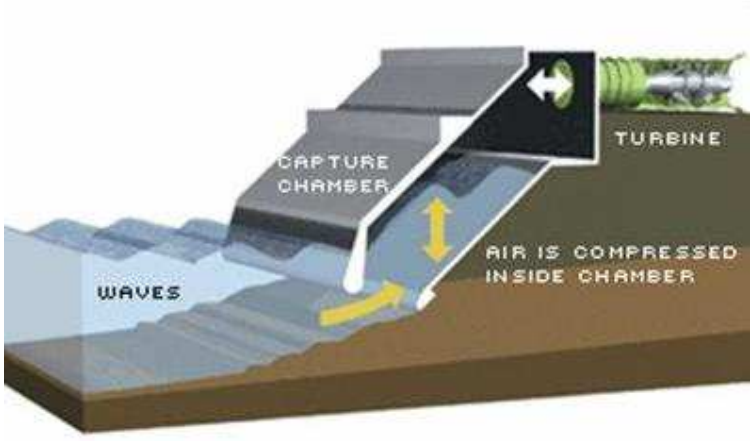

Figure 1-7: Principle design of oscillating water column [OWC Wave Energy, 2010]

1.3 The oscillating water column

Amongst the many types of wave energy devices available for harnessing the power of the seas, the oscillating water column device is arguably the most viable. The reason being the design of the capture chamber of the OWC is most suited to convert the slow, 0.1 Hz, random, and high force motion of the water waves into low force-high speed airflow capable of driving turbo-machinery.

The OWC being a coastal wave device would cause less interference to other users of the sea, such as those involved with fishing or transport, and as there are no moving parts in the water, would have less impact on marine life, indeed an offshore OWC may even support sea life by introducing an artificial reef. The only concerns occurring from the introduction of an OWC are issues of noise pollution and damage to the natural beauty of a seascape, both issues may be mitigated by situating the OWC in a far offshore platform.

However, an OWC that is firmly fixed onto a cliff wall has considerable stability advantages when compared to a moored deep-water system. As mentioned previously, wave power density in coastal waters is considerably less than in the open sea; though this can be countered through natural focussing. That is, by placing the devices in gullies that face into the direction of the prevailing wind to focus the energy of the water waves as shown in figure 1-8.

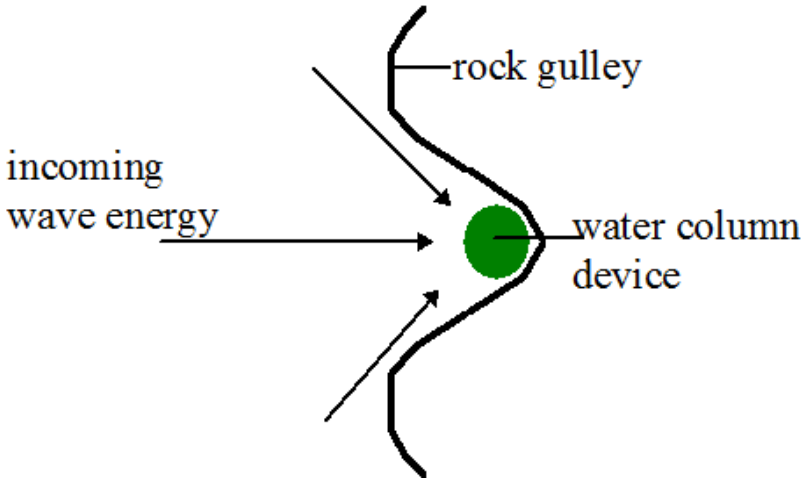

Figure 1-8: Natural focussing of wave energy [Bryden, 2009]

An air turbine is required to convert the energy in the airflow into rotary motion to drive an electrical generator. The Wells turbine is comprised of untwisted, chambered aerofoil sections with symmetrical profiles radiating from a central hub. This design gives it the unique ability to transform the random oscillating airflow past the OWC chamber into unidirectional torque for power generation, as opposed to a chambered aerofoil turbine, which would experience an effect deceleration when the air flowed past in the opposite direction.

Since its invention in 1976 by A.A. Wells (Burdekin, 2007), most researchers have focused on improving its efficiency and its range of efficient operation. Compared to other conventional air turbines (e.g. Francis turbine) the Wells turbine has a lower efficiency and a narrow operational region. Nevertheless, it can extract power at low airflow rates, when other turbines would be ineffective.

Examples of the oscillating water column in commercial use include, the Ocean Energy Buoy, a deep-water device anchored far off-shore, utilising the waves generated by storms. Full scale buoys have an output of approximately 500MW, they are assembled on land and can be transport by boat to the most suitable locations for power generation. Another example is the Mutriku wave energy plant, operated in Spain, in which both the capture chamber and Wells turbines are housed in offshore breakwater structures that originally protected the coastline from severe wave activity. This project was the first in which multiple Wells turbines were utilised in one plant. A final example is the land installed marine powered energy transformer or LIMPET, situated on the Isle of Islay, Scotland, the details of which form the basis of this thesis. Its design was the result of collaboration between the Scottish renewable energy company, Wavegen, and the Queens University Belfast. The image in figure 1-9 shows the LIMPET situated on the Isle of Islay.

Figure 1-9: The LIMPET OWC wave energy convertor [NNMREC (OSU), 2015]

Full details regarding the construction and management of the LIMPET are given in the DTI (2002), highlighting the importance of the Islay device for developments of onshore and offshore generation and as well as its position as a test bed for further equipment research. The LIMPET consisted of two research elements; firstly, the original device, rated at 500kW, that was later reduced to 250kW due to an initial over-estimation of the wave power expected to reach the water columns. Secondly, a separate section attached to an air outlet, allowing for the testing of prototype turbo generation equipment, the latest being an 18.5kW rated generator. Wavegen was bought out by the German company Voith Hydro during the course of this PhD, and the LIMPET was shut down in 2013, however the CFD and analytical modelling of Wells turbine and various generator casings will be based on the dimensions of the prototype equipment. The details of the Wells turbine and the finned generator are given in table 1-1.

Wells Turbine Data	
Turbine Diameter	0.75m
Blade Cord	0.2m
Solidity	0.63
Hub to Tip Ratio	0.58
Number of Blades	3
Blade Form	NACA 0020
Operational Speed	2000 rpm

Finned Generator Data	
Axial Length	0.35 m
Casing Diameter	0.14 m
Fin Height	0.02 m
Fin Thickness	0.002 m
Number of Fins	36
Degree Spacing	10°
Power Rating	18.5 kW

Table 1-1: Details of the prototype equipment to study in this thesis

Given that the LIMPET was installed in a relatively inaccessible location on Islay, the device was controlled and monitored via a semi-automatic system that sent continuous streams of data allowing for remote access and operation. QUB (2002) explains how the current LIMPET device evolved from a 75kW prototype device located on an adjacent site, installed on Islay in 1991. The prototype was

designed by the Queens University Belfast and over a course of 8 years operated as a research project supplying vital information necessary for the final construction of the LIMPET.

1.3.1 Islay

A number of surveys were carried out by the Queens University Belfast to find suitable locations for installing wave devices around Britain. Locations with highly favourable wave activity included the north coast of Scotland, the coasts of some of Scotland's isles, as well as the coastal regions of Devon and Cornwall (DTI, 2002). Any location choice for situating the LIMPET OWC would require deliberation with the local populous, consideration of the methods of construction and a close proximity to the electrical grid. The optimal location for the device was finally decided to be the Isle of Islay for the following reasons:

- A high wave energy climate
- A viable grid connection
- An enthusiastic local population
- Suitable access for construction, installation and monitoring
- A low tidal range resulting in less structural reinforcement for construction and therefore lower overall costs

The stages involved in constructing the LIMPET chamber are shown in figure 1-10. The chamber was created within an excavated rock face using reinforced concrete. After chamber completion the outstanding rock bund was removed thus providing access to the sea. Whilst the LIMPET was a success, recent findings would indicate room for improvement in the system design. For instance a parallel channel towards the OWC chamber is detrimental to wave flow and lowers the proportion of energy available for extraction. Instead, a tapered inlet toward the device would improve the interaction of waves with the OWC chamber.

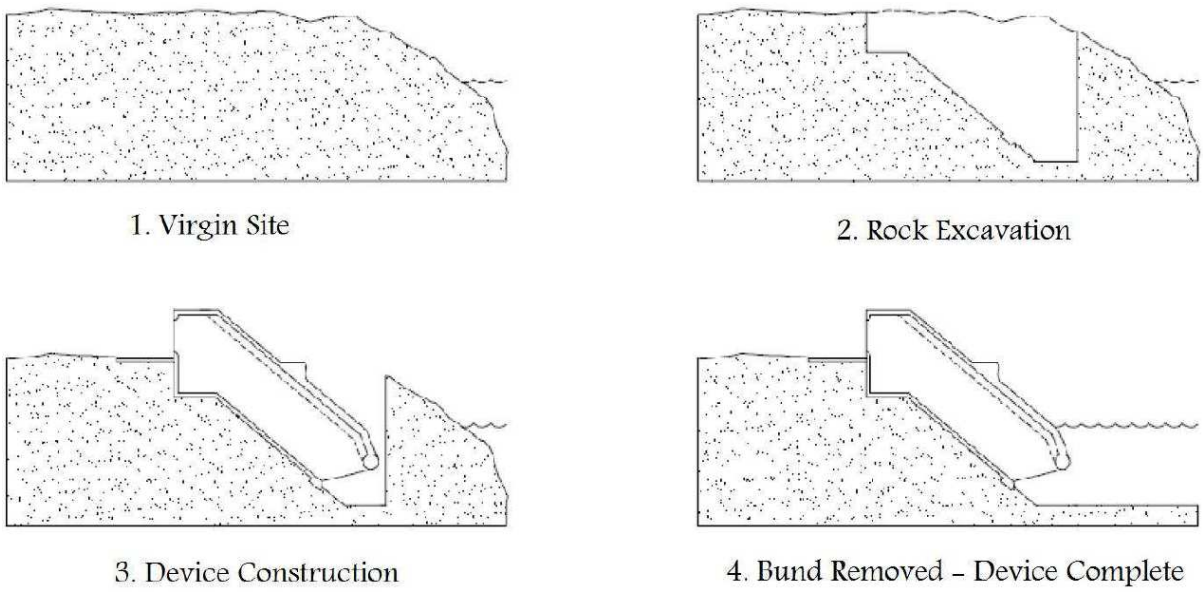

Figure 1-10: Construction of LIMPET inverted chamber [DTI, 2002]

1.3.2 The Wells turbine

The operation characteristics of the Wells turbine are based on classical aerofoil theory which states that an aerofoil inclined at an angle of incidence α to a fluid flow produces a lift force *L* normal to the free stream. The aerofoil also experiences a drag force *D* in a direction parallel to the free stream. Components of these lift and drag forces can be resolved into a net tangential force (F_T) acting in the plane of rotation and a net axial force (F_A) acting normal to the plane of rotation as shown in figure 1-11. Whilst the expressions for the net tangential and axial forces are given in equations 1-1 and 1-2 respectively.

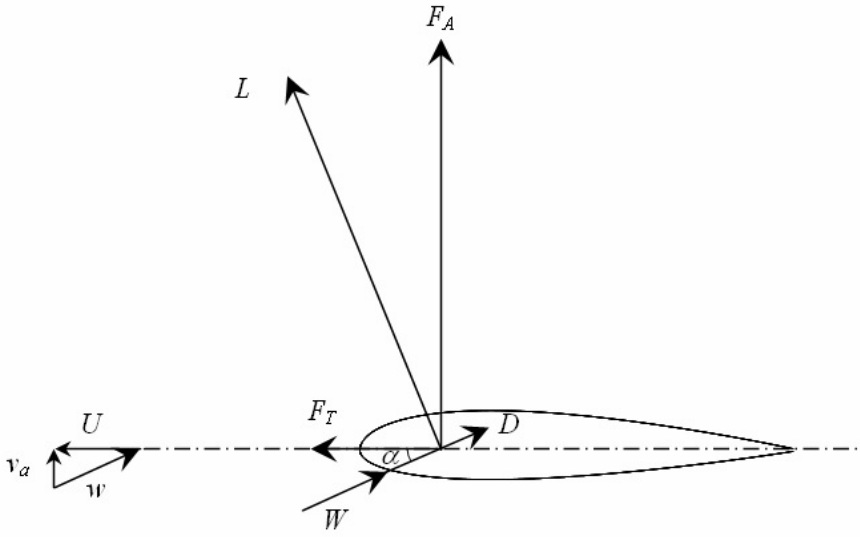

Figure 1-11: Forces on Wells turbine blades [Mamun, 2006]

$$F_T = Lsin \propto -Dcos \propto \quad (1\text{-}1)$$

$$F_A = Lcos \propto +Dsin \propto \quad (1\text{-}2)$$

The axial force creates a bending moment along the radius of the turbine blades and will tend to cause a slight deflection during operation, whereas the tangential force is utilised for rotation. As the aerofoil is symmetrical the direction of the net tangential force will be the same for positive and negative values of α and hence the rotation of the turbine continues independently of the airflow direction. The direction of the tangential force would only become negative when the drag force became dominant over the lift force, such as when the turbine stalls or at very low incoming flow speeds.

Electricity must be initially supplied to the generator from the grid to bring the turbine up to the necessary operational speed. Increasing the blade solidity of the turbine would allow the turbine to self-start however this increase would be detrimental to turbine performance (Raghunathan, 1995). An alternative means for both self-starting and maintaining the lift is to incorporate blade pitching into the Wells turbine design. Laboratory testing of such a design has been carried out however no full scale commercial device has been deployed (Tease, 2003).

As mentioned previously, the nature of an OWC capture camber converts the high force/low velocity motion of water waves into low force/high velocity airflow. Since the costs of electrical generators typically rise faster with torque than rotational speeds, the generators needed are compact and can be purchased ready-made or "off-the-shelf" as opposed to much larger generators that would need to be custom made to deal with very high values of torque. (Hodgins, 2009).

1.4 The issue of suitable power take-off

Given that such electrical generators used in the turbo-generation sections of an oscillating water column are not specifically made-to-order, they do not take into account their operating environment, and likely under-rated in terms of thermal performance. After work by Hodgins, it is generally understood that the generator situated between the Wells turbines would certainly stand to benefit thermally from the back and forth airflow, and that the airflow tends to impinge on the generator. However, no work has been done to investigate the magnitude of this benefit.

As discussed, the wave resource has variation in both the long (seasonal) and short (hourly) term. Figure 1-12 shows the probability of wave height and power high in the short term. During these

periods of high wave activity more power can be produced, however the given generator would be pushed beyond its rating.

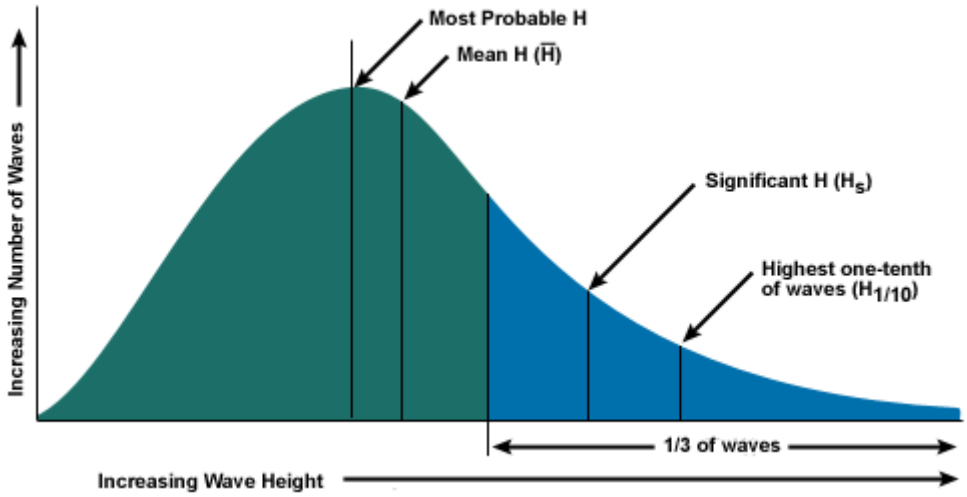

Figure 1-12: The Varying Resource [Met Service, 2015]

For a synchronous speed generator, the sudden increase in airflow past the turbine blades causes an increase in generator torque which counteracts the effect of any acceleration experienced by the rotor, thereby, keeping the rotor spinning at a fixed speed. This "push-back" from the electrical grid when producing additional power, though maintaining the generator at a synchronous speed (often 50Hz), results in persistent surges in the generator torque and can cause wear and eventual damage.

An alternative is to use an asynchronous generator which would allow the rotor to speed up during periods of high wave activity to produce additional power at frequencies higher than the synchronous frequency of the grid. The generator would not be connected to the grid directly, instead, the additional AC power produced by the generator would be converted to DC, and then converted to AC power at the desired output frequency for the grid by an inverter.

Any additional power produced in the generator would naturally result in greater losses (I^2R) associated with a higher electrical current. The requirement of limiting the consequent temperature rises in the windings, due to these additional heat losses, are the basis for the power rating of the generator. However, the occurrence of airflow impingement, were it to greatly improve the rate of convection cooling at the generator surface, would allow a given generator to safely produce power at values higher than its originally defined rating.

The electrical generators used in OWCs are classified as a totally enclosed fan cooled (TEFC) machines. Air is blown axially through the fin channels of the generator; the airflow velocity is related to the rotational speed of the connecting shaft. Figure 1-13 shows the relationship between shaft speed and airflow through the fin channels at the outlet of various generator designs. The higher velocity of

air flow (V) through the fin channels for larger machines can be intuitively understood to be due to the greater associated (dimensional) size of the fin channels and thereby lower flow resistance.

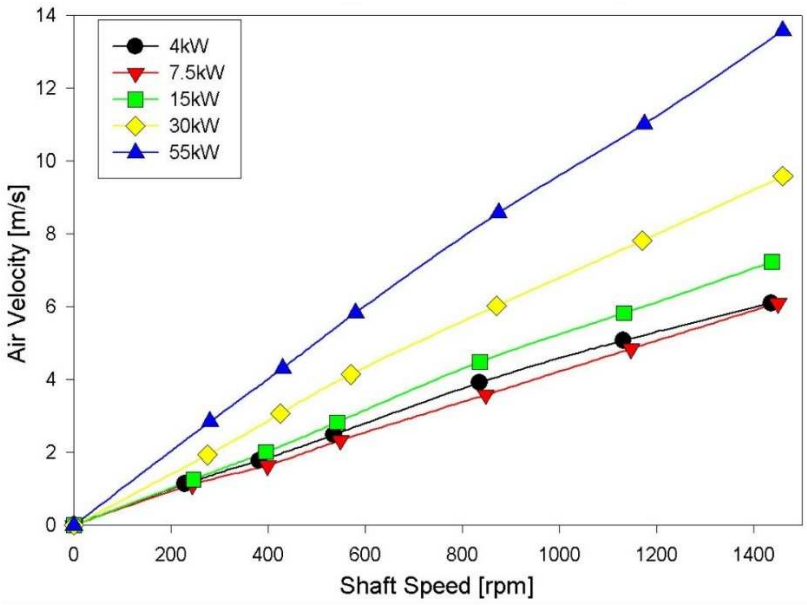

Figure 1-13: Air velocity through fin channel with varying rotational speed of motors as collected by Staton *et al* [2005]

The occurrence of impingement is when a flow impacts orthogonally to a flat surface. After impacting the surface, the flow will generally proceed to flow parallel to the flat surface. The nature of orthogonal flow causes a thinner boundary layer in the area of impingement, and as a result of the change in direction the airflow in the surrounding areas of the impingement tends to be more turbulent. For these reasons the heat transfer from such a surface in this event is much greater as compared to purely parallel flow. Consequently, impinging flow is a desired heat transfer method and used in a variety of industrial applications including the cooling of electronic components.

The rating of the induction generator in the LIMPET is 18.5 kW; however, this value is based on the assumption that the built-in rotating shaft fan is the only cause of forced convection though the fin channels, rather than the airflow impingement caused by the Wells turbine. The values of heat transfer in the region of airflow impingement can be up to three times higher than where the flow is purely parallel given the same flow velocity. For a required heat transfer coefficient, switching to the impingement method can reduce the required flow rate by two orders of magnitude (Zuckerman *et al*, 2006). Figure 1-14 below shows a diagram of the generator situated between two (bi-plane) Wells turbines experiencing impingement from the air flowing past the blades.

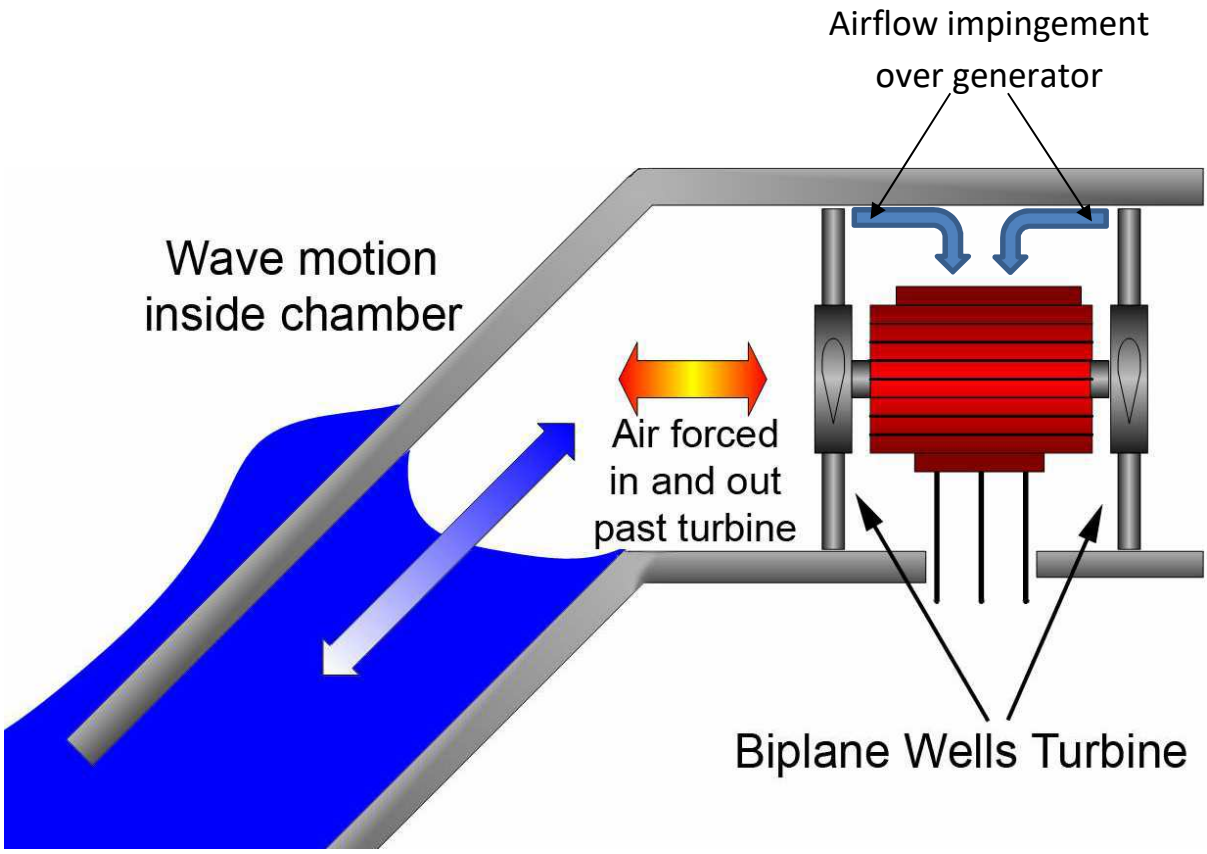

Figure 1-14: Diagram of air flowing back and forth between biplane Wells turbines [Hodgins, 2010]

1.5 The aim of this PhD and outline of the thesis

Over the past two decades much experimental work has been carried out on the Wells turbine by focusing mainly on the overall operating characteristics and the internal flow phenomena around the turbine blade. However, with the recent advances in computer hardware and software it has become practical to create computational fluid dynamic simulations of three dimensional turbulent flows through complex geometries. Numerical approaches are increasingly becoming vital for analysis and design, they not only allow for the visualization of the fluid flow field but also the scalar distributions (such as pressure or temperature) on the geometry in question.

Various numerical studies have been carried out on the Wells turbine due to its importance in the oscillating water column. The majority of these studies were aimed at improving aerodynamic performance through both steady-state and unsteady simulations. However, no study has ventured downstream of the Wells turbine to examine the effects on the cooling of the electric generator due to the resulting airflow impingement.

The purpose of this thesis is to examine and understand the dependency of the heat transfer from the finned generator to the design of the upstream Wells turbine. Computational fluid dynamic simulations of a monoplane Wells turbine will be carried out with varying design parameters. The goal is to correlate the cooling of the finned generator cooling with changes to the turbine tip-shroud

clearance, blade profile, solidity and hub to tip ratio across a range of flow coefficients. The flow coefficients will be altered by fixing a rotational velocity and varying the incoming airspeed, and later by fixing the incoming speed and varying the rotational velocity.

As the generators used in such wave power devices do not take into account the planned OWC environment. Knowledge of such dependencies would be very beneficial to designers of future oscillating water columns. The ability to improve the cooling would allow for a greater potential power output without overheating the generator, thereby maximising power generation and reducing long-term maintenance costs.

The next chapter will present a literature review on the cooling of electrical machines, and the two approaches of analytical and numerical modelling will be discussed. As well as highlighting areas of previously published work on both the Wells turbine and thermal analysis of electrical machines, the gaps in knowledge regarding the combination of these areas and hence the need for this PhD work will be explained.

Chapter 3 will provide an introduction to heat transfer, focusing initially on the heat conduction equation, and then expanding the theory to include convection and fluid flow. After covering the concepts of the velocity and thermal boundary layers, the chapter will focus on the difference between laminar and turbulent flow, specifically the increase in momentum and heat transfer brought about due to turbulence. Correlations for heat transfer can only be derived analytically in cases of laminar flow, whilst numerical methods, such as CFD, must be relied upon for scenarios of turbulent flow, as in this thesis.

Chapter 4 will delve into the Navier-Stokes equations, composed of the continuity, momentum and energy equations, which are the basis for CFD analysis. The reason being, similar to other finite element or finite volume approaches, CFD packages are often considered by their users as a "black-box" tool to obtain answers to engineering problems without a true understanding of the underlying physics involved, and therefore, the limitations of applicability. This chapter will attempt to clarify the theory behind CFD.

Chapters 5 will demonstrate the techniques for solving the momentum and energy equations analytically, leading to correlations for the thickness of the velocity and thermal boundary layers above a flat plate undergoing laminar flow. Thereafter, expanding into external forced convection, turbulent correlations, for flow above flat plates and more importantly, for flow through fin channels, will be outlined. Throughout this chapter the laminar correlations will be derived whereas the equivalent turbulent correlations will be stated outright. The three-dimensional velocity fluctuations that occur inherently due to turbulence make it essentially impossible to solve the Navier-Stokes equations analytically, hence such turbulent correlations are obtained empirically.

Chapter 6 will be the final theory chapter and will explain the limitations of applying the Navier-Stokes equations through a fluid flow domain as the turbulent eddies progressively reduce below the cell size of the mesh. The procedure for "Reynolds averaging" these equations as well as providing closure via the method of turbulence modelling will be covered. The last section will discuss the importance of refined meshing techniques at wall boundaries, as the velocity of fluid flow within the boundary layer reduces rapidly upon approaching the wall.

Chapter 7 will provide details regarding the setup of the computational fluid dynamic simulations for this thesis. The procedure for determining the choice of mesh size will also be explained, as well as outlining the results of a mesh independence study.

Chapter 8 will explain the notion of unsteady simulations in contrast to steady-state. The results of unsteady simulations will be compared with their equivalent steady-state results to judge whether the use of steady-state assumptions is viable for this work.

Chapter 9 will collate the results and provide a discussion for the analytical modelling and CFD simulations. Comparisons between the analytical modelling and CFD simulations will be made for smooth and finned generators cooling without the occurrence of airflow impingement.

Chapter 10 will finally present the conclusions of this thesis. Demonstrating how this work is an original contribution to knowledge, the main findings of this work, and recommendations for areas of further study.

The theory of heat transfer and fluid flow outlined between chapters 2 and 6 is very comprehensive. For the reader more experienced in this subject, it is not necessary to go through all of it in order to follow and understand the important findings of the thesis.

2.0 LITERATURE REVIEW

Historically, when investigating or re-examining the design of electrical machines, the majority of analysis is carried out in terms of the electromagnetics, whilst seldom is any thermal analysis considered. Staton *et al* (2005) of Motor-CAD states that this becomes most clear when surveying the number of papers published in both of these subjects, particularly in the cases dealing with small to medium sized motors. The only way to assess the thermal performance of a given machine is by the power rating, or some other defined limiting value such as the maximum allowable current density. However, these values, which tend to be variables related to the size of the machine do not give any indications of the weakness in the design such that the machine may be improved to reduce the temperatures at the same operating speed. With increasing demand for increasing power density, energy efficiency, cost reduction and the desire to make full use of new materials and topologies, the need has arisen for the analysis of the thermal circuits in electrical machines to rival that of the electromagnetic analysis. This section will explain the concept of losses in electrical machines and their relation to temperature rise. The various methods of modelling such thermal losses will be expounded, with greatest consideration to computational fluid dynamics. Finally, previous findings for electrical machines and the Wells turbine through the use of CFD will be discussed, whilst the areas yet to be explored, hence the focus of this thesis, will be explained.

2.1 Thermal losses in electrical machines

The fact that there is not equal emphasis placed on both aspects is surprising given that the “losses” in an electrical machine are dependent on the temperature and vice versa. To be clearer, the generation of heat in an electrical machine is a consequence of an inefficiency in the production of electricity, and hence is viewed as a loss. At the same time, the rising temperature of the machine tends to increase the extent of these losses. Boglietti (2009) explains the likely reason that thermal analysis generally receives less attention than the electromagnetic revolves around the different disciplines that deal with each. That is, electromagnetic analysis would be best dealt with by electrical engineers, whilst the thermal analysis aspects would be left to mechanical engineers.

The losses that occur in an electrical machine can be categorised under that of copper and iron. Copper losses are due to the electrical resistance of the copper windings, the rate of heat loss is proportional to the square of electrical current generated. Whilst the iron components contribute to eddy current losses, where heat is generated due to the presence of a changing electromagnetic field in the iron, these losses are unavoidable as this is a crucial aspect of the operating procedure for an electrical machine, including induction or synchronous generators.

These make up the majority of the losses as they are associated with the generation of electricity. The copper losses in the stator and rotor account for approximately 30% and 20% respectfully of the total losses in the machine, whilst the iron losses can contribute approximately 35% - 45%. However, additionally, there are losses associated with the air resistance experienced by components of the generator due to the motion of the rotor, this is referred to as windage, and can be as low as 5% - 15%. Finally, there can be "stray" losses, though these are difficult to account for, they tend to be less than 1%, and are often assumed to be associated with inaccuracies in the designing and modelling of the machine.

Though a motors performance is governed by its thermal and electromagnetic design, there are additional considerations than the mutual dependency of the temperature and losses. Iron losses tend to be easier to dissipate than copper loss due to the iron stator's closer proximity and ability to conduct heat towards the housing. Whilst the end windings, are likely to be subject to far greater convection cooling as compared to the majority of the machine. Figure 2-1 shows the heat paths from the core of an induction machine to the outer casing. Heat will flow either by conduction between components in good thermal contact or by convection in the air enclosed by the endcaps.

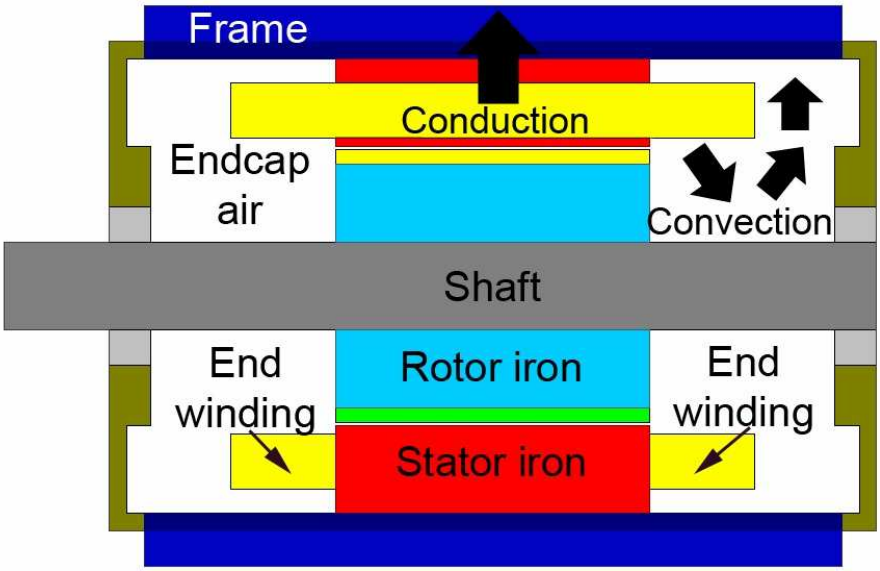

Figure 2-1: Main heat paths inside an induction machine [Hodgins, 2009]

The outer casings of electrical machines may be cooled via either natural or forced convection. Heat transfer by natural convection is primarily related to the temperature difference between the heated surface and surrounding fluid, as well as the fluid properties. Whilst heat transfer by forced convection is primarily a function of the fluid velocity and fluid properties. In such a case, the temperature of the fluid would only affect the heat transfer coefficient to the extent that it would alter the fluid properties, rather than due to buoyancy effects. As such, heat correlations for surfaces undergoing forced convection tend to be expressed as a function of Reynolds number.

It can be easier to predict the rate of heat transfer by natural convection rather than forced convection, in that the function for the natural convection coefficient does not require the local velocity to be known. This is mostly the case in machines designed for cooling by natural convection, which are often fitted with fins aligned to allow natural flow within such fin channels. This is because of analytical correlations that are able to predict the velocities achieved by buoyancy driven air flow for common machine geometries. As these natural convection currents are taken into account, the correlations are a function of the surface and ambient temperature, and characteristic dimensions of the machine. It should be noted that such corrections are very sensitive to the physical orientation (angle) of the machines. For example, some vertical fins fixed into a wall with heated air flowing upwards through the fin channels would give a very different flow pattern to horizontal fins fixed to the same wall.

Staton and Cavagnino (2008) outline the many well proven correlations to predict the heat transfer coefficient in such cases of natural convection. However, in the case of totally enclosed fan cooled machines, he explains that the prediction becomes quite complex. Though the fins included on such a machine housing would be aligned for forced convection through the fin channels, the fan component, driven by the rotation of the rotor shaft can often operate at (or beyond) the point of stall, and thereby natural convection would in-fact dominate, resulting in poor cooling. For this reason, it becomes necessary to also determine natural convection correlations for such fin arrangements.

In the case of smooth housings, flat plate correlations can be used to predict the average heat transfer coefficient. The equations can differ slightly depending on assumptions of whether the flow over the entire housing is laminar or turbulent, but also depending on whether the flow regime began as laminar and transitioned to turbulent at a point along the surface. Such correlations are very common, and can be often found in heat transfer textbooks, examples include “Heat Transfer” by Mills (1999). The greater difficultly however, is in obtaining a correlation for the heat transfer coefficient when flow is forced through an open fin channel like those often utilised in electrical machines. The only correlation for such scenarios is provided by Heiles (1952), which he developed after extensive experimental testing on electrical motors. The correlation is very complex and incorporates the overall hydraulic diameter of the fin channel as a separate variable. The correlation assumes the velocity to be constant through the fin channel and also the flow to always be turbulent due to the use of cowlings and fans in TEFC machines. This is the primary correlation used by analytical modelling software when considering open fin channel flow.

Empirical data collected by Staton *et al* (2005) for such TEFC machines, shows how, as well as the tendency for fin channels of TEFC machines to be blocked by bolt lugs and terminal boxes, at the same time, there tends to be a leakage of air out of the fin channels resulting in lower flow velocities at the downstream end of the generator as compared to the upstream end as shown in figure 2-2.

Where PU refers to the "per-unit" length of the machine, that is, 0 and 1 designate the nearest and furthest extents of the machine. Staton notes that the leakage factor is a complex function of fan, fin and cowling design as well as rotational speed.

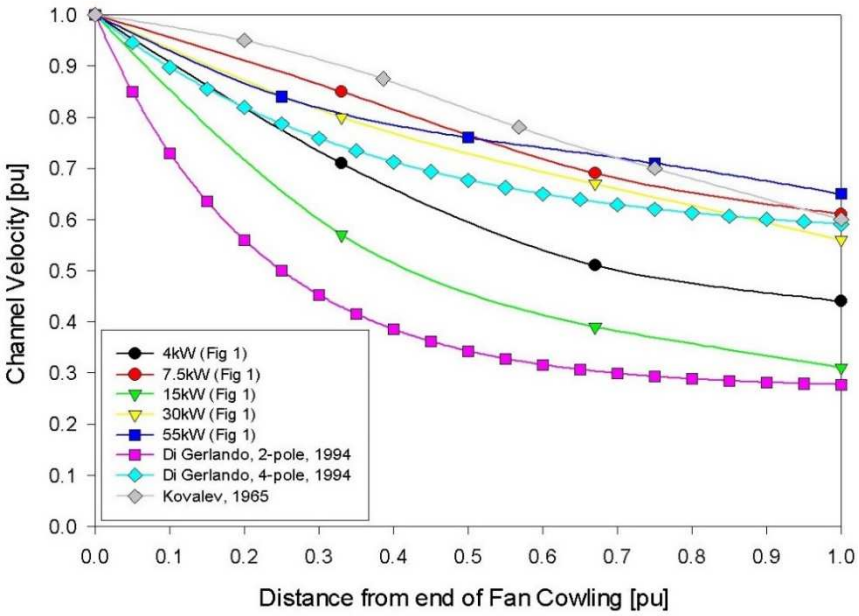

Figure 2-2: Air velocity reductions through fin channels of motors with distance from fan as collected by Staton *et al* (2005)

Additionally, testing between open and closed fin channels was performed by Kovalev (1965). Closed fin channels required a greater force and therefore a larger fan. However, for equivalent inlet velocities, the heat transfer coefficient for open fin channels was reduced by only 10% despite a greater reduction in velocity at the outlet of the channel. This was understood to be a consequence of the added turbulence resulting from the rotating fan upstream. Similar results were found by Benecke (1966).

The extent of temperature rise is what ultimately determines the rating of an electrical machine, specifically, it is the rising temperature of the windings, which in turn would compromise the various types of insulation in the machine. High temperatures can also reduce the performance of permeant magnets (when present) and the consequent operating life, for which reason accurately defining the rating of a machine is so important. Acceptable operating temperatures are often defined by the manufacturers of the insulation used and the aim is to maintain temperatures within the machine at just below these values, as operating at a temperature too low would essentially be an uneconomic use of material. A light insulator, that would fail at even moderately high temperatures, would require the machine to operate at a temperature below the rating of the insulation, and consequently, at a low current density, thereby limiting the torque that could be produced.

Excessive rises in temperature can be prevented by altering the design to further allow heat generated by the machine to dissipate to the surrounding air, water or earth. As such, direct cooling methods in the form of convection across the outer housing by a continuous fresh supply of water or air, may be supplemented by a cooling medium inside the generator, such as oil (of higher thermal conductivity than air) to better transfer heat from the core of the machine to the ventilating surfaces. However, given the complexities of such designs, the most common method encountered for electrical machines is that of direct air cooling. Though in terms of the number of machines, air cooling is the most popular method, it should be noted that very large electrical machines, such as those situated in power stations, are often water cooled. Therefore, in terms of the sum of machine power, water cooling may take the lead over air cooling.

2.2 Thermal modelling of electrical machines

Even in the case of direct air cooling, the requirement of thermal analysis is vital for arriving at the most suitable design. There are two approaches to undertake thermal analysis in the case of an electric motor, the first is analytical lumped-circuit modelling whilst the second option is to use numerical modelling. The choice of the analytical technique provides very fast results; however, the major difficulty lies in accurately defining a circuit to correctly model all the heat flow paths within machine. In essence the lumped circuit model works because the transport of heat throughout the machine can be likened to an electrical network, by defining the extent of resistance to conduction, convection and radiation in each heat path. An example of a heat transfer network for an electrical motor is shown in figure 2-3.

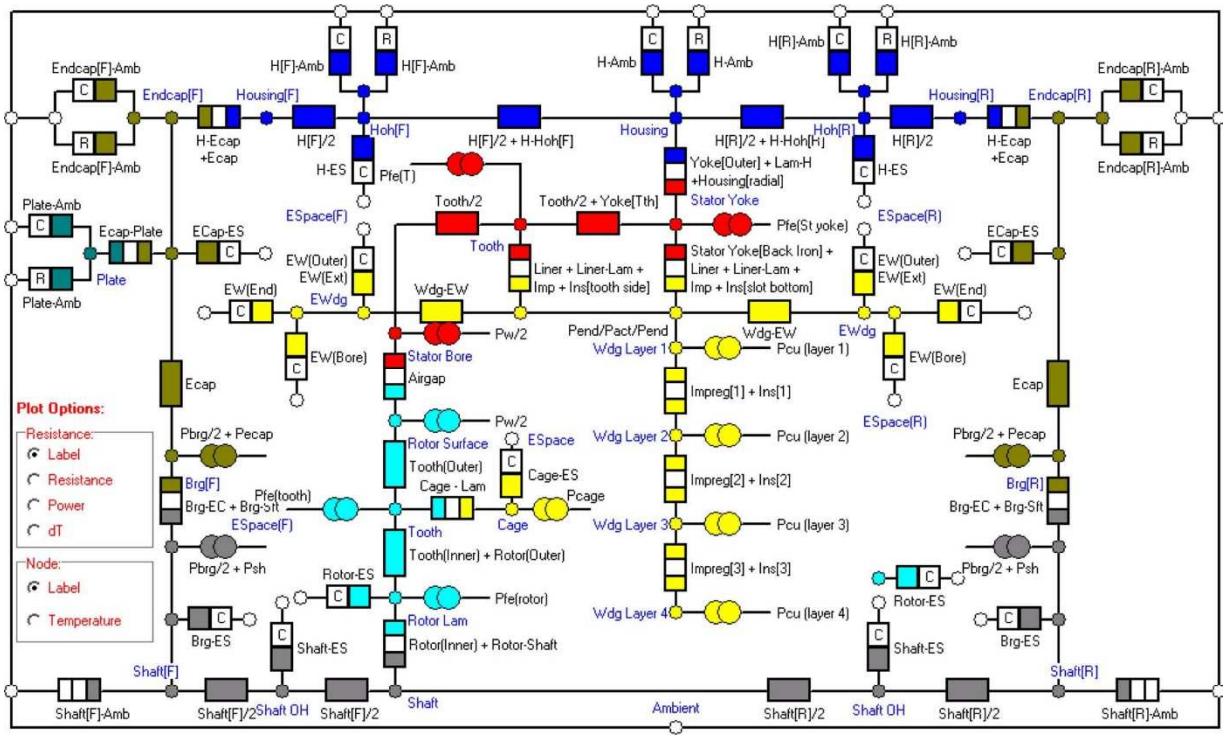

Figure 2-3: Heat transfer network for an electrical motor [Boglietti, 2009]

The calculation of conduction resistance is the path length divided by the product of the cross-sectional path area and thermal conductivity of the material. Whilst the combined convection and radiation resistance can be defined by the path length divided by the product of the surface area and total heat transfer coefficient. These resistances can be separated by separating the coefficients. The radiation heat transfer coefficient will be a function of the surface properties, such as emissivity and view factor. The emissivity will depend on the type of material whilst the view factor will depend on the geometry. The convection heat transfer coefficient is based on the velocity gradient of the fluid at the surface and is most often defined by empirical formulations. Many convection correlations have already been derived for the types of shapes encountered in the construction of electrical machines and are readily available in the heat transfer literature, in forms that incorporate whether the cooling is by natural or forced convection, as already mentioned in section 2.1.

The alternative to this approach is numerical analysis, which opens the opportunity to model any device geometry. This technique however, as well as having a long setup time, often comes with a very high computational cost relative to analytical techniques. Numerical analysis is generally of two categories, finite element analysis (FEA) and computational fluid dynamics (CFD). The use of CFD in the case of electrical machines is advantageous to investigate instances of complex air flow, such as around the end windings of the motor. FEA is best suited to analyse the conduction of heat through the solid components. As it can only model the solid geometry, the convection occurring at the

boundaries of a given geometry must be dealt with through analytical or empirical algorithms similar to the techniques used in lumped parameter modelling.

In recent years there have been several papers published with regards to the thermal analysis of electric machines. The majority of such papers deal with thermal aspects that may be difficult to analyse due to particular motor designs. Often the focus tends to be on how to estimate levels of cooling for various casing designs when undergoing different forms of convection. These issues will be elaborated on further in the coming sections. Though a sudden rise in awareness is leading to increased work aimed at developing electrical motor thermal models, "the number of published technical papers relating to the thermal analysis of electric motors is still many orders of magnitude fewer than those associated with electromagnetic analysis" Staton *et al* (2005).

It is common to see a combined thermal and electromagnetic analysis, in which investigations into the thermal aspects were achieved using the lumped-circuit or thermal network technique. An example is work by Alberti *et al* (2008) in which a combination of finite element analysis and analytical techniques were used to judge the performance of induction motors, including the temperature rise of various machine parts. The goal was to achieve a way of rapidly obtaining machine performance, by minimising the FE analysis whilst using a lumped-parameter thermal network, as traditional coupled thermal-magnetic analysis can take up considerable computational time. The predicted temperatures were compared with results obtained through experimental testing and demonstrate the model as accurate. Concluding that the model can be extended to any motor adopting the same lamination and winding distribution as the present work.

Dorell (2006) performed a combined electromagnetic and thermal study of a permanent magnet motor, using two commercial packages, SPEED and Motor-CAD for each aspect. Dorell explains that though normally, both design procedures are carried out separately, it was possible to link these packages in a modern Windows environment. Measured and simulated temperatures of the end windings, frame and end-cap were compared, and the results were verified experimentally. In work by Y. See (2000), a thermal network was used to model a 5 hp induction motor, in which air ducts were built into the stator and rotor as forced cooling channels. The temperature of the coolant was measured throughout the motor and showed very good agreement with the results of the model.

Finally, Trigeol *et al* (2006) used a combined network and CFD method for modelling the machine. In this case, a lumped parameter model was used to predict the heat flow through the solid structure, whilst the CFD was used to simulate the convection occurring at the outer surface. Temperature values obtained by experiment and simulation were compared across the machine, and showed good agreement for the end windings, embedded windings, stator teeth, stator back iron, and housing.

The approaches demonstrated in the published work reveal that whilst using finite element analysis to solve for heat conduction through the solid regions of a machine, analytical techniques are often coupled into the analysis to account for heat convection at the outer surface. Though this combination may be sufficient for simpler flow scenarios, and certainly for cases of laminar flow, as the flow becomes more complex, computational fluid dynamics becomes the tool of choice to provide an accurate solution. This thesis involves turbulent airflow passing through a rotating turbine prior to interacting with the finned surface of an electrical machine. As no analytical technique exists to account for such airflow interactions, and as the internal details of the machine will not be included, a purely CFD approach will be taken to investigate this problem.

It is noteworthy that in none of these papers was CFD alone used as a technique to model the entire electrical machine, a reason for this will be discussed further on. The remainder of this chapter will focus on numerical modelling, specifically computational fluid dynamics.

The use of CFD for engineering applications can be traced back further than two decades, when it existed in the form of very simple commercial codes. The capabilities of the hardware at this time was so limited that small practical benefits to industry through numerical modelling would come at a very high computational cost. A better approach for industry was to collaborate with universities, specifically in the form of research projects aimed at evaluating the accuracy of numerical codes. In the majority of cases, the goal of a simulation was to obtain the heat transfer coefficient across a surface undergoing forced convection. This value could then be compared with equivalent results that had been measured experimentally or derived through analytical correlations.

In later years, a company would suggest an engineering problem (often with a known solution) in the area of fluid flow, turbulence or heat transfer, the most common examples given were based around coolant flow and isolated fan studies. With the extent of papers being published validating CFD, by the 1990s confidence in this approach began to arise, leading to more complicated designs that could otherwise not be tested experimentally to be investigated numerically. Indeed, currently CFD is the primary approach to understanding the flow of fluid in and around electrical machines, without which, the continuing progress towards higher power densities would be very slow.

2.3 The role of computational fluid dynamics

The process of CFD is based around discretising a domain through a finite volume technique, after which, Navier-Stokes equations are solved across the cells. The Navier-Stokes equations account for continuity, x, y, z momentum, and energy. Such an approach is termed a direct numerical solution (DNS), and its accuracy is ultimately dependent on the fineness of the mesh or individual cell size. This can certainly be achieved for laminar flows but would be essentially impossible for turbulent flows.

For the latter, there occur chaotic velocity variations in the body of flow termed as turbulent eddies that persist even to very small scales until finally dissipating as heat energy whilst over flow surfaces a laminar sublayer develops resulting in very steep changes of fluid velocity upon approaching a wall boundary. These flow phenomena are the reason for greater momentum and heat transfer encountered in turbulent flow. To capture such phenomenon correctly would necessitate very fine cell sizes, and consequently a very larger total cell count within the domain. Should this be achieved, the computing power required to run the simulation to a reasonable solution time would surpass the capabilities of even the most powerful super clusters.

To overcome this problem, many CFD codes will solve the finite volume domain by complementing the original Navier-Stokes equations with alternative turbulence models and wall functions, thereby allowing the use of more reasonable mesh sizes. The turbulent effects not otherwise simulated due to the coarseness of the mesh would instead be accounted for by the assumptions made in a chosen turbulence model. There are a variety of choices available to model (rather than simulate) turbulence in the flow to a reasonable degree of accuracy. The choice of each model depends on the flow conditions. Different models are more suited to a particular set of flow conditions, examples include the occurrence of flow separation, substantial body forces, or an overall rotating flow.

In addition to the knowledge of the underlying physics used in the CFD codes, it is vital for a CFD engineer to have the skills to convert any given CAD geometry into a discretised grid ready for the application of appropriate boundary conditions. The aspect of meshing makes running transient simulations computationally expensive, especially in cases when the mesh will be deforming due to rigid body motion. The beginning of CFD analysis involves importing in a 3D model produced in a CAD package. A crucial aspect to consider when selecting CFD software is how well it can deal with potential defects occurring due to the 3D model being converted and exported as a generic CAD file before sending it to the CFD engineer. A majority of time lost in a CFD project is in overcoming simulation problems due to inadequate mesh resolutions around complex geometries whilst trying to balance computational accuracy against computational expense.

The prospect of receiving a separately produced CAD model can lead to long lasting impediments when overcoming the obstacles related to meshing. Very often when dealing with electrical machines, automated meshing techniques are disregarded in favour of volumetric controls that specify the extent of mesh fineness at defined regions such as very narrow gaps within the flow domain. Many CFD codes would also require the domain to be split into different regions associated with rotating and stationary parts.

There are different types of analysis available when using CFD to examine electrical machines. The first type is that of internal flow, where ventilation is driven by a fan, such flow is most often encountered in TEFC motors or generators, here CFD can be used to analyse how airflow through the

generator assists in transferring heat from the overhanging end-windings to the outer housing. An example includes work by Lampard *et al* (1997) in which the effects of end-winding porosity on flow generated by the rotor were investigated. It was found that low porosity end-windings were found to create a choking effect on the generator airflow, and that the tangential momentum of the airflow is lost as it passes through the end-windings. The second type of analysis is related to the external flow around the outside of the generator and the associated heat transfer to the surrounding environment, which will be the focus of this thesis.

The third type of analysis involves fan design, as due to material costs, manufacturing processes and limitations in available space, fans used in electrical machines often times will provide poor aerodynamic efficiency, and as such is a very important area reserved for CFD. An example of such work was carried out by Connor (2013), in performing a steady-state conjugate heat transfer analysis of a mid-sized four pole synchronous electric generator. Both the airflow and thermal aspects of the model were validated using by measuring the mass flow rate and temperature values measured across an experimental test-rig. The CFD results revealed that the air resistance acting on the rotating fan accounted for 87% of the windage.

The final type relates to supporting analysis, such as in cases of water flow in cooling jackets, as well as the cooling of associated power electronics. This can be seen in the work of Liu *et al* (2015) who performed a thermal analysis of a water-jacket cooled electric motor, using analytical and experimental methods. Though the analytical solution was obtained using a lumped parameter thermal network (LPTN) the convection boundary was based on results obtained from CFD simulations of the machine externals.

After importing in a CAD geometry, a flow domain must be created and discretized, either around or inside the given model. Taking the example of a totally enclosed fan cooled electrical machine, the paths through the machine would form part of the flow domain across which pressure drops could then be determined by simulation. Boundary conditions must be applied to allow a solution to emerge, these include inlet conditions in the form of mass flow rates or total pressure, and most often atmospheric pressure at the outlets. Entire regions within the domain may be set as rotating to account for the forces imparted to the flow from a given geometry part, with exceptions applied as appropriate, in the form of zero tangential velocity, to any stationary wall boundary encompassed by such a region. In cases where heat is involved, the energy equation must be solved through the application of a boundary condition such as an assumed heat flux or surface temperature.

Importantly, when applying a temperature boundary condition during cases of forced convention, the value of defined surface temperature does not affect the resulting heat transfer coefficient, however this would not be true in laminar flows of very low Reynolds number, as the role of natural convection (driven by fluid buoyancy and surface temperatures) becomes greater, though this is rare.

The flow rate of fluid through ducts in machines are perhaps the easiest of results to validate and can be accomplished by measuring the velocity of flow (with the appropriate equipment) down a channel of known cross-sectional area. Similarly, the average heat transfer coefficient can be validated by the use of sensors to measure the varying temperatures around a body of known surface area.

Aside from dealing with convection through fluid flows, CFD can also be used to simulate heat conduction through solid components, effectively replacing the role of thermal finite element analysis (FEA). As such, CFD can be used to validate lumped parameter models. The ability to couple the simulation of heat conduction through solid bodies with convection at the solid-fluid interface is termed conjugate heat transfer. After a heat convection analysis, a purely heat conduction based analysis can be performed separately by disabling all but the energy equation. It was mentioned previously that it is rare to encounter a conjugate heat transfer simulation of an electrical machine. This is because a complete solution would involve applying heat source conditions to the copper and iron components and monitoring the temperature distribution across the outer casing until it stabilised, similar to a real-life test-rig. Unfortunately, reaching a stable temperature distribution can take up to 30 minutes, whereas a common maximum range that can be reasonably reached with CFD is closer to 5 seconds.

An alternative approach is to disregard the internal workings of the generator and instead apply a fixed temperature boundary to the outer surface of the casing and obtain the heat transfer coefficient at the solid-fluid interface. Given that this value is a function of the fluid velocity gradients at the interface it would not take long for an average value to stabilise. Normally heat would travel from the copper and iron sources to the outer casing, raising the temperature of the internal components and the outer casing until, based on the value of the convection heat transfer coefficient, the total rate of heat leaving the casing reaches the rate of heat being generated within the core. With knowledge of the internal heat source and heat transfer coefficient, an average temperature for the outer casing can then be calculated from the straightforward convection heat transfer equation that relates these variables to the temperature difference between the heated surface and ambient air.

2.3.1 Past CFD work in the cooling of electrical machines

Maughan *et al* (1990) performed numerical analysis to investigate convection past heated surfaces finding that the addition of longitudinal finned horizontal channels significantly enhanced the heat transfer due to the increase in available surface area. The analysis demonstrated a rise in heat transfer with increased fin height, but significant decreases, as the number of fins increase due to the reduced fin spacing. Importantly, this analysis was performed under laminar flow conditions. Burchell (2009) reported that Dr. Tease of Wavegen, based on his own experimental testing on smooth and finned housings, suggested that any increase in heat transfer by the addition of fins would be negligible.

This can be explained by the occurrence of leakage flow mentioned earlier. Experimental studies were conducted by Thombre and Sukhatme (1995) to confirm such leakage during fluid flow past fin arrays and its negative effect on heat transfer. After confirming this phenomenon, the ability to mitigate such an effect by the addition of a shroud over the arrays was investigated. This did indeed prove to reduce leakage flow and improve the cooling. It was further found that increasing the clearance between the fin tips and shroud cover had a detrimental effect on the heat transfer coefficients. These results corroborated earlier findings by Sparrow *et al* (1986) in which the effect of varying clearances for encompassing shrouds over generators were investigated, the difference being, Sparrow *et al* did not compare such finding against a bare fin array.

Micallef *et al* (2008) used computational fluid-dynamics modelling to investigate the cooling of the end region of a two-pole strip-wound TEFC induction motor. He suggests two design principles to improve heat transfer. Firstly, achieving higher velocities on the end shield and frame of a TEFC machine, in addition to the end winding. Secondly, to direct air over the most thermally critical surfaces, such as the tips of the end winding, as well as into parts of the end winding that have the lowest airflow resistance. As the modelling was validated by experimental measurements, in concluding his work, he mentions that CFD is effective to investigate the cooling arrangements in the end region of electrical machines.

Picking *et al* (2001) used CFD to model the ventilation and cooling of the rotors of salient pole machines. The airflow rate predicted by the CFD was compared with experimental values obtained by traversing through the duct outlets. Pickering highlights the agreement of the CFD results with the velocity profiles at the outlets of the radial ducts. Slight errors in terms of heat transfer of two finger outlets were associated with CAD simplifications in such ducts for reasons of meshing.

Liao *et al* (1999) performed a thermal management study of AC induction motors using computational fluid dynamics modelling to obtain a temperature and fluid flow solution. Highlighting that the life and performance of the AC induction motor is intimately linked to the motor temperature, as the stator winding temperature directly impacts the insulation system durability, whilst waste heat rejected through the housing can affect bearing temperatures and lead to fatigue. The internal and external temperature distributions across the housings were validated using thermal imaging and thermocouple data to confirm the accuracy of the CFD, which predicted the stator winding temperature rise within 3° C.

Further studies into improving heat transfer from electrical machines have looked at the addition of perforations to fin arrays. Shaeri and Yaghoubi (2009) and Sahin *et al* (2008), studied and compared the heat transfer coefficient from normal shrouded fins to porous and perforated fins for improving heat transfer whilst also reducing the weight and cost of heat exchanger equipment. The results of these studies demonstrate general improvement in the efficiency of heat transfer with perforated fins.

However, such perforations are only suitable for fins of large width and therefore would not be applicable to the thin width fins incorporated into small or medium sized generators, including the 18.5kW machine used by Wavegen, the dimensions of which form the basis for decided the geometry to be investigated in the CFD simulations of this thesis.

Despite the many studies carried out investigating the effect of design changes to generators to the improvement of heat transfer. The majority of focus is for cases of laminar flow, indeed, the only empirical correlation related to heat transfer coefficients for turbulent flow within fin channels was derived by Heiles in 1952 and assumes the flow to be purely axial. This thesis will not only investigate the effect of turbulent airflow past a finned generator housing, but more importantly, the additional effects of turbulent flow downstream of a rotating turbine and how this heat transfer varies with changing turbine designs.

The generator to be investigated in this thesis operates in the environment of an oscillating water column. The OWC converts the motion of water waves into a bi-directional flow of air forced back and forth through a rotating Wells turbine that powers an induction generator along its connecting shaft and is amongst the most popular ways of extracting wave energy from the sea. The generator itself is situated in between two sets of rotating turbines and consequently benefits from the cooling effect of the bidirectional airflow. Periods of high power output are attained by such generators when run on forced overload, this is dependent on the amplitude of the airflow velocity through the turbines and hence occurs mainly at times of high wave activity. The maximum value of this overload is limited by the internal temperature of the generator which is dependent on the cooling ability of the surrounding air and its interaction with the generator surface.

2.3.2 Past CFD work on the Wells turbine

The Wells turbine is a self-rectifying axial flow turbine consisting of untwisted rotor blades set radically at 90 degrees stagger. The aerofoil cross section of each blade is symmetrical; as a result, the tangential force acting on the blades is only in one direction despite the changing direction of incoming air flow. This eliminates the need for flow rectifying valves and guide vanes when producing power.

Over the past two decades much experimental work has been carried out on the Wells turbine mainly on improving performance focusing mainly on the overall operating characteristics than the internal flow phenomena. However, with the recent advances in computer hardware and software it has become practical to create computational fluid dynamic simulations of three dimensional turbulent flows through complex geometry. Numerical approaches are increasingly becoming vital for analysis and design and demand for it will continue to grow into the future.

The majority of experimental and numerical investigations into the Wells turbine have been carried out under steady unidirectional flow conditions. When analysing turbine performance, the low frequencies of sea waves are often used to justify a quasi-static approach. Recently, a few works have shown that taking this approach may not be completely representative, due to the phenomena of hysteresis, arising from the actual working conditions of the turbine at sea, in which the airflow is bidirectional and randomly variable.

Torresi *et al* (2008) used numerical simulations to provide an accurate description of the steady three-dimensional flow field in a high solidity (8 blade) Wells turbine used in an oscillating water column. The commercial code FLUENT was used to model the single monoplane turbine. The blades modelled were of constant chord length with a NACA 0015 profile. The flow domain was restricted to the turbine blades by using duct walls to account for the hub and outer shroud as illustrated in figure 2-4.

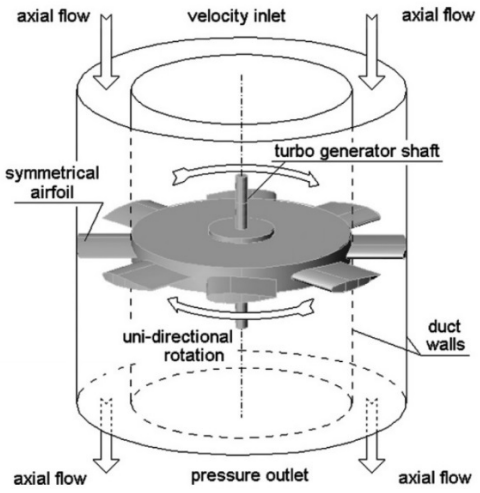

Figure 2-4: Geometry of the flow domain for high solidity Wells turbine by Toressi *et al* (2008)

The analysis used incompressible Reynolds Averaged Navier-Stokes (RANS) equations to solve the domain alongside a non-inertial rotating reference frame (or frozen rotor) approach for account for the turbine motion; this is a common approach when modelling a steady flow. The Spalart-Allmaras turbulence model was used to provide closure to the RANS equations and is a common choice for aerofoil simulations. By utilising a very fine mesh they were able to resolve the main flow features included the tip leakage flow. Toressi mentions that only recently has tip clearance flow been modelled in 3D simulations and explains the importance of analysing such tip leakage flow as it is the most important secondary flow in turbo machinery rotors. The method of varying the tip clearance was done by increasing the radius of the casing enshrouding the turbine. Good agreement with experimental data by Curran and Gato (1997) is reported in terms of efficiency, torque and total pressure drop over a range of flow rates. With regards to the effects of tip clearance on turbine performance, it was found to affect the torque and stagnation pressure drop coefficients as well as the

efficiency. Increasing the tip clearance reduced the stagnation pressure drop and torque coefficient. It was found that increasing the clearance gap provided a relief effect from the tip-clearance flow preventing separation of the flow on the blade suction side thus improving turbine performance. When the tip-gap becomes too high, this benefit to performance is defeated by the drop in pressure and the resulting energy loss. Such an analysis underlines the importance of optimising the tip-gap for improving the turbine performance in terms of torque coefficient and efficiency. Efficiency is defined as the useful work done by the turbine, divided by the product of the total pressure drop and flow rate across the blade. The findings by Toressi *et al* for the effect of tip clearance on turbine efficiency are given in figure 2-5 below. Where U* refers to the flow rate coefficient, defined as the ratio of the incoming air velocity and blade tangential tip speed, and TG refers to the tip-gap.

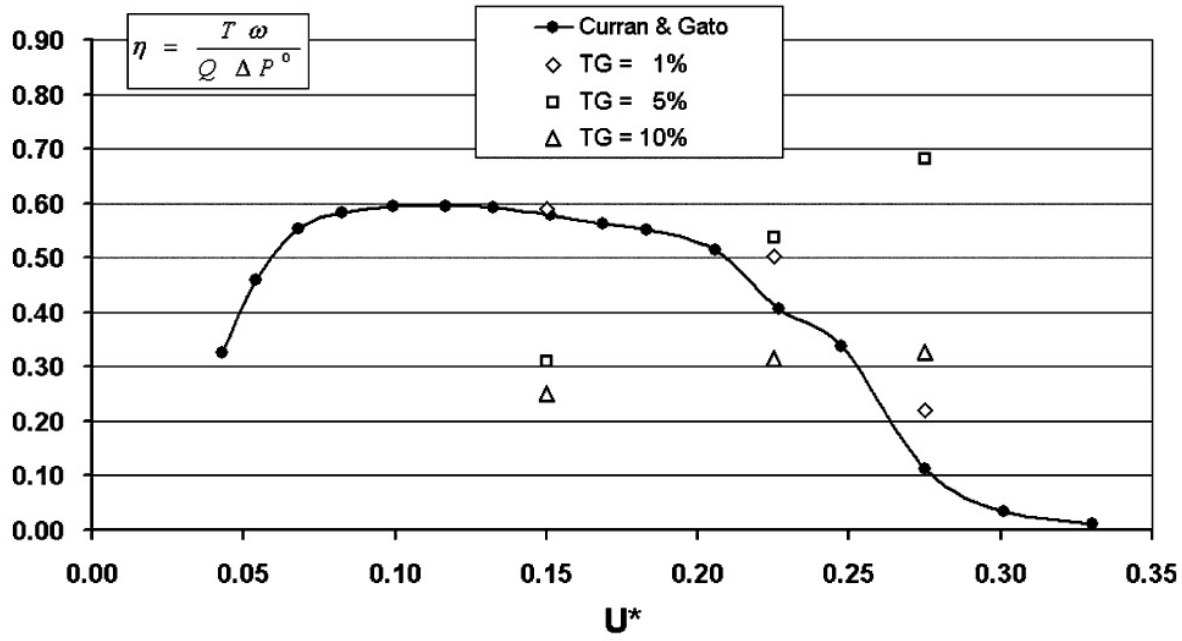

Figure 2-5: Efficiency for varying tip clearances by Toressi *et al* (2008)

Dhanasekaran *et al* (2005) conducted a computational analysis to investigate the performance of the Wells turbine for wave energy conversion. The commercial code FLUENT was used and the monoplane turbine blades were of constant chord with NACA 0021 profiles. The simulations were performed in unidirectional flow as experiments by Raghunathan and Ombaka (1984) indicate the change in power output and efficiency under oscillating flow conditions is within 3 to 5% of unidirectional flow conditions. As the flow was unidirectional, the simulation was run in steady-state, alongside the rotating reference fame. Similar to the work of Toressi *et al*, the RANS approach was used, however the choice of turbulence model to provide closure to equations was k-epsilon. This turbulence model is the most popular and has become the industry standard choice in CFD. It falls into the category of the two-equation models, the simplicity of the assumptions made in the closure method make it most robust, which ultimately contributed to its widespread use when modelling industrial applications.

The rotational speed of the turbine was kept constant while the inlet velocity was increased to obtain various flow coefficients. Dhanasekaran found the computational results of axial velocity upstream and downstream of the turbine matched very well with the measured values for all flow coefficients, the exception being at the hub and tip regions where the CFD values under predicted the measured values. The computational and measured values for turbine efficiency also matched well and an accurate turbine stalling point was found at a flow coefficient of approximately 0.2. On the suction side of the blade the static pressure in the leading-edge region increased with the flow coefficient due to an increased angle of attack. The percentage of chord length (CL) that this region of high pressure occupies also increases with flow coefficient. The turbine was observed to stall upon reaching a flow coefficient of 0.228, when the high-pressure region has exceeded the position of maximum thickness of the blade (30.3% CL). It must be said that though the CFD result matched very well, this does not mean that reality was simulated by the CFD perfectly, rather, as CFD tends to be within a bound of assumptions, very close results can be the result of one assumption "cancelling the other out".

Dhanasekaran explains that the merging of wakes behind the blades in the radial portion between 0.45 -1.0 led the turbine to stall, whilst the tip leakage flow acted to push these wakes further away behind the blade. This confirms experiments by Raghunathan *et al* that demonstrated how reducing the tip clearance, thereby weakening the tip leakage flow, advanced the onset of turbine stalling.

Kim *et al* (2002) investigated the effect of both blade sweep and blade profile on the performance of the Wells turbine. The commercial code Fluent was used, and simulations were conducted under steady-state flow conditions. The two blade designs compared were the NACA 0020 and CA9 profiles, the details of the two turbines are listed in table 2-1.

	NACA0020 blade	CA9 blade
Number of planes	1	
Number of blades N	6	
Chord length l	90 mm	
Solidity at mean radius σ_R	0.67	
Aspect ratio AR	0.5	
Hub to tip ratio v	0.7	
Tip diameter D_t	298 mm	
Tip clearance	1 mm	
Blade thickness	0.21 l	0.15 l
Location of blade thickness	0.3 l	0.198 l

Table 2-1: Comparison of details between two blade profiles by T.M. Kim *et al* (2002)

The turbine geometry was further modified by changing the blade sweep parameter *f*. In this case $f = g/l$, where g is the proportion of the leading-edge offsetting of the blade from an axis while l is the full chord length of the blade as illustrated in figure 2-6.

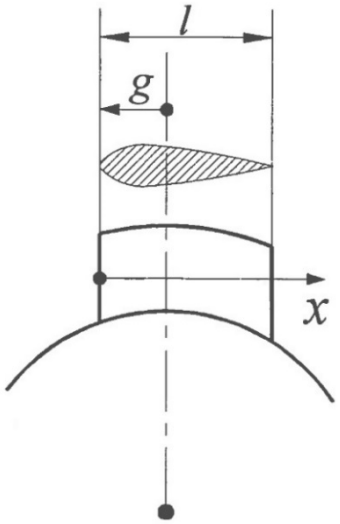

Figure 2-6: Schematic for adjusting blade sweep by Kim *et al* (2002)

In analysing the performance of the blade profiles, the turbine rotor speed was varied from a high speed to a low speed incrementally whilst the axial inlet velocity was kept constant. The domain surrounding the blade geometry, as shown in figure 2-7, was 6 and 10 chord lengths (l) upstream and downstream respectively.

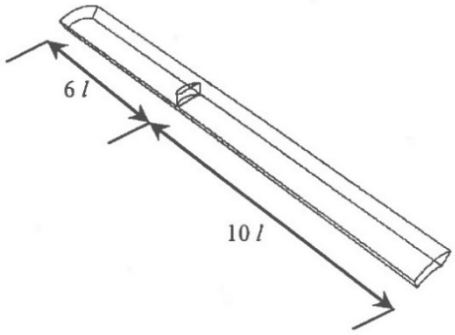

Figure 2-7: Outline for computational domain used by Kim *et al* (2002)

Initial experimental results for the NACA 0020 profile at the original blade sweep ratio of 0.35 were compared to CFD simulations at blade sweep values between 0.25 and 0.75. The results are demonstrated in figure 2-8. Where α_R° is the angle of attack, *f* defines the value of blade sweep, and η is the efficiency.

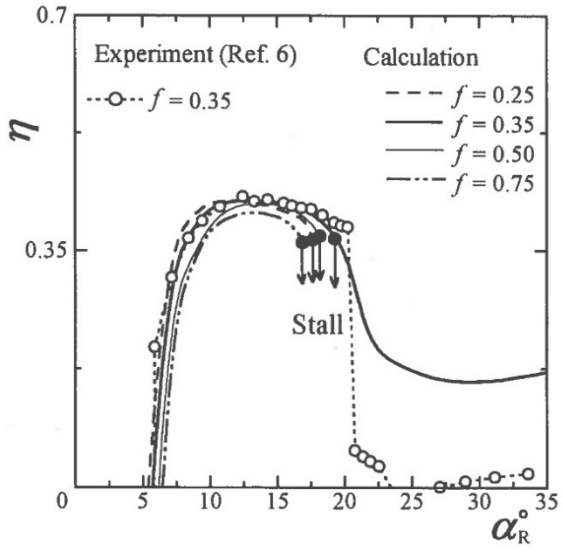

Figure 2-8: Turbine efficiency for varying blade sweep by Kim *et al* (2002)

When analysing the NACA 0020 blade profile, the efficiency was plotted against increasing angle of attack for each blade sweep ratio. The efficiency was seen to increase and decrease with the rising angle of attack. Sudden drops in efficiency corresponded with stalling of the turbine. The stall points for the 0.35 ratio matched well with previously documented experimental results. The angle of stall was found to be 19.3 degrees. The optimal value was determined to be 0.35 when considering the maximum achieved efficiency and resistance aerofoil stall. It was noted also that the CFD results for the 0.35 ratio had a wide discrepancy with experimental results after the point of stall. Following this, CFD simulations were conducted to compare the NACA 0020 profile with the CA9 profile at sweep ratios of 0.35 and 0.50, the results are shown in figure 2-9.

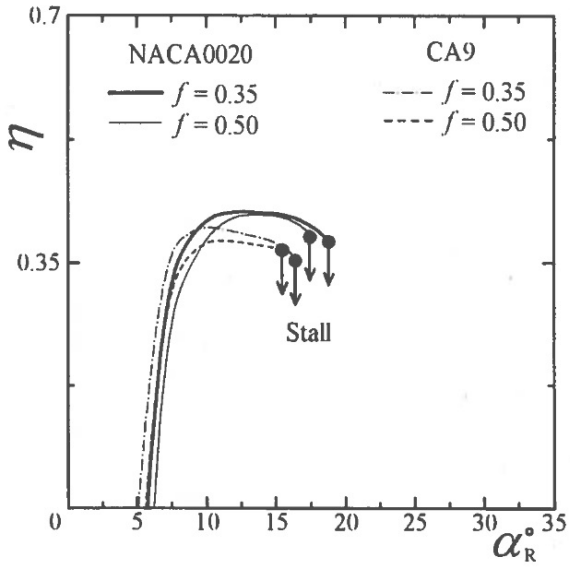

Figure 2-9: Turbine efficiency for varying blade profiles by Kim *et al* (2002)

The results for the CA9 blade differ from the NACA 0020 blade in the sense that the turbine stalls earlier for the 0.35 ratio than in the case of 0.50. It was also found that in the regions up to an attack angle of 9.5 degrees the efficiencies of the CA9 blade were slightly ahead than the NACA 0020 blade. However overall it was concluded that the NACA 0020 performs better than the CA9 blade. For both ratios the NACA 0020 has a higher maximum efficiency and is able to withstand a higher attack angle before stalling compared to the CA9 blade.

A major difference in opinion regarding using the quasi-static approach arose after Kinoue *et al* (2003), while conducting unsteady CFD simulations to measure the pressure drop across the turbine, observed hysteric effects under oscillating flow conditions. The relationship between airspeed and pressure drop was not unique but dependent on whether the airspeed was increasing or decreasing. This was especially evident when the amplitude of the airflow became large.

Kinoue investigated the mechanism of hysteretic characteristics across the Wells turbine for wave power conversion. He explains that though it is reasonable to employ quasi-static analysis of Wells turbine blade it may produce inaccurate results because of hysteretic characteristics in unsteady flow. Unsteady three-dimensional Navier-Stokes numerical simulations were conducted using FLUENT. These simulations revealed hysteretic behaviour in the plots of total pressure and torque coefficients against attack angles, as shown in figure 2-10, which qualitatively agreed very well with experimental results. In the simulations the rotor speed was kept constant and the axial velocity was increased and decreased to vary the angle of attack.

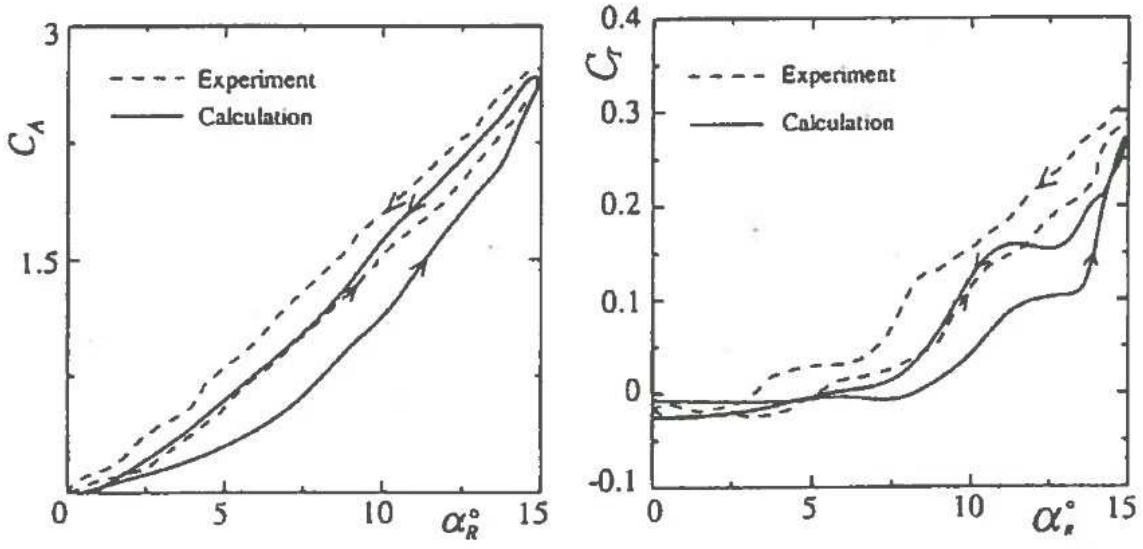

Figure 2-10: Hysteresis observed in total pressure coefficient (left) and torque coefficient (right) by Kinoue *et al* (2003)

In the analysis it was found that during acceleration the boundary layer was thicker along the suction surface and the region of separation was larger than in the decelerating flow. It was found that at the

trailing edge of the suction surface the flow is downward and that there is a clockwise vortex within the wake, as demonstrated in figure 2-11, which is responsible for the hysteretic behaviour. As the attack of angle increases rapidly, as in acceleration, this wake was found to intensify. During acceleration, the increased vortex intensity causes the region of separation to extend towards the mid span of the blade causing a reduction of the torque and total pressure coefficients. While in the decelerating flow, this vortex is weakened, and the separation region is reduced.

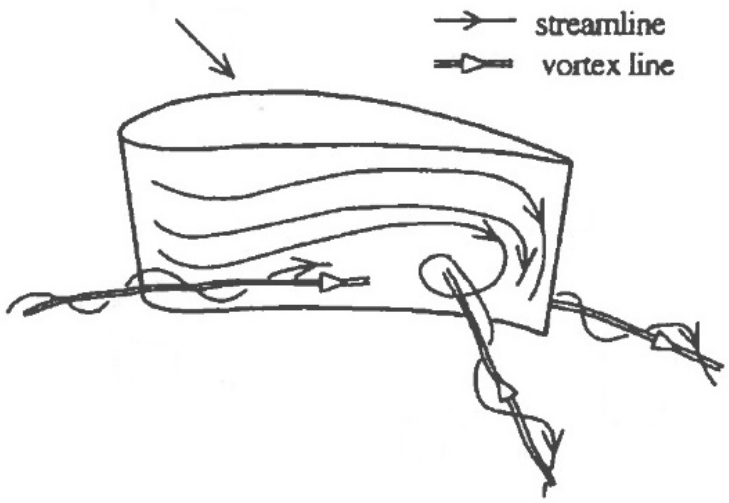

Figure 2-11: Flow structures across suction side of blade by Kinoue *et al* (2003)

2.4 The setup of CFD simulations for this thesis

The Wells turbine can be set up in three configurations for the cooling of electrical equipment in the OWC. Monoplane - a single turbine. Biplane – two turbines placed on opposite sides of the generator "co-rotating" in the same direction. Contra-rotating – The same setup as the biplane except the turbines rotate in opposite directions, and generally give a reduced performance.

Folley *et al* (2006) carried out experiments to compare these three configurations of the Wells turbine used in the LIMPET. In his report he mentions the number of studies investigating the effect of unsteady flow of Wells turbine performance suggest the quasi-static assumption is not always valid due to the hysteresis in the pressure-flow characteristics. However, he also mentions that the contra-rotating Wells turbine shows a more significant difference in performance between constant and unsteady flow conditions.

He points of that the frequency of flow oscillations in the wave converter is typically less than 0.2Hz, therefore if the time taken to reach stable flow conditions is longer than 5 seconds this would invalidate the quasi-static assumptions. In constant flow tests it was found that after a change in flow the contra-rotating turbine would take between 20 and 30 seconds to stabilise whereas both the monoplane and biplane turbines showed no discernible time to reach a stable state.

Folley calls into question the extensive use of quasi-static state numerical modelling of turbines as such models would not identify essentially transient and possibly chaotic characteristics. He does however give credit to the fact that, to date, quasi-state modelling of other forms of Wells turbines has produced adequate results. He finally concludes that quasi-static assumptions are insufficient to predict the performance of a contra-rotating Wells turbine however these assumptions appear to be acceptable when determining the performance of a monoplane or biplane (co-rotating blades) Wells turbine.

Considering the published work into the Wells turbine, though there has been focus into co-rotating turbines and the subsequent flow interaction between two turbines, never has any research been done into flow interactions from the Wells turbine with generation equipment. This thesis is unique in that it will essentially be a combination of research into the Wells turbine as well as external cooling of electrical machines. Similar to previous work on the Wells turbine, published work on TEFC electrical machines will often focus on a standalone generator rather than considering the effects of the operating environment.

This present work may also fall into a fan-design type analysis, in which a monoplane Wells turbine can be considered the cooling fan of the machine, and downstream effects, specifically interactions of airflow impingement on the heated generator, due to changes in blade design, are investigated. In each simulation the inlet airflow will be set at a constant (unidirectional) velocity and would thereby satisfy the steady-state analysis requirements outlined by Foley.

The goal will be to identify trends, and hence the optimal design to maximise cooling from the generator. Furthermore, given that the trends found by CFD will be validated by experimental results, it would provide an opportunity to demonstrate the accuracy of such commonly used “industry standard” assumptions when modelling turbomachinery. An important point of note is that despite separate numerical modelling work of electrical generators and Wells turbines in the past, this work will be unique in attempting to simulate the both the performance of the Wells turbine and downstream generator together.

3.0 HEAT CONDUCTION, CONVECTION AND FLUID FLOW

This chapter will cover the essential knowledge in understanding the theory of heat transfer and fluid flow. The first section will deal with the significance of the heat conduction equation. Given that the CFD code uses a complete energy equation, defined as the "heat equation" for cases of pure conduction, a breakdown of this equation is required to understand the workings of CFD.

The remaining sections will deal with heat transfer from a solid surface by the bulk motion of a surrounding fluid, thereby expanding the theory of heat transfer to that of convection and fluid flow. After covering the concepts of the velocity and thermal boundary layers, the final part of this chapter will focus on the difference between laminar and turbulent flow, specifically the increase in momentum and heat transfer brought about due to turbulence. Correlations for heat transfer can only be derived analytically in cases of laminar flow, whilst numerical methods, such as CFD, must be relied upon for scenarios of turbulent flow, as in this PhD work.

3.1 The Heat Conduction Equation

Fourier's law of heat conduction states that the rate of heat conduction is proportional to the thermal conductivity *k* of the material, the area *A*, oriented normal to the direction of heat transfer and the temperature gradient *-dT/dn* at the point of heat transfer as shown in equation 3.1. The negative sign results in positive values for heat transfer in the direction of falling temperature.

$$\dot{Q}_n = -kA\frac{\partial T}{\partial n} \tag{3.1}$$

This vector can be broken down into its three x, y and z components.

$$\overrightarrow{\dot{Q}_n} = \dot{Q}_x\vec{\imath} + \dot{Q}_y\vec{\jmath} + \dot{Q}_z\vec{k} \tag{3.2}$$

$$\dot{Q}_x = -kA_x\frac{\partial T}{\partial x} \qquad \dot{Q}_y = -kA_y\frac{\partial T}{\partial y} \qquad \dot{Q}_z = -kA_z\frac{\partial T}{\partial z} \tag{3.3}$$

Heat conduction is referred to as steady when the temperature distribution throughout the medium is constant with time whilst unsteady when the temperature distribution varies with time. The heat conduction may be significant in one dimension and negligible in the other two dimensions and hence denoted as one-dimensional heat conduction. Within a medium undergoing heat conduction there can be chemical, electrical or nuclear energy being converted into thermal energy. This is characterised as heat generation and is a volumetric phenomenon as it occurs throughout the body of the medium.

3.1.1 General Heat Conduction Equation

Though many practical cases of heat transfer occur in one dimension, for cases of multidirectional heat transfer a general heat conduction differential equation is required. Given a rectangular volume element as shown in figure 3-1 with lengths dx, dy and dz, density ρ and heat capacity C. The element may even represent a stationary volume of fluid, so long as the flow of energy is by conduction only, and not supplemented by fluid flow (convection).

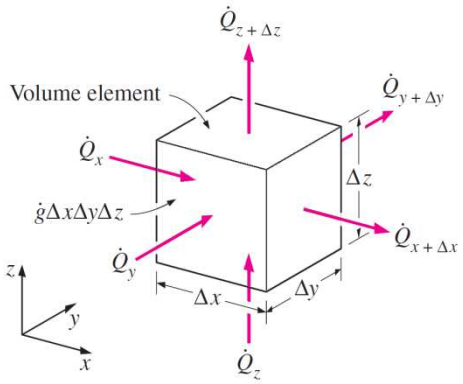

Figure 3-1: Heat conduction in three dimensions through rectangular volume element [Cengel, 2011]

An energy balance for this element can be written as:

$$\begin{pmatrix}Rate\ of\ heat\\ conduction\\ at\ x,y\ and\ z\end{pmatrix}-\begin{pmatrix}Rate\ of\ heat\\ conduction\\ at\ x+\Delta x\\ y+\Delta y,and\ z+\Delta z\end{pmatrix}+\begin{pmatrix}Rate\ of\ heat\\ generation\\ inside\ the\\ element\end{pmatrix}=\begin{pmatrix}Rate\ of\ change\\ of\ the\ energy\\ content\ of\ the\\ element\end{pmatrix}$$

In energy terms it can be written as

$$\dot{Q}_x+\dot{Q}_y+\dot{Q}_z-\dot{Q}_{x+\Delta x}-\dot{Q}_{y+\Delta y}-\dot{Q}_{z+\Delta z}+\dot{G}_{element}=\frac{\Delta E_{element}}{\Delta t} \tag{3.4}$$

The change in the energy content of an element by would be $Q=mC_v\Delta T$, where m is the total mass of the element, C_v is the specific heat capacity at constant volume and ΔT is the change in temperature of the element due the heat transfer. Since the volume of the element is $V_{element}=dxdydz$, the rate of change in energy of the element and the rate of energy generation inside the element can be further expressed as

$$\Delta E_{element}=E_{t+\Delta t}-E_t=mC(T_{t+\Delta t}-T_t)=\rho CA\Delta x\Delta y\Delta z(T_{t+\Delta t}-T_t) \tag{3.5}$$

$$\dot{G}_{element}=\dot{g}V_{element}=\dot{g}A\Delta x\Delta y\Delta z \tag{3.6}$$

Through substitution this becomes

$$\dot{Q}_x + \dot{Q}_y + \dot{Q}_z - \dot{Q}_{x+\Delta x} - \dot{Q}_{y+\Delta y} - \dot{Q}_{z+\Delta z} + \dot{g}A\Delta x\Delta y\Delta z = \rho CA\Delta x\Delta y\Delta z\frac{(T_{t+\Delta t} - T_t)}{\Delta t} \tag{3.6}$$

Dividing both sides by the volume of the element $dxdydz$, this becomes

$$-\frac{1}{\Delta y\Delta z}\frac{\dot{Q}_{x+\Delta x} - \dot{Q}_x}{\Delta x} - \frac{1}{\Delta x\Delta z}\frac{\dot{Q}_{y+\Delta y} - \dot{Q}_y}{\Delta y} - \frac{1}{\Delta x\Delta y}\frac{\dot{Q}_{z+\Delta z} - \dot{Q}_z}{\Delta z} + \dot{g} = \rho C\frac{(T_{t+\Delta t} - T_t)}{\Delta t} \tag{3.7}$$

Taking account that the heat transfer areas in each direction as consisting of the other two directions, that is, $A_x = dydz$, $A_y = dxdz$, $A_z = dydx$ and recalling Fourier's law of heat conduction and taking the limit of dx, dy and dz to zero. The three-dimensional terms on the left-hand side of the equation become:

$$-\frac{1}{\Delta y\Delta z}\frac{d\dot{Q}_x}{dx} = -\frac{1}{\Delta y\Delta z}\frac{\partial}{\partial x}\left(-kA_x\frac{\partial T}{\partial x}\right) = -\frac{1}{\Delta y\Delta z}\frac{\partial}{\partial x}\left(-k\Delta y\Delta z\frac{\partial T}{\partial x}\right) = \frac{\partial}{\partial x}\left(k\frac{\partial T}{\partial x}\right) \tag{3.9}$$

$$-\frac{1}{\Delta x\Delta z}\frac{d\dot{Q}_y}{dy} = -\frac{1}{\Delta x\Delta z}\frac{\partial}{\partial y}\left(-kA_y\frac{\partial T}{\partial y}\right) = -\frac{1}{\Delta x\Delta z}\frac{\partial}{\partial y}\left(-k\Delta x\Delta z\frac{\partial T}{\partial y}\right) = \frac{\partial}{\partial y}\left(k\frac{\partial T}{\partial y}\right) \tag{3.10}$$

$$-\frac{1}{\Delta x\Delta y}\frac{d\dot{Q}_z}{dz} = -\frac{1}{\Delta x\Delta y}\frac{\partial}{\partial z}\left(-kA_z\frac{\partial T}{\partial z}\right) = -\frac{1}{\Delta x\Delta y}\frac{\partial}{\partial z}\left(-k\Delta x\Delta y\frac{\partial T}{\partial z}\right) = \frac{\partial}{\partial z}\left(k\frac{\partial T}{\partial z}\right) \tag{3.11}$$

Through substitution this becomes

$$\frac{\partial}{\partial x}\left(k\frac{\partial T}{\partial x}\right) + \frac{\partial}{\partial y}\left(k\frac{\partial T}{\partial y}\right) + \frac{\partial}{\partial z}\left(k\frac{\partial T}{\partial z}\right) + \dot{g} = \rho C\frac{\partial T}{\partial t} \tag{3.12}$$

Finally taking the limit of T and t to zero and assuming the thermal conductivity k to be constant the equation becomes

$$\frac{\partial^2 T}{\partial x^2} + \frac{\partial^2 T}{\partial y^2} + \frac{\partial^2 T}{\partial z^2} + \frac{\dot{g}}{k} = \frac{1}{\propto}\frac{\partial T}{\partial t} \tag{3.13}$$

The property $\propto$ represents the thermal diffusivity, and represents the rate at which the heat moves through the material. The equation can be reduced under the conditions of steady-state, as well as transient with no heat generation. In cases of one-directional heat transfer in the x-direction, the y and z terms would drop out.

3.1.2 The Meaning of the Heat Equation

One Dimensional Heat Conduction

It is important to understand the meaning of the heat equation. The equations for steady state and transient one-dimensional heat conduction one expressed as

$$\frac{d^2T}{dx^2} = 0 \qquad and \qquad \frac{d^2T}{dx^2} = \frac{1}{\propto}\frac{dT}{dt} \tag{3.14}$$

Integrating the steady state equation twice shows that the temperature between the two boundaries of a medium varies linearly with position as revealed by the general solution below.

$$T(x) = C_1 x + C_2 \tag{3.15}$$

Should the distribution of temperature not be linear, the transient heat equation states that the temperature will change with time at a rate equal to the concavity of the temperature distribution, that is, how rapidly the temperature gradient changes with position, until the distribution becomes linear and then remains at this steady state. This progress can be seen in the figure 3-2 below, the change in temperature with time occurs most in the centre of the temperature distribution where the concavity is also greatest.

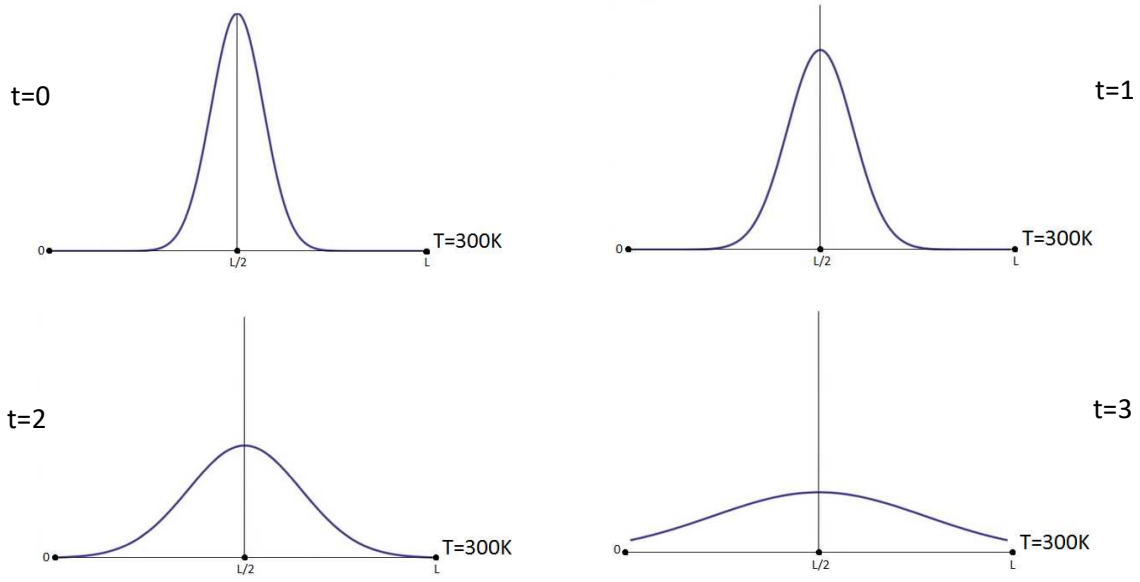

Figure 3-2: One dimensional temperature distribution over time [Commutant, 2011]

The term $\propto = k/\rho C$, representing the thermal diffusivity, is seen only in the transient heat equations. Unlike the thermal conductivity k, which is related to the rate of steady heat conduction, the thermal diffusivity is related to the overall speed throughout the medium at which the heat conduction rate

changes until it reaches steady state. The specific heat capacity variable can include a subscript to define whether the medium is at constant pressure C_p or constant volume C_v.

Two-Dimensional Heat Conduction

Similarly, when the heat equation describes two dimensional steady-state heat conduction it is expressed as:

$$\frac{d^2T}{dx^2} + \frac{d^2T}{dy^2} = 0 \tag{3.16}$$

A two-dimensional steady state temperature distribution $T = T(x, y)$ is shown in figure 3-3 below, the temperature boundary condition on the right wall is a parabola with a maximum value in the centre at $T = 400K$ whilst the other boundaries are fixed temperatures at $T = 300K$. As required by the equation, at every point, if the rate of change of the temperature gradient is increasing in the positive x direction then it will be decreasing by the same magnitude in the positive y direction.

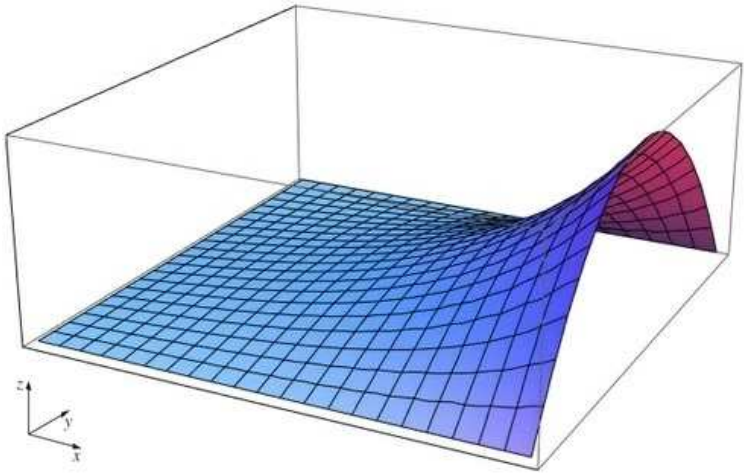

Figure 3-3: Two dimensional steady-state temperature distribution [Commutant, 2011]

Similar to the one-dimensional case, in a transient situation the time rate of change of temperature from any initial condition is equal to the sum of these concavity values until they become equal and opposite.

3.1.3 Heat Generation in a Solid

When heat generation is included in the conduction equation it is expressed per unit volume of the medium and is donated by g, in the unit W/m3. Under steady conditions the energy balance can be for heat generation within a solid can be expressed as:

$$\begin{pmatrix} Rate\ of\ Heat\ Transfer \\ from\ the\ solid \end{pmatrix} = \begin{pmatrix} Rate\ of\ Energy\ Generation \\ within\ the\ solid \end{pmatrix}$$

In energy terms it can be written as:

$$\dot{Q} = \dot{g}V \tag{3.17}$$

The heat transfer rate from the solid surface can be expressed through Newton's law of cooling as:

$$\dot{Q} = hA_s(T_s - T_\infty) \tag{3.18}$$

Combining these equations and solving for surface temperature T_s gives

$$T_s = T_\infty + \frac{\dot{g}V}{hA_s} \tag{3.19}$$

For a large plane wall of thickness $2L$ the surface area would be $2A$ whilst the volume would $2LA$ therefore the equation would reduce to

$$T_s = T_\infty + \frac{\dot{g}L}{h} \tag{3.20}$$

For a long solid cylinder of radius r_0, the surface area would be $A_0 = 2\pi r_0 L$ and $V = \pi r_0^2 L$ thereby reducing the equation to:

$$T_s = T_\infty + \frac{\dot{g}r_0}{2h} \tag{3.21}$$

3.2 Convection and the Nusselt Number

In the case of a stationary surrounding fluid, the initial heat transfer by heat conduction reduces the relative density of the surrounding fluid, and motion ensues, due to the natural buoyancy effects that cause such warmer (less dense) fluids to rise against gravity. Hence, heat transfer by convection is inevitable between solid-fluid interfaces. The rate of convection heat transfer can be expressed by Newton's law of cooling given in equation 3.22; the equivalent heat flux (heat transfer per unit area) through the fluid layer is expressed by equation 3.23.

$$\dot{Q}_{convection} = hA_s(T_s - T_{inf}) \tag{3.22}$$

(3.23)

$$\dot{q}_{convection} = h\Delta T$$

Where h is the convection heat transfer coefficient, T_s is the surface temperature and T_{inf} is the free-stream temperature. During heat convection, the fluid in direct contact with the surface is at rest; hence the mechanism of heat transfer at this point is purely by conduction. The equation for the heat flux is therefore

$$\dot{q}_{convection} = k_{fluid} \left. \frac{\partial T}{\partial y} \right|_{y=0} \tag{3.24}$$

Where T is a function of y and hence $(\partial T/\partial y)_{y=0}$ is the temperature gradient at the surface, by combining equations 3.22 and 3.24, the convection coefficient can be expressed as below

$$h = \frac{k_{fluid} \left. \frac{dT}{dy} \right|_{y=0}}{(T_s - T_{inf})} \tag{3.25}$$

Given that in the absolute absence of fluid flow the heat transfer would only occur by conduction from the surface to the fluid, and given that the fluid in contact with the surface assumes the same surface temperate, the heat flux through a layer of fluid of this L and temperature difference $\Delta T = T_2 - T_1$ would be

$$\dot{q}_{conduction} = k\Delta T/L \tag{3.26}$$

In heat transfer studies it is common to use a dimensionless heat transfer coefficient, known as the Nusselt number, to judge the enhancement of heat transfer due to the use of convection as compared to if the heat transfer was by conduction alone. It is therefore based on the ratio of the convective and conductive heat fluxes.

$$\frac{\dot{q}_{convection}}{\dot{q}_{conduction}} = \frac{h\Delta T}{k\Delta T/L} = \frac{hL_c}{k} = Nu \tag{3.27}$$

Where L_c is the characteristic length of the surface over which the convection is occurring. When comparing surfaces, a larger Nusselt number indicates more effective convection, whilst a Nusselt number of Nu = 1, based on equation 4.4, represents a surface undergoing heat transfer by conduction alone.

3.3 The Classification of Fluid Flows

As convection heat transfer is dependent on fluid flow it is important to mention the characteristic that distinguish the various categories of such fluid flow. These classifications based on whether the flow is viscous or inviscid, internal or external, compressible or incompressible and laminar or turbulent.

As fluid flowing with a given velocity passes over a surface, the fluid layer in contact with the wall will be stationary; this layer effectively slows down the subsequent layers further away from the wall. The result is a velocity distribution that gradually approaches the free stream velocity at increasing distances away from the wall, this internal resistance to flow is referred to as viscosity. The flow in the layers closer to the wall is called viscous flow, however even in the free stream region there are still cohesive forces that can contribute to slight viscous effects. No fluid flow is truly free from viscosity. However, should the viscosity be sufficiently low, such effects can be neglected, simplifying any consequent analysis without a great loss in accuracy. The name given to such an idealised flow with zero viscosity is inviscid flow.

Should the fluid flow be completely bounded by solid surfaces it is defined as internal flow, such when flowing through a pipe or duct. If the fluid flows over a surface or within a confined channel it is characterised as external flow. Depending on whether the flow is internal and external, different characteristic lengths must be used when determining flow behaviour and extents of heat transfer.

Considering a stationary liquid, the observed density change is negligible with increasing pressure, and hence is classified as an incompressible substance; the same cannot be said of gases. However, should this pressure be applied to induce fluid flow, gases can also be treated as incompressible if the change in density remains less than 5%, which is the case when the velocity of the flow remains under 30% the speed of sound in that gas, that is, at a Mach number lower than 0.3. Therefore, airflow with a velocity less than 100 m/s would be treated as incompressible.

The flow behaviour of a moving fluid may be observed to be either smooth or chaotic. This chaotic behaviour is more prevalent for fluids of lower viscosity. When the streamlines of fluid flow are seen to be smooth and ordered such a flow is defined as laminar. As the flow velocity increases these streamlines overlap and mix with each other in a chaotic fashion, defined as turbulent flow. The transition of a flow from a laminar to turbulent regime increases the power required to maintain the volume rate of flow, as well as increasing the rate of heat transfer experienced by the surfaces in contact with the fluid.

3.4 The Velocity Boundary Layer

As discussed previously, when a fluid with a uniform velocity flows over a flat plate, the velocity of fluid in contact with the plate surface will be zero; the effect of this is the slowing down of the layers further above. The effect of this velocity reduction diminishes with normal distance away from the plate surface until the velocity becomes essentially constant with distance. This constant velocity is referred to as the free-stream velocity and is equal to the undisturbed uniform velocity of the flow prior to interacting with the plate.

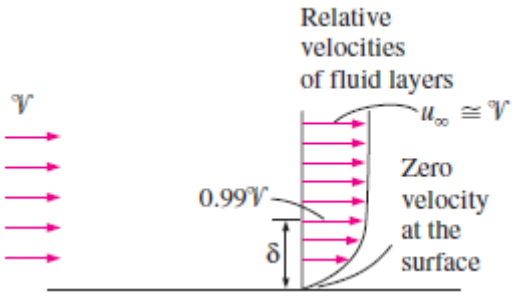

Figure 3-4: The velocity boundary layer above a flat plate [Cengel, 2011]

This effect of velocity reduction due to the no slip condition is demonstrated in figure 3-4, the region defined as δ is the velocity boundary layer. It is the distance from the plate surface up to which the velocity approaches 99% of the free-stream velocity u_∞. The flow can be divided into two regions based on the line at which the velocity $u = 0.99u_\infty$. Below this line is the boundary layer region in which the effects of fluid viscosity and shearing forces dominate the flow, resulting in the changes of velocity throughout. Above this line is the inviscid flow region where the velocity is essentially constant as the frictional forces due to fluid viscosity have very little effect.

Retuning back to the surface of the plate, as a fluid flows over this flat plate due to the no slip condition, the flowing fluid exerts a friction force on the plate surface in the direction of motion. The shear stress imposed from a moving fluid is proportional to the velocity gradient at that point, therefore the shear stress at the surface of a plate is

$$\tau_s = \mu \left.\frac{\partial u}{\partial y}\right|_{y=0} \tag{3.28}$$

Where μ represents the dynamic viscosity of the fluid with units $kg/m.s$, the ratio of dynamic viscosity to the fluid density is often referred to in the study of heat transfer; the name given to this ratio is the kinematic viscosity with units m^2/s.

Viscosity is a measure of a fluid's resistance to flow, with rising temperature it is found to decrease in liquids and increase in gases. Looking at equation 3.28 the shear stress is seen to be proportional to

the shear rate (or the velocity gradient at the surface). Newtonian fluids are defined by this linear relationship, such that the fluid viscosity remains constant, independent of the shear rate. A fluid is defined as non-Newtonian, when the apparent viscosity of the fluid increases or decreases with rising shear rate.

As Equation 3.28 requires information regarding the external flow velocity profile to calculate the shear stress it can be more practical to use equation 3.29, which calculates the shear stress based on the upstream free stream velocity V, the fluid density and a friction coefficient often derived from experiment. (3.29)

$$\tau_s = C_f \frac{\rho V^2}{2}$$

The total friction force over a surface is calculated by equation 3.30. Given that the frictional coefficient will vary along a surface, when calculating the friction force over a given surface area A, an average value for the friction coefficient is used.

$$F_f = C_f A_s \frac{\rho V^2}{2} \quad (3.30)$$

The value of the friction coefficient relates both to the power required to drive the flow and the resulting heat transfer coefficient of the surface in contact with the flow.

3.4.1 Further Understanding of Shear Stress

Just as there is a shear force from the moving fluid on a boundary surface, similarly, there is a shear force between each layer of fluid as a faster layer exerts a friction force on its adjacent slower layer. Another understanding of shear stress is achieved by the definition that force equals the rate of change of momentum, and hence the shear stress can be understood to be momentum flux.

Just as heat flux represents the rate at which heat flows from a boundary of higher temperature to a boundary of lower temperature, the shear stress represents the rate at which momentum flows from a layer of higher velocity to a layer of lower velocity. This analogy made clear by the fact that the equation for shear stress has the same form as that for heat flux, hence when describing momentum flux in a flowing fluid, a negative sign would be included in the equation to indicate the direction from higher to lower velocities.

As a fluid initially flows over a no-slip boundary, the fluid velocity at the boundary would be zero; this zero velocity, would over time, progress normal to the boundary surface until the entire fluid flow

came to a rest. The momentum in the fluid flow can be understood as being transferred from the initial free-stream to the slower fluid layers until finally being dissipated to the surface boundary.

In steady flow the applied pressure to induce fluid flow is balanced by the equal opposing shear force from the boundary surface; this maintains the flow speed despite the continuous momentum losses to the no-slip boundary.

3.5 The Thermal Boundary Layer

As fluid of a given temperature flows over an isothermal surface of another temperature T_s, the fluid in contact with the surface will attain thermal equilibrium with the surface temperature due to the no slip condition. Heat is transferred from the fluid layer to the adjacent fluid layers causing a progressive temperature change in the direction normal from the surface until the temperature approaches the original fluid temperature T_{inf} at a distance sufficiently far from the surface. An example of the temperature profile through the moving fluid is shown in figure 3-5. For convenience, the surface temperature is less than the temperature of the fluid to demonstrate the temperature increasing in the same direction as the velocity increases, that is, away from the surface.

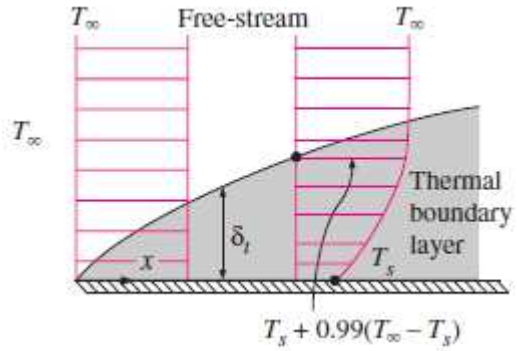

Figure 3-5: The thermal boundary layer over a cooler flat plate [Cengel, 2011]

Similar to the velocity boundary layer, the region in which the temperature changes are significant is called the thermal boundary layer. Given that the temperature varies between the T_s and T_{inf}, the thickness of the thermal boundary layer is defined as the distance from the surface at which the temperature difference is 99% of this total, as explained in equation 3.31.

$$T - T_s = 0.99(T_{inf} - T_s) \tag{3.31}$$

Taking a special case where the surface temperature $T_s = 0$, the equation becomes $T = 0.99T_{inf}$, similar to the case for the thickness of the boundary layer where $u = 0.99u_{inf}$.The thermal boundary layer becomes thicker downstream as the effects of heating transfer accumulate, similar to how the effects of shear frictional force accumulate in the velocity boundary layer.

The convection heat transfer coefficient from a surface is related to the temperature gradient at the point of contact. Whilst the temperature profile within the fluid above a heated surface is related to the velocity of the fluid flow over it. In convective heat transfer, unlike pure heat conduction, the steady-state temperature gradient through the fluid in a direction away from the surface will not be constant. Rather, the temperature gradient would be greater nearer the heated surface (indicative of the higher heat flux) and tend to zero asymptotically whilst approaching the free-stream temperature.

Over a heated or cooled surface, the thermal boundary layer develops simultaneously with the velocity boundary layer. Given that the temperature within the fluid is related to the fluid velocity it follows that the heat transfer coefficient will therefore be affected by the thickness of the velocity boundary layer relative to the thickness of the thermal boundary layer.

Recalling from section 3.1 the diffusivity term represented the rate at which the temperature changes within a medium due to an accumulation of energy. Given that during convection, the medium (in this case the fluid) is in motion, the diffusivity term represents how far the change in temperature will extend, and hence the thickness of the thermal boundary layer.

For a given velocity, a fluid with a higher thermal conductivity will develop a thicker thermal boundary layer as the heat will diffuse from the heated surface further, the result being that the distance from the wall in which the temperature changes are significant will be extend further. Similarly, for a given velocity, a more viscous fluid will have a greater resistance to flow and therefore will develop a thicker boundary layer, that is, the effect on the moment of the fluid flow in the direction perpendicular to the wall will extend (or diffuse) further.

The Prandtl number is a dimensionless ratio of the molecular diffusivity of momentum against the molecular diffusivity of heat, and hence is used to describe the relevant thickness of the velocity and thermal boundary layers.

$$Pr = \frac{\text{molecular diffusivity of momentum}}{\text{molecular diffusivity of heat}} \tag{3.32}$$

Gases generally have Prandtl numbers of approximately 1, indicating that momentum and heat dissipate approximately at the same rate. Liquid metals have very low Prandtl numbers, often less than 0.01. Whilst the Prandtl numbers of heavy oils can exceed 100,000. Consequently, the thermal boundary layer is much thicker as compared to the velocity boundary layer in liquid metals (good conductors of heat) whilst the opposite is true in the case of oils.

3.6 Laminar and Turbulent flow

When examining the flow in a pipe or over a plate, the flow initially will be streamlined and ordered, however further downstream the flow will become chaotic and disordered. The initial flow is defined as laminar flow and is recognisable by the smooth streamlines that do not overlap and constant values of velocity throughout the flow region. The flow downstream is defined as turbulent and is instead recognised by the chaotic overlapping of streamlines and irregular fluctuations in velocity.

The transition of flow from laminar to turbulent flow generally does not occur all of a sudden but rather will gradually progress with increasing chaotic velocity fluctuations until it becomes fully turbulent flow. The velocity fluctuations are a result of the rapid mixing of fluid particles from adjacent layers, as indicated by the overlapping of streamlines, resulting in a transfer of momentum across the layers. The transition from a laminar to turbulent boundary layer, even at low velocities, can be "triggered" by the use of obstacles or uneven surfaces which can introduce flow instabilities and hence turbulence to an otherwise stable laminar flow.

Figure 3-6 shows the development of the boundary layer along a flat plate progressing from a laminar to a turbulent flow regime. The velocity profile of laminar flow is approximately parabolic whilst the profile of turbulent flow is flat in the core of the flow with a sharper reduction close to the walls.

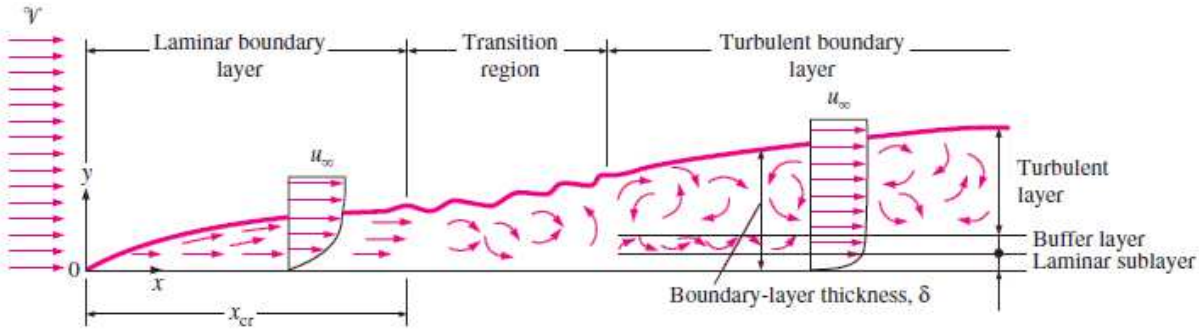

Figure 3-6: Laminar and turbulent flow over a flat plate [Cengel, 2011]

Examining figure 3-6, the turbulent boundary layer is seen to comprise of three layers. The layer in contact with the surface is known as the viscous or laminar sub layer. In this layer, as the name suggests, viscous forces dominate the flow, resulting in laminar streamlines. The flow velocity in this layer is seen to increase linearly with distance from the wall. Above this is the buffer layer, turbulent effects exist in this layer however they are less significant than the moment transfer due to diffusion. Finally, above this is the turbulent layer, here the effects of turbulence on the transfer of momentum and heat outweigh the diffusion effects that would otherwise transfer momentum and heat.

The continuous velocity fluctuations throughout the turbulent fluid flow causes intense mixing and thus increase the momentum transfer and heat transfer between the fluid particles. This results in an increased friction force experienced by the surface over which the fluid flows, as well as an increase

in the convective heat transfer rate. The coefficients of friction and heat transfer approach their maximum values as the flow becomes fully developed. Given the explanation from section 4.3 that the boundary layer thickness indicates the extent to which momentum diffuses in the direction normal to a surface, the increased momentum transfer in the turbulent flow results in a thicker boundary layer relative to purely laminar flow.

It is common to encounter turbulent flow in engineering applications where it is utilised to take advantage of the increased heat transfer rate associated with it, however due to the accompanied increase in friction it also requires more cost, often in the form of pumping power, to maintain its benefit. Additional ways of increasing heat transfer from a surface can be to increase the surface area exposed to a flowing fluid, as well as the adjusting the angle of the surface so that the flow is impinging the surface at right angles rather than moving parallel to it.

3.6.1 Reynolds number

As fluid flows over a surface the initial laminar boundary layer will become turbulent depending on a number of factors related both to the fluid and the surface. In terms of the surface, these include the geometry, roughness and temperature, whilst for the fluid, these include the free-stream velocity, density, viscosity and other fluid properties.

The flow regime is determined essentially by the ratio of inertia forces over viscous forces acting on the flow. This ratio is defined as the Reynolds number, a dimensionless quantity, which in the case of external flow is expressed as

$$Re = \frac{\text{Ineria Force}}{\text{Viscous Force}} = \frac{\rho V L_c}{\mu} = \frac{V L_c}{v} \tag{3.33}$$

Where V refers to the free-stream upstream velocity of the flow, L_c is a characteristic length for a given geometry, and $v = \rho/\mu$ is the kinematic viscosity of the fluid.

The characteristic length for a flat plate is the distance x from the leading edge. To achieve a high Reynolds number, the inertial forces, which depend on the velocity and density of the flow, would have to be large as compared to the viscous forces. These weaker viscous forces would not be able to prevent the rapid mixing of fluid particles from adjacent fluid layers, resulting in the continuous velocity fluctuations throughout the fluid indicative of turbulent flow. For a fluid flowing under the same inertial forces, but having a higher viscosity would reduce the Reynolds number. In this case the viscous forces would be more able to prevent the streamlines from overlapping thereby reducing the turbulence in the flow.

The units of the kinematic viscosity v are the same as thermal diffusivity α and hence can be regarded as the molecular diffusivity of momentum, as mentioned in the explanation of the Prandtl number. The higher the kinematic viscosity of a fluid, the further that the effects on momentum, demonstrated by the boundary layer thickness, will extend from the stationary surface towards the free-stream, and hence a lower Reynolds number.

The value of the Reynolds number is referred to as the critical Reynolds number. This value differs depending on the flow geometry. In the case of external flow over a flat plate the value is given to be $Re_{cr} = ux_{cr}/v = 5x10^5$, where the value of x_{cr} represents the distance from the leading edge at which point the flow will begin to transition from laminar to turbulent. The value of x_{cr} can vary depending on the level of turbulence in the free stream.

3.7 Heat and Momentum Transfer in Turbulent flow

Given that the majority of mass flows that occur in engineering applications are turbulent it is important to understand the effect that turbulence has on both wall shear stress and heat transfer. The rapid and random velocity fluctuations that occur in the turbulent boundary layer are called eddies. Such eddies provide an additional mechanism for both momentum and heat transfer.

When the flow regime is laminar, the fluid flow is characterised by ordered streamlines that do not overlap, momentum and heat is transported across these streamlines in a manner termed as molecular diffusion as explained previously when discussing momentum flux.

Whereas in the turbulent boundary layer, the transport of momentum and heat across the stream lines occurs by the transverse motion of eddies, as these eddies progress they mix with the flow, gradually losing their intensities. The transport of momentum and heat by these eddies is much greater in comparison to that achieved through molecular diffusion alone, resulting in far higher coefficients for skin fiction and heat transfer.

A fluid flow can be described as steady when the flow properties at any particular location remain constant with time; this is certainly possible in laminar flow. However, when steady flow is achieved for turbulent flow, eddies will cause significant fluctuations of the flow properties with time, including the values of velocity, pressure and temperature.

An example of the instantaneous velocity component u, in a steady turbulent flow is shown in figure 3-7, it is seen that the instantaneous velocity values fluctuate about a mean value, suggesting that this velocity value can be expressed as a sum of the mean value $\bar{u}$ and a fluctuating component u'.

$$u = \bar{u} + u' \tag{3.34}$$

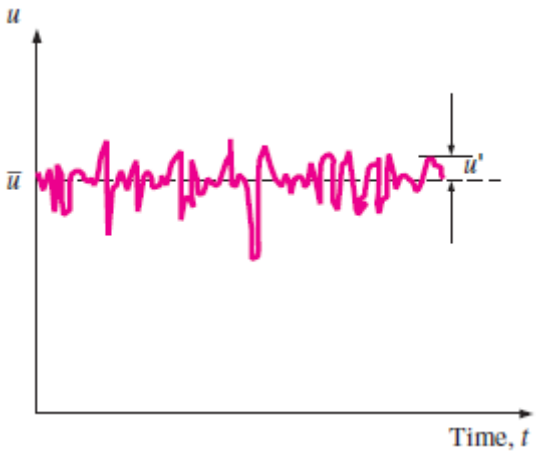

Figure 3-7: Fluctuations of velocity component u with time [Cengel, 2011]

Similarly, the other properties in the flow such as pressure and temperature, can be expressed as $P = \bar{P} + P'$ and $T = \bar{T} + T'$. The mean value of a turbulent flow property is obtained by taking a time average over an interval sufficiently large as to render the net effects of the turbulent fluctuations zero, thereby making the time average of the fluctuating component zero, hence $\overline{u'} = 0$.

The value of the fluctuating component of a flow property is often only a few percent of the mean value, however as the frequency of these eddies is so high, in the order of thousands per second, they provide a very effective means for the transport of both momentum and thermal energy. In the case of steady turbulent flow, the time independent values are indicated by an overbar.

Given such a steady horizontal flow of fluid over a surface, though the fluid would have no mean vertical flow value, there would still be turbulent velocity fluctuations in the vertical direction, the mass flow rate per surface area of these eddies normal to the horizontal flow would be $\rho v'$. Recalling equation 3.5, the change in fluid energy with temperature is $q = mC_p dT$ (at constant pressure), the rate of change of energy due to mass transfer would therefore be $\dot{q} = \dot{m}C_p dT$. Since T' is the temperature variation from the mean value due to turbulent eddies, the rate of heat flux, or in this case the rate of thermal energy transport by these turbulent eddies is $\dot{q}_t = \rho C_p v'T'$.

Recalling that the rate of momentum diffusion in laminar flow was simply the shear stress in the flow $\tau = -\mu(\partial u/\partial y)$, a similar approach could be taken for turbulent flow to obtain the equivalent shear stress $\tau = -\mu(\partial \bar{u}/\partial y)$, where $\bar{u}$ represents the mean value in the steady flow, however experimental studies indicate that the shear stress is larger due to the turbulence in the flow. Therefore, in turbulent flow, the total shear stress can be divided into two components, a laminar component, which as mentioned previously results from the friction between the different flow speeds of adjacent fluid layers, expressed as $\tau_{laminar} = -\mu(\partial \bar{u}/\partial y)$ and a turbulent component, which results from the friction between the fluctuating fluid particles. The expression for the total shear stress is thereby

$$\tau_{total} = \tau_{laminar} + \tau_{turbulent} \tag{3.35}$$

Using a similar approach to find the turbulent heat flow, the rate of momentum transfer in a direction normal to the flow can be determined, by considering the same mass flow rate of eddies (or turbulent fluid particles) as before, passing through an area dA, and hence expressed as $\rho v' dA$. The result of this mass flow is a loss of momentum from the faster fluid particles to the slower fluid particles arriving. The turbulent fluctuation in horizontal velocity u′ is transferred between the faster and slower particles, the rate of increase of momentum for these arriving particles is therefore $(\rho v' dA)u'$. Given that a force exerted on a body equals the rate of change in momentum, the horizontal force acting parallel to the area dA can be understood to be $dF = -\rho u' v' dA$, the shear force per unit area due to turbulent eddies can be expressed as $dF/dA = -\rho u' v'$, and is understood to be the instantaneous turbulent shear stress. The turbulent component of the total shear stress in steady flow can therefore be expressed as

$$\tau_{turb} = -\rho \overline{u'v'} \tag{3.36}$$

This is referred to as the turbulent shear stress; the term $\overline{u'v'}$ is the product of $u'$and v' averaged over time and is not zero. It should not be confused with $\bar{u}'.\bar{v}' = 0$ which is the product of two zero values, $\bar{u}' = 0$ and $\bar{v}' = 0$. It is indicated from experimental results that $\overline{u'v'}$ is a negative quantity. Terms similar to $-\rho u' v'$ are described as Reynolds stresses, the negative sign ensures the value of the resultant stress is positive.

There are a number of semi-empirical formulations which attempt to relate these Reynolds stresses with time averaged velocity gradients as a means of providing mathematical closure to the equations of motion, such formulations are referred to as turbulence models.

The motion of eddies, results in the transport of fluid particles, which consequently increases the exchange of momentum and heat across the flow. Such a transfer of momentum and heat in turbulent boundary layers by eddies is comparable to molecular momentum and heat diffusion and as such the turbulent component to wall shear stress and heat transfer can be expressed as such

$$\tau_{turb} = -\rho \overline{u'v'} = \mu_t \frac{\partial \bar{u}}{\partial y} \qquad \text{and} \qquad \dot{q}_t = \rho C_p v' T' = -k_t \frac{\partial \bar{T}}{\partial y} \tag{3.37}$$

The terms μ_t and k_t are the turbulent equivalent of viscosity and thermal conductively, to account for the higher quantities of momentum and heat exchanged in the flow by the motion of turbulent eddies

as opposed to molecular diffusion. The total shear stress and total heat transfer can now be easily expressed as

$$\tau_{total} = (\mu + \mu_t)\frac{\partial \bar{u}}{\partial y} = \rho(v + \varepsilon_M)\frac{\partial \bar{u}}{\partial y} \tag{3.38}$$

and

$$\dot{q}_{total} = -(k + k_t)\frac{\partial \bar{T}}{\partial y} = -\rho C_p(\alpha + \varepsilon_H)\frac{\partial \bar{T}}{\partial y} \tag{3.39}$$

Where the terms $\varepsilon_M = \mu_t/\rho$ and $\varepsilon_H = kT/\rho C_p$ are called the eddy diffusivity of momentum and eddy diffusivity of heat respectively.

The motion of eddies is most prevalent in the core of the turbulent boundary layer, but this motion diminishes rapidly nearer the wall due to the no slip condition. Consequently, in this core region, the eddy diffusivities of momentum and heat are higher than their molecular counterparts, resulting in near uniform velocity and temperature profiles further from the wall, which suddenly become very steep in the thin layer closest to the wall.

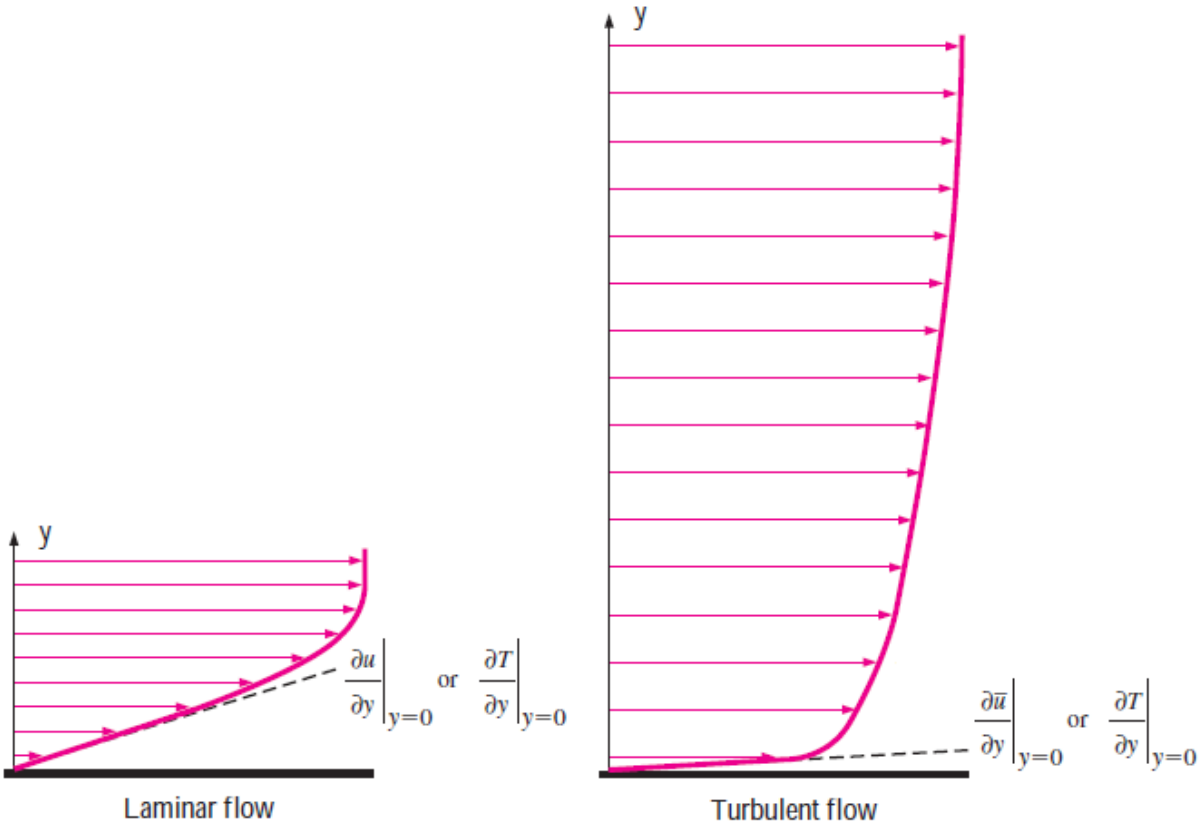

Figure 3-8: The gradients of velocity and temperature at the wall for laminar and turbulent flow [Cengel, 2011]

The sudden reduction of momentum and heat diffusivity results in larger velocity and temperature gradients at the wall surface, as demonstrated in figure 3-8, and hence is the reason that wall shear stress and wall heat flux is higher in turbulent flow as compared to laminar flow.

It is important to note that unlike the molecular diffusivities of momentum and heat, which are properties of the fluid, the eddy diffusivities, are properties that will vary with the flow conditions. Though appealing as a concept for dealing with turbulent flow, the values of the eddy diffusivities are not constant as they decrease in the direction towards the wall and rapidly become zero at the wall.

3.8 Summary

In this chapter, after introducing the heat conduction equation, the Nusselt number and its relation to convection was covered. The velocity and thermal boundary layers were explained, as well as how they vary as the flow changes from laminar to turbulent. Finally, the transfer of momentum and heat through the boundary layer between the wall and freestream was discussed.

The next chapter will focus on the Navier-Stokes equations, these are the governing equations of fluid flow and relate to the conservation of momentum and energy. The equations will be derived by applying conservation principles through a control volume.

4.0 THE NAVIER-STOKES EQUATIONS

After having covered the physical descriptions of convection, this section will deal with the governing equations of fluid flow and their application in the boundary layer. These are termed the Navier-Stokes equations, composed of the continuity, momentum and energy equations, which are the basis for CFD analysis.

Similar to other finite element or finite volume approaches, CFD packages are often considered by their users as a "black-box" tool to obtain answers to engineering problems without a true understanding of the underlying physics involved, and therefore, the limitations of applicability. Therefore, this chapter will attempt to clarify the theory behind CFD.

The equations will be initially derived using the concept of surface and volume integrals and will then be simplified using theorems that relate the different types of integrals such as the divergence and gradient theorem. The relations between these integrals details on such theorems can be found in standard mathematical texts such as by Spiegel, (2009).

Given a finite control volume v bounded by an outer surface S as shown in figure 4-1, $\boldsymbol{V}$ represents the flow velocity at any given elemental surface area represented by the vector $d\boldsymbol{S}$. By convention, the area vector points out of the control volume in a direction normal to the control surface at that point. The three fundamental laws of mass, momentum and energy conservation can then be applied to this fluid element to arrive at the continuity, momentum and energy equations for flow in a laminar boundary layer. These three equations are essential for solving fluid flow problems using computational fluid dynamics.

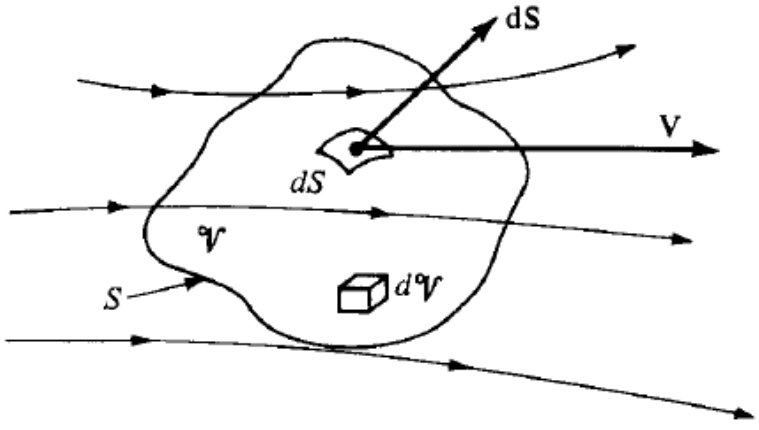

Figure 4-1: Finite control volume fixed in space [Anderson, 2011]

4.1 The Continuity Equation

The continuity equation is based on the principle that, like energy, mass cannot be created or destroyed, assuming no transformation of mass into energy or vice-versa. Hence it can be stated that the rate at which mass exits through a control surface must be equal to the rate at which mass decreases within the equivalent encompassed control volume.

The rate of mass flow is the product of density, velocity and cross-sectional area (normal to the velocity vector) that the fluid passes through, therefore the rate at which mass flows out of the entire control surface S can be defined as:

$$\oiint_S \rho \boldsymbol{V} \cdot \boldsymbol{dS} \tag{4.1}$$

The amount of mass within a given elemental volume $d\mathrm{V}$ is defined as $\rho d\mathrm{V}$. Should the density vary throughout the flow, then the total mass can be determined by summing the above term over the entire control volume V. Therefore, the time rate decrease of mass inside the control volume V, can be defined as

$$-\frac{\partial}{\partial t}\oiiint_v \rho d\mathrm{V} \tag{4.2}$$

Based on the continuity principle, these terms are equal. Given that one term is negative their sum would equal zero as demonstrated below.

$$-\frac{\partial}{\partial t}\oiiint_v \rho d\mathrm{V} + \oiint_S \rho \boldsymbol{V} \cdot \boldsymbol{dS} = 0 \tag{4.3}$$

The divergence theorem can be applied to the second term, converting the surface integral into an equivalent volume integral, such that

$$\oiint_S \rho \boldsymbol{V} \cdot \boldsymbol{dS} = \oiiint_v \nabla \cdot (\rho \boldsymbol{V}) d\mathrm{V} \tag{4.4}$$

Substituting this new volume integral into equation 4.3 and separating out the resulting integrand, equation 4.3 becomes

$$\iiint_{v} \left[\frac{\partial \rho}{\partial t} + \nabla \cdot (\rho \boldsymbol{V})\right] d\mathrm{V} \tag{4.5}$$

Examining equation 4.5, the only way for the integral to be zero for any given control volume would be if the integrand was zero at all points within that control volume, hence

$$\frac{\partial \rho}{\partial t} + \nabla \cdot (\rho \boldsymbol{V}) = 0 \tag{4.6}$$

Equation 4.6 is the continuity equation; its partial differential form relates the flow variables at a point in the flow in contrast to equation 4.3 which dealt with these variables over a finite space. In the case of steady flow, $d/dt = 0$, equations 4.3 and 4.6 reduce to

$$\iint_{s} \rho \boldsymbol{V} \cdot \boldsymbol{dS} = 0 \tag{4.7}$$

and

$$\nabla \cdot (\rho \boldsymbol{V}) = 0 \tag{4.8}$$

Assuming a fluid of constant density, the density term may be removed, and by the definition of the del operator, $\nabla = i(\partial/\partial x) + j(\partial/\partial y) + k(\partial/\partial z)$, equation 4.8 can be expanded to

$$\frac{\partial u}{\partial x} + \frac{\partial v}{\partial y} + \frac{\partial \omega}{\partial z} = 0 \tag{4.9}$$

4.1.1 Further Understanding of the Continuity Equation

Given a fluid flowing parallel to a surface as shown in figure 4-2, x is defined as the direction of fluid flow, whilst y is defined as the direction normal to the surface. For analysis, a differential volume element can be taken with a length of dx, and a height of dy, and a unit value of depth in the z-direction. The flow velocity of the free-stream is u_∞, whilst the flow in the boundary layer is two-dimensional, the x and y components of this velocity are defined as u and v respectively.

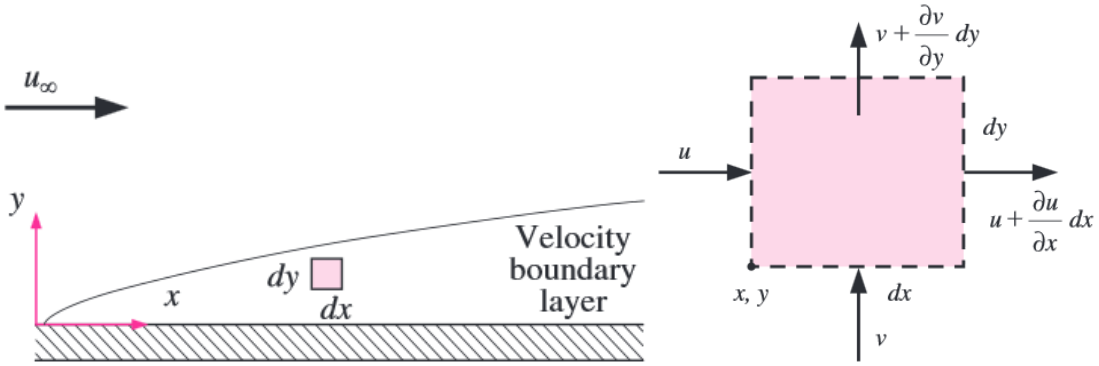

Figure 4-2: Velocity boundary layer in two-dimensional flow (left) and the differential control volume (right) [Cengel, 2011]

The velocities through a control volume in two dimensional flows are also demonstrated in figure 4-2. As the amount of mass inside the control volume must remain constant for steady flow, it follows that any increase with distance of the horizontal velocity u through this volume must be balanced by an equal decrease with distance of the vertical velocity v.

4.2 The Momentum Equation

The momentum equation is based on a second physical principle relating to motion; it states that force is equal to the time rate of change of momentum. This is expressed by a differential form of Newton's second law demonstrated in equation 4.10.

$$\boldsymbol{F} = \frac{d}{dt}(m\boldsymbol{V}) \tag{4.10}$$

Considering again the finite control volume in figure 4-1, the forces acting on this flowing fluid can be categorised into surface forces, which act on the control surface S, due to pressure and shear stress, and body forces, such as gravity, which act from a distance upon the fluid volume V.

Taking F to represent a body force per unit mass acting on the fluid volume V, the force acting on a volume element dV can be expressed as $\rho.\boldsymbol{f}.d\mathrm{V}$. Should the density vary throughout the flow, then the total body force can be determined by summing the above term over the entire control volume V such that

$$\iiint_{v} \rho \boldsymbol{f} d\mathrm{V} \tag{4.11}$$

Similarly, the pressure force acting on an area $d\boldsymbol{S}$ can be expressed as $-P\,d\boldsymbol{S}$. The negative sign indicates that the pressure force acts in an opposite direction to $d\boldsymbol{S}$, and hence effectively acts to

compress the fluid in the control volume. Therefore, the total pressure force can be obtained by summing this force over the entire control surface area S such that

$$-\oiint_S P\, d\boldsymbol{S} \tag{4.12}$$

Shear and normal viscous stresses also contribute to the surface forces acting on the fluid, its derivation will be saved till after compiling the full momentum equation. At this stage the contribution of the viscous force is recognised and represented as $\boldsymbol{F}_{viscous}$. The total force acting on the fluid in the control volume can therefore be expressed as

$$\boldsymbol{F} = \iiint_{\mathrm{V}} \rho \boldsymbol{f} d\mathrm{V} - \oiint_S P\, d\boldsymbol{S} + \boldsymbol{F}_{viscous} \tag{4.13}$$

These forces will result in an acceleration or time rate change of momentum of the fluid. This change can be observed occurring in two forms, as a steady net flow of momentum out through the control surface S, and as an unsteady change of momentum within the control volume V.

The steady form is understood by considering that a flow through the fixed control volume would, due to these forces, have an increased momentum at the point of exit than at the point of entry, resulting in a positive net flow out of momentum. Whilst the unsteady form is understood to represent how the flow within the control volume would also experience a change in momentum over time as opposed to space.

Recalling from section 4.1 that the mass flow through an area dS was defined as $\rho\boldsymbol{V} \cdot d\boldsymbol{S}$, then the flow of momentum can be defined as $(\rho\boldsymbol{V} \cdot d\boldsymbol{S})\boldsymbol{V}$. The total momentum flowing out of the entire control surface S is therefore defined as

$$\oiint_S (\rho\boldsymbol{V} \cdot d\boldsymbol{S})\boldsymbol{V} \tag{4.14}$$

The momentum of the fluid within an elemental volume $d\mathrm{V}$ is given by $(\rho d\mathrm{V})\boldsymbol{V}$, therefore the unsteady increase of this momentum within the entire control volume V can be expressed by

$$\frac{\partial}{\partial t}\iiint_{\mathrm{V}} \rho \boldsymbol{V} d\mathrm{V} \tag{4.15}$$

The combination of these terms gives an expression for the total time rate of change of momentum of a fluid flowing through a fixed control volume, based on Newton's second law, balancing these terms with the force terms derived previously yields

$$\frac{\partial}{\partial t}\iiint_{\mathrm{V}} \rho \boldsymbol{V} d\mathrm{V} + \iint_{S} (\rho \boldsymbol{V} \cdot d\boldsymbol{S})\boldsymbol{V} = -\iint_{S} P\, d\boldsymbol{S} + \iiint_{\mathrm{V}} \rho \boldsymbol{f} d\mathrm{V} + \boldsymbol{F}_{viscous} \tag{4.16}$$

Equation 4.16 is the momentum equation in integral form; by converting the surface integrals into volume integrals the partial differential form can be achieved, which relates to the flow at any distinct point in space as opposed to across a finite region of space. The gradient theorem can be applied to the pressure force term such that

$$-\iint_{S} P\, \boldsymbol{dS} = -\iiint_{\mathrm{V}} \nabla \mathrm{P}\, d\mathrm{V} \tag{4.17}$$

Equation 4.17 can be further simplified by bringing the time derivative into the integral, and because each term now contains a separate vector, the full equation can be rewritten as a combination of three scalar equations based on the Cartesian coordinates, $\boldsymbol{V} = u\boldsymbol{i} + v\boldsymbol{j} + \omega\boldsymbol{k}$. Taking only the x-component equation 4.16 becomes

$$\iiint_{\mathrm{V}} \frac{\partial(\rho u)}{\partial t} dv + \iint_{S} (\rho \boldsymbol{V} \cdot \boldsymbol{dS})u = -\iiint_{\mathrm{V}} \frac{\partial P}{\partial x}\, dv + \iiint_{\mathrm{V}} \rho f_x d\mathrm{V} + (F_x)_{viscous} \tag{4.18}$$

Inspecting the second term of equation 4.18, the product $\boldsymbol{V} \cdot d\boldsymbol{S}$ yields a scalar therefore is not separated into components, however the divergence theorem can be applied to the surface integral such that

$$\iint_{S} (\rho \boldsymbol{V} \cdot \boldsymbol{dS})u = \iint_{S} (\rho u \boldsymbol{V}) \cdot \boldsymbol{dS} = \iiint_{\mathrm{V}} \nabla \cdot (\rho u \boldsymbol{V}) \partial \mathrm{V} \tag{4.19}$$

Substituting this into equation 4.18 results in

$$\iiint_{V} \left[\frac{\partial(\rho u)}{\partial t} + \nabla \cdot (\rho u \boldsymbol{V}) + \frac{\partial P}{\partial x} - \rho f_x - (F_x)_{viscous}\right] \partial \mathrm{V} = 0 \tag{4.20}$$

Similar to deriving the continuity equation, the integrand must equal zero at every point in the flow, hence

$$\frac{\partial(\rho u)}{\partial t} + \nabla \cdot (\rho u \boldsymbol{V}) = -\frac{\partial P}{\partial x} + \rho f_x + (F_x)_{viscous} \tag{4.21}$$

Equation 4.21 is the x component of the momentum equation expressed in partial differential form, as this came from the integrand, each term in the equation is a force per unit volume, the equivalent y and z components are expressed in equations 4.22 and 4.23. It is important to note that only equation 4.21 would be required when describing one dimensional flow, both equations 4.21 and 4.22 would be required when examining two dimensional flows and all three equations would be required for three dimensional flows. The implication of two dimensional flows is that the velocity component u would vary in both dimensions, and based on the continuity equation, would necessitate velocity component v to also change in both dimensions.

$$\frac{\partial(\rho v)}{\partial t} + \nabla \cdot (\rho v \boldsymbol{V}) = -\frac{\partial P}{\partial y} + \rho f_y + (F_y)_{viscous} \tag{4.22}$$

and

$$\frac{\partial(\rho \omega)}{\partial t} + \nabla \cdot (\rho \omega \boldsymbol{V}) = -\frac{\partial P}{\partial z} + \rho f_z + (F_z)_{viscous} \tag{4.23}$$

4.2.1 Revealing the Viscous Forces

To understand the viscous forces experienced by the fluid in a differential control volume, a similar approach to section 4.1.1 can be taken by considering a two-dimensional flow over a surface and examining the surface forces experienced in the x-direction as shown in figure 4-3.

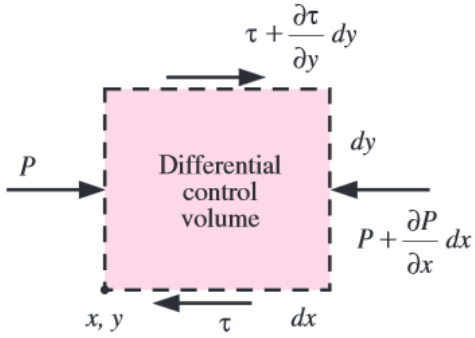

Figure 4-3: Two-dimensional differential control volume showing pressure and viscous effects in x-direction [Cengel, 2011]

The variations of pressure and viscous forces can be observed at the extents on this control volume. The viscous forces can be split into two components which act along and normal to a surface referred to as shear stresses and normal stresses respectively. Viscous forces are related to velocity gradients, in the differential control volume the normal stresses are related to the velocity gradients du/dx and dv/dy, however these are very small as compared to the velocity gradient du/dy to which shear stress in related. For this reason, normal stresses are not included in this analysis; these stresses are understood to only play a significant role in near super-sonic flows or shock waves in which there are considerable velocity changes in the direction of fluid flow.

Examining figure 4-3 the net surface forces acting on the differential control volume in the x-direction can be summed up such that

$$F_{surface,_x} = \left(\frac{\partial \tau}{\partial y} dy\right)(dx.1) - \left(\frac{\partial P}{\partial x} dx\right)(dy.1) = \left(\frac{\partial \tau}{\partial y} - \frac{\partial P}{\partial x}\right)(dx.dy.1) \tag{4.24}$$

From section 4.3 the shear stress at a surface is $\tau_s = \mu\,(\partial u/\partial y)$, substituting this into equation 4.24 and dividing by $dx.dy.1$ to give the force per unit volume, the viscous term becomes clear and therefore the x-momentum equation in the case of two-dimensional flow over a surface can be expressed as

$$\frac{\partial(\rho u)}{\partial t} + \nabla \cdot (\rho u \boldsymbol{V}) = -\frac{\partial P}{\partial x} + \rho f_x + \mu \frac{\partial^2 u}{\partial y^2} \tag{4.25}$$

Whilst the equivalent y components of the momentum equation is expressed as below

$$\frac{\partial(\rho v)}{\partial t} + \nabla \cdot (\rho v \boldsymbol{V}) = -\frac{\partial P}{\partial y} - \rho g + \mu \frac{\partial^2 v}{\partial x^2} \tag{4.26}$$

Generally, the only body force acting in the y direction is due to gravitational acceleration, and hence f_y was replaced by $-g$ in the above equation.

4.2.2 Further Understanding of the Momentum Equation

The above equations contain a convective term defined with a persistent vector $\boldsymbol{V}$, the significance of this term can be understood by considering unsteady two-dimensional flow such that the horizontal velocity component $u = u(x, y, t)$, the total differential of u is

$$du = \frac{\partial u}{\partial x}dx + \frac{\partial u}{\partial y}dy + \frac{\partial u}{\partial t}dt \tag{4.27}$$

The total acceleration of the flow in the x direction is therefore

$$a_x = \frac{du}{dt} = \frac{\partial u}{\partial x}\frac{dx}{dt} + \frac{\partial u}{\partial y}\frac{dy}{dt} + \frac{\partial u}{\partial t} = u\frac{\partial u}{\partial x} + v\frac{\partial u}{\partial y} + \frac{\partial u}{\partial t} \tag{4.28}$$

Recalling that the momentum equation is simply an expression of Newton's second law and the right side of equation 4.25 is force per unit volume, given that $m = \sigma \mathrm{V}$, then the left side would be the equivalent of density times acceleration as demonstrated in equations 4.29 and 4.30 below

$$\delta m\,.\ a_x = F_{surface,_x} = \rho(dx.dy.1)\ a_x \tag{4.29}$$

$$\frac{F_{surface,_x}}{Volume} = \rho a_x \tag{4.30}$$

The product of density and acceleration can be written as

$$\rho a_x = \rho\frac{\partial u}{\partial t} + \rho\left(u\frac{\partial u}{\partial x} + v\frac{\partial u}{\partial y}\right) \tag{4.31}$$

Assuming constant density, the x-component of the momentum equation can therefore be rewritten as

$$\frac{\partial(\rho u)}{\partial t} + \rho\left(u\frac{\partial u}{\partial x} + v\frac{\partial u}{\partial y}\right) = -\frac{\partial P}{\partial x} + \rho f_x + \mu\frac{\partial^2 u}{\partial y^2} \tag{4.32}$$

It is clear that in the case of two dimensional flows, where $\boldsymbol{V} = (u, v, 0)$ then

$$\nabla \cdot (\rho u \boldsymbol{V}) = \rho \left(u \frac{\partial u}{\partial x} + v \frac{\partial u}{\partial y} \right) \tag{4.33}$$

The number of components in the velocity vector $\boldsymbol{V}$, and hence whether the flow is one, two or three dimensional will determine the number of partial derivatives in the right-hand term given that it is a dot product of the del operator and velocity vector.

The left-hand term was originally derived by considering the change of momentum with position in the flow due to forces acting on the fluid, similarly the right-hand term, in brackets, relates to the rate of change of velocity with distance, otherwise known as the convective acceleration. Consequently, the term in brackets multiplied by density gives the value of force (per unit volume) that a steady flow would impose on a solid body if upon impact the fluid was brought to a complete rest. For the case of steady two-dimensional flow and neglecting body forces, expect gravity, the x and y components of the momentum equation can be expressed as below.

$$\rho \left(u \frac{\partial u}{\partial x} + v \frac{\partial u}{\partial y} \right) = -\frac{\partial P}{\partial x} + \mu \frac{\partial^2 u}{\partial y^2} \tag{4.34}$$

$$\rho \left(u \frac{\partial v}{\partial x} + v \frac{\partial v}{\partial y} \right) = -\rho g - \frac{\partial P}{\partial y} + \mu \frac{\partial^2 v}{\partial x^2} \tag{4.35}$$

4.3 Boundary Layer Approximations

When applying these equations to the boundary layer, some observations can be made to simply them. Firstly, the velocity in the flow direction will be far greater in magnitude than in the direction normal to the surface, therefore $u \gg v$. Also, the normal velocity doesn't change very much in either the x or y directions, therefore dv/dx and dv/dy are negligible. It is clear that velocity in the flow direction, u, varies far more in the y direction as compared to the x direction, therefore $du/dy \gg du/dx$. These velocity gradients are similar to the temperature gradients, as would be observed if the surface over which the fluid flows is heated or cooled, the temperature would vary far more in the y direction than along the surface, hence $dT/dy \gg dT/dx$. These statements are known as boundary layer approximations, and greatly simplify the momentum equations in order to easily obtain analytical solutions to such flow problems with only a slight loss in accuracy.

Applying these approximations to the y momentum equation, and neglecting any gravitational effects reduces equation 4.35 to

$$\frac{dP}{dy} = 0 \tag{4.36}$$

This suggests a negligible variation in pressure in a direction normal to the flow surface through the boundary layer, and therefore, pressure in the boundary layer is only dependant on the x position, $P = P(x)$, hence, $\partial P/\partial x$ becomes dP/dx. This implies that the pressure at any point in the x direction on the flow surface and inside the boundary layer would equal the pressure in the free-stream at the equivalent x position; and the pressure in the free-stream can be obtained more easily due to the lack of viscous effects.

The velocity characteristics in the free-stream region of fluid flowing over a flat plate, is $u = u_\infty = constant$, hence $du/dx = 0$ and $v = 0$. Putting these values into the x-momentum equating reveals $dP/dx = 0$. It can be said therefore, in fluid flow over a flat plate, the pressure remains constant along the entire length, both inside and outside of the laminar boundary layer.

4.3.1 Suitability of the Boundary Layer Approximations

It is important to note, that although equation 4.36 suggested that $dP/dx = 0$, this was achieved by neglecting gravitational effects. Including gravity would give the familiar result $dP/dy = \rho g \Delta y$, meaning that pressure in the boundary layer varies linearly with height. In a thin boundary layer, the pressure difference between the surface and free-stream could be considered negligible. However, a very thick boundary layer would cause this approximation to break down, in which case the statement regarding pressure remaining constant along the length of the plate, would no longer be valid.

Hence, this approximation is specifically suited to a laminar flow. At higher Reynolds numbers, the boundary layer would begin to become turbulent and the steady nature of the momentum equations and boundary layer approximations used in this procedure would not be valid for such a flow. The approximations would also become invalid in the case of flow separation, due to the occurrence of reversed flow in the separated region.

4.4 The Energy Equation

The final of the convection equations is the energy equation, which, due to some overlap will the heat equation, will be derived in a similar fashion to the heat equation in section. The energy equation is a statement that the time rate increase of energy within a control volume is equal to the net rate of flow of energy into the control volume, in addition to any volumetric energy generation. Energy can be transferred by heat, mass and work, however making the assumption of no external work acting on the control volume, the energy balance can be written as

$$(\dot{E}_{in} - \dot{E}_{out})_{by\ heat} + (\dot{E}_{in} - \dot{E}_{out})_{by\ mass} + \dot{E}_{Generation} = \frac{dE}{dt} \tag{4.37}$$

The energy per unit mass contained in a fluid is defined by $e_{fluid} = h$, where h is the enthalpy, referring to the sum of both internal energy and flow energy, $h = u + PV$. The internal energy relates to the molecular kinetic and potential energy of a system and hence determines the fluid temperature. Whilst the flow energy is a product of the pressure and volume of the system, this essentially refers the required energy of the fluid to exist within a given volume of space against the surrounding pressure. Effectively it is the energy required to push the rest of the environment "out of the way" in making room for the fluid.

In the derivation of the energy equation, the fluid properties, density ρ, specific heat capacity C_P, dynamic viscosity μ, and thermal conductivity k are assumed to be constant. As such, the energy in the fluid per unit mass can be expressed as $e_{fluid} = h = C_P T$.

Figure 4-4 demonstrates two-dimensional flow of energy by mass and heat through a differential control volume, given that energy is a scalar quantity, flows of energy in different forms and directions can be summed into one single equation, and not three components like that of momentum.

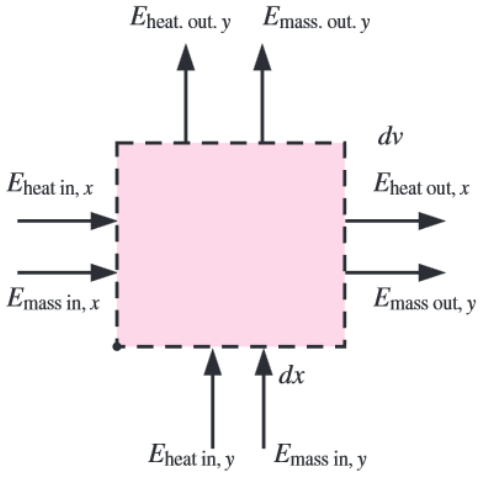

Figure 4-4: Two-dimensional differential control volume showing energy flow by mass and heat [Cengel, 2011]

Dealing with energy transfer due to the flow of mass, given that mass enters from the left side of the control volume, the flow of energy into and out of the control volume is given by

$$(\dot{E}_{in} - \dot{E}_{out})_{by\ mass,\ x} = (\dot{m}e_{stream})_x - \left[(\dot{m}e_{stream})_x + \frac{\partial(\dot{m}e_{stream})_x}{\partial x}dx\right] \tag{4.38}$$

The rate of mass flow is $m = \rho u(dy.1)$, therefore net increase of energy can be simplified to give

$$(\dot{E}_{in} - \dot{E}_{out})_{by\ mass,\ x} = \frac{\partial[\rho u(dy.1)C_P T]}{\partial x} dx \tag{4.39}$$

Both the horizontal velocity u, and temperature T are variables of x, hence the product rule is used after separating the constants of density, specific heat and the term dy, such that

$$(\dot{E}_{in} - \dot{E}_{out})_{by\ mass,\ x} = \frac{\partial[\rho u(dy.1)C_P T]}{\partial x} dx = -\rho C_P \left(u\frac{\partial T}{\partial x} + T\frac{\partial u}{\partial x}\right) dxdy \tag{4.40}$$

Using the same technique for the vertical velocity in the y-direction arrives at the result

$$(\dot{E}_{in} - \dot{E}_{out})_{by\ mass,\ y} = -\rho C_P \left(v\frac{\partial T}{\partial y} + T\frac{\partial v}{\partial y}\right) dxdy \tag{4.41}$$

Adding these terms gives the total rate of energy transfer into the control volume due to mass flow as

$$(\dot{E}_{in} - \dot{E}_{out})_{by\ mass} = -\rho C_P \left(u\frac{\partial T}{\partial x} + T\frac{\partial u}{\partial x}\right) dxdy - \rho C_P \left(v\frac{\partial T}{\partial y} + T\frac{\partial v}{\partial y}\right) dxdy \tag{4.42}$$

Based on the continuity equation, $\partial u/dx + \partial v/dy = 0$, the T terms will cancel to simplify as

$$(\dot{E}_{in} - \dot{E}_{out})_{by\ mass} = -\rho C_P \left(u\frac{\partial T}{\partial x} + v\frac{\partial T}{\partial y}\right) dxdy \tag{4.43}$$

The energy transfer due to the flow of heat is obtained by first considering two-dimensional heat conduction in the x-direction through the differential control volume such that

$$(\dot{E}_{in} - \dot{E}_{out})_{by\ heat,\ x} = \dot{Q}_x - \left(\dot{Q}_x + \frac{\partial \dot{Q}_x}{\partial x} dx\right) \tag{4.44}$$

Based on Fourier's law of heat conduction that states $Q = kA(dT/dx)$, and separating out the constants of thermal conductivity and the term dy, the equation simplifies such that

$$(\dot{E}_{in} - \dot{E}_{out})_{by\ heat,\ x} = -\frac{\partial}{\partial x}\left(-k(dy.1)\frac{\partial T}{\partial x}\right) dx = k\frac{\partial^2 T}{\partial x^2} dxdy \tag{4.45}$$

The same technique applied in the y-direction gives the result

$$(\dot{E}_{in} - \dot{E}_{out})_{by\ heat,\ y} = -\frac{\partial}{\partial y}\left(-k(dx.1)\frac{\partial T}{\partial y}\right)dy = k\frac{\partial^2 T}{\partial y^2}dxdy \tag{4.46}$$

Adding these terms gives the total rate of energy transfer into the control volume due to heat flow as

$$(\dot{E}_{in} - \dot{E}_{out})_{by\ heat} = k\frac{\partial^2 T}{\partial x^2}dxdy + k\frac{\partial^2 T}{\partial y^2}dxdy = k\left(\frac{\partial^2 T}{\partial x^2} + \frac{\partial^2 T}{\partial y^2}\right)dxdy \tag{4.47}$$

The time rate of energy accumulation within the element of volume $dx.dy.1$ can be expressed as

$$\frac{dE}{dt} = \rho C_P \frac{dT}{dt}dx.dy.1 \tag{4.48}$$

Whilst the rate of energy generation inside the element can be expressed as

$$\dot{G} = \dot{g}\mathrm{V} = \mathrm{g}.dx.dy.1 \tag{4.49}$$

Equating these terms, and diving out the volume $dx.dy.1$, gives the final energy equation in differential form as below

$$\rho C_P\left(u\frac{\partial T}{\partial x} + v\frac{\partial T}{\partial y}\right) = k\left(\frac{\partial^2 T}{\partial x^2} + \frac{\partial^2 T}{\partial y^2}\right) \tag{4.50}$$

4.4.1 Sources of Heat Generation

An additional method of energy transfer through the control volume can be due to body and surface forces. The contribution of the work done per unit volume by a body force would be added to the right-hand side of the energy equation. The term consists of the acting force multiplied by the component of velocity in the direction of this force, or simply, the dot product of the body force and associated velocity of the fluid. However, such a contribution is only included when there are significant electric or magnetic effects acting on the fluid.

The contributions due to surface forces can be divided into pressure acting normally on the fluid and viscous shear stresses. The force due to pressure, or flow work, is already included in the energy equation by taking the enthalpy to represent the microscopic energy of the fluid instead of just the internal energy. As for the heating effects of viscous shear stresses, these can generally be neglected as their contribution to temperature rise tends to be insignificant even at moderate velocities.

However, for applications in which their effects are unavoidable, such as spaces shuttles re-entering the atmosphere, the product of the fluid viscosity and a viscous dissipation function can be added to the right-hand side of the equation as below, taking the place of heat generation within the fluid.

$$\rho C_P \left(u \frac{\partial T}{\partial x} + v \frac{\partial T}{\partial y} \right) = k \left(\frac{\partial^2 T}{\partial x^2} + \frac{\partial^2 T}{\partial y^2} \right) + \mu \Phi \tag{4.51}$$

where

$$\Phi = 2 \left[\left(\frac{\partial u}{\partial x} \right)^2 + \left(\frac{\partial v}{\partial y} \right)^2 \right] + \left(\frac{\partial u}{\partial y} + \frac{\partial v}{\partial x} \right)^2 \tag{4.52}$$

The partial differential form of this equation describes the time rate of increase of temperature at any given point, due to the distribution of fluid temperature and fluid velocity around that point. In the case of a stationary fluid, where $u = v = 0$, then the energy equation would simply reduce to the unsteady two-dimensional heat conduction equation.

4.5 Summary

In this chapter, the Navier-Stokes equations were derived by applying the principles of conservation of mass, momentum and energy across a control volume. The equations were expressed in various forms, the importance of which will be discussed in later chapters. The five equations can be used to solve for five unknowns, pressure, the three velocity components and temperature. The next chapter will deal with solving these equations to obtain solutions for laminar flow.

5.0 THE EQUATIONS OF CONVECTION AND EXTERNAL FLOW

In the previous chapter, the continuity, momentum and energy equations were derived and explained. Using appropriate boundary conditions these equations can be applied to flat plates to provide analytical solutions for velocity and consequent temperature profiles. Such solutions would even be applicable to slightly contoured surfaces like that of turbine blades with only a slight loss in accuracy. Knowledge of the velocity and temperature profiles above a surface allow for, by their definition, the determination of both the wall shear stress and heat flux at any point on that surface. This chapter will explain the methods involved for obtaining these profiles and outline the resulting heat convection equations. The later part of the chapter will expand on external forced convection with more focus on the practical aspects related to the components in the turbo generation section of the OWC. Turbulent correlations for flow above flat plates, applicable to turbine blades and smooth housings, will be covered prior to the subject of flow through fin channels.

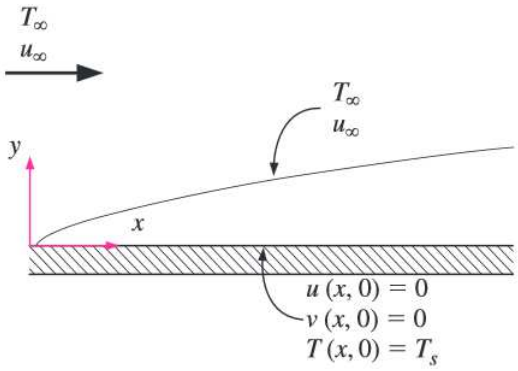

Figure 5-1: Boundary conditions applied to flow over a flat plate [Cengel, 2011]

Taking the case of laminar flow over a flat plate as shown in figure 5-1, the fluid travels in the x direction over the surface and encounters the leading edge with a uniform free-stream velocity u_∞. Assuming a steady flow of fluid with constant properties and negligible viscous heating, the continuity, momentum and energy equations can be reduced to

Continuity
$$\frac{\partial u}{\partial x} + \frac{\partial v}{\partial y} = 0 \tag{5.1}$$

Momentum
$$u\frac{\partial u}{\partial x} + v\frac{\partial u}{\partial y} = v\frac{\partial^2 u}{dy^2} \tag{5.2}$$

Energy
$$u\frac{\partial T}{\partial x} + v\frac{\partial T}{\partial y} = \propto \frac{\partial^2 T}{dy^2} \tag{5.3}$$

The first two equations can be used to solve for the two velocity components u and v, knowing the velocity distribution allows not only for the determination of the wall values but also the velocity boundary layer thickness δ based on the extent defined as where the local velocity approaches 99% of the free-stream. Finally, having obtained the values of u and v for any point in the flow, the energy equation can be solved to determine the temperatures at those equivalent points as well.

5.1 Solving the Momentum Equation

The German engineer H. Blasius, a student of L. Prandtl, attempted to solve these equations analytically, to determine the thickness of the velocity and thermal boundary layers in laminar flow. He observed that as the general shape of the velocity profile remains similar for varying velocities, and therefore reasoned that the non-dimensional velocity ratio u/u_∞ at any point within the boundary layer would remain constant against the non-dimensional distance y/δ away from the plate.

Based on findings by Stokes that the laminar boundary layer thickness δ was proportional to $\sqrt{vx/u_\infty^2}$. Blasius created what he termed a non-dimensional similarity variable to effectively define the relative height position within any given boundary layer,

$$\eta = y\sqrt{\frac{u_\infty}{vx}} \tag{5.4}$$

Therefore, the velocity ratio u/u_∞ can be understood to be a function of η. Blasius next introduced a stream function $\psi(x, y)$ such that when differentiated into partial terms would reveal the components of velocity in the flow along any given stream line

$$u = \frac{\partial \psi}{\partial y} \qquad \text{and} \qquad v = -\frac{\partial \psi}{\partial x} \tag{5.5}$$

These velocity terms when substituted would satisfy the continuity equation, a final term that Blasius created was defined as the dependent variable $f(\eta)$, where

$$f(\eta) = \frac{\psi}{u_\infty\sqrt{vx/u_\infty}} \tag{5.6}$$

This can be thought of as a function of η as it comprises the stream function, and thereby contains all the terms of the similarly variable, despite being non-dimensional it is also related to the velocity components in the flow.

Based on these functions the velocity components can be refined as below

$$u = \frac{\partial \psi}{\partial y} = \frac{\partial \psi}{\partial \eta}\frac{\partial \eta}{\partial y} = u_\infty \sqrt{\frac{vx}{u_\infty}}\frac{df}{d\eta}\sqrt{\frac{u_\infty}{vx}} = u_\infty \frac{df}{d\eta} \tag{5.7}$$

$$v = -\frac{\partial \psi}{\partial x} = -u_\infty \sqrt{\frac{vx}{u_\infty}}\frac{df}{dx} - \frac{u_\infty}{2}\sqrt{\frac{v}{u_\infty x}}f = \frac{1}{2}\sqrt{\frac{u_\infty v}{x}}\left(\eta\frac{df}{d\eta} - f\right) \tag{5.8}$$

The terms that make up the momentum equation can be obtained by the partial derivatives of these terms such that

$$\frac{\partial u}{\partial x} = -\frac{u_\infty}{2x}\eta\frac{d^2 f}{d\eta^2} \qquad \frac{\partial u}{\partial y} = u_\infty\sqrt{\frac{u_\infty}{vx}}\frac{d^2 f}{d\eta^2} \qquad \frac{\partial^2 u}{\partial y^2} = \frac{u_\infty^2}{vx}\frac{d^3 f}{d\eta^3} \tag{5.9}$$

Substituting these into the momentum equations and simplifying, results in an ordinary differential equation

$$2\frac{d^3 f}{d\eta^3} + f\frac{d^2 f}{d\eta^2} = 0 \tag{5.10}$$

This equation would require three boundary conditions for a full solution, three terms can be defined based on the relation between f and η, and the differing velocity ratio $u/u_\infty = df/d\eta$ at the wall and beyond the boundary layer such that

$$f(0) = 0 \qquad \left.\frac{df}{d\eta}\right|_{\eta=0} = 0 \qquad \left.\frac{df}{d\eta}\right|_{\eta=\infty} = 1 \tag{5.11}$$

Even with these conditions equation 5.10 cannot be solved analytically due to its non-linear nature; Blasius instead used a power series expansion approach to obtain a solution, the result from this was termed the Blasius solution. More accurate solutions were later obtained by the use of numerical approaches; the results from such solutions are shown in table 5-1 below.

η	f	$\frac{df}{d\eta} = \frac{u}{u_\infty}$	$\frac{d^2f}{d\eta^2}$
0	0	0	0.332
0.5	0.042	0.166	0.331
1.0	0.166	0.330	0.323
1.5	0.370	0.487	0.303
2.0	0.650	0.630	0.267
2.5	0.996	0.751	0.217
3.0	1.397	0.846	0.161
3.5	1.838	0.913	0.108
4.0	2.306	0.956	0.064
4.5	2.790	0.980	0.034
5.0	3.283	0.992	0.016
5.5	3.781	0.997	0.007
6.0	4.280	0.999	0.002
∞	∞	1	0

Table 5-1: Similarity function *f* and its derivatives in a laminar boundary layer over a flat plate [Cengel, 2011]

A non-dimensional velocity profile from a wall surface to beyond the boundary layer can be obtained by plotting η against u/u_∞, and matches very well with experimental results. By defining the boundary layer edge as when $u/u_\infty = 0.99$, the closest match is when $\eta = 5$, corresponding to $u/u_\infty = 0.992$. Taking the edge of the boundary layer as when $y = \delta$, the similarity variable can be defined as $5.0 = \delta\sqrt{u_\infty/\nu x}$ and as such the thickness on the boundary layer can be expressed as

$$\delta = \frac{5.0}{\sqrt{u_\infty/\nu x}} = \frac{5.0x}{\sqrt{Re_x}} \tag{5.12}$$

Equation 5.12 demonstrates how the boundary layer thickness increases downstream, and at a fixed x-position this thickness increases with higher fluid kinematic viscosity, but decreases with higher free-stream velocity. Using the relation for du/dy derived in equation 5.9 the wall shear stress, by its definition, can be derived as

$$\tau_w = \mu \left.\frac{\partial u}{\partial y}\right|_{y=0} = \mu u_\infty \sqrt{\frac{u_\infty}{\nu x}} \left.\frac{d^2 f}{d\eta^2}\right|_{\eta=0} \tag{5.13}$$

From table 5-1 the value of the second derivative of f when $\eta = 0$ is observed to be 0.332, such that

$$\tau_w = 0.332 u_\infty \sqrt{\frac{\rho \mu u_\infty}{x}} = \frac{0.332 \rho u_\infty^2}{\sqrt{Re_x}} \tag{5.14}$$

Consequently, the local skin friction coefficient can be obtained as

$$C_{f,x} = \frac{\tau_w}{\rho V^2/2} = \frac{\tau_w}{\rho u_\infty^2/2} = 0.664 Re_x^{-1/2} \tag{5.15}$$

The wall shear stress and skin friction are seen to decrease along the plate as $x^{-1/2}$

5.2 Solving the Energy Equation

A very similar approach can be used to solve the energy equation; taking the two constants of surface temperature T_s and free-stream temperature T_∞, a dimensionless temperature θ can be introduced as

$$\theta(x,y) = \frac{T(x,y) - T_s}{T_\infty - T_s} \tag{5.16}$$

Through substitution, the energy equation would then become

$$u\frac{\partial\theta}{\partial x} + v\frac{\partial\theta}{\partial y} = \propto \frac{\partial^2\theta}{dy^2} \tag{5.17}$$

Like velocity profiles, temperature profiles above a heated plate tend to have a similar shape irrespective of the free-stream velocity. As the thickness of the thermal boundary layer is also proportional to $\sqrt{vx/u_\infty}$, the similarity variable is also η. Given that η is a non-dimensional distance from the wall, and is a function of x and y, whilst theta is a non-dimensional function of flow temperature with is also dependent on x and y, therefore $\theta = \theta(\eta)$. By the use of the chain rule, substituting the expressions for u and v from equations 5.7 and 5.8, the energy equation becomes

$$u_\infty \frac{df}{d\eta}\frac{d\theta}{d\eta}\frac{\partial\eta}{\partial x} + \frac{1}{2}\sqrt{\frac{u_\infty v}{x}}\left(\eta\frac{df}{d\eta} - f\right)\frac{d\theta}{d\eta}\frac{\partial\eta}{\partial y} = \propto \frac{d^2\theta}{d\eta^2}\left(\frac{\partial\eta}{\partial y}\right)^2 \tag{5.18}$$

This can be simplified whilst considering $\mathrm{Pr} = v/\propto$, it becomes

$$2\frac{d^2\theta}{d\eta^2} + \mathrm{Pr}f\frac{d\theta}{d\eta} = 0 \tag{5.19}$$

The two boundary conditions for a full solution would be $\theta(0) = 0$ and $\theta(\infty) = 1$, the equation would again have to be solved numerically. For a value of $\mathrm{Pr} = 1$, this equation would become equation 5.10, if θ were replaced with $df/d\eta$. Considering that $df/d\eta = u/u_\infty$, this confirms that a fluid with $\mathrm{Pr} = 1$, the non-dimensional temperature profile matches the non-dimensional velocity profile over an isothermal flat plate. As such, the boundary conditions for $df/d\eta$, are identical to that of θ, and a numerical method for obtaining the solution would again lead to table 5-1, therefore the value of the non-dimensional temperature gradient at the plate surface (when $y = 0$ or $\eta = 0$) for a fluid of $\mathrm{Pr} = 1$, from table 5-1 is given below

$$d\theta/d\eta = d^2f/d\eta^2 = 0.332 \tag{5.20}$$

In cases when the Prandtl number is greater than 0.6, from numerical methods it found that that this non-dimensional wall temperature gradient is proportional to $\mathrm{Pr}^{1/3}$, thus can be expressed as

$$\left.\frac{d\theta}{d\eta}\right|_{\eta=0} = 0.332\mathrm{Pr}^{1/3} \tag{5.21}$$

From this equation, and using the chain rule to expand $\partial\theta/\partial y$ the temperature gradient at the surface can be expressed as

$$\left.\frac{\partial T}{\partial y}\right|_{y=0} = (T_\infty - T_s)\left.\frac{\partial\theta}{\partial y}\right|_{y=0} = (T_\infty - T_s)\left.\frac{d\theta}{d\eta}\right|_{\eta=0}\left.\frac{\partial\eta}{\partial y}\right|_{y=0} = 0.332\mathrm{Pr}^{1/3}(T_\infty - T_s)\sqrt{\frac{u_\infty}{vx}} \tag{5.22}$$

From this result, the local convection coefficient and consequent Nusselt number can be expressed as shown in equations 5.23 and 5.24 for Prandtl numbers higher than 0.6.

$$h_x = \frac{q_s}{T_s - T_\infty} = \frac{-k(\partial T/\partial y)|_{y=0}}{T_s - T_\infty} = 0.332\mathrm{Pr}^{1/3}k\sqrt{\frac{u_\infty}{vx}} \tag{5.23}$$

$$Nu_x = \frac{h_x x}{k} = 0.332Pr^{1/3}Re_x^{1/2} \tag{5.24}$$

Based on the results of solving equation 5.19 by numerical methods for varying Prandtl numbers, the ratio between the velocity and thermal boundary layers is found to be $\mathrm{Pr}^{1/3}$, hence $\delta/\delta_t = \mathrm{Pr}^{1/3}$. Therefore, the thermal boundary layer thickness can be expressed as

$$\delta_t = \frac{\delta}{\mathrm{Pr}^{1/3}} = \frac{5.0x}{\mathrm{Pr}^{1/3}\sqrt{Re_x}} \tag{5.25}$$

It is important to note that equations 5.23 to 5.24 apply only to laminar flow based on the assumptions made in their derivation. Also, the fluid properties that would be affected by the varying temperature in the flow are evaluated at an average temperature known as the film temperature, given by $T_f = (T_s + T_\infty)/2$. Finally, it is observed that the friction coefficient can be reduced to a function of the Reynolds number, whilst the Nusselt number can be reduced to a function of the Reynolds and

Prandtl numbers. As such, these friction and convection coefficients are related, when Pr ~ 1, by a correlation known as the Reynolds analogy given by

$$C_{f,x}\frac{Re_L}{2} = Nu_x \tag{5.26}$$

and when $(0.6 < \mathrm{Pr} < 60)$ the coefficients are related by an equivalent modified Reynolds analogy defined as

$$C_{f,x}\frac{Re_L}{2} = Nu_x \mathrm{Pr}^{-1/3} \tag{5.27}$$

5.3 External Flow

The definition of external flow was covered in section 3.3, the drag force experienced by a body in external flow can be divided into skin friction drag, due to the wall shear stress, and form drag, due to pressure changes in the flow which are related to the shape and orientation of the body. The total drag force experienced by a body is proportional to the upstream velocity, the density of the fluid and the area projected on a plane normal to the flow direction. However, given the additional dependencies on the body shape and orientation, an additional drag coefficient C_d must be included in the force equation. The total drag coefficient is therefore

$$C_d = \frac{F_d}{\frac{1}{2}\rho A V^2} \tag{5.28}$$

Similar to the drag force, this coefficient can also be separated into friction and pressure components such that $C_d = C_{d,friction} + C_{d,pressure}$, the pressure component of drag is zero for a surface oriented normal to the flow, consequently the drag coefficient for parallel flow over a flat plate is simply the friction coefficient already defined in section 5.1.

5.3.1 Friction, Pressure Drag and the importance of fluid viscosity

At low Reynolds numbers this frictional force is dominant, including in the case of streamlined aerofoils. In laminar flow, the surface roughness does not affect the associated drag coefficient, in contrast to turbulent flow, where the drag coefficient is proportional to surface roughness defined as the extent to which slight irregularities on a surface protrude into the viscous sub-layer relative to the surface length ε/L. The surface is considered smooth in turbulent flow when the ratio between the protrusion height and characteristic length is less than $1\mathrm{x}10^{-5}$.

Considering fluid being forced to flow around a curved body, the presence of this body in the airflow necessitates an increased velocity in the reduced flow area surrounding with region occupied by the cylinder to maintain the flow rate as per the continuity principle. Outside the boundary layer, in the inviscid flow region, the energy sum of pressure and velocity along a streamline will be constant. Therefore, the pressure upstream will increase as the flow approaches the centre of the cylinder but similarly increase past this point downstream. However, in the boundary layer, viscous losses act to ultimately prevent the flow from recovering to this equivalent velocity against the rising downstream pressure of inviscid flow. The result is detachment of flow from the body and a separation region of diminished velocity and pressure can be observed by streamlines showing recirculation and back flow downstream of the body, the region in which these effects occur is referred to as the wake. Figure 5-2 shows the flow separation around a cylinder; the separation region extends to the point at which the two streamlines reattach whilst the wake extends until the flow regains its prior velocity.

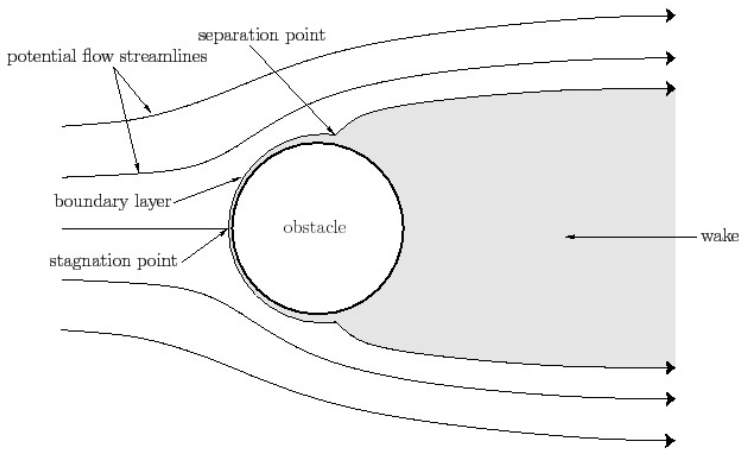

Figure 5-2: Flow separation and reattachment past a cylinder, including wake region [Fitzpatrick, 2012]

Flow separation is the principal cause of pressure drag experienced by non-streamlined bodies; the extent of diminished pressure is proportional to the size of the separation region. The drag force is proportional to the pressures acting on the front and back of the body and the extent of the area in contact with the oncoming flow. Ultimately however, it must be stated that both friction and pressure drag is contingent on the fluid viscosity. Since an inviscid flow around a body (regardless of shape and orientation) would impart no initial shear forces on the body, there would consequently be no boundary layer or separation region and thus no pressure losses would arise to contribute a drag force.

The tangential flow speed is zero at the stagnation point, and is seen to increase until reaching a maximum at the 90-degree point. The velocity after this point begins to decrease, it is under these such circumstances that boundary layer separation occurs. In an ideal case of zero fluid viscosity, the velocity past 90 degrees would recover, however this is not the case in reality. Instead the pressure in the wake does not recover fully and remains closer to the lower pressure. This pressure difference is the cause of form drag.

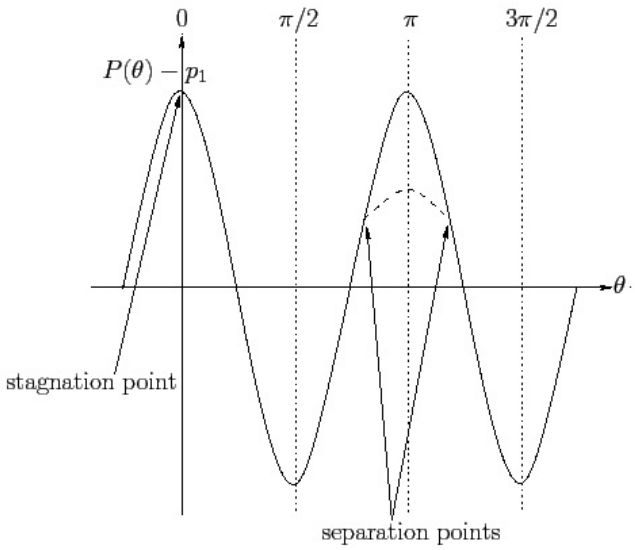

Figure 5-3: Pressure variation over surface of cylinder [Fitzpatrick, 2012]

Figure 5-3 shows the drag force across the full 360 degrees of the cylinder, including the highest pressure at the stagnation point where the velocity is zero, as well as the effect of boundary layer separation beyond the separation points. The cause of separation is the reducing flow velocity due to the increased pressure, the extents of flow nearer the wall experience greater relative speed reductions resulting in the separated flow.

The above case relates to a stationary cylinder, introducing the scenario for clockwise rotation on the cylinder, would accelerate and decelerate the tangential flow speed of the fluid above and below the cylinder respectively. Resulting in a relative reduction in pressure above the cylinder, producing lift, the relative difference between the tangential flow velocity above and below the cylinder is termed "circulation" as demonstrated in figure 5-4 and is crucial in obtaining a lift force.

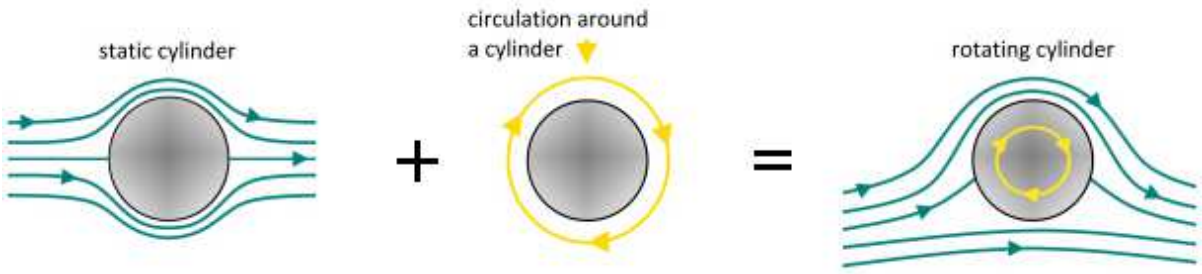

Figure 5-4: Aerodynamic effect of circulation on cylinder [Baer, 2015]

Taking the case of an aerofoil, here, circulation is a consequence of the conservation of momentum due to a starting vortex, introduced by the downward flow of air which can be caused by a chamber profile and/or an angle of attack, shown in figure 5-5 below.

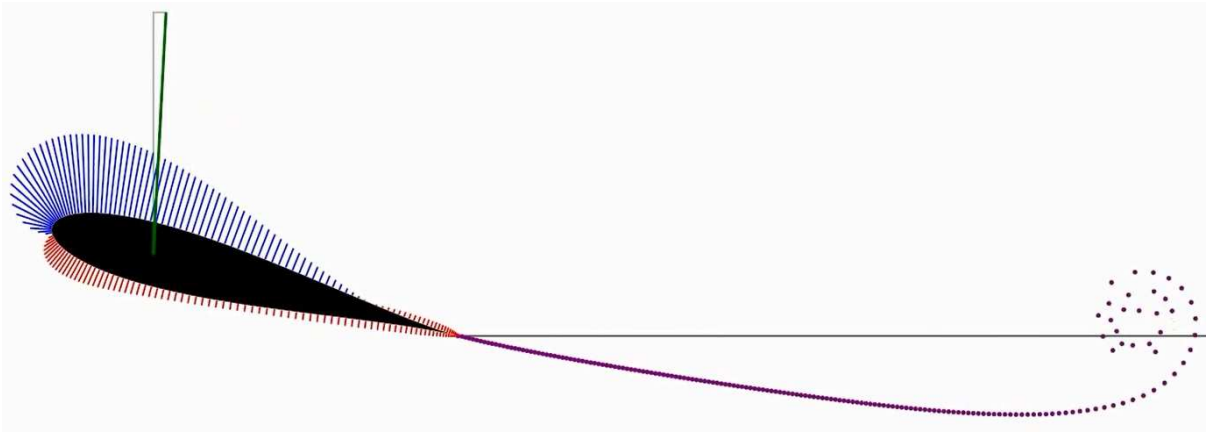

Figure 5-5: Starting vortex created due to downward flow of air [Nathan, 2011]

The extent of lift experienced by an aerofoil can be expressed by the Kutta-Zhukovsky theorem, given as below

$$Lift = airspeed\ x\ circulation\ x\ density\ x\ span \tag{5.29}$$

As circulation is proportional to the coefficient of lift and airspeed, equation 5.29 is consistent with the common definition of the lift force being proportional to the coefficient of lift, airspeed squared and cord-length, as demonstrated in equation 5.30.

$$L = 0.5 C_L \rho A V^2 \tag{5.30}$$

Focusing of the pressure above and below a chambered aerofoil, the pressure just above the aerofoil is lower and rises to ambient upon reaching the free-stream. However, the pressure below the aerofoil remains ambient. The airflow traveling above the aerofoil experiences ambient pressure before the aerofoil and lower pressure before encountering the higher (ambient) pressure downstream of the wing, demonstrated in figure 5-6. The increase in pressure experienced past the aerofoil is referred to as an adverse pressure gradient, and increases with angle of attack eventually leading to flow separation, which results in greatly increased drag and a consequent loss of lift.

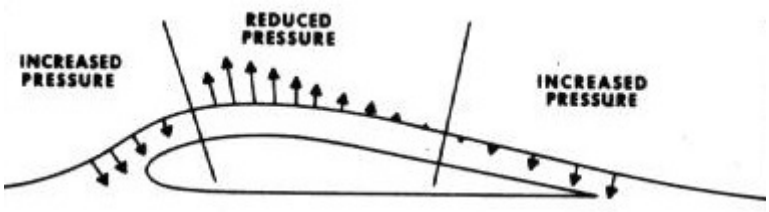

Figure 5-6: Regions of increased and reduced pressure along the top of aerofoil [Avstop, 2015]

The combination of form and skin friction drag is referred to as parasitic drag. The difference in pressure causes air to flow from the bottom to the top of the aerofoil at the wind tips. Such wing-tip

vortices are proportional to the circulation, and their production reduces the kinetic energy of the aerofoil, and therefore, are a source of drag, referred to as (lift) induced drag. Recalling the Kutta-Zhukovsky theorem, to achieve the same lift force for an aerofoil travelling at lower velocities, rather than attempting to raise the circulation, the span of the aerofoil can be elongated, thereby avoiding increases in induced drag.

5.3.2 Heat Transfer

It was discussed in section 6.2 that the local and average Nusselt numbers were effectively functions of the Reynolds and Prandtl number having, and as such, the variables that determine the drag forces, also determine the heat transfer from a surface.

Consequently, after obtaining heat transfer rates by experiment, for straightforward flows over a surface, a Nusselt number can often be determined and expressed as a power-law relation with the form:

$$Nu = CRe_L^m Pr^n \tag{5.31}$$

where m and n are constant exponents, whilst the constant C is a variable subject to the flow conditions and the geometry.

Temperature variations in a flowing fluid, from a heated surface up to the edge of the thermal boundary layer, leads to variations in the temperature dependent properties. The problem can therefore be simplified, without a significant loss in accuracy, by taking fixed values for these properties through the entire flow, defined at what is known as a film temperature, the arithmetic average temperature between the surface and free-stream $T_f = (T_s - T_\infty)/2$.

Given that the local friction and convection coefficients vary along a surface due to the growing velocity and thermal boundary layers, the total effect along the entire surface can be determined by first obtaining the average values for these coefficients by integrating along the full length such that

$$C_D = \frac{1}{L}\int_0^L C_{D,x}\,dx \tag{5.32}$$

and

$$h = \frac{1}{L}\int_0^L h_x\,dx \tag{5.33}$$

5.4 External Flow Over Flat Plates

In the case of flow over flat plates, as well as slightly curved surfaces such as aerofoils, the transition from laminar to turbulent generally occurs at a critical Reynolds numbers defined as

$$Re_{cr} = \frac{\rho V x_{cr}}{\mu} = 5 \text{ x } 10^5 \tag{5.34}$$

Though this value is taken as quite common, a critical Reynolds number can vary from $1\text{x}10^5$ to as high as $3\text{x}10^6$, subject to the surface roughness and extent of turbulence in the free-stream.

5.4.1 Friction Coefficient

The boundary layer thickness and coefficient of friction for laminar flow was already derived in section 6.1, the corresponding turbulent flow relations are expressed below for comparison.

Laminar: $\delta_{v,x} = \frac{5x}{Re_x^{1/2}}$ and $C_{f,x} = \frac{0.664}{Re_x^{1/2}}$ $Re_x < 5 \text{ x } 10^5$ (5.35)

Turbulent: $\delta_{v,x} = \frac{0.382x}{Re_x^{1/5}}$ and $C_{f,x} = \frac{0.0592}{Re_x^{1/5}}$ $5 \text{ x } 10^5 \leq Re_x \leq 10^7$ (5.36)

The local values of the coefficients are found to be higher in turbulent flow than in laminar due to intense mixing arising in the turbulent boundary layer. The frictional coefficient decreases in the flow direction, by a factor of $x^{-1/2}$in laminar flow, reaching its maximum value once the boundary layer becomes turbulent, and then continues to reduce by a factor of $x^{-1/5}$. As mentioned, an average value for these friction coefficients over the entire plate can be obtained through integration, resulting in,

Laminar: $C_f = \frac{1.328}{Re_L^{1/2}}$ $Re_L < 5 \text{ x } 10^5$ (5.37)

Turbulent: $C_f = \frac{0.074}{Re_L^{1/5}}$ $5 \text{ x } 10^5 \leq Re_L \leq 10^7$ (5.38)

It is clear that equation 5.37 requires the flow to be laminar over the entire plate; similarly, equation 5.38 assumes the flow to be turbulent over the entire plate, or rather that the critical length x_{cr} at which the flow begins to become turbulent is negligible compared to the full length of the plate. For a plate length sufficient to allow a flow to become turbulent but along which the laminar portion cannot

be disregarded, the average friction coefficient can again be determined by integrating over both the laminar $0 \leq x \leq x_{cr}$ and turbulent $x_{cr} \leq x \leq L$ regions such that

$$C_f = \frac{1}{L}\left(\int_0^{x_{cr}} C_{f,x\ laminar}dx + \int_{x_{cr}}^{L} C_{f,x\ turbulent}dx\right) \tag{5.39}$$

By defining a critical Reynolds number of $Re_{cr} = 5\text{x}10^5$ the transitional region is included in the turbulent region; the average friction coefficient is determined to be

$$C_f = \frac{0.074}{Re_L^{1/5}} - \frac{1742}{Re_L} \qquad 5\text{ x }10^5 \leq Re_L \leq 10^7 \tag{5.40}$$

The constants within equation 5.39 are dependent on the value of the defined critical Reynolds number; further assumptions made for this relation include a smooth surface and flow in the free-steam to be turbulence free. It was mentioned that unlike laminar flow, the friction drag in turbulent flow is affected by surface roughness. Moreover, after the flow becomes fully turbulent $Re \geq 10^6$,the friction coefficient remains a function only of surface roughness, independent of increasing Reynolds number.

5.4.2 Heat Transfer Coefficient

As with the friction coefficient, the Nusselt number for laminar flow was derived in section 6.2, the corresponding turbulent flow coefficient also is defined below for comparison.

Laminar: $$C_f = \frac{1.328}{Re_L^{1/2}} \qquad Re_L < 5\text{ x }10^5 \tag{5.41}$$

Turbulent: $$C_f = \frac{0.074}{Re_L^{1/5}} \qquad 5\text{ x }10^5 \leq Re_L \leq 10^7 \tag{5.42}$$

Just as with the friction coefficient, the local values of the heat transfer coefficients h_x are found to be higher in turbulent flow than in laminar for the same reason of intense mixing. The heat transfer coefficient decreases in the flow direction, by a factor of $x^{-1/2}$ in laminar flow, a maximum is reached once the boundary layer becomes turbulent, thereafter continuing to reduce by a factor of $x^{-1/5}$. The variation of both the local friction and heat transfer coefficients in the flow direction along a flat plate can therefore be shown together, as in figure 5-7 below.

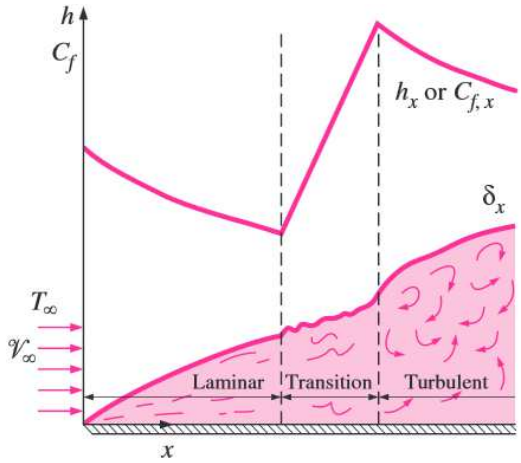

Figure 5-7: Local friction and heat transfer coefficients varying along a flat plate [Cengel, 2011]

Integrating the heat transfer coefficients to obtain an average value over the entire plate results in equations 5.43 and 5.44, the same assumptions regarding purely laminar and purely turbulent flow apply.

Laminar: $$Nu = \frac{hL}{k} = 0.664 Re_L^{0.5} Pr^{1/3} \qquad Re_L < 5 \text{ x } 10^5 \tag{5.43}$$

Turbulent: $$Nu = \frac{hL}{k} = 0.037 Re_L^{0.8} Pr^{\frac{1}{3}} \qquad 0.6 \leq \text{Pr} \leq 60 \quad 5 \text{ x } 10^5 \leq Re_L \leq 10^7 \tag{5.44}$$

Similar to the friction coefficient, by integrating the laminar and turbulent regions together will obtain an average value for when the heat transfer coefficient when the surface experiences first laminar then turbulent flow.

$$h = \frac{1}{L}\left(\int_0^{x_{cr}} h_{,x\ laminar} dx + \int_{x_{cr}}^{L} h_{,x\ turbulent} dx\right) \tag{5.45}$$

Assuming a critical Reynolds number of $5 \text{ x } 10^5$, leads to the relation in equation 5.45, the graphical representation for which is given in figure 5-8 below.

Turbulent: $$Nu = \frac{hL}{k} = (0.037 Re_L^{0.8} - 871) Pr^{\frac{1}{3}} \qquad 0.6 \leq \text{Pr} \leq 60 \quad 5\text{x}10^5 \leq Re_L \leq 10^7 \tag{5.46}$$

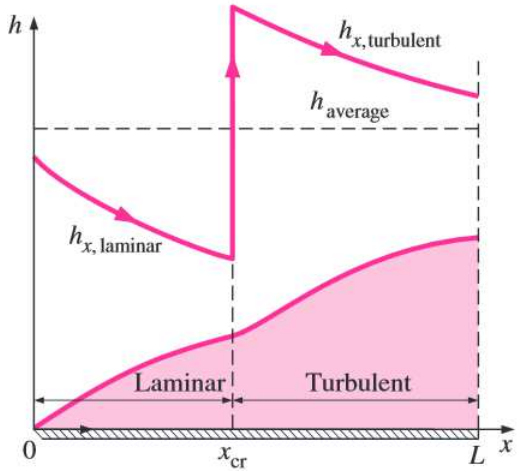

Figure 5-8: Average heat transfer coefficients along a flat plate during combined laminar and turbulent flow [Cengel, 2011]

As with the previous section, the assumption of smooth surfaces applies to the above equations, and though the heat relations were obtained for the case of isothermal surfaces, they would be applicable in determining the total rate of heat transfer across non-isothermal surfaces by setting the temperature at a constant average value.

5.5 Flow through Fin Channels

In totally enclosed fan cooled (TEFC) machines it is common to see axial fins included on the housing surface to increase the convection heat transfer. Most often these fins channels would be semi-open.

As a result, the most common internal and external flow correlations would not be valid. A special correlation for the convective heat coefficient can be applied to such semi-open fin channels based on testing by Heiles *et al* on finned induction motor housings. It was found that such fins significantly enhanced heat transfer due to the increased surface area. The calculations demonstrated that, up to an extent, heat flux increased with fin height and would significantly decrease when the spacing between the fins was reduced. The formula for the heat coefficient is given in equations 5.47 and 5.48:

$$h = \frac{\rho c_p D v}{4L}(1 - e^{-m}) \tag{5.47}$$

$$m = 0.1448 \frac{L^{0.946}}{D^{1.16}} \left(\frac{k}{\rho c_p v} \right)^{0.214} \tag{5.48}$$

Where v is the air velocity within the fin channels, D is the hydraulic diameter which in this case is taken as four times the cross-sectional area of the fin channel divided by the perimeter (including the open side), whilst L is the axial length of the fin channel. Fins of equal height extending

perpendicularly from a generator surface would cause each fin channel to have the same hydraulic area and consequently the same heat coefficient. The correlation assumes the channel flow to always be turbulent. The open side of a channel would not normally be included when calculating a hydraulic diameter however it is specifically required in the above correlation. The correlation also assumes an isothermal generator surface and the air properties would be calculated at the film temperature, which is the average temperature of the surface and freestream air.

5.6 Summary

In this chapter, the momentum and energy components of the Navier-Stokes equations were solved to obtain friction and heat correlations in cases of purely laminar flow. Including the thickness of the velocity and thermal boundary layer. The Reynolds analogies that relate the coefficients, are valid for both laminar and turbulent flow over surfaces, as the Reynolds number appears in both coefficients. They apply even in the presence of pressure gradients, otherwise defined as forced convection. Turbulent empirical correlations for cases of external forced convection were outlined in this chapter, correlations for internal forced convection, though applicable to the flow entering the encompassing shroud of the turbo generation section, are not included in this thesis. Such correlations can be found outlined by Cengal, 2011.

Though laminar correlations are often derived, the equivalent turbulent correlations tend to only be stated. The reason for this is the chaotic three-dimensional velocity fluctuations that occur inherently due to turbulence, making it impossible to solve the Navier-Stokes equations analytically. The next chapter is the final chapter related to the theory of fluid flow, and will explain the issue of turbulence, outline the complete Navier-Stokes equations, as well as discuss the concept of turbulence modelling used to solve the flow domain.

6.0 RESOLVING THE TURBULENCE

In chapter 4, the Navier-Stokes equations were discussed and derived. The next chapter demonstrated how simplified solutions of these equations could lead to friction and heat relations for laminar flow, in later chapters additional turbulent relations for external and internal flow were provided directly rather than being analytically derived from the original Navier-Stokes equations.

The reason for this is the convective acceleration term, which introduces the element of non-linearity into the NS equations, necessitating the use of (alternative) iterative techniques to obtain a solution. An exception is in the case of a one-dimensional, steady, laminar flow, in which the x-momentum equation can be simplified, the non-linearity removed, and an analytical solution can be derived. Whereas when the flow becomes turbulent, even in cases of one dimensional flow, there will exist velocity perturbations in the other two dimensions significant enough that the terms constituting the convective acceleration part of the equation cannot be disregarded. The result is a greater transfer of momentum throughout the flow.

Indeed, turbulence is observed as the emergence of chaotic three-dimensional velocity fluctuations that occur regardless of the overall flow direction. Such behaviour is not observed at low Reynolds numbers as any such chaotic behaviour would be suppressed by the inherent viscosity of the fluid leading to the ordered motion seen in laminar flow. At higher Reynolds numbers, the inertial forces overcome these viscous forces, resulting in the aforementioned turbulent flow. Aside from high Reynolds numbers, other phenomena that promote mixing of the flow such as rotating obstacles will also contribute to turbulence.

The chaotic fluctuations in the flow are termed “turbulent eddies”, these eddies begin at large scales and contribute to further momentum and heat transfer throughout the flow. Energy is diffused such that these eddies persist down to even very small scales, until finally dissipating as heat due to the viscosity of the fluid. Therefore, for truly simulating turbulent flow, when discretising of the domain, the mesh size must fine enough to account for even the smallest eddies. This approach is termed as a direct numerical solution. Solving for such a fine resolution (with a consequent very high cell count) is often times beyond the capability of even super clusters. Whereas, attempting to solve only the Navier-Stokes equations across cells in a relatively coarse mesh would give highly inaccurate results, due to absent of smaller scale turbulence. For this reason, direct numerical simulations are mostly encountered in laminar flows.

A solution to this problem is then to model rather than simulate the turbulence in the domain. This can be accomplished by decomposing the variables into time-averaged and fluctuating components. The averaged velocities can then be simulated whilst the turbulent effects not otherwise captured due to the coarseness of the mesh would instead be accounted for by the additions made to the Navier-Stokes

equations. This technique is the most common approach to solving large scale CFD problems in industry, the modified equations are termed (RANS) or Reynolds Averaged Navier-Stokes equations.

The process of Reynolds averaging results in three additional unknown variables, which must be accounted for by "turbulence models". Such models are used to express these unknown turbulent components in terms of the averaged values and thereby provide closure to the RANS equations. This chapter will demonstrate the Navier-Stokes equations in their full form, show the technique of Reynolds averaging and explain how closure is provided by the most common turbulence models.

6.1 The complete Navier-Stokes equations

The momentum equation, the most extensive of the Navier-Stokes equations, was derived through Newton's second law in section 4.2. However, a number of assumptions were made to obtain the viscous components of the equation, with little explanation of their relation to the full stress tensor acting on a volume of fluid. Aside from this, the momentum equation is often expressed in various expanded forms throughout available literature with little regard to the different assumptions made in obtaining any given form, often leaving the reader confused. These issues will be dealt with below, to finally express the Navier-Stokes equations in their complete and consistent form.

The continuity and momentum equations can be expressed most compactly in "Einstein notation" as below.

$$\frac{\partial \rho}{\partial t} + \rho \frac{\partial u_i}{\partial x_i} = 0 \tag{6.1}$$

$$\rho \frac{\partial u_i}{\partial t} + \rho \frac{\partial}{\partial x_j}\left(u_j u_i\right) = -\frac{\partial p}{\partial x_i} + \frac{\partial}{\partial x_j}\left(2\mu s_{ij}\right) \tag{6.2}$$

Equations expressed in Einstein notation can be expanded to form matrices, all the terms in which, can later be summed together. The "i" subscripts denote additional rows whilst the "j" subscripts denote additional columns, and as such are a convenient way to simplify equations that deal with 3 dimensions simultaneously.

The continuity equation can be expanded as:

$$\frac{\partial \rho}{\partial t} + \rho \frac{\partial u_i}{\partial x_i} = \frac{\partial \rho}{\partial t} + \rho \begin{bmatrix} \frac{\partial u_1}{\partial x_1} \\ \frac{\partial u_2}{\partial x_2} \\ \frac{\partial u_3}{\partial x_3} \end{bmatrix} = \frac{\partial \rho}{\partial t} + \rho \left(\frac{\partial u}{\partial x} + \frac{\partial v}{\partial y} + \frac{\partial w}{\partial z} \right) = \frac{\partial \rho}{\partial t} + \frac{\partial \rho u}{\partial x} + \frac{\partial \rho v}{\partial y} + \frac{\partial \rho w}{\partial z} = 0 \tag{6.3}$$

Whilst the momentum equation can be expanded as below:

$$\rho\frac{\partial u_i}{\partial t}+\rho\frac{\partial}{\partial x_j}(u_j u_i)=-\frac{\partial p}{\partial x_i}+\frac{\partial}{\partial x_j}(2\mu S_{ij})$$

$$\begin{bmatrix}\rho\frac{\partial u_1}{\partial t}\\ \rho\frac{\partial u_2}{\partial t}\\ \rho\frac{\partial u_3}{\partial t}\end{bmatrix}+\begin{bmatrix}\rho\frac{\partial}{\partial x_1}(u_1u_1) & \rho\frac{\partial}{\partial x_2}(u_2u_1) & \rho\frac{\partial}{\partial x_3}(u_3u_1)\\ \rho\frac{\partial}{\partial x_1}(u_1u_2) & \rho\frac{\partial}{\partial x_2}(u_2u_2) & \rho\frac{\partial}{\partial x_3}(u_3u_1)\\ \rho\frac{\partial}{\partial x_1}(u_1u_3) & \rho\frac{\partial}{\partial x_2}(u_2u_3) & \rho\frac{\partial}{\partial x_3}(u_3u_3)\end{bmatrix}=-\begin{bmatrix}\frac{\partial p}{\partial x_1}\\ \frac{\partial p}{\partial x_2}\\ \frac{\partial p}{\partial x_3}\end{bmatrix}+\begin{bmatrix}\frac{\partial}{\partial x_1}(2\mu S_{11}) & \frac{\partial}{\partial x_2}(2\mu S_{12}) & \frac{\partial}{\partial x_3}(2\mu S_{13})\\ \frac{\partial}{\partial x_1}(2\mu S_{21}) & \frac{\partial}{\partial x_2}(2\mu S_{22}) & \frac{\partial}{\partial x_3}(2\mu S_{23})\\ \frac{\partial}{\partial x_1}(2\mu S_{31}) & \frac{\partial}{\partial x_1}(2\mu S_{32}) & \frac{\partial}{\partial x_1}(2\mu S_{33})\end{bmatrix} \quad (6.4)$$

The final right-hand term in the equation includes the strain-rate tensor. For Newtonian fluids, the stresses are related to the strain-rate such that $\tau_{ij}=2\mu S_{ij}$. The equation can therefore be further expressed as

$$\begin{bmatrix}\frac{\partial\rho u}{\partial t}\\ \frac{\partial\rho v}{\partial t}\\ \frac{\partial\rho w}{\partial t}\end{bmatrix}+\begin{bmatrix}\frac{\partial(\rho u^2)}{\partial x} & \frac{\partial(\rho uv)}{\partial y} & \frac{\partial(\rho uw)}{\partial z}\\ \frac{\partial(\rho uv)}{\partial x} & \frac{\partial(\rho v^2)}{\partial y} & \frac{\partial(\rho vw)}{\partial z}\\ \frac{\partial(\rho uw)}{\partial x} & \frac{\partial(\rho vw)}{\partial y} & \frac{\partial(\rho w^2)}{\partial z}\end{bmatrix}=-\begin{bmatrix}\frac{\partial p}{\partial x}\\ \frac{\partial p}{\partial y}\\ \frac{\partial p}{\partial z}\end{bmatrix}+\begin{bmatrix}\frac{\partial(\tau_{xx})}{\partial x} & \frac{\partial(\tau_{xy})}{\partial y} & \frac{\partial(\tau_{xz})}{\partial z}\\ \frac{\partial(\tau_{yx})}{\partial x} & \frac{\partial(\tau_{yy})}{\partial y} & \frac{\partial(\tau_{yz})}{\partial z}\\ \frac{\partial(\tau_{zx})}{\partial x} & \frac{\partial(\tau_{zy})}{\partial y} & \frac{\partial(\tau_{zz})}{\partial z}\end{bmatrix} \quad (6.5)$$

The viscous stress tensor now becomes clear and describes the 3 sets of forces acting on opposite faces in the 3 dimensions as shown in figure 6-1. The tensor is symmetrical such that out of the total of 9 terms, only 6 are unknown.

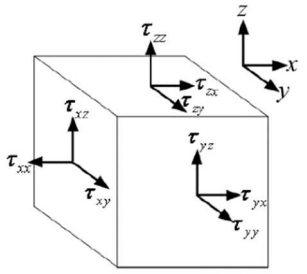

Figure 6-1: Stress tensors acting on 3D infinitesimal volume [Anderson, 2011]

As mentioned, the stresses in the fluid result in strain-rates, and these can be expressed in terms of velocity gradients such that $S_{ij}=\frac{1}{2}\left(\frac{\partial u_i}{\partial x_j}+\frac{\partial u_j}{\partial x_i}\right)$. Incorporating this into the tensor, the momentum equation is further expressed as:

$$\begin{bmatrix} \rho\frac{\partial u}{\partial t} \\ \rho\frac{\partial v}{\partial t} \\ \rho\frac{\partial w}{\partial t} \end{bmatrix} + \begin{bmatrix} \rho u\frac{\partial u}{\partial x} & \rho v\frac{\partial u}{\partial y} & \rho w\frac{\partial u}{\partial z} \\ \rho u\frac{\partial v}{\partial x} & \rho v\frac{\partial v}{\partial y} & \rho w\frac{\partial v}{\partial z} \\ \rho u\frac{\partial w}{\partial x} & \rho v\frac{\partial w}{\partial y} & \rho w\frac{\partial w}{\partial z} \end{bmatrix} = -\begin{bmatrix} \frac{\partial p}{\partial x} \\ \frac{\partial p}{\partial y} \\ \frac{\partial p}{\partial z} \end{bmatrix} + 2\mu\frac{\partial}{\partial x_j}\begin{bmatrix} \frac{1}{2}\left(\frac{\partial u_1}{\partial x_1}+\frac{\partial u_1}{\partial x_1}\right) & \frac{1}{2}\left(\frac{\partial u_1}{\partial x_2}+\frac{\partial u_2}{\partial x_1}\right) & \frac{1}{2}\left(\frac{\partial u_1}{\partial x_3}+\frac{\partial u_3}{\partial x_1}\right) \\ \frac{1}{2}\left(\frac{\partial u_2}{\partial x_1}+\frac{\partial u_1}{\partial x_2}\right) & \frac{1}{2}\left(\frac{\partial u_2}{\partial x_2}+\frac{\partial u_2}{\partial x_2}\right) & \frac{1}{2}\left(\frac{\partial u_2}{\partial x_3}+\frac{\partial u_3}{\partial x_2}\right) \\ \frac{1}{2}\left(\frac{\partial u_3}{\partial x_1}+\frac{\partial u_1}{\partial x_3}\right) & \frac{1}{2}\left(\frac{\partial u_3}{\partial x_2}+\frac{\partial u_2}{\partial x_3}\right) & \frac{1}{2}\left(\frac{\partial u_3}{\partial x_3}+\frac{\partial u_3}{\partial x_3}\right) \end{bmatrix} \tag{6.6}$$

Equation 6.7 below is the full momentum equation, applicable even to compressible flow, characterised by the 3 diagonal terms incorporating the rate of change of velocity in its respective flow direction, which is significant is super-sonic flow.

$$\begin{bmatrix} \rho\frac{\partial u}{\partial t} \\ \rho\frac{\partial v}{\partial t} \\ \rho\frac{\partial w}{\partial t} \end{bmatrix} + \begin{bmatrix} \rho u\frac{\partial u}{\partial x} & \rho v\frac{\partial u}{\partial y} & \rho w\frac{\partial u}{\partial z} \\ \rho u\frac{\partial v}{\partial x} & \rho v\frac{\partial v}{\partial y} & \rho w\frac{\partial v}{\partial z} \\ \rho u\frac{\partial w}{\partial x} & \rho v\frac{\partial w}{\partial y} & \rho w\frac{\partial w}{\partial z} \end{bmatrix} = -\begin{bmatrix} \frac{\partial p}{\partial x} \\ \frac{\partial p}{\partial y} \\ \frac{\partial p}{\partial z} \end{bmatrix} + \begin{bmatrix} 2\mu\left(\frac{\partial^2 u}{\partial x^2}\right) & \mu\left(\frac{\partial^2 u}{\partial y^2}+\frac{\partial^2 v}{\partial x\partial y}\right) & \left(\frac{\partial^2 u}{\partial z^2}+\frac{\partial^2 w}{\partial x\partial z}\right) \\ \mu\left(\frac{\partial^2 v}{\partial x^2}+\frac{\partial^2 u}{\partial y\partial x}\right) & 2\mu\left(\frac{\partial^2 v}{\partial y^2}\right) & \mu\left(\frac{\partial^2 v}{\partial z^2}+\frac{\partial^2 w}{\partial y\partial z}\right) \\ \mu\left(\frac{\partial^2 w}{\partial x^2}+\frac{\partial^2 u}{\partial z\partial x}\right) & \mu\left(\frac{\partial^2 w}{\partial y^2}+\frac{\partial^2 v}{\partial z\partial y}\right) & 2\mu\left(\frac{\partial^2 w}{\partial z^2}\right) \end{bmatrix} \tag{6.7}$$

For cases of incompressible flow, the viscous components in equation 6.7 can be simplified further. This is done by splitting the terms multiplied by 2 and rearranging the other terms into the form of the continuity equation as demonstrated below.

$$\begin{bmatrix} 2\mu\left(\frac{\partial^2 u}{\partial x^2}\right) & \mu\left(\frac{\partial^2 u}{\partial y^2}+\frac{\partial^2 v}{\partial x\partial y}\right) & \left(\frac{\partial^2 u}{\partial z^2}+\frac{\partial^2 w}{\partial x\partial z}\right) \\ \mu\left(\frac{\partial^2 v}{\partial x^2}+\frac{\partial^2 u}{\partial y\partial x}\right) & 2\mu\left(\frac{\partial^2 v}{\partial y^2}\right) & \mu\left(\frac{\partial^2 v}{\partial z^2}+\frac{\partial^2 w}{\partial y\partial z}\right) \\ \mu\left(\frac{\partial^2 w}{\partial x^2}+\frac{\partial^2 u}{\partial z\partial x}\right) & \mu\left(\frac{\partial^2 w}{\partial y^2}+\frac{\partial^2 v}{\partial z\partial y}\right) & 2\mu\left(\frac{\partial^2 w}{\partial z^2}\right) \end{bmatrix} = \mu\begin{bmatrix} \frac{\partial^2 u}{\partial x^2} & \frac{\partial^2 u}{\partial y^2} & \frac{\partial^2 u}{\partial z^2} & \frac{\partial^2 u}{\partial x^2} & \frac{\partial^2 v}{\partial x\partial y} & \frac{\partial^2 w}{\partial x\partial z} \\ \frac{\partial^2 v}{\partial x^2} & \frac{\partial^2 v}{\partial y^2} & \frac{\partial^2 v}{\partial z^2} & \frac{\partial^2 u}{\partial y\partial x} & \frac{\partial^2 v}{\partial y^2} & \frac{\partial^2 w}{\partial y\partial z} \\ \frac{\partial^2 w}{\partial x^2} & \frac{\partial^2 w}{\partial y^2} & \frac{\partial^2 w}{\partial z^2} & \frac{\partial^2 u}{\partial z\partial x} & \frac{\partial^2 v}{\partial z\partial y} & \frac{\partial^2 w}{\partial z^2} \end{bmatrix} \tag{6.8}$$

$$\mu\begin{bmatrix} \frac{\partial^2 u}{\partial x^2} & \frac{\partial^2 u}{\partial y^2} & \frac{\partial^2 u}{\partial z^2} & \frac{\partial^2 u}{\partial x^2} & \frac{\partial^2 v}{\partial x\partial y} & \frac{\partial^2 w}{\partial x\partial z} \\ \frac{\partial^2 v}{\partial x^2} & \frac{\partial^2 v}{\partial y^2} & \frac{\partial^2 v}{\partial z^2} & \frac{\partial^2 u}{\partial y\partial x} & \frac{\partial^2 v}{\partial y^2} & \frac{\partial^2 w}{\partial y\partial z} \\ \frac{\partial^2 w}{\partial x^2} & \frac{\partial^2 w}{\partial y^2} & \frac{\partial^2 w}{\partial z^2} & \frac{\partial^2 u}{\partial z\partial x} & \frac{\partial^2 v}{\partial z\partial y} & \frac{\partial^2 w}{\partial z^2} \end{bmatrix} = \begin{bmatrix} \mu\left(\frac{\partial^2 u}{\partial x^2}+\frac{\partial^2 u}{\partial y^2}+\frac{\partial^2 u}{\partial z^2}\right) & + & \mu\frac{\partial}{\partial x}\left(\frac{\partial u}{\partial x}+\frac{\partial v}{\partial y}+\frac{\partial w}{\partial z}\right) \\ \mu\left(\frac{\partial^2 v}{\partial x^2}+\frac{\partial^2 v}{\partial y^2}+\frac{\partial^2 v}{\partial z^2}\right) & + & \mu\frac{\partial}{\partial y}\left(\frac{\partial u}{\partial x}+\frac{\partial v}{\partial y}+\frac{\partial w}{\partial z}\right) \\ \mu\left(\frac{\partial^2 w}{\partial x^2}+\frac{\partial^2 w}{\partial y^2}+\frac{\partial^2 w}{\partial z^2}\right) & + & \mu\frac{\partial}{\partial z}\left(\frac{\partial u}{\partial x}+\frac{\partial v}{\partial y}+\frac{\partial w}{\partial z}\right) \end{bmatrix} \tag{6.9}$$

The right most term of equation 6.9 (in brackets) is the continuity equation for steady, incompressible flow. As this is equal to zero, $\nabla \cdot \boldsymbol{V} = 0$, it can thereby be eliminated, simplifying the momentum equation to that below.

$$\begin{bmatrix} \frac{\partial \rho u}{\partial t} \\ \frac{\partial \rho v}{\partial t} \\ \frac{\partial \rho w}{\partial t} \end{bmatrix} + \begin{bmatrix} \frac{\partial(\rho u^2)}{\partial x} + \frac{\partial(\rho uv)}{\partial y} + \frac{\partial(\rho uw)}{\partial z} \\ \frac{\partial(\rho uv)}{\partial x} + \frac{\partial(\rho v^2)}{\partial y} + \frac{\partial(\rho vw)}{\partial z} \\ \frac{\partial(\rho uw)}{\partial x} + \frac{\partial(\rho vw)}{\partial y} + \frac{\partial(\rho w^2)}{\partial z} \end{bmatrix} = -\begin{bmatrix} \frac{\partial p}{\partial x} \\ \frac{\partial p}{\partial y} \\ \frac{\partial p}{\partial z} \end{bmatrix} + \begin{bmatrix} \mu\left(\frac{\partial^2 u}{\partial x^2} + \frac{\partial^2 u}{\partial y^2} + \frac{\partial^2 u}{\partial z^2}\right) \\ \mu\left(\frac{\partial^2 v}{\partial x^2} + \frac{\partial^2 v}{\partial y^2} + \frac{\partial^2 v}{\partial z^2}\right) \\ \mu\left(\frac{\partial^2 w}{\partial x^2} + \frac{\partial^2 w}{\partial y^2} + \frac{\partial^2 w}{\partial z^2}\right) \end{bmatrix} \quad (6.10)$$

Equation 6.10 is the momentum equation in its complete form, and all the viscous terms are included relating to the 3 viscous components for each dimension. Importantly, the diagonal terms would be very small relative to the other terms when analysing a subsonic flow. The equation can be further collapsed, and the gravitational body force can also be included. Finally, by isolating vectors, equation 6.11 can be expressed as a single transport equation.

$$\begin{bmatrix} \frac{\partial \rho u}{\partial t} \\ \frac{\partial \rho v}{\partial t} \\ \frac{\partial \rho w}{\partial t} \end{bmatrix} + \begin{bmatrix} \rho(\boldsymbol{V} \cdot \nabla u) \\ \rho(\boldsymbol{V} \cdot \nabla \mathrm{v}) \\ \rho(\boldsymbol{V} \cdot \nabla \mathrm{w}) \end{bmatrix} = -\begin{bmatrix} \frac{\partial p}{\partial x} \\ \frac{\partial p}{\partial y} \\ \frac{\partial p}{\partial z} \end{bmatrix} + \begin{bmatrix} \mu\nabla^2 u \\ \mu\nabla^2 v \\ \mu\nabla^2 w \end{bmatrix} - \begin{bmatrix} \\ \\ \rho g_z \end{bmatrix} \quad (6.11)$$

$$\rho\left(\frac{\partial \boldsymbol{V}}{\partial t}\right) + \rho(\boldsymbol{V} \cdot \nabla)\boldsymbol{V} = -\nabla p + \mu\nabla^2 \boldsymbol{V} - \rho g_z \quad (6.12)$$

6.1.1 Further understanding of transport equations

Equation 6.12 expresses momentum transfer throughout the flow in the form of a "transport equation", in which accumulation and convection terms are balanced against diffusion and source terms. The generic form is given below and can be used to describe various natural phenomena with a change of variables, including modelling turbulence as will be discussed later in this chapter.

$$\rho\left(\frac{\partial \varphi}{\partial t}\right) + \rho(\boldsymbol{V} \cdot \nabla)\varphi = \gamma\nabla^2 \varphi + S_\varphi \quad (6.13)$$

The accumulation (first) term describes the transient rate of change of a given quantity within an infinitesimal volume. The convection (second) term accounts for the transport of that given quantity in response to an existing velocity field, and it is this term that leads to the non-linearity of the Navier-Stokes equations. Finally, the diffusion (third) term describes the transport of the given quantity in response to existing gradients of that same quantity. Diffusion will be a linear process provided a constant diffusion coefficient. A source (or sink) term can also be included (fourth term) to account for effects unrelated to accumulation, convection or diffusion, such as gravitational effects and pressure

gradients, or any other body and surfaces forces. Replacing φ by the temperature variable in equation 6.13 reveals the unsteady 3-dimensional energy equation as partially outlined in section 5.4.

$$\rho\left(\frac{\partial T}{\partial t}\right) + \rho(\boldsymbol{V}\cdot\nabla)T = \frac{k}{c_p}\nabla^2 T \tag{6.14}$$

A final remark relates to the transport equation in which the φ variable is set to 1. As there is no flow variable to be diffused, and in the absence of a source term, equation 6.13 collapses to the continuity equation for compressible flow as below.

$$\left(\frac{\partial \rho}{\partial t}\right) + \rho(\boldsymbol{V}\cdot\nabla) = 0 \tag{6.15}$$

6.2 The process of Reynolds averaging

The above Navier-Stokes equations can be used to simulate the flow completely. The five unknown variables of pressure (P), velocity (u,v,w), and temperature (T) can be accounted for by the solving the continuity, momentum and energy equations. In cases of compressible flow, when the density (ρ) is not a constant, an additional equation of state must be solved, a common example is the ideal gas law below, which relates such variables to the universal gas constant (R) and the molar mass (M) of the fluid involved.

$$P = \rho\frac{R}{M}T \tag{6.16}$$

Despite this, the notion of capturing all the turbulence in the flow, specifically at the smallest scales is unfeasible. Instead the terms in the Navier-Stokes equations are averaged, based on the premise that the instantaneous values of any variable fluctuate about a mean value. Allowing the use of a coarser mesh to simulate such mean values, whilst additional terms in the RANS equations, would account for the effects of turbulence in the flow.

The notion of separating an instantaneous quantity into an average and fluctuating value was discussed in section 4.6, the example given was that of a velocity component such that $u = \bar{u} + u'$. This would be done for all the unknown variables. The mean value of a turbulent flow property is obtained by taking a time average over an interval sufficiently large as to render the net effects of the turbulent fluctuations zero, thereby making the time average of the fluctuating component zero, hence $\overline{u'} = 0$. The mean value is given by

$$\overline{f}(t_0) = \frac{1}{T}\int_{t_0-T/2}^{t_0+T/2} f(t).\,dt \tag{6.17}$$

whilst

$$f(t_0) = \overline{f}(t_0) + f'(t_0) \tag{6.18}$$

The most significant result when Reynolds averaging the Navier-Stokes equations is when dealing with a product of two variables. This rule is given in equation 6.19 below, the derivations for all the rules used are detailed in the appendix.

$$\overline{fg} = \overline{f}\,\overline{g} + \overline{f'g'} \tag{6.19}$$

The continuity equation for incompressible flow can be Reynolds averaged as below

$$\overline{\frac{\partial u}{\partial x} + \frac{\partial v}{\partial y} + \frac{\partial w}{\partial z}} = \frac{\partial(\overline{\bar{u} + u'})}{\partial x} + \frac{\partial(\overline{\bar{v} + v'})}{\partial y} + \frac{\partial(\overline{\bar{w} + w'})}{\partial z} = \frac{\partial \bar{u}}{\partial x} + \frac{\partial \bar{v}}{\partial y} + \frac{\partial \bar{w}}{\partial z} = 0 \tag{6.20}$$

The final result is straightforward in that only a mean value of each velocity component remains, as the mean value of a fluctuating component is zero. Reynolds averaging of the momentum equation is detailed below

$$\begin{bmatrix} \frac{\partial \bar{u}}{\partial t} \\ \frac{\partial \bar{v}}{\partial t} \\ \frac{\partial \bar{w}}{\partial t} \end{bmatrix} + \begin{bmatrix} \frac{\partial\left(\overline{u^2}\right)}{\partial x} + \frac{\partial(\overline{uv})}{\partial y} + \frac{\partial(\overline{uw})}{\partial z} \\ \frac{\partial(\overline{uv})}{\partial x} + \frac{\partial\left(\overline{v^2}\right)}{\partial y} + \frac{\partial(\overline{vw})}{\partial z} \\ \frac{\partial(\overline{uw})}{\partial x} + \frac{\partial(\overline{vw})}{\partial y} + \frac{\partial\left(\overline{w^2}\right)}{\partial z} \end{bmatrix} = -\begin{bmatrix} \frac{\partial \bar{p}}{\partial x} \\ \frac{\partial \bar{p}}{\partial y} \\ \frac{\partial \bar{p}}{\partial z} \end{bmatrix} + \begin{bmatrix} v\left(\frac{\partial^2 \bar{u}}{\partial x^2} + \frac{\partial^2 \bar{u}}{\partial y^2} + \frac{\partial^2 \bar{u}}{\partial z^2}\right) \\ v\left(\frac{\partial^2 \bar{v}}{\partial x^2} + \frac{\partial^2 \bar{v}}{\partial y^2} + \frac{\partial^2 \bar{v}}{\partial z^2}\right) \\ v\left(\frac{\partial^2 \bar{w}}{\partial x^2} + \frac{\partial^2 \bar{w}}{\partial y^2} + \frac{\partial^2 \bar{w}}{\partial z^2}\right) \end{bmatrix} \tag{6.21}$$

The averaging is applied to the terms being differentiated, when encountering a product of two variables, it can be expanded out as in equation 6.22 below to become

$$\begin{bmatrix} \frac{\partial \bar{u}}{\partial t} \\ \frac{\partial \bar{v}}{\partial t} \\ \frac{\partial \bar{w}}{\partial t} \end{bmatrix} + \begin{bmatrix} \frac{\partial\left(\bar{u}^2 + \overline{u'u'}\right)}{\partial x} + \frac{\partial\left(\overline{uv} + \overline{u'v'}\right)}{\partial y} + \frac{\partial\left(\overline{uw + \overline{u'w'}}\right)}{\partial z} \\ \frac{\partial\left(\overline{uv} + \overline{u'v'}\right)}{\partial x} + \frac{\partial\left(\overline{v^2} + \overline{v'v'}\right)}{\partial y} + \frac{\partial\left(\overline{vw + \overline{v'w'}}\right)}{\partial z} \\ \frac{\partial\left(\overline{uw} + \overline{u'w'}\right)}{\partial x} + \frac{\partial\left(\overline{vw} + \overline{v'w'}\right)}{\partial y} + \frac{\partial\left(\overline{w^2} + \overline{w'w'}\right)}{\partial z} \end{bmatrix} = -\begin{bmatrix} \frac{\partial \bar{p}}{\partial x} \\ \frac{\partial \bar{p}}{\partial y} \\ \frac{\partial \bar{p}}{\partial z} \end{bmatrix} + \begin{bmatrix} v\left(\frac{\partial^2 \bar{u}}{\partial x^2} + \frac{\partial^2 \bar{u}}{\partial y^2} + \frac{\partial^2 \bar{u}}{\partial z^2}\right) \\ v\left(\frac{\partial^2 \bar{v}}{\partial x^2} + \frac{\partial^2 \bar{v}}{\partial y^2} + \frac{\partial^2 \bar{v}}{\partial z^2}\right) \\ v\left(\frac{\partial^2 \bar{w}}{\partial x^2} + \frac{\partial^2 \bar{w}}{\partial y^2} + \frac{\partial^2 \bar{w}}{\partial z^2}\right) \end{bmatrix} \tag{6.22}$$

The nine terms comprising of the fluctuating components can be separated and taken to the right-hand side, this gives the Reynolds averaged momentum equation, in the form of equation 6.10.

$$\begin{bmatrix} \frac{\partial \overline{u}}{\partial t} \\ \frac{\partial \overline{v}}{\partial t} \\ \frac{\partial \overline{w}}{\partial t} \end{bmatrix} + \begin{bmatrix} \frac{\partial (\overline{u}^2)}{\partial x} + \frac{\partial (\overline{uv})}{\partial y} + \frac{\partial (\overline{uw})}{\partial z} \\ \frac{\partial (\overline{uv})}{\partial x} + \frac{\partial (\overline{v^2})}{\partial y} + \frac{\partial (\overline{vw})}{\partial z} \\ \frac{\partial (\overline{uw})}{\partial x} + \frac{\partial (\overline{vw})}{\partial y} + \frac{\partial (\overline{w^2})}{\partial z} \end{bmatrix} = - \begin{bmatrix} \frac{\partial \overline{p}}{\partial x} \\ \frac{\partial \overline{p}}{\partial y} \\ \frac{\partial \overline{p}}{\partial z} \end{bmatrix} + \begin{bmatrix} v\left(\frac{\partial^2 \overline{u}}{\partial x^2} + \frac{\partial^2 \overline{u}}{\partial y^2} + \frac{\partial^2 \overline{u}}{\partial z^2}\right) \\ v\left(\frac{\partial^2 \overline{v}}{\partial x^2} + \frac{\partial^2 \overline{v}}{\partial y^2} + \frac{\partial^2 \overline{v}}{\partial z^2}\right) \\ v\left(\frac{\partial^2 \overline{w}}{\partial x^2} + \frac{\partial^2 \overline{w}}{\partial y^2} + \frac{\partial^2 \overline{w}}{\partial z^2}\right) \end{bmatrix} - \begin{bmatrix} \frac{\partial (\overline{u'u'})}{\partial x} + \frac{\partial (\overline{u'v'})}{\partial y} + \frac{\partial (\overline{u'w'})}{\partial z} \\ \frac{\partial (\overline{u'v'})}{\partial x} + \frac{\partial (\overline{v'v'})}{\partial y} + \frac{\partial (\overline{v'w'})}{\partial z} \\ \frac{\partial (\overline{u'w'})}{\partial x} + \frac{\partial (\overline{v'w'})}{\partial y} + \frac{\partial (\overline{w'w'})}{\partial z} \end{bmatrix} \quad (6.23)$$

The difference between equation 6.10 and 6.23 arising from Reynolds averaging, aside from the variables becoming mean values, is that there have appeared a set of nine negative terms on the right-hand side. The symmetrical nature of these terms gives a resemblance to the stress tensor encountered earlier in equation 6.5 and are therefore referred to as "Reynolds Stresses".

Equation 6.23 can be converted to Einstein notation to be expressed as in equation 6.24. Though this equation relates to incompressible flow, in cases of compressible flow, the term for the "Reynolds stresses" can be combined with the original stress tensor, thereby accounting for turbulence effects within the single diffusion term, as shown in equation 6.25.

$$\rho \frac{\partial \overline{u}_i}{\partial t} + \rho \frac{\partial}{\partial x_j}\left(\overline{u}_i \overline{u}_j\right) = -\frac{\partial \overline{p}}{\partial x_i} + \mu \frac{\partial^2 \overline{u}_i}{\partial x_j^2} - \rho \frac{\partial}{\partial x_j}\left(\overline{u_i' u_j'}\right) \quad (6.24)$$

$$\rho \frac{\partial \overline{u}_i}{\partial t} + \rho \frac{\partial}{\partial x_j}\left(\overline{u}_i \overline{u}_j\right) = -\frac{\partial \overline{p}}{\partial x_i} + \frac{\partial}{\partial x_j}\left(2\mu S_{ij} - \rho \overline{u_i' u_j'}\right) \quad (6.25)$$

The Reynolds stress tensor $\tau_{turb} = \rho \overline{u_i' u_j'}$ arising due to Reynolds averaging of the momentum equation has resulted in 3 new variables, u', v', w', but no new equations to provide closure. A point of note is that these variables to not occur separately in the RANS equations but rather as nine products, and due to the symmetrical nature of this stress tensor, there are only six unknowns. A way to provide closure is therefore to express these six unknowns in terms of the four mean variables that can be solved, these being $\overline{u}, \overline{v}, \overline{w}$ and $\overline{p}$, this technique is known as turbulence modelling.

6.3 Turbulence modelling

Relating the Reynolds stresses to the mean flow variables was first proposed by Joseph Boussinesq (Schmitt, 2007), for which he introduced the concepts of the eddy viscosity and turbulent kinetic energy. All of the RANS turbulence models rely on the Boussinesq approximation outlined below.

$$-\overline{u_i' u_j'} = 2v_t S_{ij} - \frac{2}{3} K \delta_{ij} \tag{6.26}$$

$$S_{ij} = \frac{1}{2}\left(\frac{\partial \overline{u}_i}{\partial x_j} + \frac{\partial \overline{u}_j}{\partial x_i}\right) \tag{6.27}$$

Where v_t is the eddy viscosity, and S_{ij} is the mean rate of strain tensor mentioned previously. The turbulent kinetic energy is based on the velocity fluctuations defined as

$$K = \frac{1}{2}\overline{u_i' u_i'} = \frac{1}{2}\left(\overline{(u_1')^2} + \overline{(u_2')^2} + \overline{(u_3')^2}\right) = \frac{1}{2}\left(\overline{(u')^2} + \overline{(v')^2} + \overline{(w')^2}\right) \tag{6.28}$$

Whilst δ_{ij} is the Kronecker delta function, to produce an identity matrix as shown below

$$\delta_{ij} = \begin{cases} 0, & \text{if } i \neq j \\ 1, & \text{if } i = j \end{cases} = \begin{pmatrix} 1 & 0 & 0 \\ 0 & 1 & 0 \\ 0 & 0 & 1 \end{pmatrix} \tag{6.29}$$

The last remaining unknown after applying the Boussinesq approximation is the turbulent viscosity, this variable is solved differently depending on the choice of turbulence model. The two most popular of which are known as k-epsilon $(k-\epsilon)$ and k-omega $(k-\omega)$ and are both categorised as two-equation models. The turbulent viscosity is defined as a ratio of turbulent kinetic energy (k) and turbulent dissipation (ϵ or ω) of this kinetic energy; each turbulence model attempts to solve for these two variables by means of transport equations.

The transport equations for the k-epsilon turbulence model are outlined below, whilst addition turbulence models are expounded in the appendix.

Turbulent Kinetic Energy (k)

$$\frac{\partial(\rho k)}{\partial t} + \frac{\partial(\rho k u_i)}{\partial x_i} = \frac{\partial}{\partial x_j}\left[\frac{\mu_t}{\sigma_k}\frac{\partial k}{\partial x_j}\right] + 2\mu_t E_{ij} E_{ij} - \rho\epsilon \tag{6.30}$$

Turbulent Dissipation (ϵ)

$$\frac{\partial(\rho\epsilon)}{\partial t} + \frac{\partial(\rho\epsilon u_i)}{\partial x_i} = \frac{\partial}{\partial x_j}\left[\frac{\mu_t}{\sigma_\epsilon}\frac{\partial \epsilon}{\partial x_j}\right] + C_{1\epsilon}\frac{\epsilon}{k} 2\mu_t E_{ij} E_{ij} - C_{2\epsilon}\rho\frac{\epsilon^2}{k} \tag{6.31}$$

Here u_i is the velocity component, E_{ij} is the deformation rate whilst μ_t represents the eddy viscosity necessary to close the Boussinesq approximation, defined as below

$$\mu_t = \rho C_\mu \frac{k^2}{\epsilon} \tag{6.32}$$

The equation also contains a number of constants that are based on data fitting from experiments across a wide range of turbulent flows, and are a given as

$$C_\mu = 0.09 \qquad \sigma_k = 1.00 \qquad \sigma_\epsilon = 1.30 \qquad C_{1\epsilon} = 1.44 \qquad C_{2\epsilon} = 1.92 \tag{6.33}$$

The coefficients will differ in different turbulence models, whilst the sign of ω is to describe turbulent dissipation in the k-omega model. However, the meaning of the transport equations remains the same in any case and can be understood as described previously in section 6.1.1, in the above transport equation the rates of production and destruction (source and sink terms) of k or ω are also included.

It was said by Cengel and Cimbala (2006) "No turbulence model is universal, and a turbulent flow CFD solution is only as good as the appropriateness and validity of the turbulence model used in the calculation". The k-epsilon turbulence model has traditionally been the most popular and robust of the two-equation models, and as such is the most widely validated model for industrial applications and environmental flows. It is best suited to free-shear layer flows (outside the boundary layer) in the presence of small pressure gradients. The model has been shown experimentally to lose accuracy when simulating flows with large adverse pressure gradients. For such flows an alternative is the k-omega turbulence model that gives better performance for complex boundary layer flows under adverse pressure gradients and flow separation. The ability to model the boundary layer requires a good mesh resolution at the wall, which will be discussed in the next section, and at times the prediction of flow separation by this model may be early and therefore in excess.

A compromise is the k-omega SST (shear strain transport) model and is now becoming popular especially when simulating turbomachinery. The primary reason is its ability to use the k-omega formulation for flow in the inner parts of the boundary layer whilst alternating to the k-epsilon formulation in the free-stream where the standard k-omega model tends is over-sensitive to the turbulence properties of the incoming flow. As this work will attempt to simulate both the generator and upstream Wells turbine in an oscillating water column environment, the k-omega SST turbulence model is judged as best suited and will be used when testing all the varying designs.

6.4 The law of the wall

The concept of the boundary layer and the rapid changes in parallel flow velocity when approaching a wall was covered in section 4.3. Beginning at the wall, the boundary layer can be divided into three regions, the viscous sub-layer, the buffer layer, and the log-law layer. Each layer is characterised by relative distance from the wall, observable by the significance of viscous forces acting in the flow.

It was briefly covered in section 6.1 that distances from the wall, and velocities in the boundary layer could be expressed in non-dimensional form. Such a wall distance is defined as y^+, whilst the equivalent flow velocity (at that wall distance) is defined as u^+. Both such variables are made non-dimensional by

relating them to the friction velocity u^*, which is based on the wall shear stress. The expressions for these variables are given below.

$$u^+ = \frac{\overline{u}}{u^*} \qquad u^* = \sqrt{\frac{\tau_w}{\rho}} \qquad y^+ = \frac{yu^*}{v} \tag{6.34}$$

Where τ_w is the wall shear stress, y is the normal distance from the wall, whilst $\overline{u}$ is the flow velocity as a function of y.

The laminar sublayer, where viscous forces dominate the flow, extends for values of $y^+ < 5$. In this region the relationship between u^+ and y^+ is linear. Such that

$$u^+ = y^+ \tag{6.35}$$

The outer region of the turbulent boundary layer begins at approximately at $y^+ > 30$, it is often referred to as the log-law layer due to the relationship between u^+ and y^+ in this region. For a smooth wall, the correlation is

$$u^+ = \frac{1}{0.41} lny^+ + 5 \tag{6.36}$$

The region between these is known as the buffer layer, ranging between $5 < y^+ < 30$, where neither the inertial or viscous forces are more significant. Though there is no specific relationship between u^+ and y^+ is this region, a value of $y^+ = 11$ can be used to distinguish the separation of the previous two relationships. Alternative laws can be used to essentially blend the linear and logarithmic laws of the wall to represent the velocity profiles in this buffer layer. The three layers of the turbulent boundary layer and the form of the wall laws are shown in figure 6-2.

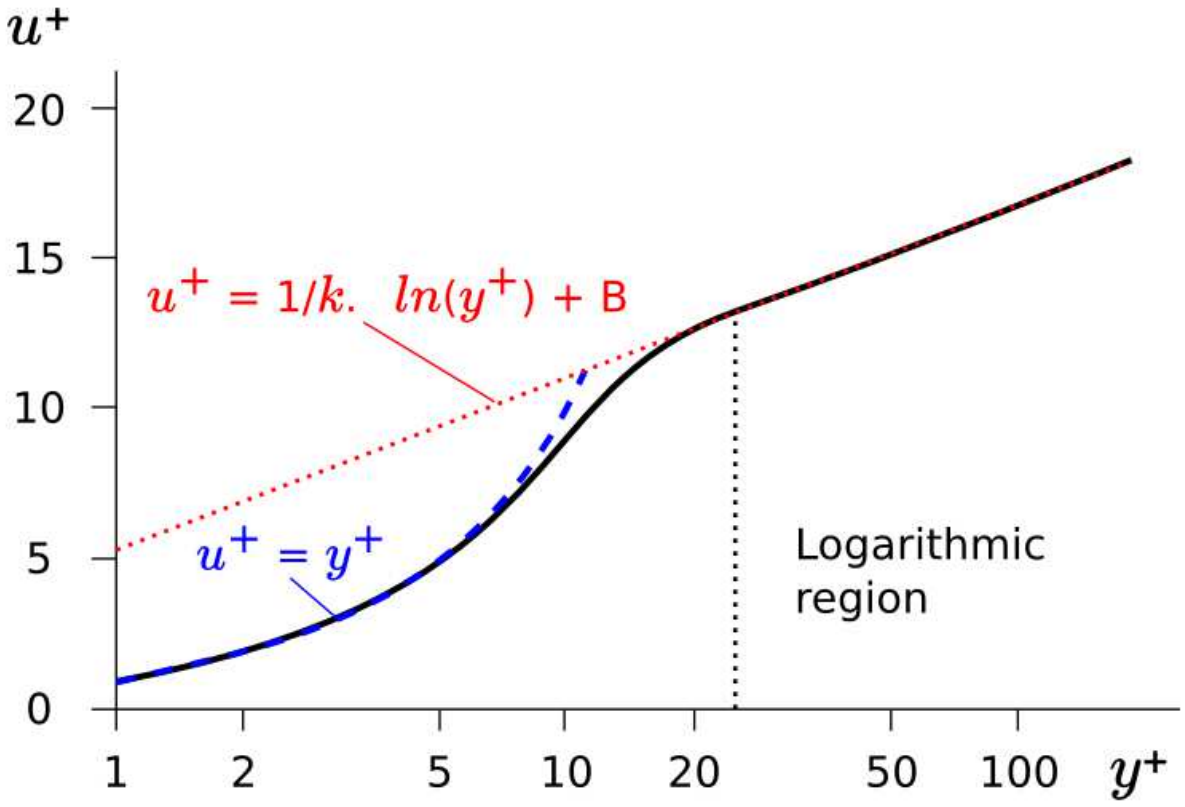

Figure 6-2: The law of the wall [CFD-Online, 2011]

Figure 6-3 shows the two types of "wall treatment" to solve for the distributions of flow variables such as velocity and temperature when approaching the wall. In the case of high y^+ wall treatment, the wall laws and blending techniques mentioned previously are utilised to derive the flow variables as functions of wall distance from the viscous sublayer to the log-law layer. In this case, the mesh resolution close to the wall can remain coarse as in the turbulent core, and as such, the centroid of the wall cell will be $y^+ > 30$. Such an approach is clearly less computationally expensive.

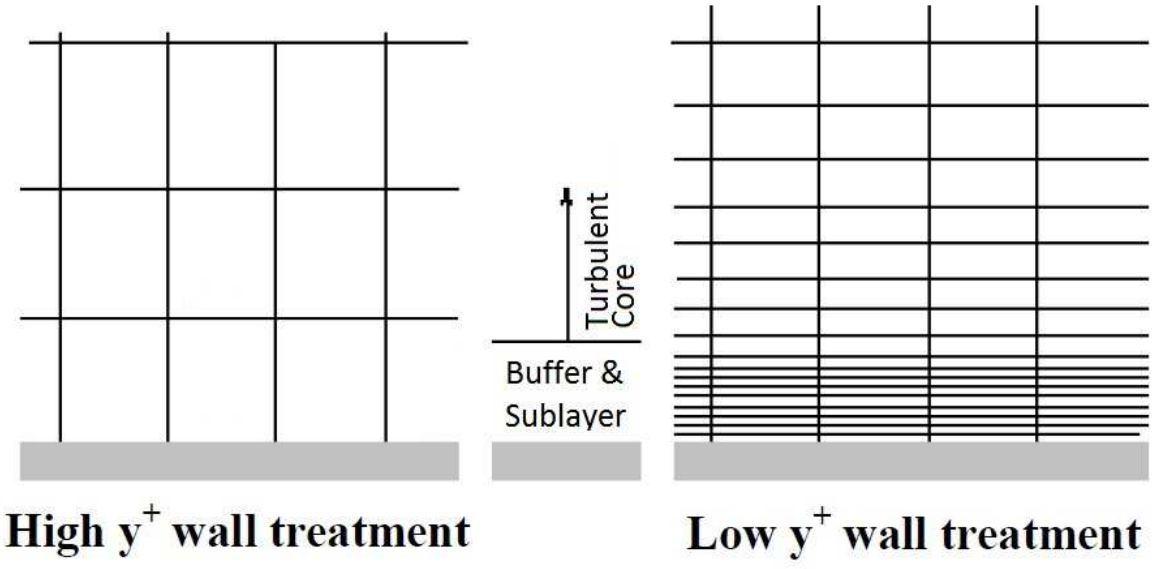

Figure 6-3: Types of wall treatment - high y^+ (left) and low y^+ (right) [CD-Adapco, 2011]

In the case of low y^+ wall treatment the viscous sub-layer is resolved without the use of wall laws, allowing the use of turbulence models within the boundary layer. The rapidly changing flow velocity when approaching closer distances to the wall demands a finer mesh resolution. To accurately resolve the boundary layer, the centroid of the wall cell will need to be approximately at $y^+ = 1$, the aspect of refined meshing at wall boundaries is the key cause of computational expense in CFD simulations. It is important to note that the non-dimensional y^+ value of the wall-cell is related to the Reynolds number. At higher velocities, the boundary layer thickness will be reduced, for such a case the fixed wall-cell centroid will thereby extend further into the boundary layer, raising the wall y^+ value.

Many RANS turbulence models (including k-omega SST) allow for an "all y^+" hybrid approach where throughout the meshed domain, the utilisation of wall laws will depend on the wall y^+ values which will vary depending on the refinement of the mesh along the various wall boundaries. In this work, the goal will be to maintain a wall y^+ under 1 throughout the domain, thereby avoiding the use of wall-laws and blending techniques in the buffer layer.

6.5 Summary

In this chapter, the Navier-Stokes equations were outlined completely, the different forms were explained to be related to assumptions of incompressible flow, the final form of which was expressed as a transport equation. The concept of Reynolds averaging was introduced to express the momentum equation in terms of mean flow values, various approaches of turbulence modelling were expounded as methods to express the unknown variables revealed after the Reynolds averaging, in terms of the mean flow values. This chapter concludes the theory of fluid flow, the next chapter will focus the setup of the numerical (CFD) approach used in this work.

7.0 CFD MODELLING AND MESH INDEPENDENCE STUDY

The chapters so far have covered the theoretical aspects of heat transfer, fluid flow and turbulence. Prior to outlining the results, this chapter will provide the necessary details surrounding the setup of the computational fluid dynamic simulations and the mesh independence study performed to choose the appropriate size of mesh.

7.1 Setup of the CFD simulations

The role of CFD in this work is to simulate the turbo generation section of the oscillating water column, specifically the workings within the shroud through which air flows past the Wells turbine and across the induction generator. After importing the CAD of this geometry, the process of CFD involves extracting the internal volume within the shroud to create a single domain of airflow, the edges of which are treated as fluid boundaries, rather than including solid regions such as the attenuators and turbine.

Applying a fixed temperature condition to the fluid boundary representing the outside casing of the generator would not be realistic as the protruding fins would have a slightly lower temperature than the casing. For this reason, aside from the fluid domain, of ambient temperature 300K (27°C), the generator was also maintained as a separate solid region. The generator region is included as a hollow casing, with a fixed temperature set at 333K (60°C) on the inner wall resulting in a temperature distribution throughout the generator casing such that the fins are the coolest parts. Finally the heat transfer coefficient ($W/m^2.K$) and boundary heat flux (W/m^2) can be solved and visualised at the interface between the solid generator and airflow whilst the value of total heat transfer (W) from the outer casing is monitored.

The fluid domain is split into three regions, the middle region (encompassing the Wells turbine) is given a steady-state motion category, referred to as a “rotating reference frame”. Within such a region, forces from the wall boundaries, in this case, representing the Wells turbine, will impart forces onto the flowing fluid. An exception is made to the outer boundary of this region representing the shroud wall, which is separately defined as having an absolute zero tangential wall velocity. An unstructured polyhedral mesh was used throughout the domain for both the fluid and solid regions. Other choices did include a structured mesh, referred to as a trimmer mesh, commonly used for aerofoils. However, such a mesh was not appropriate for this approach due to interfaces between the stationary and rotating regions which would result in the mesh generated being non-conformal and hence give inaccurate results.

Boundary conditions must be applied at the extents of the domain to solve for the fluid flow within. The two conditions are a velocity inlet and pressure outlet, the inlet condition specifies a uniform velocity entering the domain, whilst the outlet condition specifies that the flow will reach atmospheric pressure upon leaving the domain. The remaining walls are defined by adiabatic boundary conditions to best represent surfaces of relatively low thermal conductivities (as compared to the finned generator casing).

An adiabatic condition necessitates that no heat is transferred through these surfaces, though the surface temperatures of the boundary may change. In contrast, an isothermal boundary condition would necessitate heat transfer through such surfaces to maintain the boundary at a given temperature. The final boundary condition is the interface between the solid generator and airflow. Figure 7-1 shows the inlet outlet and wall boundaries in the meshed domain; the interface is seen in green. The full length of the domain is 3.5m.

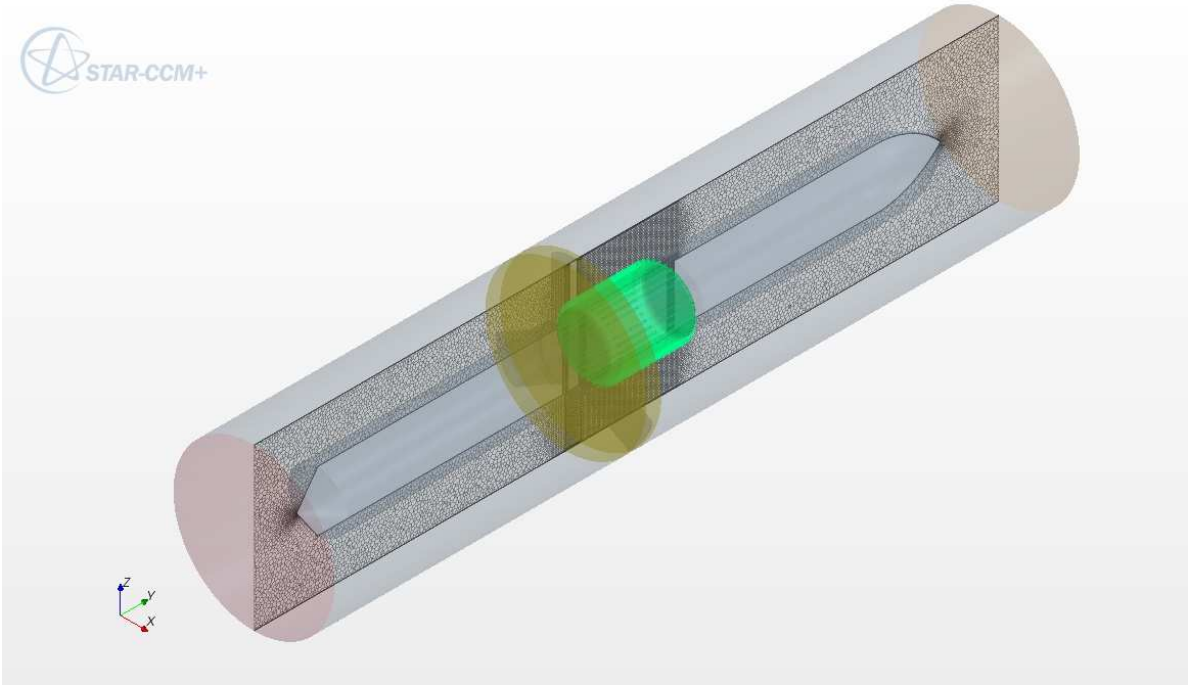

Figure 7-1: Boundaries throughout the domain

Though in reality, the incoming airflow into the turbo generation section would have been due to pressurised air being forced back and forth by the rising and falling water levels in the OWC collector tank, to include this region in the simulations was considered too computationally expensive, especially in contrast to a uniform velocity inlet boundary. Positioning the velocity inlet boundary further upstream ensures a fully developed flow prior to interaction with the regions of interest, whilst positioning the pressure outlet further downstream is important to reduce the occurrence of reversed flow through this boundary. The distance upstream of the velocity inlet from the turbine was 1.5m, equivalent to 7.5 blade cord-lengths, whilst the outlet was 10 cord-lengths downstream of the turbine. The distances of the boundaries in this work were based on the actual length of the encompassing shroud of the LIMPET OWC, and were not extended, due to issues of computational cost. These positions were considered sufficient as Toressi *et al*, when investigating a high solidity Wells turbine, mentioned using a domain with values of 2 and 7 cord-lengths, for the upstream and downstream distances, respectfully.

Admittedly, despite these distances, during the simulations, the phenomenon of reserved flow did at times appear. Reversed flow occurs when the pressure in the cell adjacent to the pressure outlet boundary is lower than that of the boundary itself, and this pressure difference is large enough to result in flow entering the domain from the outlet. The cause is commonly the specification of a uniform outlet pressure when the flow near such a boundary is highly non-uniform, such as when the boundary is placed just behind a step or obstacle in the flow. In the case of these simulations, the cause is the end of the downstream attenuator being so close to the outlet. A solution would have been to simply extend the outlet further downstream, however, the computational cost was considered too high. Potentially, the effects of such recirculating flow can head upstream and even interfere with the areas of interest. In the case of these simulations, the effects of reversed flow on the cooling of the generator was considered negligible, as the velocity scenes (to be shown in chapter 9) did not demonstrate any flow reversal upstream of the second attenuator.

The gradient of airflow at the boundary surface of the generator determines the heat transfer coefficient along the interface, allowing the temperature throughout the solid generator shell to be solved based on the fixed temperature value defined at the inner wall boundary. The application of the fixed temperature condition is shown at the left of figure 7-2 below, whilst details of the generator and fin geometries are shown in the middle and right respectively. Finally, details of the blade profile (with a 0.2m cord-length) and turbine dimensions as compared to the generator, are shown in figures 7-3 and 7-4, respectively.

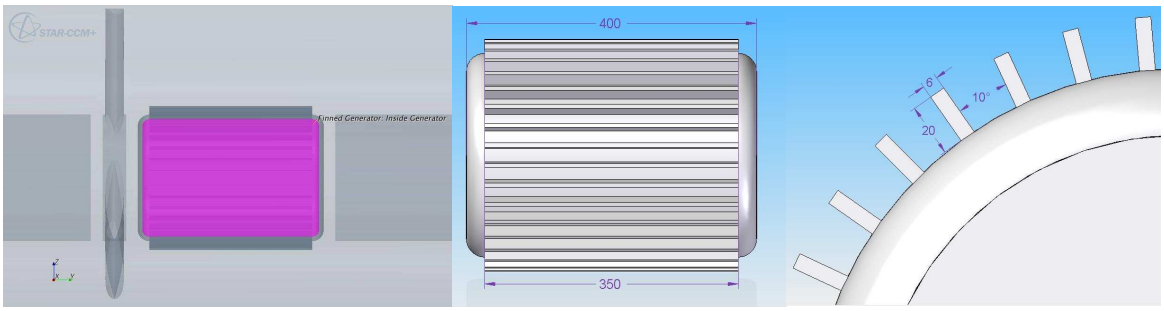

Figure 7-2: Fixed temperature boundary (left), length of generator (middle) dimensions of fins (right)

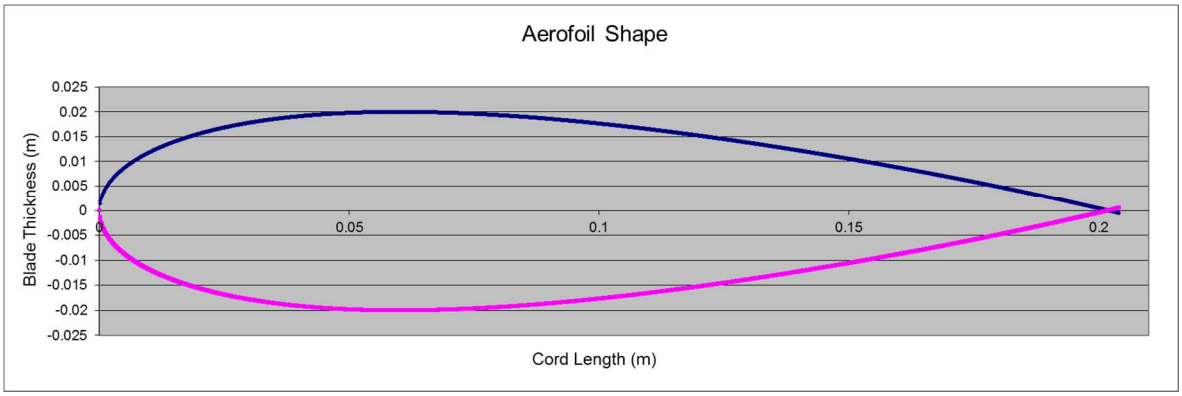

Figure 7-3: Aerofoil shape of the Wells turbine for NACA 0020 profile

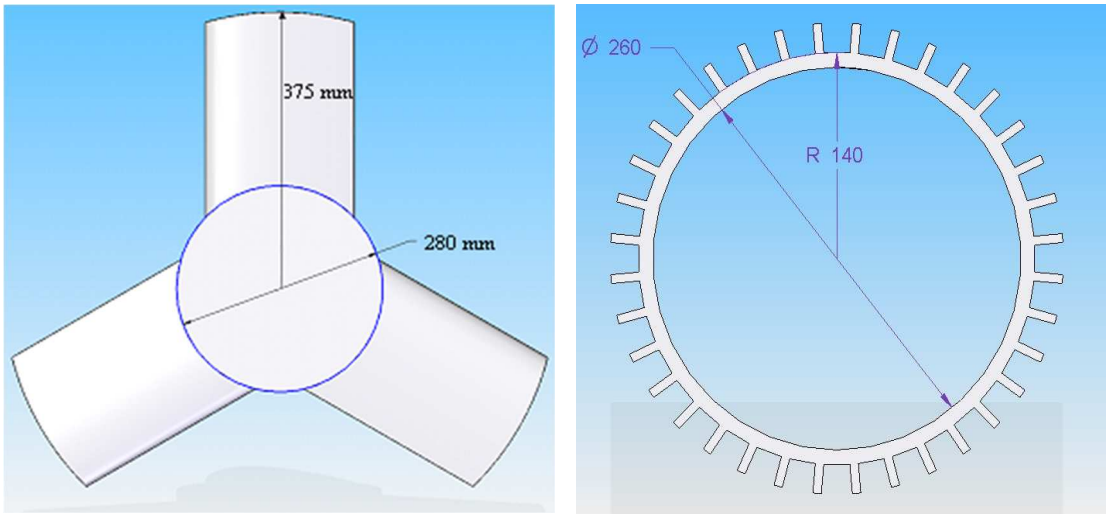

Figure 7-4: Wells turbine dimensions as compared to generator dimensions

The variables of heat transfer, boundary heat flux and average heat transfer coefficient will be investigated against the flow rate coefficient, defined as the incoming axial velocity divided by the constant tangential blade tip velocity. Plane sections to monitor the pressure drop across the turbine are shown in left of figure 7-5 whilst the distribution of pressure around a generic aerofoil is shown on the right. Section 6.1 already described how a component of the lift, generated by the difference in high and low pressure, creates torque to accelerate the turbine. The terms of turbine torque coefficient, turbine pressure drop coefficient and efficiency are given in equations 7.1 to 7.3 below.

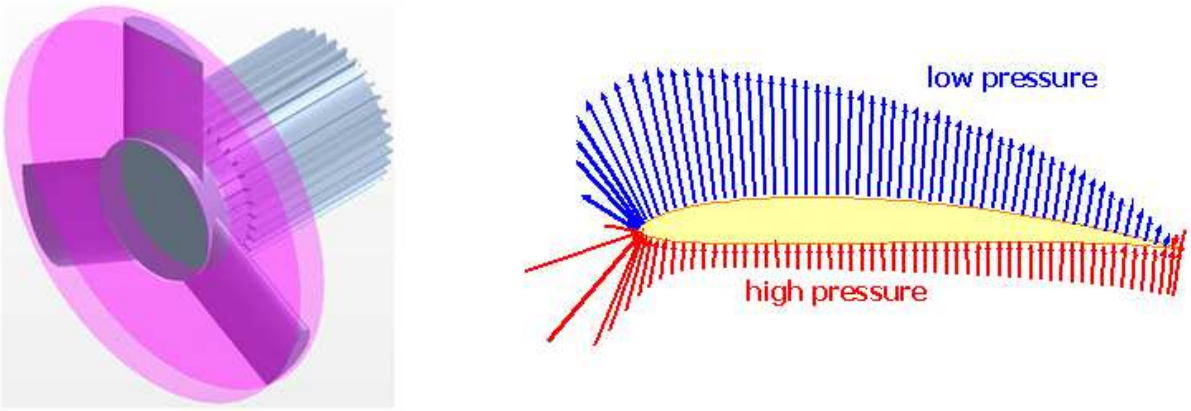

Figure 7-5: Plane section to monitor turbine pressure drop [left] and distribution of pressure around a generic aerofoil [right] [MH-Aerotools, 2004]

$$T^* = \frac{T}{\rho\omega^2 R_{tip}^5} \tag{7.1}$$

$$\Delta P^* = \frac{\Delta P_0}{\rho\omega^2 R_{tip}^2} \tag{7.2}$$

$$\eta = \frac{T\omega}{Q\Delta P_0} \tag{7.3}$$

Where T is the turbine's shaft torque, ρ = 1.225 kg/m^3 is the air density, ω is the angular velocity of the turbine, ΔP^0 is the stagnation pressure drop taken across either side of the turbine, R_{tip} is radius to the turbine tip, and Q volumetric flow rate. Additional variables that were monitored in an attempt to understand the causes of the varying rates of heat transfer with turbine design changes were the extent of mass flow radially towards the generator at two different radii, as well as the velocity distributions within the fin channels. The cylindrical sections for monitoring these variables are shown in figure 7-6.

These cylinder sections allow the visualisation of a vector fields, the "normal velocity" referred to the component of velocity flowing perpendicularly or "normal" to the cylinder section. That is, the flow inwards/towards the generator and is related to the mass flow rate towards the generator.

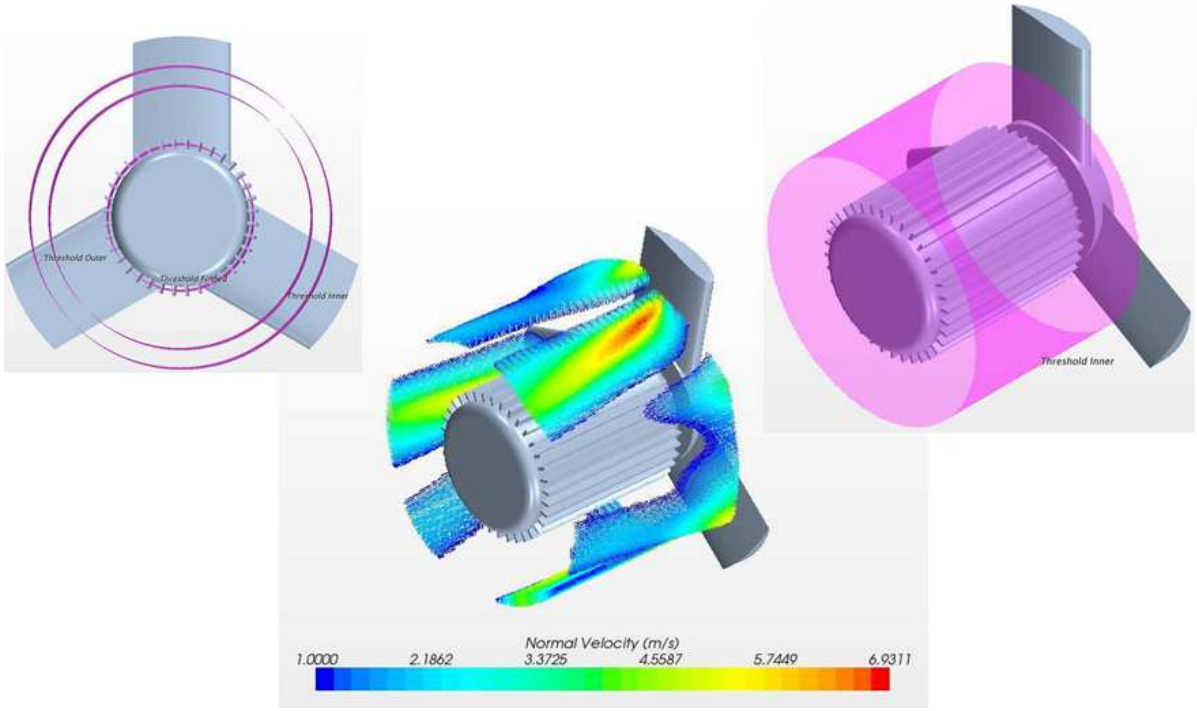

Figure 7-6: Cylindrical sections at three radii (left), velocity scenes of airflow impingement (middle), diagonal view of cylindrical section (right)

The K-Omega (SST) turbulence model was used to model the turbulence within the domain. The choice of this model was based on previous sets of work by Toressi *et al*, from both 2004 and 2008, where high solidity Wells turbines were simulated, the results of which showed good agreement with separate experimental work carried out by Curran and Gato (1997).

Additionally, N. Zuckerman and N.Loir (2006) carried out CFD simulations investigating the effects of heat transfer due to jet impingement, validated the results against empirical correlations. The work

focused on comparing the accuracy of the different available turbulence models and noting the relative strengths and drawbacks of each approach. The K-Omega (SST) was found to be the most accurate at predicting the Nusselt number at the surface of jet impingement from amongst all the linear eddy viscosity turbulence models commonly used in industrial work.

The changes in design of the Wells turbine will be the turbine tip clearance, blade profile and turbine solidity. The clearance (as a percentage of blade cord length) between the tip of the turbine and the encompassing shroud, will be changed by reducing the diameter of the shroud rather than changing any dimensions of the turbine. Whereas adjusting the blade profile will involve reducing the thickness of symmetric NACA aerofoil. Finally, increasing the solidity will involve increasing the number of blades, whilst reducing the relative cord-length, so as to maintain the same hub to tip ratio. The initial turbine design to be placed upstream of the generator will be a 3-bladed turbine, with a NACA0020 profile, at a 10% tip clearance.

7.2 Choice of mesh size and mesh independence study

In the case of the 10% tip clearance design, the decision for the mesh size began at the tip of the turbine blade. The height of the wall cell was defined as 1.71×10^{-5} c, where c is the blade cord length, the range of this value was based, in part, on work by Toressi *et al* (2008). The sizing of the polyhedral mesh in the flow domain was chosen to give a satisfactory blend with the highest prism layer cell. The base size used was 0.03m, mesh sizes throughout the domain are defined as percentages of this base size. Beginning within the fin channels, the mesh size is 2.85mm (9.5%), outside the fin channels a transitional mesh of 4.05mm (13.5%) is used, and beyond this, is the region of the wake in which the mesh size is 4.95mm (16.5%). The mesh size encompassing the turbine is also 4.05mm (13.5%), whilst in the tip-gap, the mesh size is again 2.85mm (9.5%). Finally, at the walls of the encompassing shroud the mesh size is 3.75mm (12.5%). Outside of the areas of interest, throughout the remainder of the domain, a coarser target mesh size of 7.5mm (25%) is used, alongside an equivalent defined 7.5mm (25%) mesh just upstream of the turbine. The mesh sizes were also determined from work by A.K. Kuczaj *et al*, who investigated the effects of mesh size on predicting fluid flow and heat transfer during turbulent mixing of flow in a T-Junction. The velocity profiles through the junctions were compared against experimental results, for mesh sizes of 8mm, 4mm and 2mm. The findings showed overall consistent results for the different mesh sizes, especially between 4mm and 2mm. Hence, the mesh sizes chosen in this PhD work was considered sufficient for obtaining a good solution.

Cuts through the geometries are taken to show the mesh at different cross-sections. Figure 7-7 demonstrates an axial mesh view to reveal both upstream and downstream of the generator. Whilst figure 7-8 shows a radial mesh view through the finned generator and a close up of the fin channels.

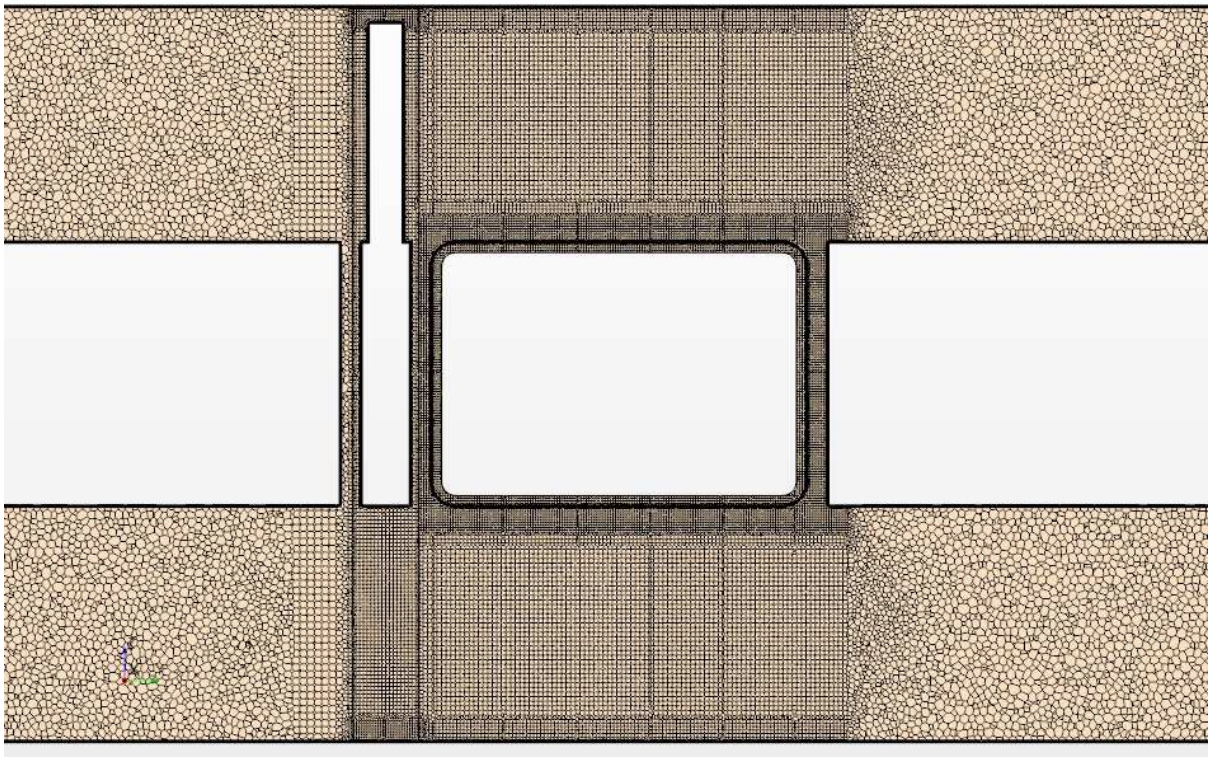

Figure 7-7: Axial view of mesh

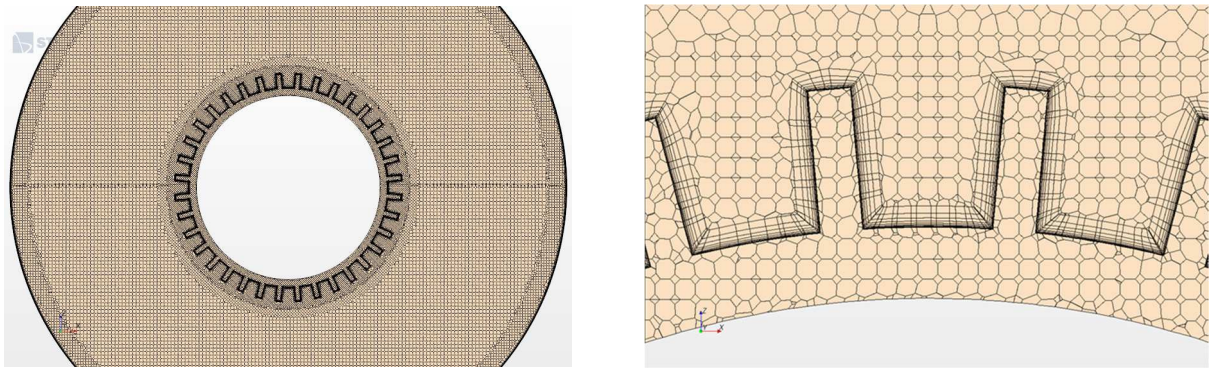

Figure 7-8: Radial view of mesh through finned generator (left) and close-up (right)

The prism layer is referred to as the cells that become progressively thinner nearer a wall to adequately resolve the flow within the boundary layer, an issue discussed in section 8.4, and can also be seen in detail on the right of figure 7-8 showing a close up of the fin channels. A stretching ratio of 1.5 is used, and within the regions of interest, 12 layers are set for all walls except surrounding the turbine where 15 layers are required due to the higher velocities. The choice of layers and stretching ratio was made to ensure the wall cell y^+ values were approximately under 1 throughout the domain.

It was mentioned in the previous chapter that solving the Navier-Stokes equations with a coarse grid would give inaccurate results as it would not sufficiently account for the turbulent fluctuations in the flow. When refining a grid, though a finer mesh would serve to capture even smaller eddies, these eddies

would be too small to have any significant effect on the solution. Therefore, there comes a point during mesh refinement where a solution can be described as independent of the mesh resolution.

Conducting a mesh independence study generally involves running a simulation at three different mesh sizes. During each run, an appropriate value of interest is monitored until it becomes steady and the residual error reaches 10^{-4}, after which the solution is considered to have converged. Next, the mesh is refined throughout the entire domain, often to double the resolution of the previous mesh, and the simulation is run until it converges again.

The change in the value of interest being monitored is investigated, should the value be similar to that achieved by the coarser mesh the solution can be considered to be mesh independent. If the value has changed considerably, the resolution is once again doubled and re-run to convergence. Often, the extent of change in the value of interest is lesser between the second and third run than between the first and second. The importance of a conducting a mesh independence study is to ensure that the results in the solution are related to the boundary conditions and physics used in the simulations rather than the mesh density.

An additional implication is that the finest grid resolution possible need not be always be relied upon. Instead, it is possible that a coarser grid may give sufficiently accurate results, for considerably less computing power.

7.2.1 Richardson Extrapolation

Taking the scenario of three grids sizes defined (in order of increasing fineness) as h_3, h_2 and h_1, and relating them to a respective value of interest defined asf_3, f_2 andf_1, a value f_0 can be extrapolated for when the grid size approaches zero, h_0. This is referred to as the Richardson extrapolation, the details of which are given below.

$$f_{h=0} \cong f_1 + \frac{f_1 + f_2}{r^p - 1} \tag{7.4}$$

Where $r = h_2/h_1$, and

$$p = \ln\left(\frac{f_3 - f_2}{f_2 - f_1}\right)/\ln(r) \tag{7.5}$$

The *r* term is referred to as the refinement ratio, whilst the *p* term is the order of convergence, and as such, indication of the speed at which the solution converges. The values for the grids used in this work, and the consequent results obtained are given in table 7-1, the same values, with the addition of the Richardson extrapolated value is included in figure 7-9 below.

Grid	Base-Size (m)	Heat Transfer (W)
1	0.015	1255.90
2	0.03	1238.40
3	0.06	1144.85

Table 7-1: Values of heat transfer against base-size

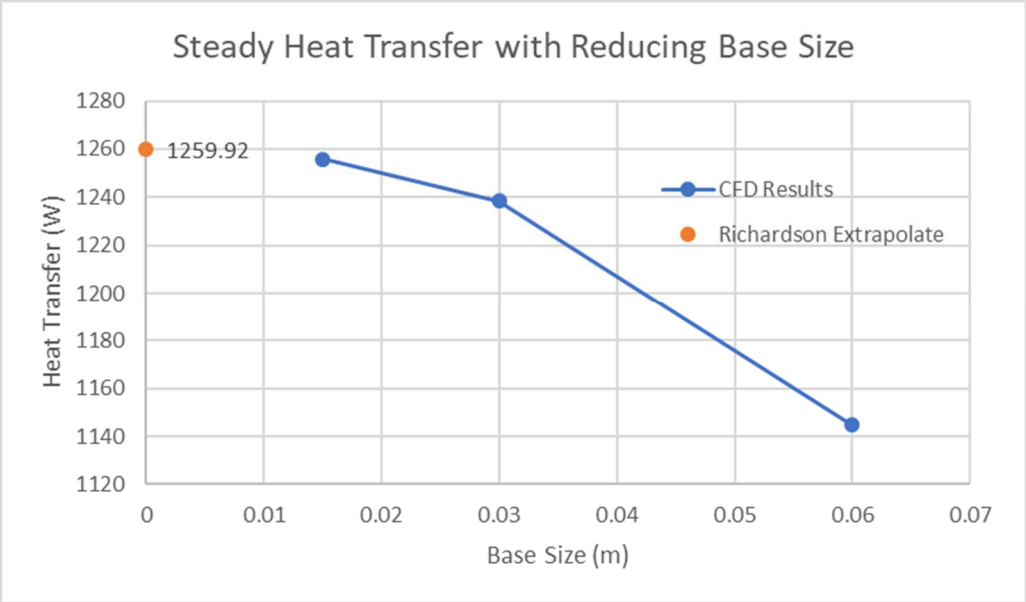

Figure 7-9: Results of mesh refinement study

The value of p in equation 7.5 is found to be 2.418.

7.2.2 Grid Convergence Index

The concept of a grid convergence index (GCI) was suggested by Roache (1998). This index compares the extrapolated value to the values obtained by the CFD for various grid sizes, to ultimately provide an error band for the extrapolated value based on first grid-step (from grid one to grid two). However, three grid sizes, and therefore two grid-steps are required to check whether the solutions are within an asymptotic range of convergence.

The GCI is essentially a measure of how far a given grid-step is from the extrapolated value and indicates how much the solution would change with further grid refinement. Therefore, a smaller GCI suggests the computed value is closer to the asymptotic range.

For grids 1 and 2 the GCI is

$$GCI_{12} = \frac{F_S|\epsilon_{12}|}{r^p - 1} \tag{7.6}$$

Where F_S is a factor of safety, taken as 3.0 for a total comparison of two grids, and 1.25 for comparisons of three (or more) grids. $\in_{12}$ is the relative difference between the two values of interest at grid sizes 1 and 2, such that $\in_{12}= (f_2 - f_1)/f_1$.

The values of GCI for grids 1 and 2, as well as 2 and 3, are given in table 7-2 below.

Grid Step	Refinement Ratio, r	GCI
1-2	2	0.40
2-3	2	2.17

Table 7-2: Values of grid convergence index for each grid-step

The solution is considered to be within the asymptotic range and therefore grid independent for the condition outlined in equation 7.7 below, the result of this ratio is given in table 7.3.

$$\frac{GCI_{23}}{r^p GCI_{12}} \approx 1 \tag{7.7}$$

Grid Range	Ratio, GCI
1-2, 2-3	0.986063

Table 7-3: Values of grid convergence index ratio over grid range

The value of the ratio is approximately 1, therefore it can be said that the solutions on grids 1, 2 and 3 are mesh independent. If the base size used is less than 0.06m, the solution will be in the asymptotic range. Though the computational power available did not allow for the continuous use of grid 2, however a mesh better than grid 3 was desired for the range of simulations.

Grid 2 was used, with some tweaks to save on computational cost, the outer most regions of the mesh were defined at 50% of the base-size (equivalent to grid 3) rather than the 25% used in the mesh refinement study, also, the number of prism layers in these outer regions was reduced from 10, to 6, thereby relying on the law of the wall. The result for this custom mesh is included in figure 7-10.

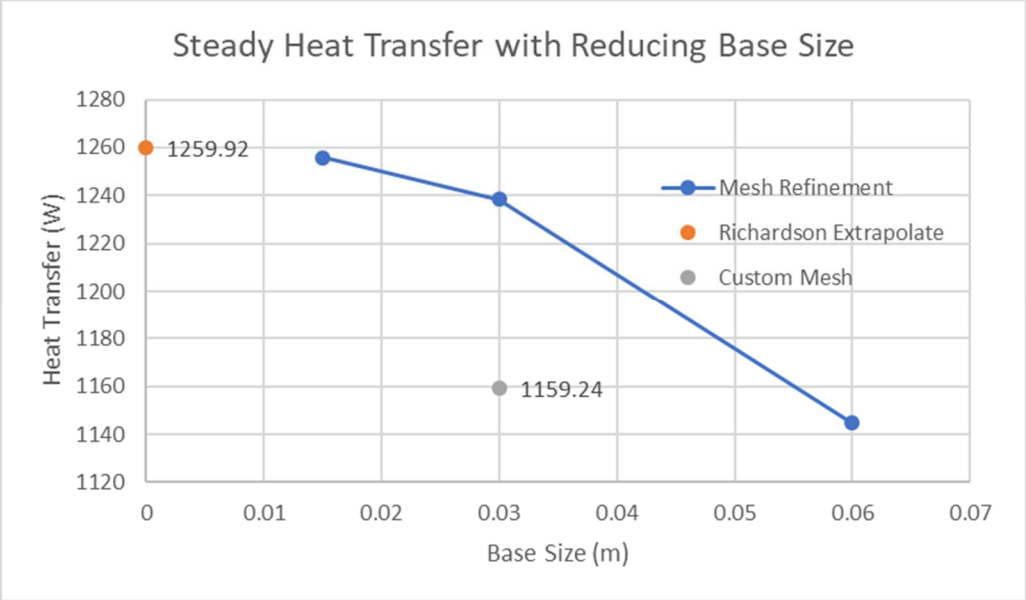

Figure 7-10: Results of mesh refinement study and value for custom mesh

The result is 6.8% lower than the equivalent grid 2 value, and as it is within the asymptotic range, this custom mesh was considered sufficient for further simulations.

7.3 Summary

The intention of this chapter was to cover all the necessary details required to adequately reproduce the computational fluid dynamic simulations performed in this PhD work. This is especially important if further work to broaden the range of knowledge in this area was to be undertaken in the future. The procedure for the mesh independence study was outlined, revealing an asymptotic range of base size from 0.015m to 0.06m. Consequently, a base size of 0.03m, with slight changes to cut down on computational cost, was chosen for the remaining simulations.

8.0 STEADY-STATE

Having chosen the mesh parameters for the flow domain, this chapter will outline the decision as to whether to perform steady or unsteady simulations over the range of flow coefficients to be investigated. The issue at hand is whether steady-state assumptions can be justified for the airflow interactions with the generator downstream of a single turbine.

A point of note from section 2.4 was that Folley *et al* (2006), after having performed unsteady experimental investigations on bi-plane Wells turbines, where one turbine experiences the downstream wake of the other, accepted that quasi-static assumptions are valid for two turbines rotating the same way, but not for two contra-rotating turbines.

The initial condition for an unsteady simulation is most often the stabilised result from an equivalent steady-state simulation. After explaining the choice of time-step, the results for such unsteady simulations will be compared against the equivalent steady-state results for all the turbine designs.

8.1 Choice of time-step

The procedure for an unsteady simulation is analogous to combining a sequence of steady simulations. Though a full steady-state solution is run over many iterations, an unsteady simulation is composed of running a shorter number of "inner" iterations per time-step, that is, obtaining a solution for each relevant moment in time. The smaller the time-step (duration from one relevant moment to another) the greater the number of total iterations encompassing a length of time.

The choice of the time-step value is generally determined by the dimensions of the mesh, the speed at which the fluid is moving, and the type of numerical method used by the solver, defined as either implicit or explicit. An ideal time-step would therefore be short enough to account for the time taken for a particle (at the fluid velocity) to move a distance of one cell length, this restrictive condition is a requirement for the use of an explicit scheme. In this work, an implicit scheme was used, to avoid the solution becoming unstable when the Courant number (explained below) exceeded a value of unity.

The equation for the time-step is given in equation 8.1 below

$$\Delta t = \nu \frac{\Delta x}{u} \tag{8.1}$$

Where ν is the Courant number, thus the equation can be rearranged to express ν such that, when its value equals 1, it represents a time-step short enough to capture one cell length of distance travelled by a given particle moving at the velocity of the flow.

A Courant number of 2 would clearly double the time-step used to capture the flow behaviour. The mesh size and velocity of the flow vary throughout the domain, to ensure a choice for u at the high end

of the velocity spectrum, the value is taken to be the turbine tip speed, whilst the value for *dx* is taken to be the smallest cell size of the core mesh, which is located at the blade tip gap. As such, the (shortest) time-step value, at a ν number of 1, is taken to be

$$\Delta t = \nu \frac{\Delta x}{u} = 1 \text{ x } \frac{0.00135}{79} = 1.709\text{x}10^{-5} \tag{8.2}$$

Though the airflow though the turbo generation section of the OWC is bi-directional, the aim is to identify which designs of Wells turbine would give the most thermal advantage to the generator during operation. Rather than a single simulation with a sinusoidal inlet velocity, multiple simulations were run, each one with a different (unidirectional) inlet velocity.

The timescale of the incoming airflow (when driven by waves) can be compared to the timescale of the rotating turbine. Folley (2006) stated that the average timescale of the waves was 0.2Hz, or 5 seconds. Assuming a sinusoidal flow of air past the Wells turbine over 5 seconds, and assuming a peak airflow velocity of 20m/s during this average 5 second wave. The average acceleration can be calculated to be: (20 x 2 / 5) = 8m/s^2. Meaning an incremental increase of 1 m/s every 0.125 seconds, this equates to over 4 revolutions of the turbine. Thus, a quasi-steady-state assumption can be made for the inlet flow.

8.1.1 Results of unsteady simulations

Unsteady simulations, of the four turbine designs, were run after a steady-state result had provided an initial condition. The results of total heat transfer from the generator, for Courant numbers of 4, 2 and 1, representing a coarse, medium and fine time-step, were to be compared against the equivalent averaged steady-state results.

When plotting the heat transfer results, the simulation time was not used as the independent variable. Instead, a characteristic of the turbine movement was used. As the turbine is three-bladed, one-third of a revolution can be used to categorise a “cycle”, at the end of which, the turbine will have revolved to a new angular position geometrically identical to the position at the beginning of each cycle.

The number of inner iterations (per time-step) was set at 10. Ideally, the unsteady simulations would have been run to a solution time over which the turbine would have completed approximately 50 revolutions or 150 blade rotation cycles. However, this is unfeasible given the computational capacity limitations. Therefore, each turbine design was run through a minimum of 20 blade rotation cycles. An average value of heat transfer from the last 3 cycles was calculated and compared against the equivalent steady-state value. As the equivalent steady-state result is run over tens of thousands of iterations over which the heat transfer value converges to become essentially constant (steady), an average value was calculated from the last three thousand iterations. The maximum and minimum values, due to the fluctuations in such a result, inherent in using a steady-state solver, were also included for analysis.

Were the results of the unsteady simulations to corroborate the steady-state trends in terms of whether the overall heat transfer from the generator improves or worsens with changes to turbine design, they would provide justification that results of the steady-state simulations were sufficiently trustworthy to identify such heat transfer trends over a full range of flow coefficients.

Unsteady results were obtained fastest (at levels of equivalent computing power) for the design with the greatest turbine tip clearance, this being 10% of the cord length. Therefore, for this design, after the initial steady-state simulations, the same result was computed with a coarse, then medium and then fine time-step, whilst the other designs were competed only with a coarse time-step.

Results of comparisons between steady and unsteady simulations

The steady and unsteady results of heat transfer from the generator for a 3 bladed, 10% tip-clearance, NACA0020 profile turbine at an incoming flow velocity of 12m/s is shown in figures 8-1 and 8-2 below. In figure 8-1, the steady results in terms of iteration (on the x-axis) are overlapped with the equivalent unsteady results, computed with a coarse, medium and fine time-step, in terms of blade angular cycles. Whilst figure 8-3 shows the average of these three unsteady results over the last three blade cycles alongside the average steady-state value within the bounds of the minimum and maximum range.

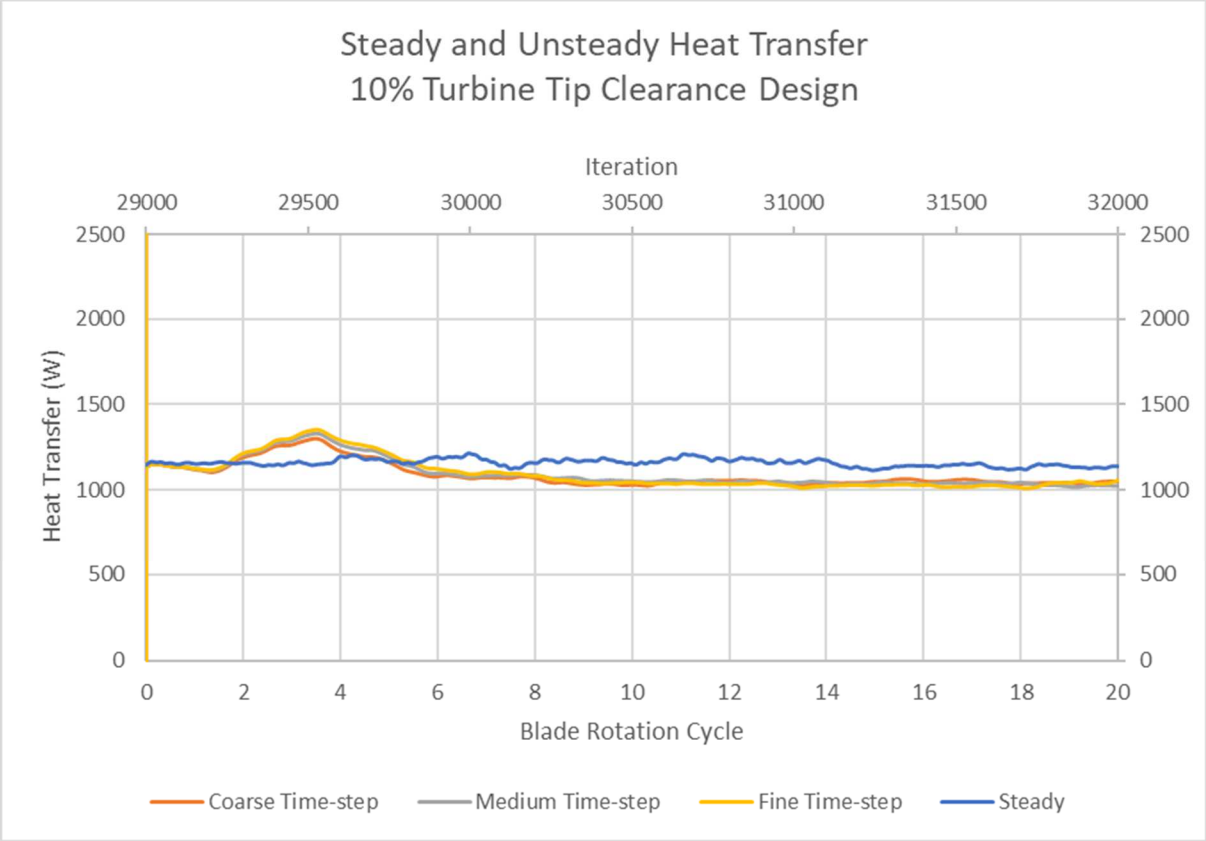

Figure 8-1: Steady and unsteady results of heat transfer for a 10% turbine tip clearance design

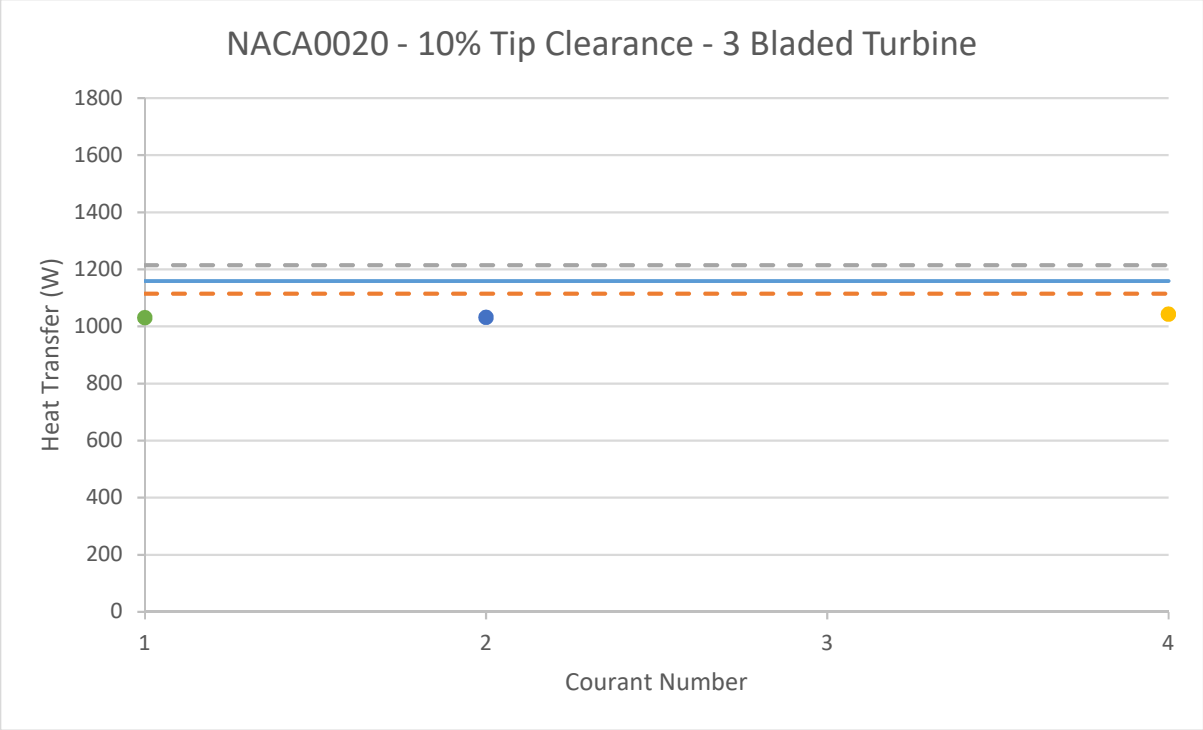

Figure 8-2: Steady-state and unsteady results of heat transfer for a 10% turbine tip clearance design against Courant number

Figure 8-2 shows a less than 1% change in heat transfer when reducing the Courant number from 4 to 2, whilst showing a less than 0.1%. change when reducing the Courant number from 2 to 1. Given the computational expense in simulating at a Courant number of 1 or 2, a Courant number of 4 was considered sufficient for the remaining unsteady simulations of the other turbine designs.

Unsteady heat transfer results in terms of blade angular cycles, computed with a coarse time-step (Courant number of 4), are shown in figures 8-3, 8-4 and 8-5 for a 3 bladed, 2% tip-clearance, NACA0020 profile turbine; 3 bladed, 2% tip-clearance, NACA0016 profile turbine; and 5 bladed, 2% tip-clearance, NACA0020 profile turbine respectively, each at an incoming flow velocity of 12m/s. Again, the equivalent steady results in terms of iteration (on the x-axis) are overlapped.

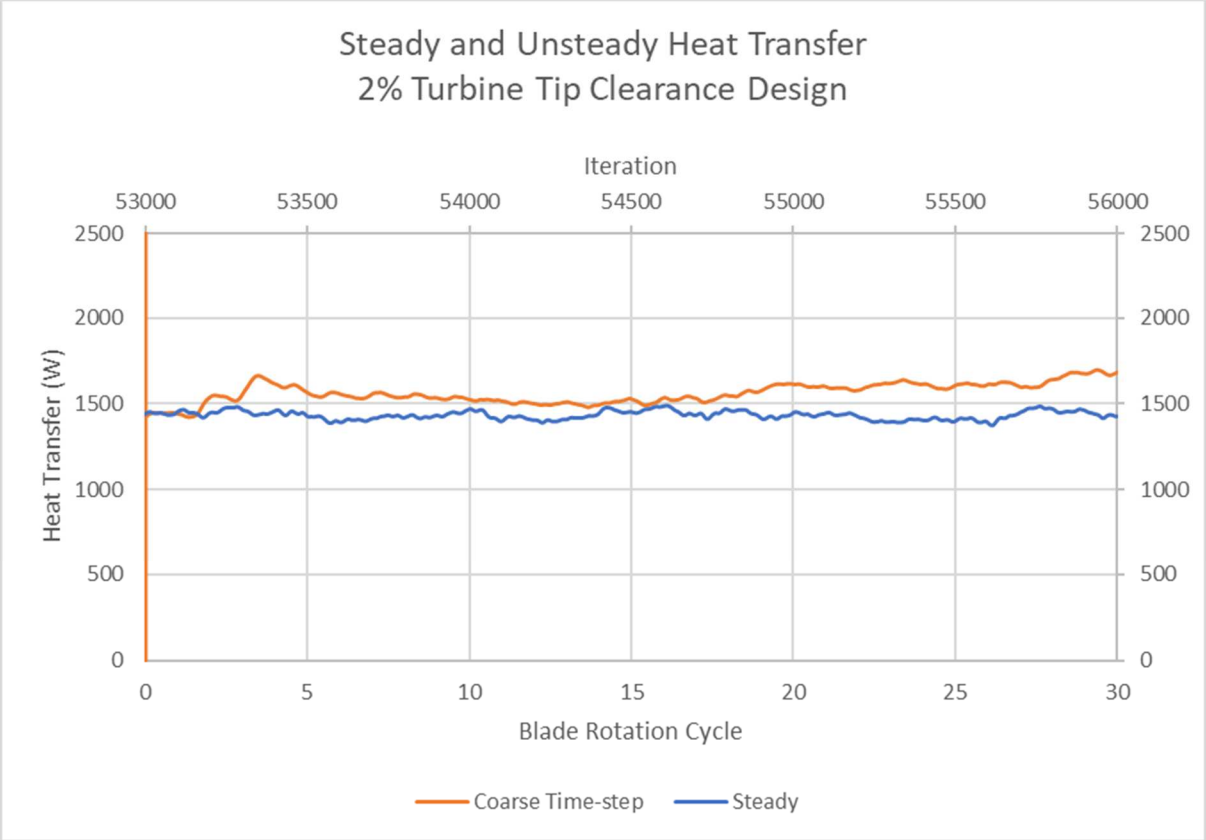

Figure 8-3: Steady and unsteady results of heat transfer for a 2% turbine tip clearance design

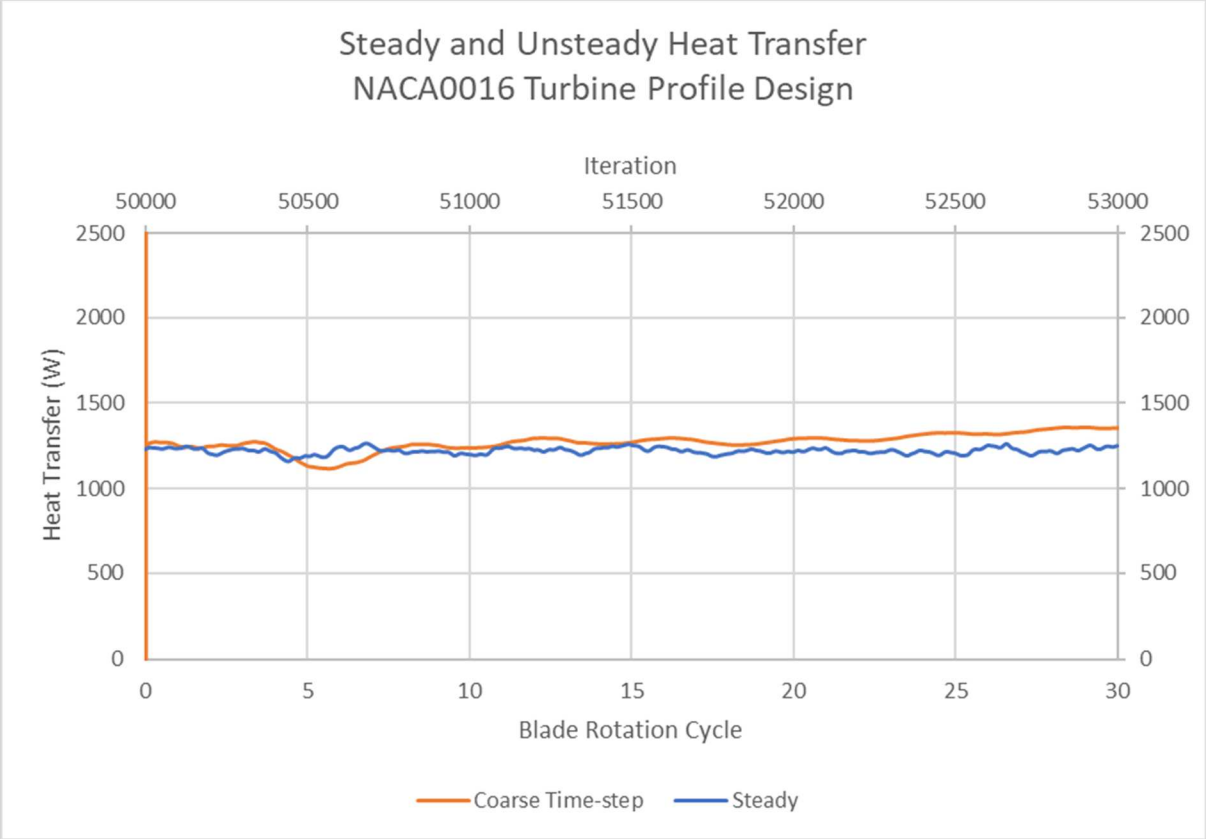

Figure 8-4: Steady and unsteady results of heat transfer for a NACA16 profile design

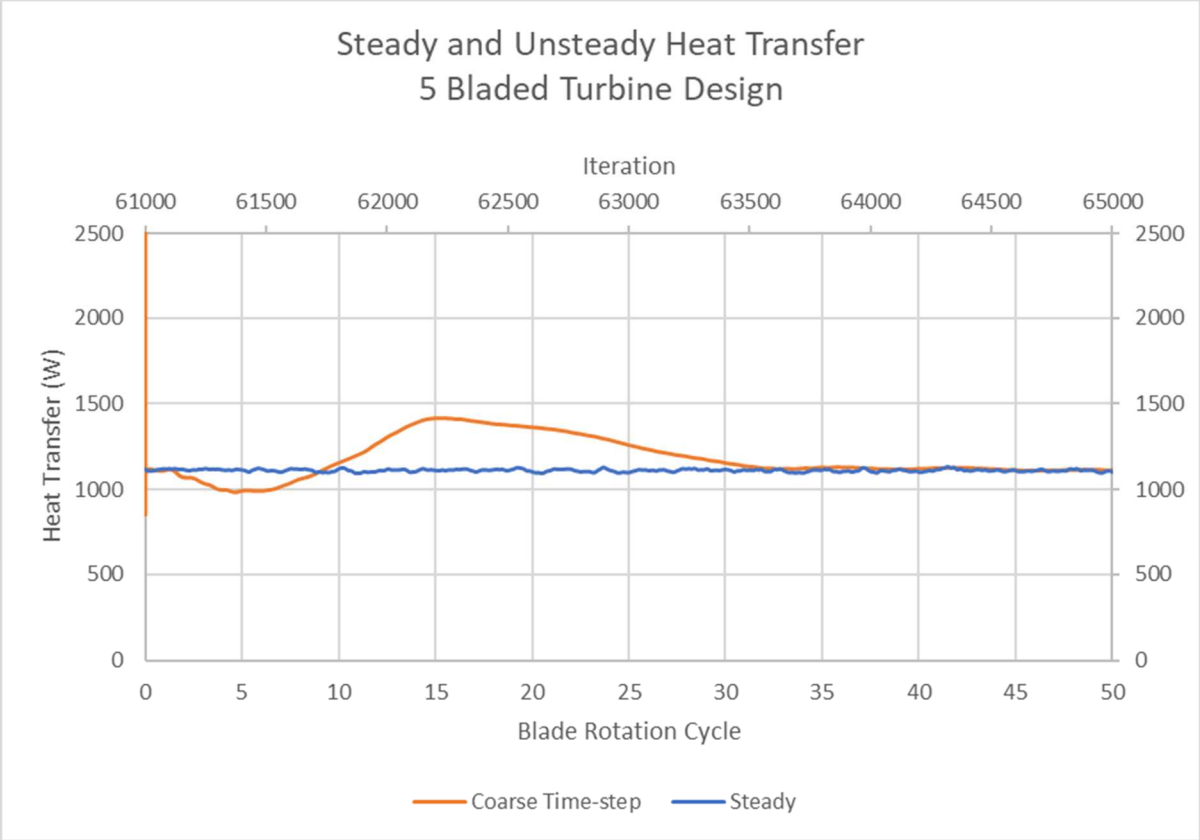

Figure 8-5: Steady and unsteady results of heat transfer for a 5-bladed turbine design

The results of heat transfer can be seen to stabilise within 20 cycles (or 6 revolutions). Undeniably, it is expected that with further cycles the heat transfer results would still fluctuate and oscillate around a mean value, but ultimately, over the course of 50 revolutions, these fluctuations would become minimal.

Figure 8-6 shows the unsteady heat transfer results computed with the coarse time-step, averaged over the last three cycles, alongside the average steady-state value, for each of the turbine designs.

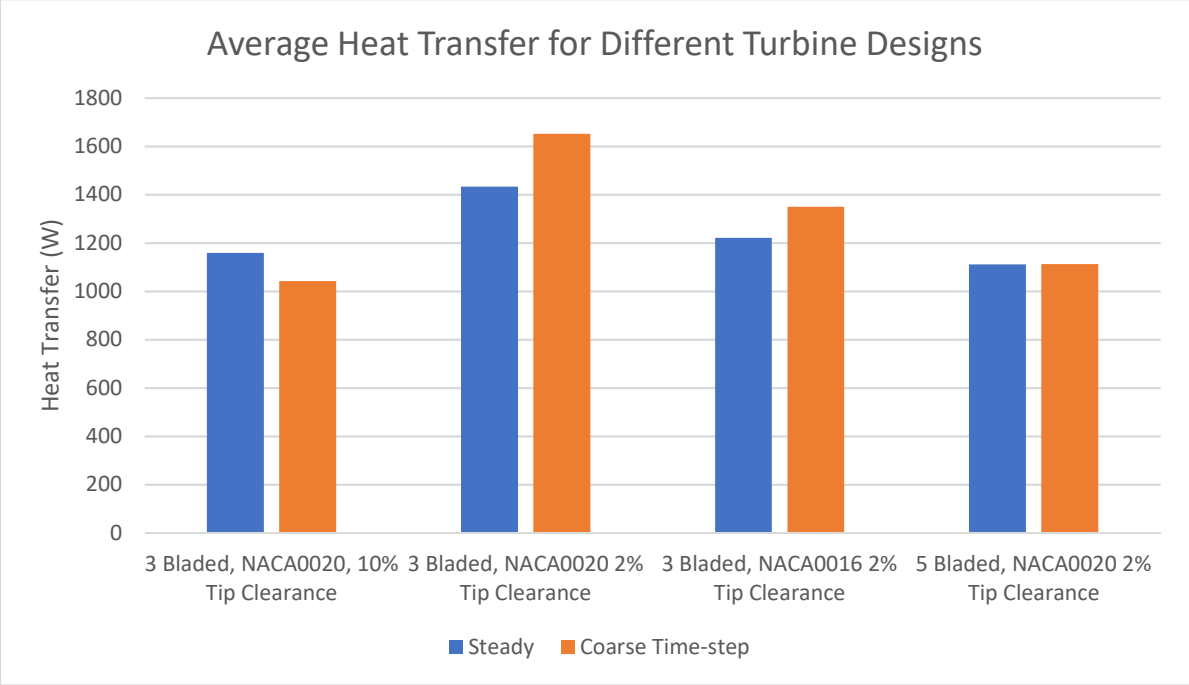

Figure 8-6: Steady and unsteady results of heat transfer for each turbine designs

Figures 8-1, 8-3, 8-4 and 8-5 demonstrated a steadying of heat transfer from the generator with time, most prominently for the 10% turbine tip clearance design. Such figures also showed that the results of the unsteady simulations were consistently steady over multiple blade cycles, as opposed to displaying unsteady fluctuations of heat transfer in a timescale between two blade cycles. Moreover, figure 8-6 shows that the unsteady simulations highlight the same trends as the steady simulations in relation to improving heat transfer, that is, by decreasing tip clearance, using thicker blade profiles and reducing turbine solidity. For these reasons, and given that the aim of this thesis is to determine whether a relative change in turbine design would serve to benefit or compromise the thermal performance of the downstream generator, the use of a steady-state solver for further simulations is considered justified.

8.2 Discussion

The validity for using steady-state can also be judged from the perspective of the thermo-fluid dynamics occurring in this scenario. The applicability of steady-state for this flow scenario ultimately comes downs to the thermal and fluid dynamics downstream of the turbine. The airflow impinging over the generator acts to provide cooling. A judgment for the applicability of steady-state assumptions may be based on the different time-scales that the heat and flow act over in which they transfer energy and momentum to the fluid. Aside from the fact that constant input parameters have been used in each simulation, that is, a constant inlet flow speed, turbine rotational speed and uniform temperature on the inner wall of the solid generator casing.

The time-scale of the effects on the flow due to the movement of the blades can be judged against the time-scale of the effects on the flow due to the heat from the generator. Though there are many

dimensionless numbers to characterise the behaviour of flow under forced convection, the issue of steady-state may be clarified by first considering the turbo generation section in a scenario where the blades are stationery, the only fluid flow would then arise purely from natural convection. Certainly, the buoyancy effects that give rise to the complexity in the flow prevent such flows from being characterised as steady.

Such flows are characterised as Rayleigh-Taylor instabilities, the instability manifests at the interface of two fluids of different densities. In the case of buoyancy driven flow, the scenario is of the lighter fluid pushing against a heavier fluid. A mushroom cloud formed during a nuclear explosion is a particularly famous example. Figure 8-7 shows an example of a colder fluid descending into a hotter fluid, a "mushroom cap" formation can be seen in the last (right-most) frame.

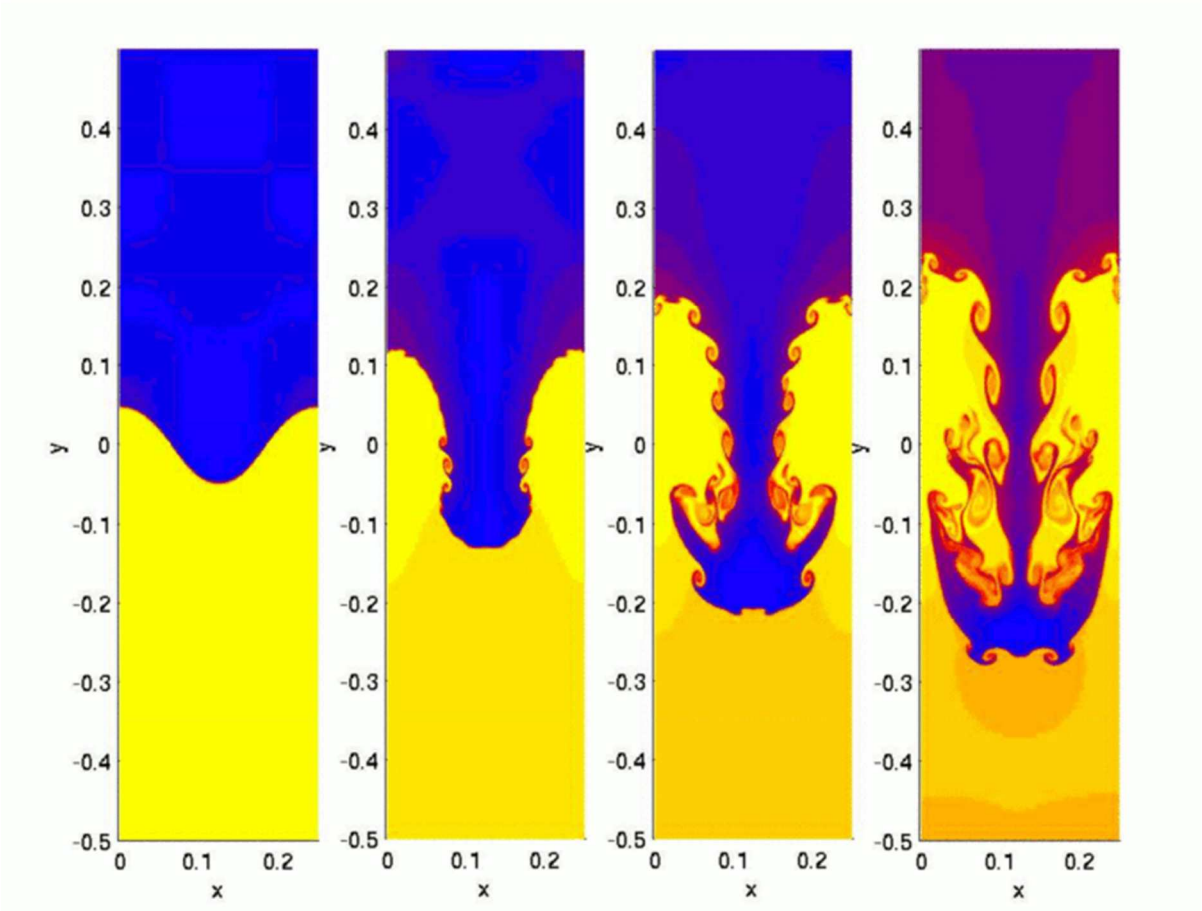

Figure 8-7: Rayleigh-Taylor instability between interface of cold fluid and hot fluid [Shengtai Li, Hui Li (2006)]

The formation and dissipation of such flows due to the heat from the generator will have an associated time-scale. The significance of the instability can be intuitively understood to be greater for fluids of lower viscosity. Just as the Reynolds numbers is used to define the character of fluid flow in forced convection, the Grashof number is the equivalent dimensionless number for flows of natural convection and is given in equation 8.3 below. The value for the Grashof number in these simulations is 3147,

which is relatively low, a value within the range of $10^3 < \mathrm{Gr} < 10^6$ results in a laminar boundary layer in cases of purely natural convection for vertical flat plates.

$$\mathrm{Gr}_L = \frac{g\beta(T_S - T_\infty)L^3}{\nu^2} \tag{8.3}$$

This form of the equation confirms that natural convection increases with reducing viscosity. A final dimensionless number is the Richardson number, this is defined as the ratio of the Grashof number over the Reynolds number, or, the buoyancy over the flow shear, and ultimately, the ratio between the timescale of effects due to natural convection over the timescale of effects due to forced convection. The Richardson number is given in equation 8.4, a value less than unity means that buoyancy effects are unimportant in the flow, the value in these simulations is 0.00066.

$$\mathrm{Ri} = \frac{g\beta(T_S - T_\infty)L}{V^2} \tag{8.4}$$

To put things into perspective, in the case of no forced convection (due to blade motion), the formation and diffusion of buoyancy driven flow would have a long time-scale and certainly invalidate a steady-state assumption. The addition of forced convection however, diminishes the role these instabilities play in the flow. Indeed, the shorter the time-scale of the effects of forced convection from the rotating turbine, that is, the higher the Reynolds number, the more a steady-state assumption is applicable to the flow.

With a constant inlet flow speed, and constant turbine rotational speed, the total extent of impingement over the generator would be overall constant, especially given the high rotational speed of 2000RPM. The very short time-scale of the blade motion would explain why the total heat transfer from the generator stabilises to a near constant value as seen in the case of the 10% turbine tip clearance design. The next chapter will detail all steady state results, where proceeding with unsteady simulations would be too computationally expensive.

9.0 RESULTS AND DISCUSSION

This section collates the results of analytical modelling and CFD simulations. The first stage was to observe analytically the extent of benefit achievable by the addition of fins to a smooth generator casing. The second stage was to validate the capability of CFD simulations to determine the heat transfer rates from a finned generator undergoing cooling. After determining the accuracy of the computational process, CFD simulations were performed to judge the effect of different Wells turbine designs on the cooling rates of the downstream generator.

9.1 Axial airflow along generators without impingement

9.1.1 Analytical modelling for smooth and finned casings

The first analysis was to use the analytical equations to compare how the average heat flux and consequent total heat transfer compared for smooth and finned cylinders during purely axial flow. In the case of smooth casings, the Nusselt number and consequent heat values can be obtained from equations 5.43 and 5.44 depending on the flow regime determined by the Reynolds number. Whilst for finned housings, the Heiles correlation outlined in equations 5.47 and 5.48 assumes the flow would become turbulent upon entry into the fin channels.

Figures 9-1 and 9-2 demonstrate comparisons of the average heat flux and total heat transfer between smooth and finned housings against flow velocity. The velocity referred to for the smooth housing is that of the free-stream whilst the velocity in the case of the finned housing is defined by the flow down the fin channels. Given that the nature of the flow is external in the case of the smooth housing, the critical Reynolds number is defined as 500,000. The results below are based on housings with axial lengths of 1m, allowing for the effect of the flow becoming turbulent on the heat values to be observed within reasonable range. The diameters of the housings however, are taken as mentioned in section 7.1.

The choice of axes used in figure 9-1 is based on equation 5.46, which relates the heat transfer coefficient to the Reynolds number of the incoming flow. It is more practical to define the x-axis as the incoming flow to see how changing the characteristic length affects the heat values over a range of velocities. The heat transfer coefficient has the units W/m^2K, as the temperature difference between the surface and ambient air will be 33 degrees (333K-300K) throughout all the simulations, the y-axis is defined as heat flux with the units W/m^2.

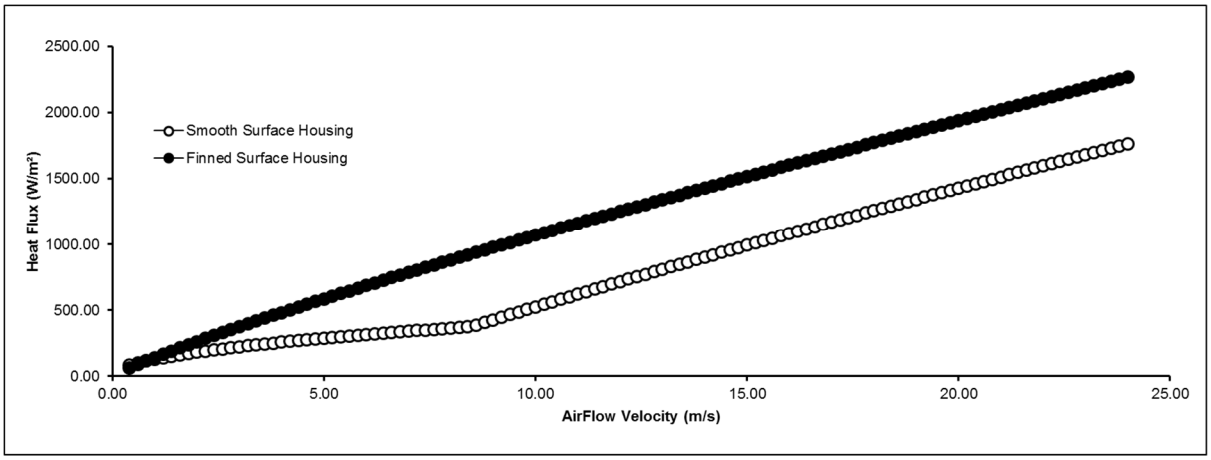

Figure 9-1: Average heat flux along different housings against flow velocity (accounting for laminar flow)

Figure 9-1 indicates the average heat flux along both a smooth and finned housings. In the case of the smooth housing, heat values are proportional to a Reynolds number defined by the axial length of the generator housing and the free-stream velocity. The trend of heat flux for the smooth housing differs for low and high incoming velocities, accounting for whether the flow is still laminar at furthest extent of the smooth housing, or rather, becomes turbulent at some point along the length.

For the defined critical Reynolds number, a turbulent boundary layer beyond the initial laminar boundary layer will be present should the free-stream velocity exceed 8 m/s. The start of the turbulent boundary layer would begin at the furthest extent of the housing and proceed upstream with increasing velocities. The effect of the developing turbulent boundary layer is marked by a rise in the rate at which the average heat flux increases with velocity.

After the turbulent region begins to develop, the rate at which heat flux rises with velocity is approximately equal. However, given that the heat flux from the finned generator is consistently higher than that of the smooth and that the finned generator has a greater overall surface area, the differences between the values of heat transfer increase with higher velocity. Examining figure 9-2, in order to achieve the same heat transfer rate for an airflow velocity of 6 m/s within the fin channels the velocity of the free stream must be 24 m/s above a smooth casing.

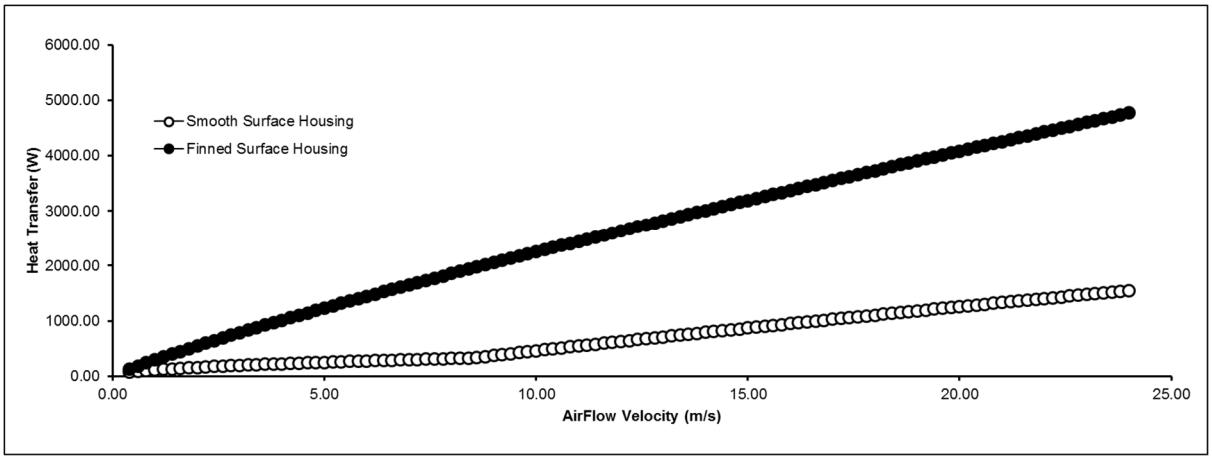

Figure 9-2: Total heat transfer along different housings against flow velocity (accounting for laminar flow)

This means that a finned generator would require the velocities in the fin channels to be at least 25% of the free-stream for the choice of the finned design to be better than the smooth. Given that the flow within the turbo generation section of the oscillating water column would be downstream of a rotating turbine, it would be worthwhile to contrast the results with when assuming the boundary layer is turbulent along the full length of the casing. Equation 5.44 can be replaced with equation 5.46 modifying the heat flux trends as shown in figure 9-3 below.

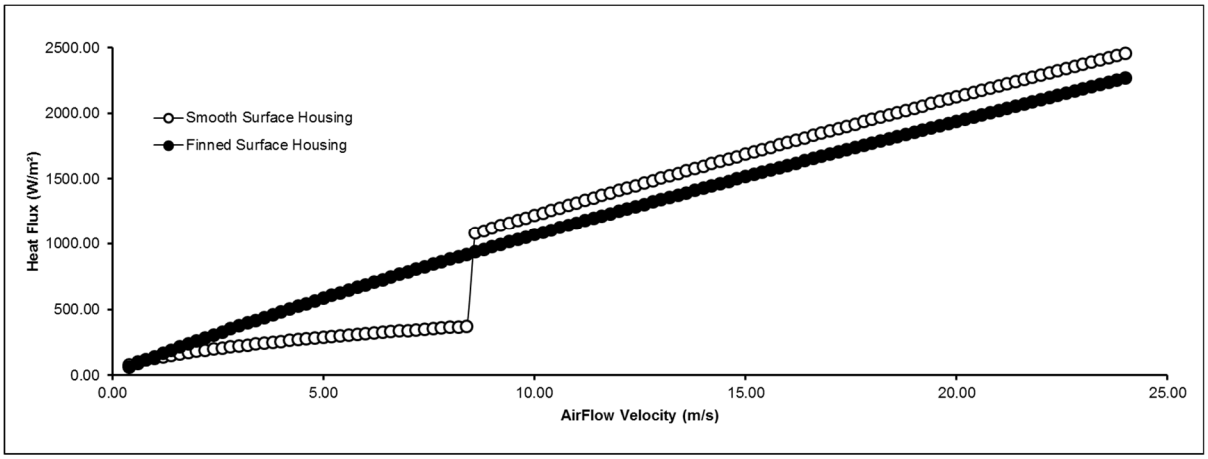

Figure 9-3: Average heat flux along different housings against flow velocity (assuming purely turbulent flow)

Above the critical Reynolds number, the resulting heat flux from the smooth casing is greater than the finned. Though this leads to higher heat transfer values, just as before, as the addition of fins increases the total surface area, the rate of heat transfer from the finned housing generator still outperforms the smooth housing. The updated heat transfer trends are shown in figure 9-4 below.

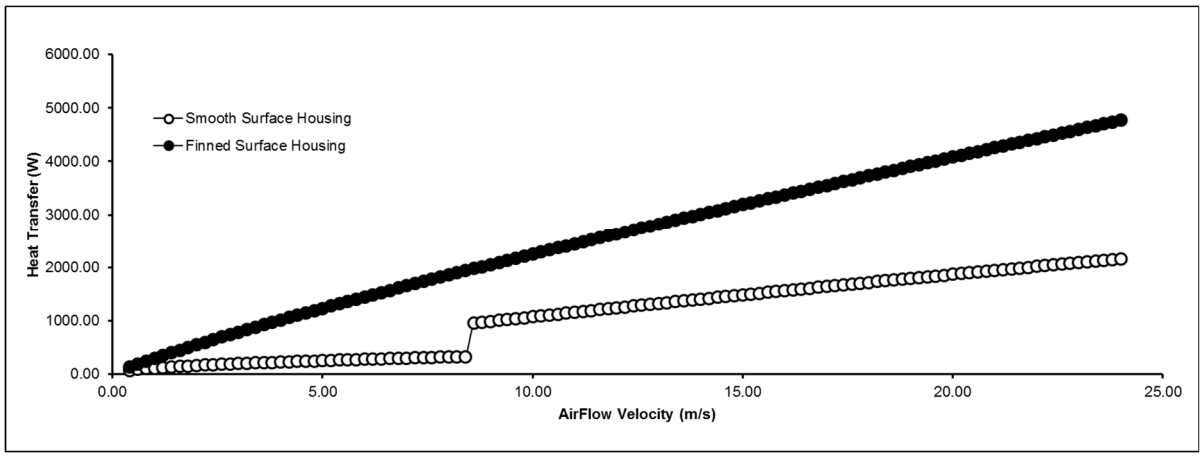

Figure 9-4: Average heat transfer along different housings against flow velocity (assuming purely turbulent flow)

It should be noted that though the heat flux values from the smooth housing are higher across the range shown in figure 9-3, as the velocity tends to infinity, given the nature of the equations this heat flux will fall below that of the finned, ensuring that the thermal performance of a finned housing prevails. Examining the updated heat transfer trends, in achieving approximately the same heat transfer rate as the smooth housing when the free-stream velocity is 24 m/s, the required airflow velocity within the fin channels has risen from 6 m/s to 8 m/s.

9.1.2 CFD simulations of finned generators with various layouts at 10 m/s

After the thermal advantage of a finned housing against a smooth were demonstrated in the previous section, CFD simulations were carried out to examine the effects of varying attenuator layouts on the heat transfer. The attenuators are essentially long cylinders with their axis aligned with the rotational axis of the turbine. The diameter of the cylinder is approximately that of the diameter of the turbine hub. As such, they create the effect of an annulus, in the case of a generator, the air is made to flow along the finned surface of the generator without impacting the end-caps of the generator, and in the case of the upstream turbine, the air is directed to flow past the turbine blades rather than interacting with the turbine hubs and wasting energy.

These simulations were carried out for generators with finned housings only, with a constant free-stream velocity set at 10 m/s. The first scenario was a finned generator cooled under axial flow, without obstacles, and it was observed that vortices formed at the entry of the fin channels, and a clear transition from laminar to turbulent flow along the length of the fin channel could be seen. The addition of an attenuator placed upstream of the generator prevented such vortices from forming and thereby increased the heat transfer. Finally the attenuator was moved closer to the generator so that less energy was lost in the air gap upstream; the resulting maximum heat transfer determined that this design arrangement would be used for all latter simulations. Figures 9-5 to 9-7 show the effect of attenuators upstream of a

finned generator and table 9-1 demonstrates the respective heat transfer results. The velocities values shown in the vector scenes below range from between 0 m/s to 16 m/s approximately.

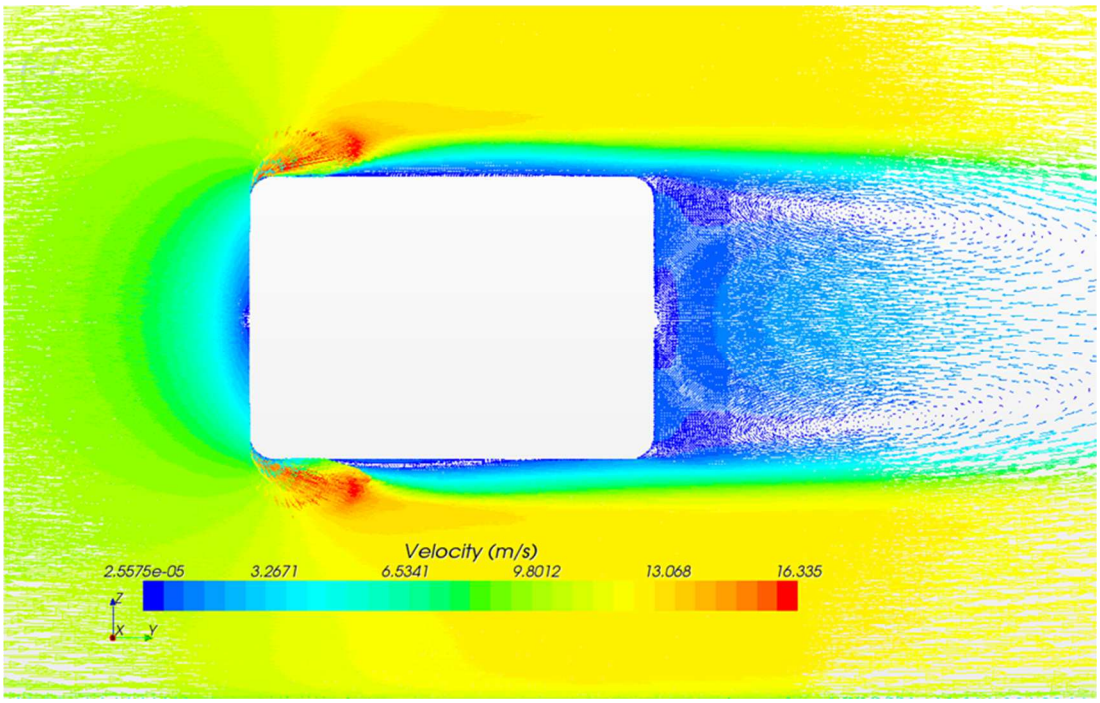

Figure 9-5: Velocity scene showing the effect of attenuators placed upstream of the finned generator - layout a

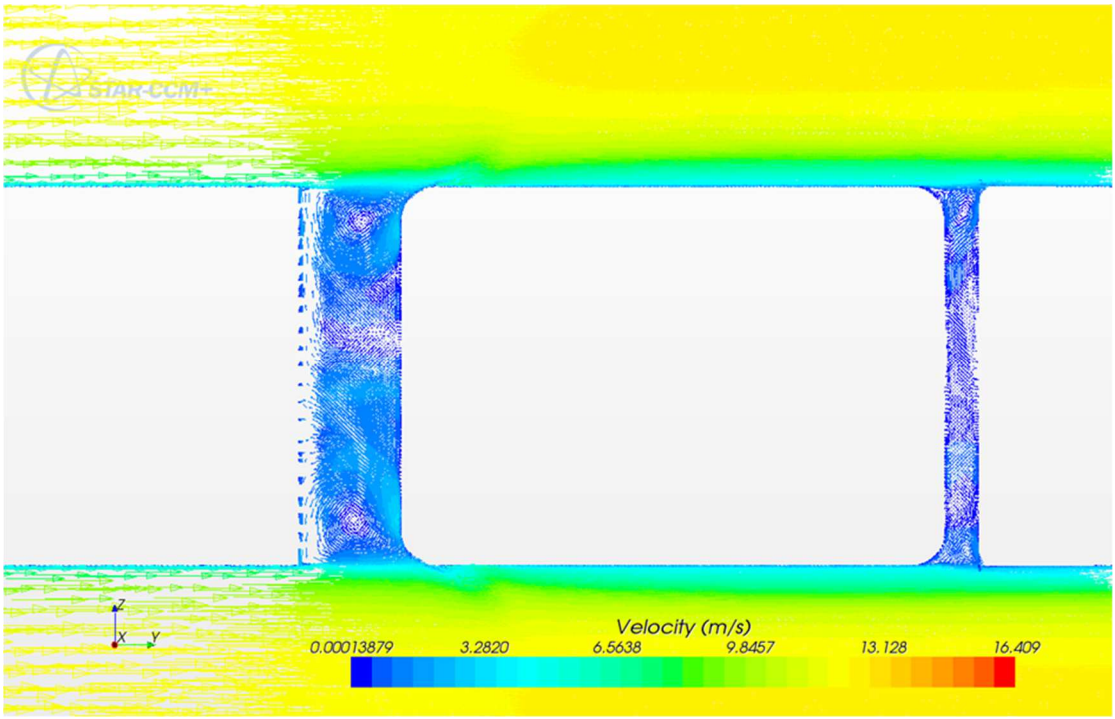

Figure 9-6: Velocity scenes showing the effect of attenuators placed upstream of the finned generator - layout b

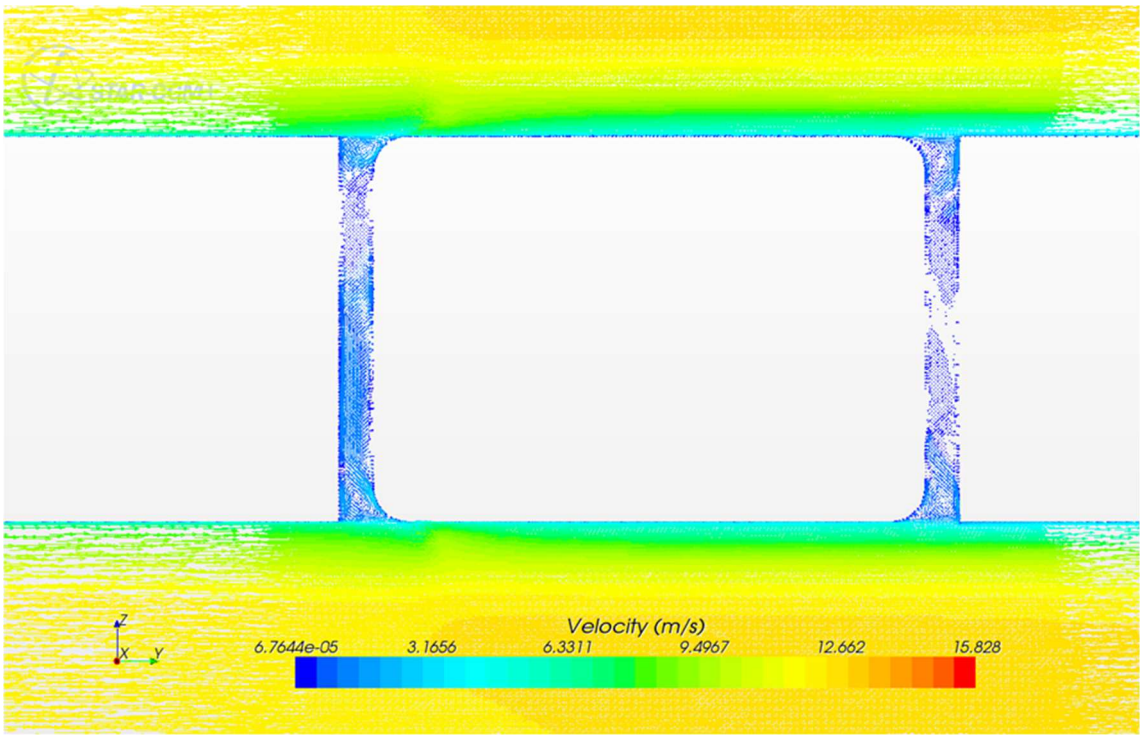

Figure 9-7: Velocity scenes showing the effect of attenuators placed upstream of the finned generator - layout c

Comparisons of heat transfer for different layouts of attenuators for finned generator			
	Layout A Finned	Layout B Finned	Layout C Finned
Total Heat Transfer	842W	867W	927W

Table 9-1: Heat transfer from generators under different attenuator arrangements

Leakage Flow

Focussing on the third layout, the velocity distributions through the fin channels were tabulated in the axial (j) and leakage (k) directions, to observe how the airflow velocity would reduce along the housing due to flow leaking out of the fin channels. The majority of leakage occurs closest to the channel entrance. Figure 9-8 demonstrates how the velocity in the j direction becomes constant as the leakage becomes zero. Figure 9-4 in the earlier section demonstrated that for the finned generator to be viable, the average velocity within the fin channels must be at least 33% of the free-stream, whilst the simulations demonstrate the fin channel velocity does not reduce below 65%.

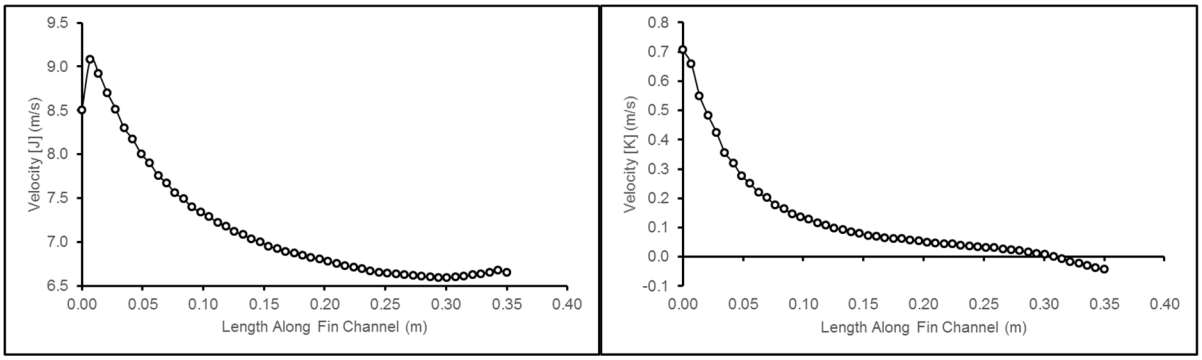

Figure 9-8: Velocity distributions through fin channels, axial (left) and leakage (right)

The results in figure 9-8 can be compared with those of other machines as shown in figure 9-9. The reduction is a complex function of fan design, speed, motor size, fin design, fin roughness and restrictions. It suffices to say that any level of forced convection through the fin channels of a housing (by a fan or otherwise) will result in leakage flow.

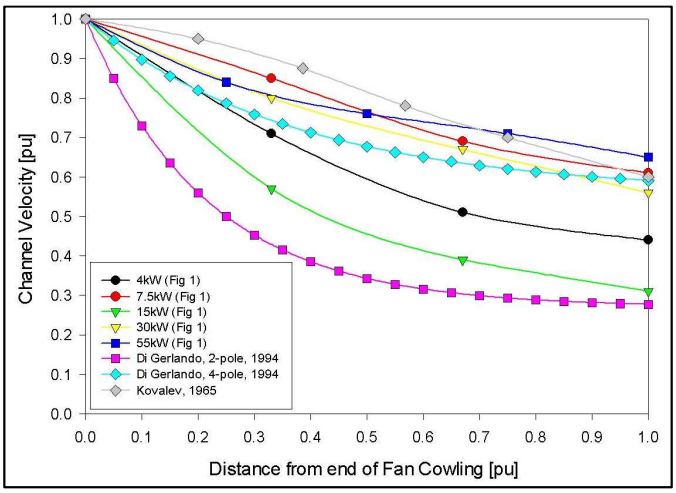

Figure 9-9: Airflow leakage along fin channels

9.1.3 Comparison between the analytical and CFD results

From these simulation results, the average airflow velocities within the fin channels were tabulated. These velocities were then input into equations 7.19 and 7.20 to obtain heat flux and heat transfer values analytically and compared with the CFD results of average heat flux and total heat transfer.

Purely Axial Flow - Finned Generator (Averages Taken within Fin Channels)		
	CFD Results	Analytical Results
Average Velocity (m/s)	7.16	7.16
Average Heat Flux (W/m^2)	1128.43	1095.49
Total Heat Transfer (W)	926.71	806.41

Table 9-2: Comparison between CFD and analytical heat results for finned generator

A comparison of CFD and analytical heat values is shown in table 9-2. The deviation in the average heat flux from the fin channels is thought to be due to the analytical formulae assuming the airflow to be purely axial whereas the end-cap assists in giving the airflow a slightly upward velocity upon entering the fin channels. The airflow velocity also reduces along the fin channels and an average is tabulated, whereas the analytical method assumes a constant velocity. The heat transfer results show a much greater deviation, this is because the Heiles correlation is based on flow through the fin channels, whilst the CFD results include the heat transfer from the fin tips of the generator.

An Optimal Fin Height

The Heiles equation defined in section 7.3 shows that for a given velocity within the fin channels, the heat flux increases with fin height, reaching a maximum and then reducing. This means that although the addition of fins raises heat transfer due to the increase in surface area, the fin dimensions are also important in that there is an optimal fin height to maximise heat flux, independent of surface area. For constant generator dimensions, the fin height at which the peak value of heat flux occurs is seen to reduce with increasing channel flow velocity. Figure 9-10 shows the variation of heat flux with fin height for a channel velocity of 7.16 m/s, corresponding to the average velocity in table 9-2. The optimal fin height is found to be between 21mm and 22mm, given that the airflow in the entire turbo generation section of the LIMPET OWC is likely to be faster than the 10 m/s velocity defined in the initial CFD simulation, a fin height of 20mm is deemed acceptable.

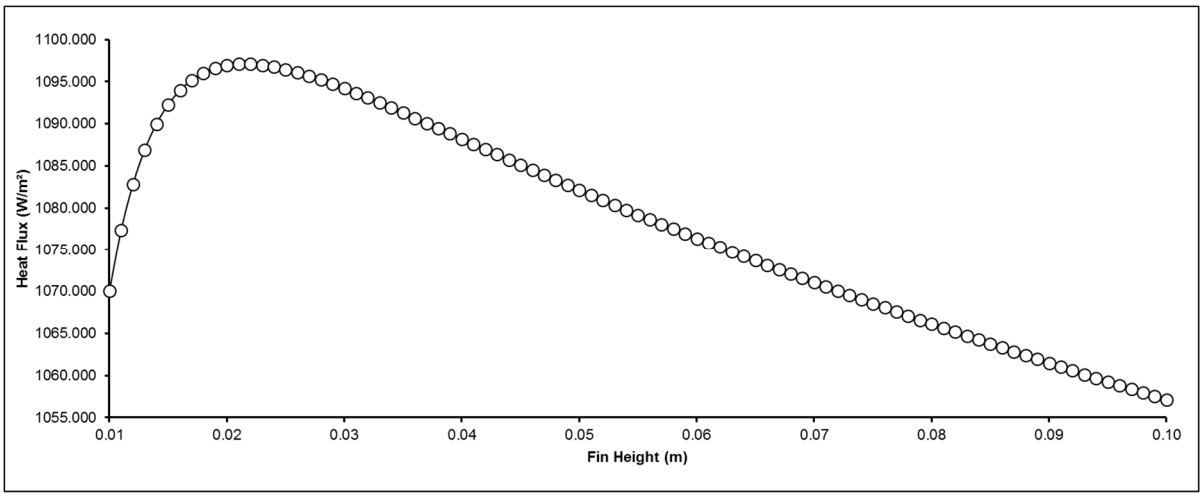

Figure 9-10: Optimal fin height demonstrating the peak heat flux for a fin channel velocity of 5 m/s

9.2 Placing a turbine upstream

The next stage was to compare the heat transfer rate from a finned generator when cooling under purely axial flow with when airflow impingement occurs due to the placement of a rotating Wells turbine upstream, as demonstrated by the vector scenes in figures 9-11 and 9-12. The same effect will also be analysed for a smooth generator. In this simulation, a NACA 0020 turbine is used and the clearance between the turbine tip and encompassing shroud is 10% of the blade cord length. Of course, for practical use, there must always be a Wells turbine interacting with the airflow, and therefore the simulations of purely axial flow are to represent the extents of cooling that would be expected from a standard fan forcing airflow through the fin channels in a TEFC induction machine.

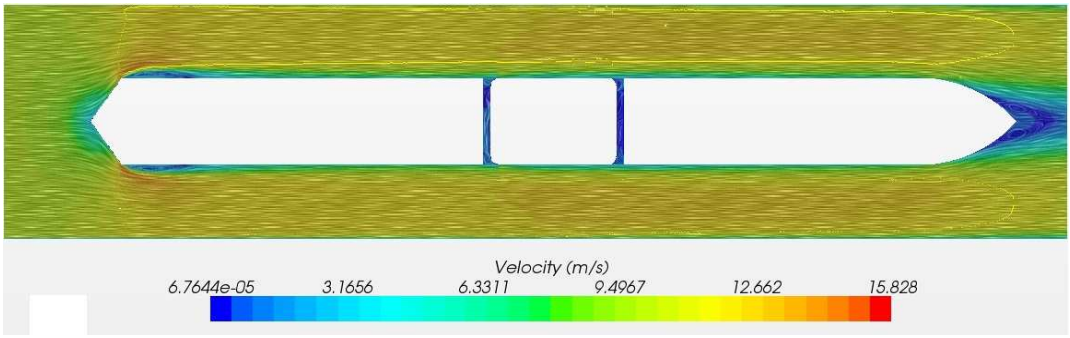

Figure 9-11: Velocity vector scene for finned generator during purely axial flow

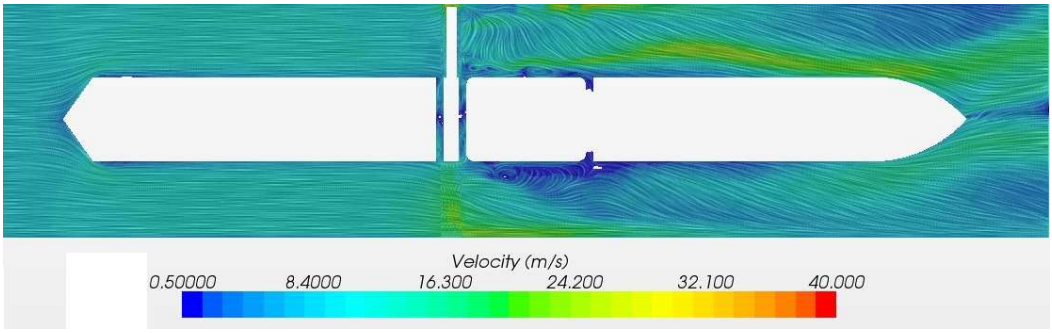

Figure 9-12: Velocity vector scene for finned generator during airflow impingement

As mentioned is section 7.2, the above velocity scenes demonstrate that any effects of reversed flow due to the downstream attenuator, do not appear to travel upstream to interfere with the generator region.

9.2.1 Comparisons of scalar scenes

The scalar scenes in figure 9-13 show the heat flux along both a finned and smooth surface generator in the case of purely axial airflow. High values of heat flux are seen at the entry to the fin channels where the axial flow velocity is the highest as previously indicated in figures 9-5 to 9-7. The advantage here is that the largest internal heat source in the electrical generator comes from the end-windings at the near and far ends, and in an oscillating flow, these maximum temperature areas would benefit from the greatest cooling. The distribution of heat flux is similar for the smooth surface.

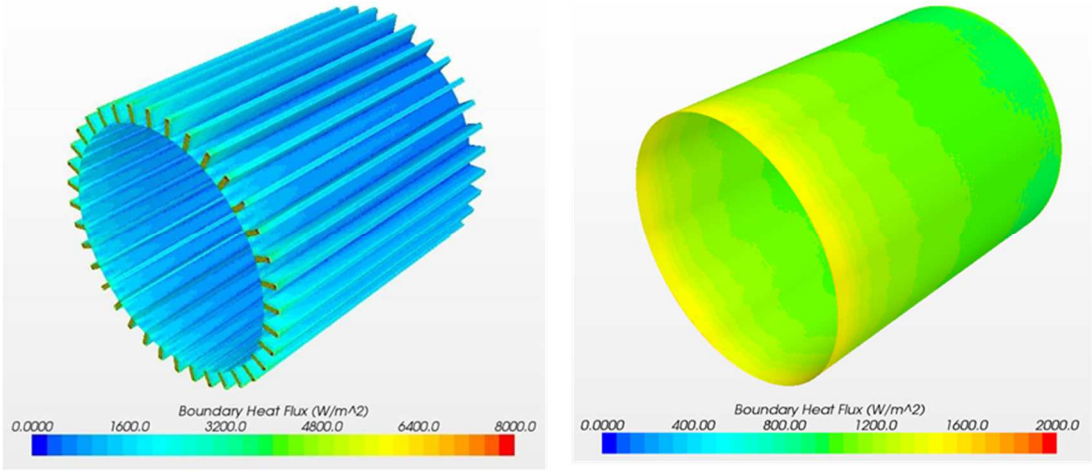

Figure 9-13: Heat flux scalar scenes for generators with finned and smooth casings under axial airflow

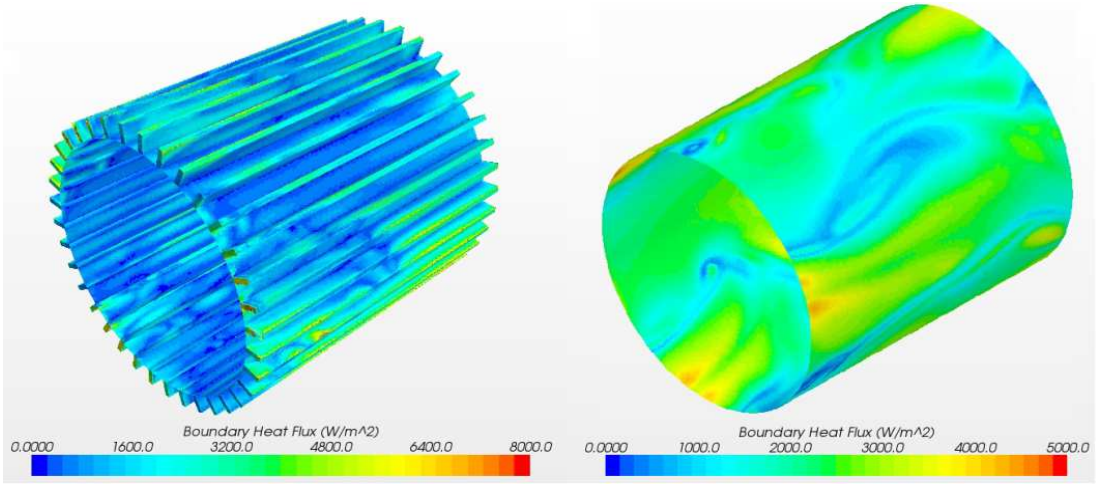

Figure 9-14: Heat flux scalar scenes for generators with finned and smooth casings under airflow impingement

The heat flux scenes shown in figure 9-14, are for the case of airflow impingement. The smooth surface generator has areas of very high heat flux values coinciding with where the impinging is greatest. The presence of fins, forces air to flow axially in the channels immediately, whereas the additional degree of freedom over the smooth generator allows for a larger heat dissipation area and higher heat flux values therein.

9.2.2 Comparisons of heat transfer results in the four scenarios

Figure 9-15 below shows the improvement in total heat transfer for airflow impingement against purely axial flow for the smooth and finned generators. Despite the smooth generator experiencing a far greater improvement in cooling due to impingement, the heat transfer was still less than the finned generator under purely axial flow. Hence the finned generator was judged to be the better choice for use in the turbo generation section.

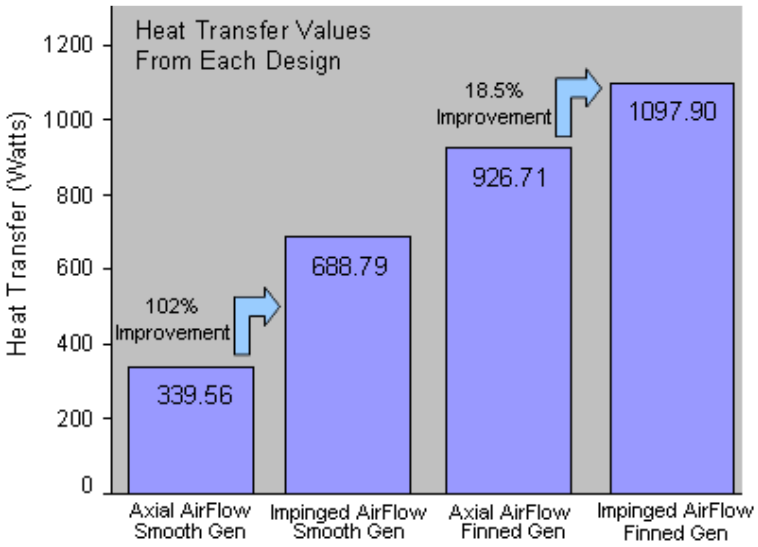

Figure 9-15: Increasing heat transfer from the varying designs

A cylindrical section was used to analyse the directions of axial airflow within the fin channels, it is seen in figure 9-16 that the majority of the airflow is flowing back towards the suction side of the blade; whist in the fin channels associated with the spaces between the turbine blades the flow is positive.

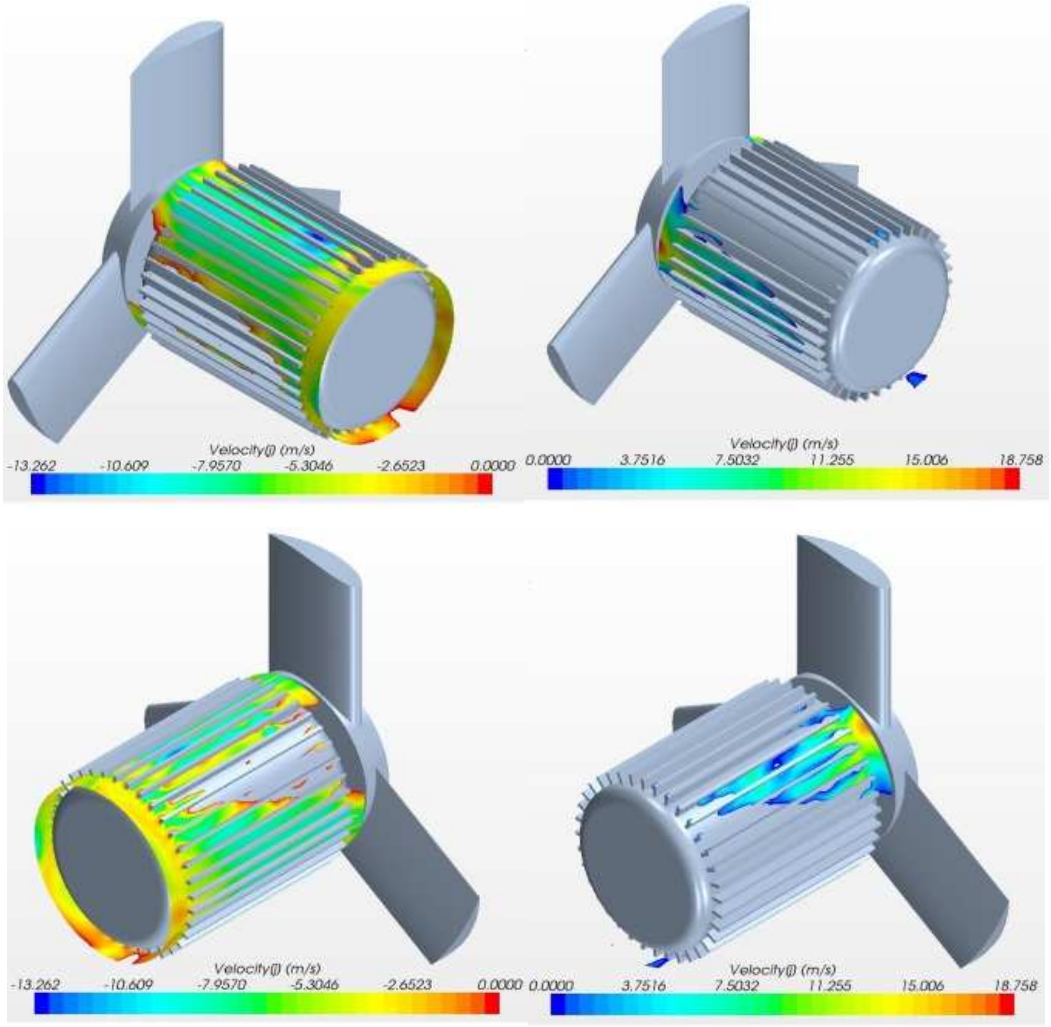

Figure 9-16: Negative/backwards (left) and positive/forwards (right) airflow through fin channels at two viewing angles

The magnitude and direction of air flowing axially within four fin channels can be seen in figure 9-17. The magnitudes are higher than in the case of no turbine along the majority of the generator length especially in the top fin channel which is associated with the majority of impingement. Considering the results of the optimal fin height, this indicates a smaller fin height could be implemented to maximise the heat flux in the channels.

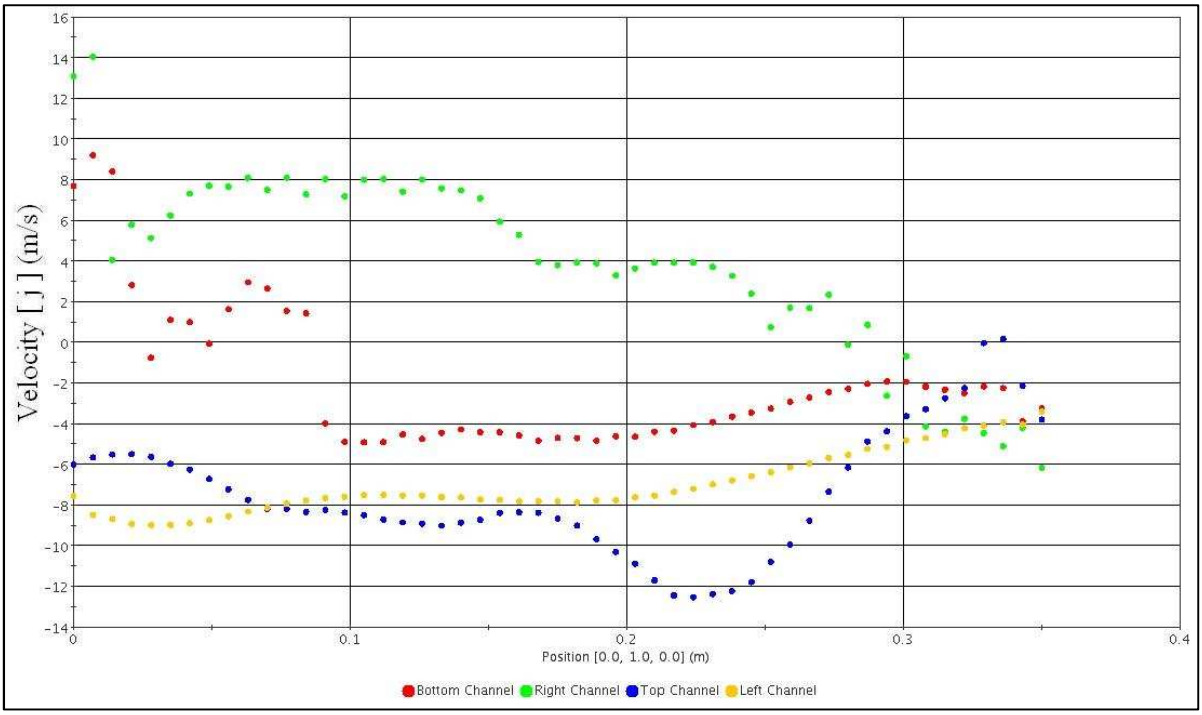

Figure 9-17: Velocity distributions through fin channels

Despite airflow impingement providing better cooling, it results in a greater difference between the highest and lowest values of heat flux across the generator casing. Figure 9-18 demonstrates the values of heat flux less than 500 W/m^2 along the finned generator under purely axial airflow and airflow impingement respectively.

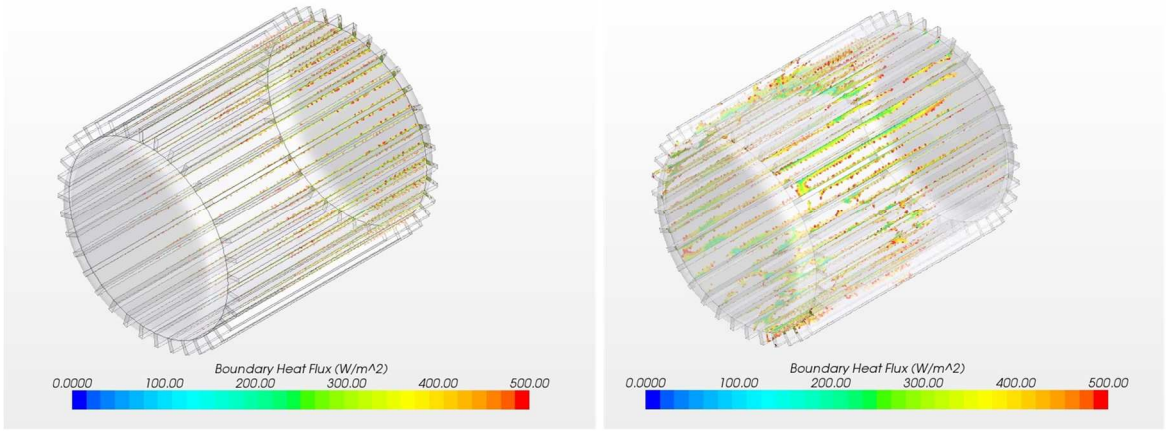

Figure 9-18: Heat flux across finned generator casing under 500 W/m^2 for axial (left) and impinging (right) flow

These low values of heat flux are more prominent on the generator undergoing impingement and can lead to regions of relatively higher temperature. Hotspots created by this non-uniform cooling can also reduce the insulation integrity and performance of permanent magnets, which is an unavoidable consequence of the impingement resulting from presence of the upstream Wells turbine.

9.3 The effects of varying the turbine tip clearance

9.3.1 Modelling the Toressi (2008) Wells turbine with the mesh and turbulence models used in this thesis

Before proceeding further with investigating the effect of additional design changes to the Wells turbine, it is important to judge the accuracy of the mesh and turbulence models in this research work. This was accomplished by importing an equivalent Wells turbine simulated by Toressi *et al* (2008) and using the same mesh and turbulence models for this work, to compare with the published results. A brief overview of the findings by Toressi *et al* will be given, after which, results of the torque coefficient will be overlaid with equivalent results from this research work.

Computational fluid dynamic simulations were conducted by Torresi *et al* (2008) to examine the effect of varying tip clearance for a single monoplane Wells turbine. The high solidity Wells turbine is initially simulated over a full range of flow coefficients at a tip clearance of 1% cord length. Toressi claims an improvement in accuracy by comparing earlier results obtained from the commonly used "K-Omega SST" (2004) turbulence model (with a coarser mesh) against a more recent "Sparalt-Almaras" (2008) turbulence model. Both models are validated against experimental results conducted by Curran and Gato (1997). The torque and efficiency results are shown in figures 9-19 and 9-20 below.

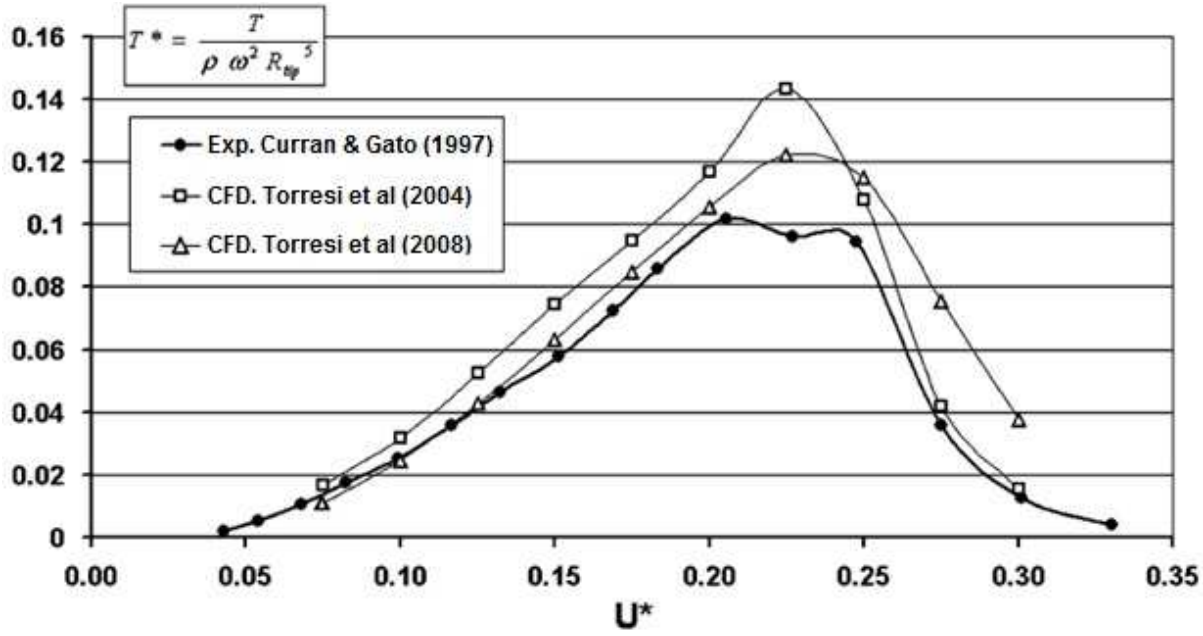

Figure 9-19: Torque coefficient against flow rate coefficient for different turbulence models by Toressi *et al*

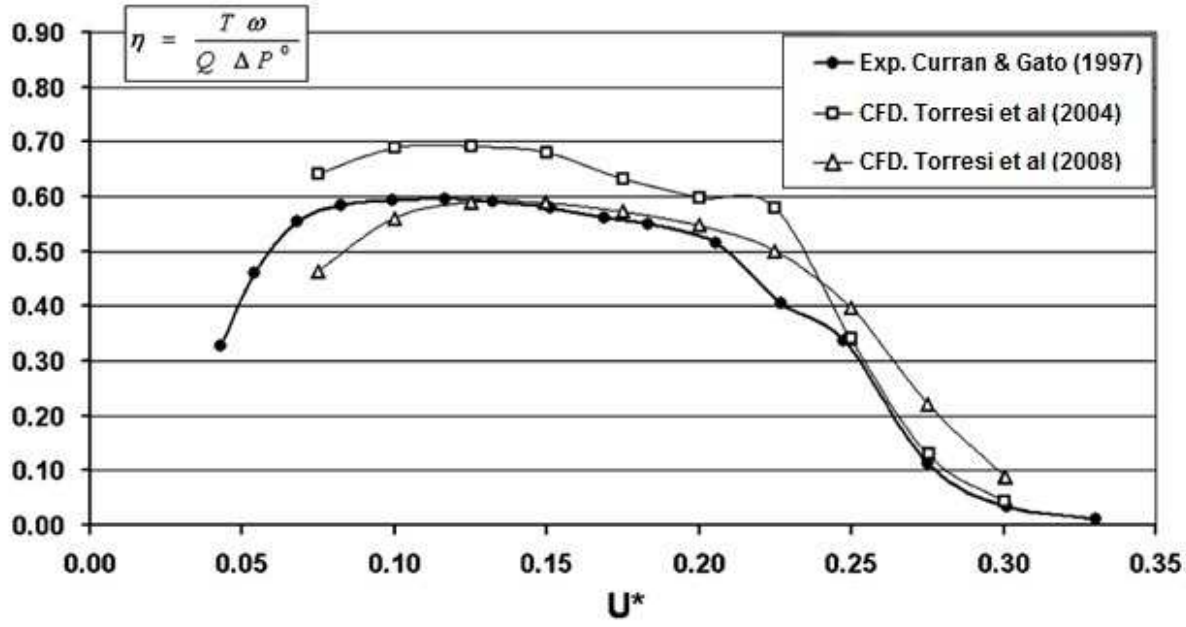

Figure 9-20: Efficiency against flow rate coefficient for different turbulence models by Toressi *et al*

The results obtained from using the Sparalt-Almaras turbulence model (2008) certainly give closer and smoother trends relative to the experimental results. The over-prediction of torque and consequent efficiency can be observed just prior to stall in the case of the K-Omega turbulence model (2004), this phenomenon is also observed in our own results and appears to be an intrinsic characteristic owing to the choice of turbulence model itself, the Sparalt-Almaras model can be seen to also over-predict values at this point, but to a lesser extent.

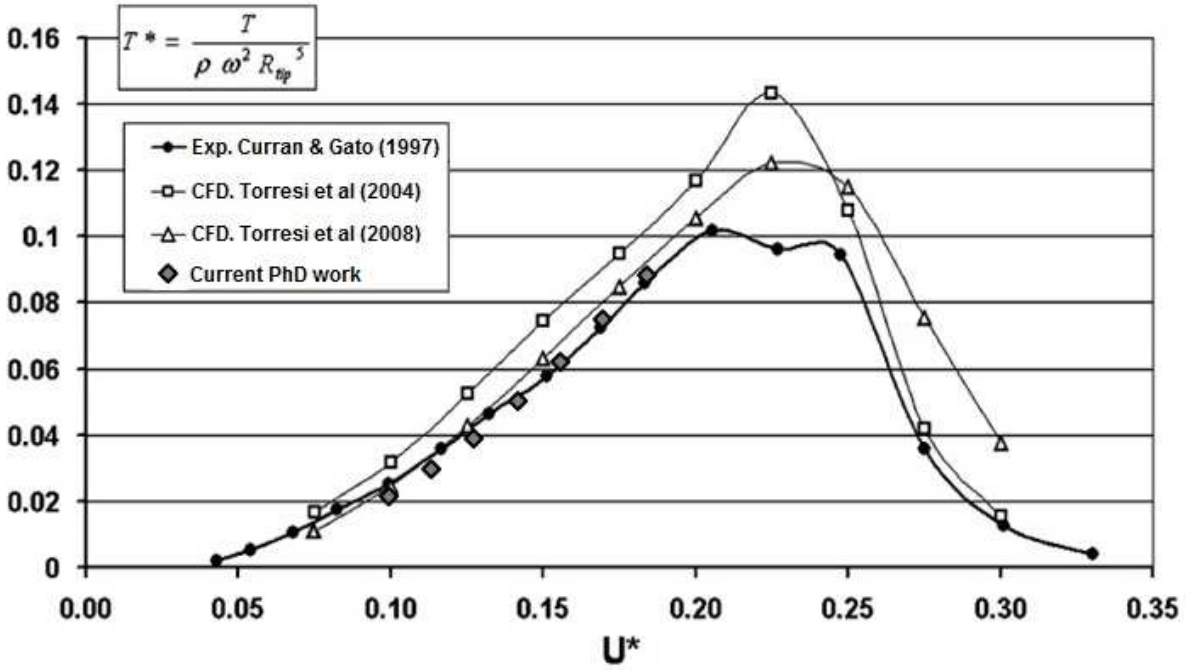

Figure 9-21: Comparison of torque coefficient results by Toressi *et al* and this PhD work

This PhD work used the K-Omega turbulence model, though the results (figure 9-21 above) slightly under-predict and over-predict the torque at low and high flow rate coefficients respectively, they are arguably as accurate as those obtained with the Spalart-Almaras. This may suggest the accuracy of the results obtained by Toressi was due to the refinement of the mesh rather than the choice of turbulence model. Indeed, the cell count for the K-Omega result was stated as 163,840, whilst that used in the Spalart-Almaras result was 1 million. The cell count in the turbine region for this PhD work was approximately 7.5 million, whilst the entire domain consists of 14.5 million cells. The results of the comparison of results, gives confidence for the trends obtained across the entire domain.

9.3.2 Results of varying tip clearance from this thesis

The next stage was to analyse what effect varying the clearance between the turbine tip and the encompassing shroud rotating had on the heat transfer from the finned generator. The vector scene in figure 9-22 is that for the case of the 2% clearance demonstrating airflow separation after the turbine blade and the resulting impingement across the finned generator. Figure 9-23 shows close-ups of the airflow after the turbine tips for both the 2% and 10% clearances.

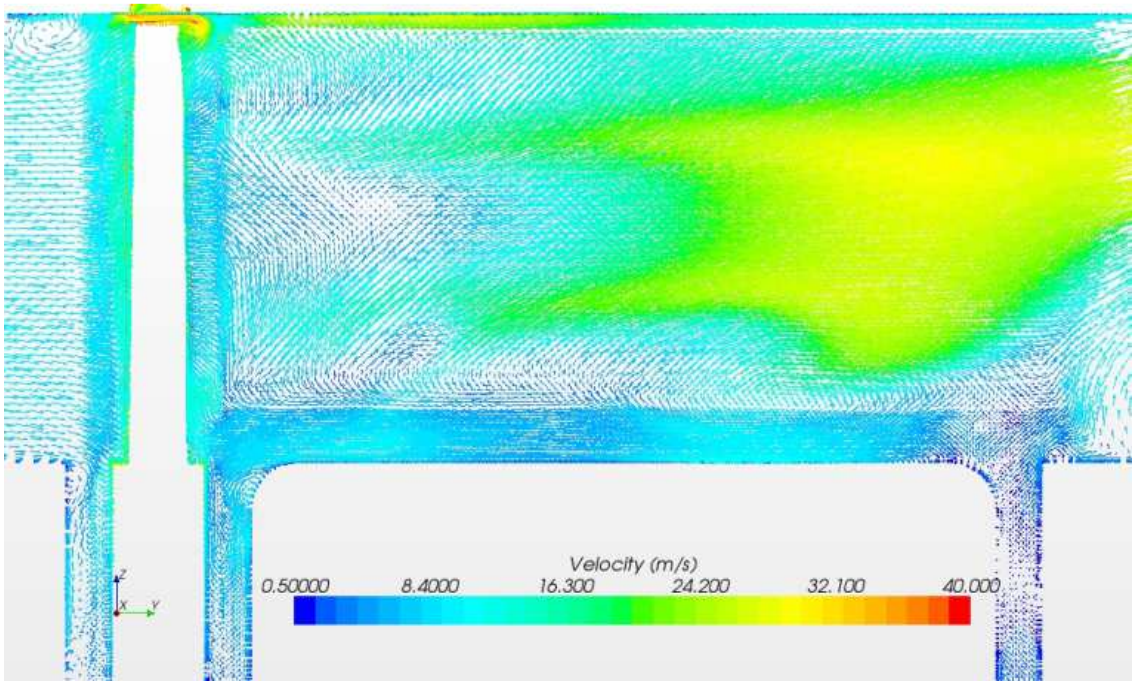

Figure 9-22: Velocity vector scene for finned generator during impinging flow at 2% turbine tip clearance

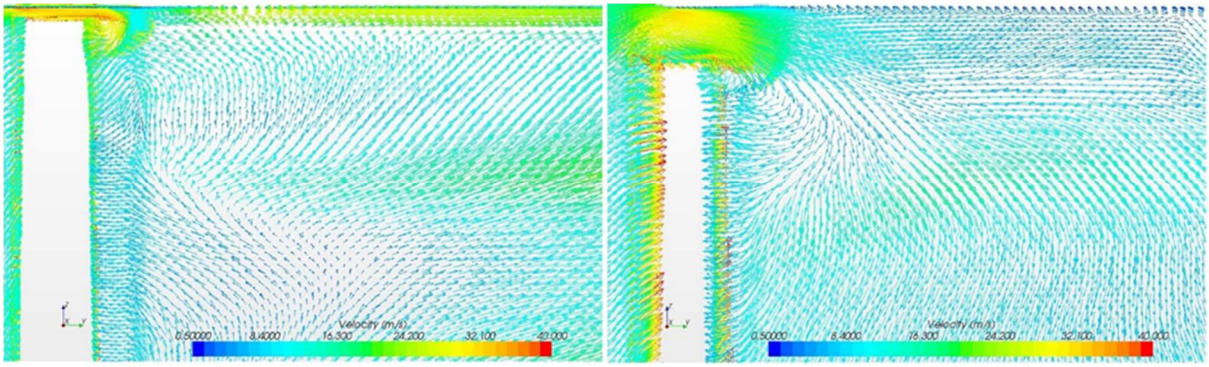

Figure 9-23: Close-up velocity vector scenes of tip-gap flow at 2% (left) and 10% (right) clearances

It can be seen that airflow exiting the tip gap interacts with the downstream of the blade far less in the case of greater clearance. Whereas for a tighter clearance the tip gap airflow is not able to avoid the suction side of the blade. Hence for greater tip clearances the turbine performance worsens due to a decrease in pressure drop across the turbine and the associated outer portions of airflow passing the turbine without energy exchange. Figures 9-24, 9-25 and 9-27 shows a comparison of the torque coefficient, pressure drop coefficient and efficiency against flow rate for the Wells turbine at the two clearance values. The flow rate coefficient is the ratio of the average incoming air velocity and blade tangential tip speed.

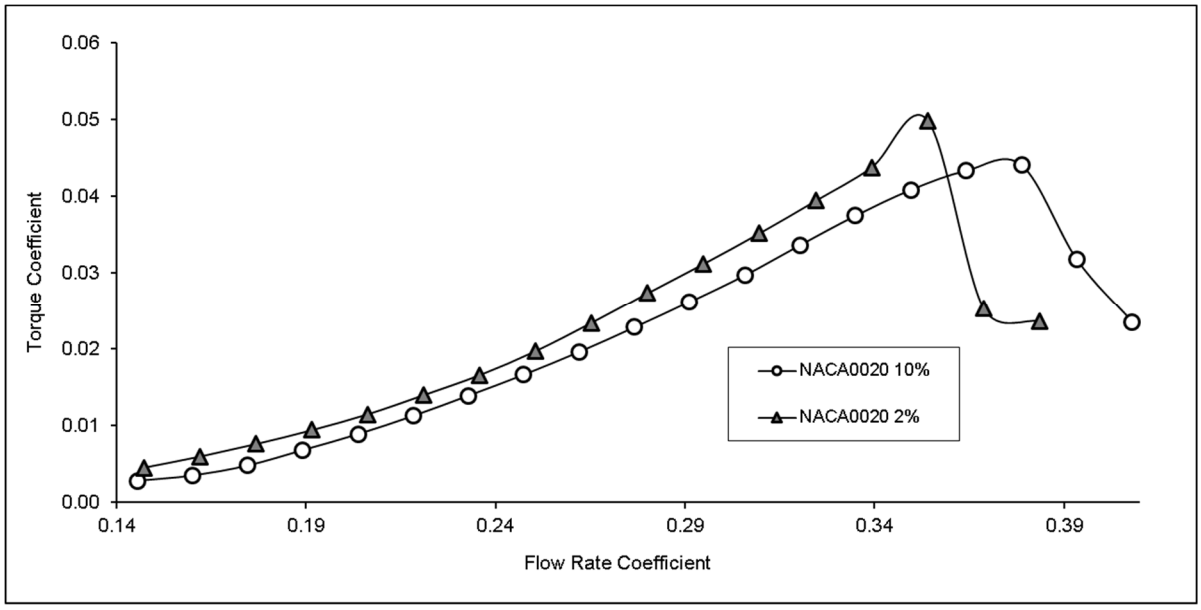

Figure 9-24: Torque coefficient against flow rate coefficient for varying turbine tip clearances

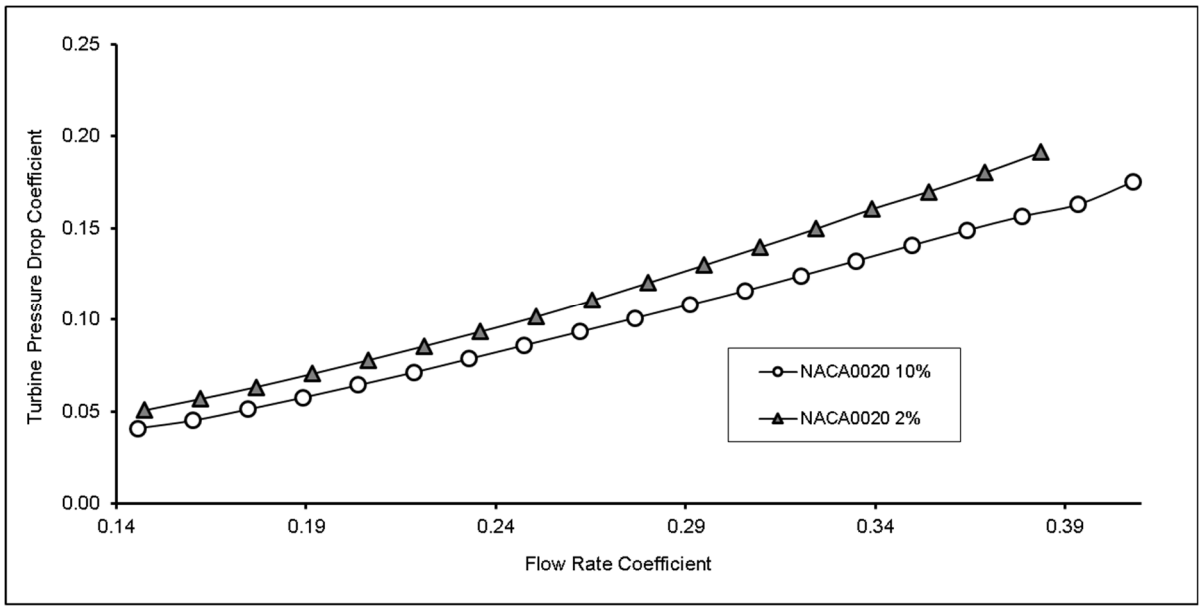

Figure 9-25: Turbine pressure drop coefficient against flow rate coefficient for varying turbine tip clearances

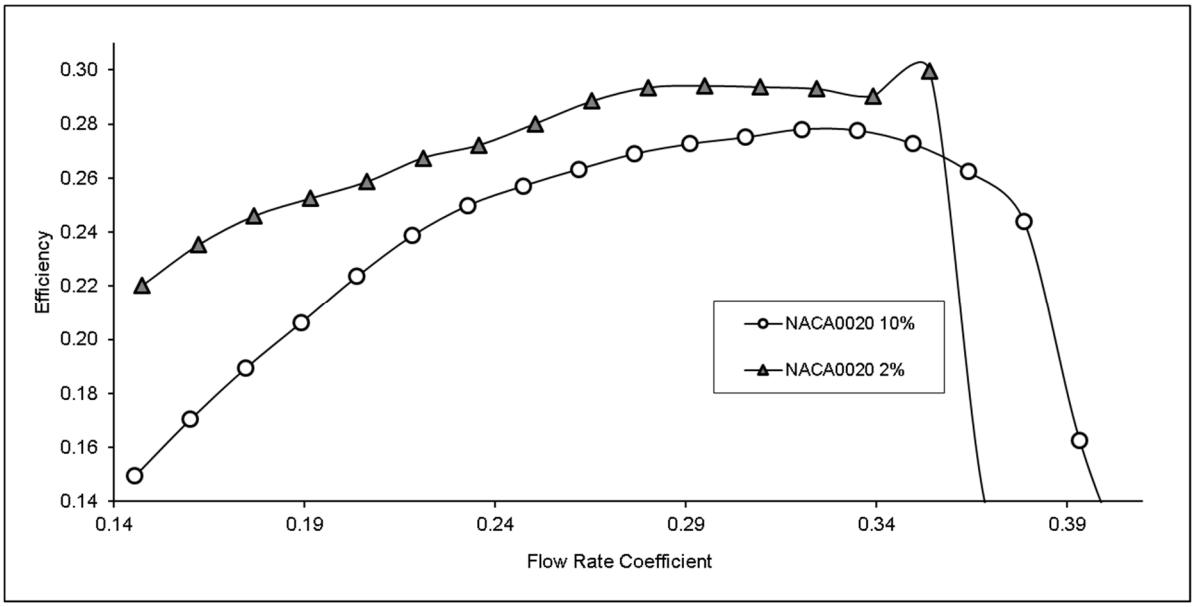

Figure 9-26: Efficiency against flow rate coefficient for varying turbine tip clearances

Reducing the clearance causes an increased turbine pressure drop; more airflow is available to interact with the suction side of the blade which has a positive effect on the turbine torque and consequent efficiency. Though the lesser clearance increases the efficiency, it is also seen to advance the occurrence of turbine stall; which will be discussed further in the analysis of results.

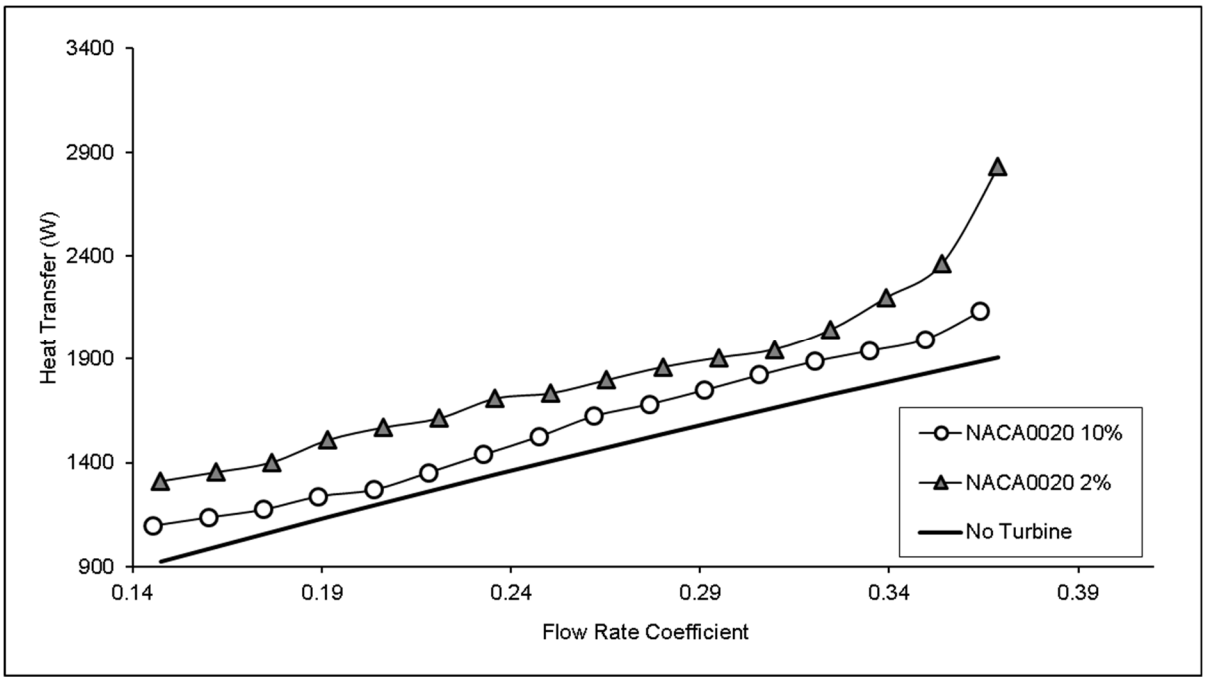

Figure 9-27: Total heat transfer against flow rate coefficient for varying turbine tip clearances

The total heat transfer from the finned generator for two different clearances are demonstrated in figure 9-27, with the heat transfer determined analytically from the Heiles relation is also included as a reference. The rate of heat transfer is observed to increase with reducing clearance. When compared to purely axial airflow, across the overall operating range of the turbine (not including stall), the cooling is seen to increase by 18.5% in the case of the greatest clearance, by 26.8% for a medium clearance and finally by 41.6% for the least clearance. As such, it can be stated that the induction generator utilised in an oscillating water column application may be safely operated beyond the pre-defined maximum rating.

When examining the heat transfer values for a flow rate coefficient beyond 0.34, it is revealed that the heat transfer is observed to spike when the turbine stalls. This is observed to occur earliest in the case of the 2% clearance, the cause of this sharp rise in cooling is no doubt due to the increased turbulence in the wake of the downstream flow after stalling.

Figures 9-28 and 9-29 show the net mass flow rates towards the generator at a radius of 310mm and 270mm, these radii values are defined as the “inner” and “outer” cylinders in the y-axis respectively, and are the same cylinder sections as those shown in figure 9-8. The mass flow rate describes the extent (in kg/s) of air flowing towards the generator specifically at the radii of these cylinder sections.

The heat transfer can be related to the net mass flow towards the generator which increases with the angle of attack, otherwise defined as the flow rate coefficient. It is found that reducing the size of the tip gap also increases the radial mass flow rate towards the generator across the range of flow rates.

This is understood to be due to the greater utilisation of airflow by the blade in the cases of lesser clearance.

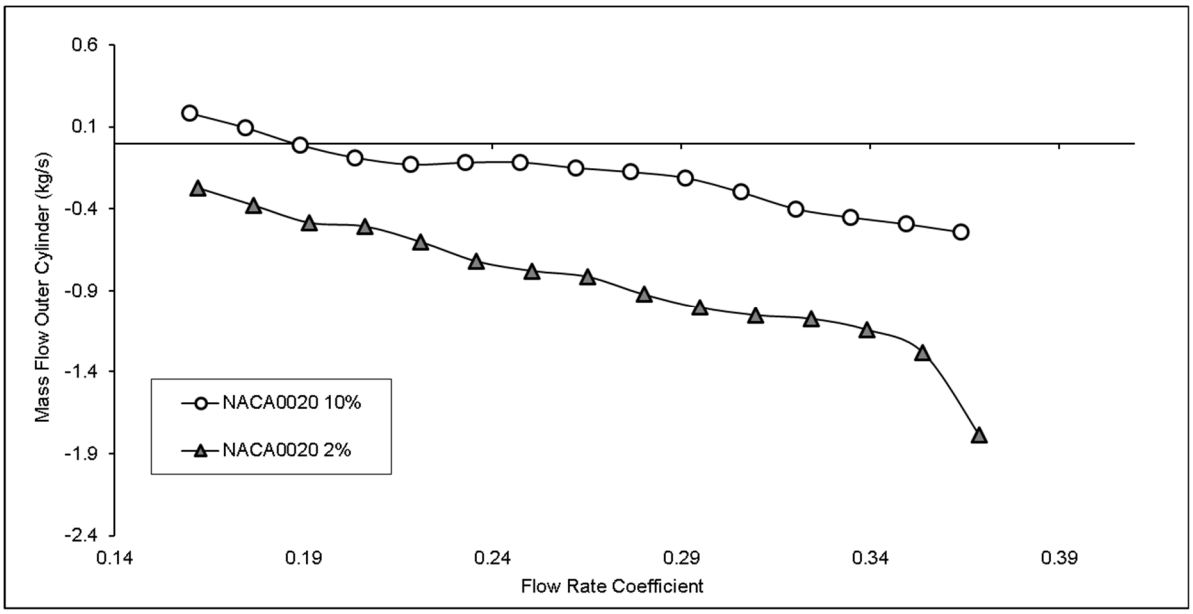

Figure 9-28: Mass flow rate towards generator at outer radius against flow rate coefficient for varying turbine tip clearances

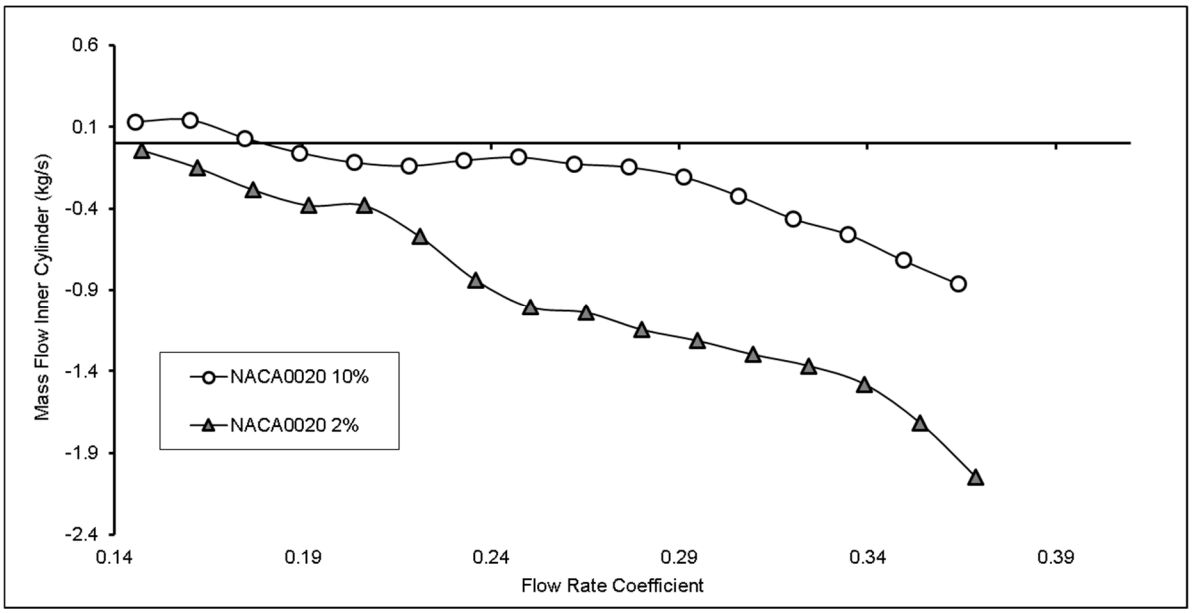

Figure 9-29: Mass flow rate towards generator at outer radius against flow rate coefficient for varying turbine tip clearances

Analysis of the results

The occurrence of earlier stalling for the case of lesser clearances is understood to be related to the tip gap leakage flow clearly noticeable in figure 9-23 which demonstrates the velocity scene in the case of a 2% tip clearance. In the case of least clearance a very high pressure drop (between the pressure and suction side of the turbine blade) is maintained by a relatively small gap between the turbine tip and encompassing shroud. The flow that passes through this gap, due to such a high pressure difference, leaves in the form of a jet which ultimately does not interact with the blade suction surface, but rather remains closer to the encompassing shroud. At higher flow coefficients, effectively higher angles of attack, separation of the boundary layer from the suction surface ensures, resulting in aerofoil stall.

However, in the case of greater clearances, the reduced pressure drop diminishes the intensity of this tip gap leakage flow, resulting in an effective secondary flow which interacts with the suction side of the turbine blade, thereby counteracting separation and postponing aerofoil stall. This extended performance lasts until, with higher flow coefficients, the leakage flow leaves with enough energy to the bypass the suction side of the blade just as in the case of lesser clearance.

The heat transfer coefficient achieved by the generator surface is related to the flow velocities in the fin channels, which is dependent on the extent of airflow directed radially towards the generator positioned downstream of the turbine. Naturally, this airflow impingement will increase with higher incoming flow velocities as is demonstrated in figures 9-28 and 9-29 showing further mass flow crossing defined cylinder boundaries towards the generator with an increasing flow rate coefficient. The link between mass flow rate and turbine clearance can also be understood by considering the tip gap leakage flow.

In cases of greater clearance, the leakage flow has less energy, due to the lower pressure drop, and does not travel far in the axial direction before having to interact with the suction side of the blade, indeed, it is the lower pressure on the downstream (suction) side of the blade that ensures the predominant flow direction in the fin channels is towards the turbine. However, for lesser clearances, when the tip gap leakage flow has a high enough velocity to travel further downstream, the extent of airflow impinging radially towards to the generator is increased, ultimately resulting in higher fin channel velocities and thereby a higher heat transfer coefficient.

9.4 The effects of varying the turbine thickness

Having established that minimising the clearance between the turbine tip and outer shroud maximises both the heat transfer from the generator and overall turbine performance, the next stage was to investigate the effect of the turbine profile by altering the thickness of the blade. The initial simulations were performed on a NACA 0020 blade profile, meaning a blade having a maximum thickness of 20% the chord length. Two additional blade profiles of NACA 0018 and NACA 0016 were simulated across

the same range of flow coefficients. Comparisons of torque coefficient, pressure drop coefficient and efficiency are shown in figures 9-30 to 9-32.

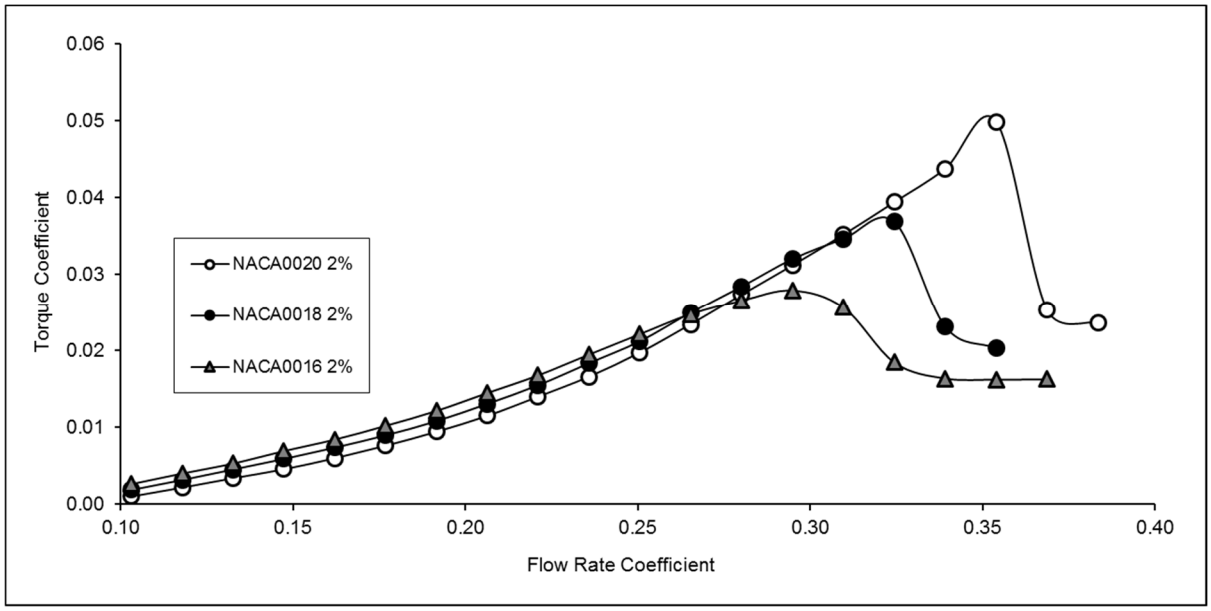

Figure 9-30: Torque coefficient against flow rate coefficient for varying turbine blade profiles

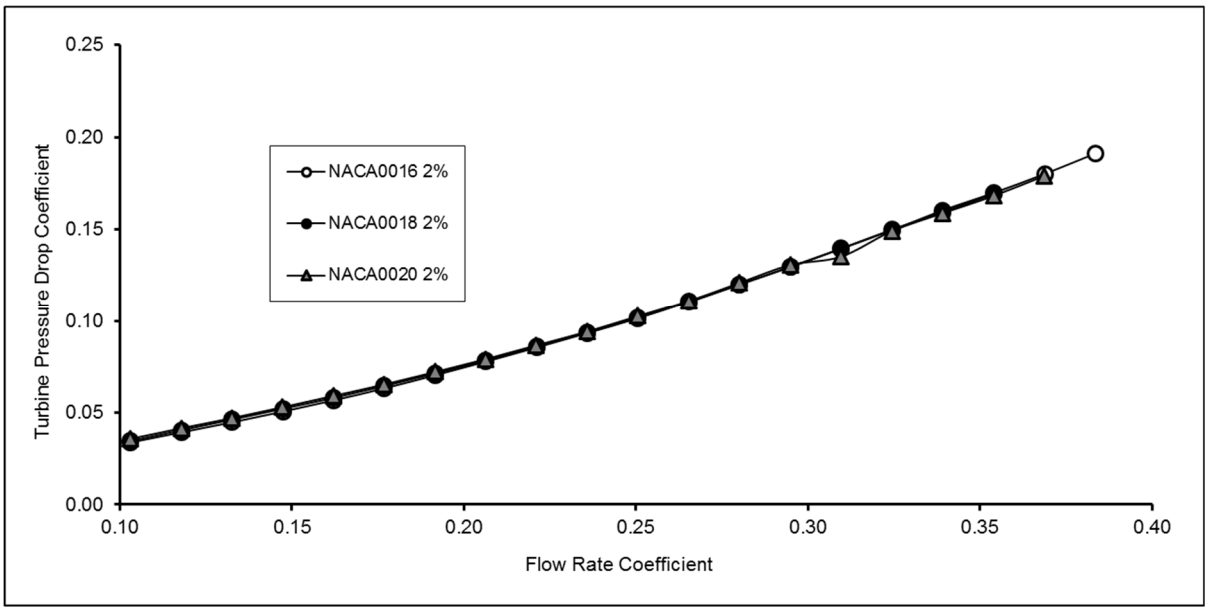

Figure 9-31: Turbine pressure drop coefficient against flow rate coefficient for varying turbine blade profiles

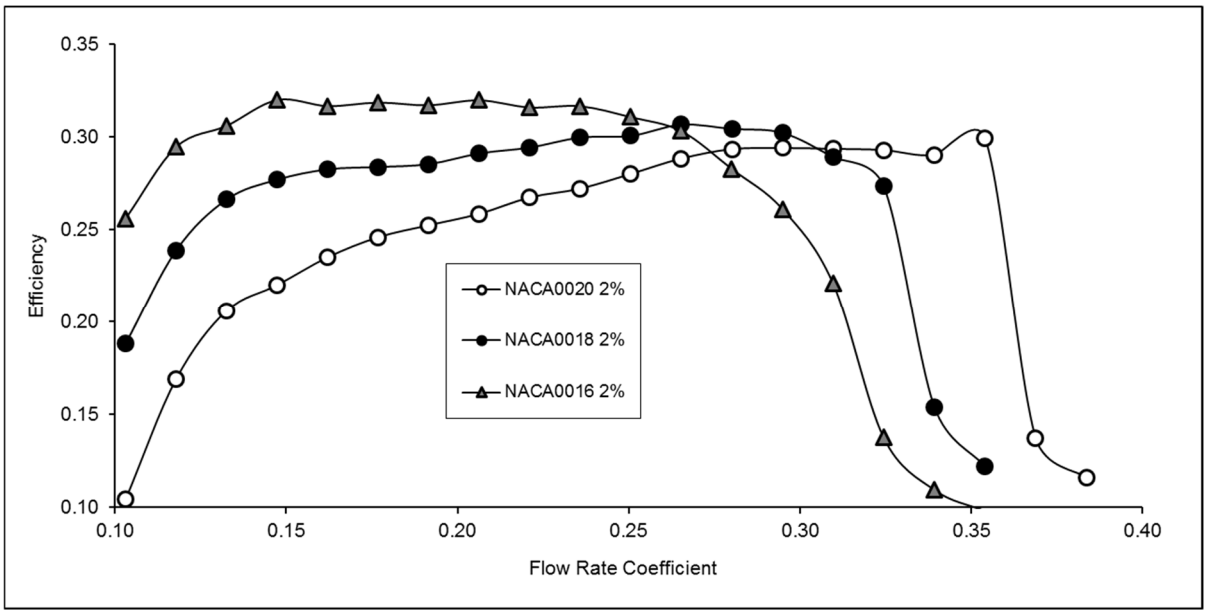

Figure 9-32: Efficiency against flow rate coefficient for varying turbine blade profiles

The results in figure 9-30 demonstrate that thinner aerofoils provide more torque relative to thicker blades in the range of flow coefficients prior to stall, however, similar to the previous torque results, the blade profiles that provide less torque also extend the occurrence of aerofoil stall. Compared to the pressure drop results of varying clearances, the changes in blade profile have relatively little effect (figure 9-31). From equation 9.3, the efficiency is seen to be proportional to the torque but inversely proportional to the turbine pressure drop, hence the improvements in efficiency are greater with a varying blade profile than with a varying clearance. The findings from these results are corroborated by experimental results conducted by NACA on a set of thin and thick aerofoil blades as shown in figures 9-33 and 9-34 below.

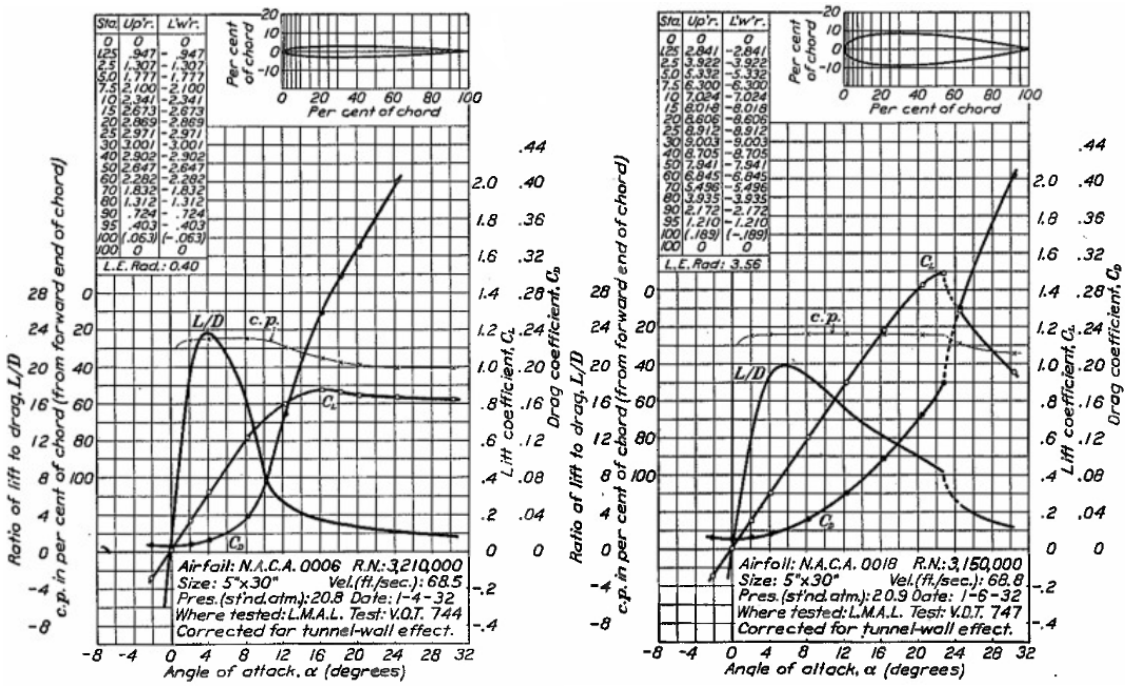

Figure 9-33: Trends for lift coefficient, drag coefficient and lift against drag ratio for NACA 0006 (left) and NACA 0018 (right) aerofoils [NACA, 1985]

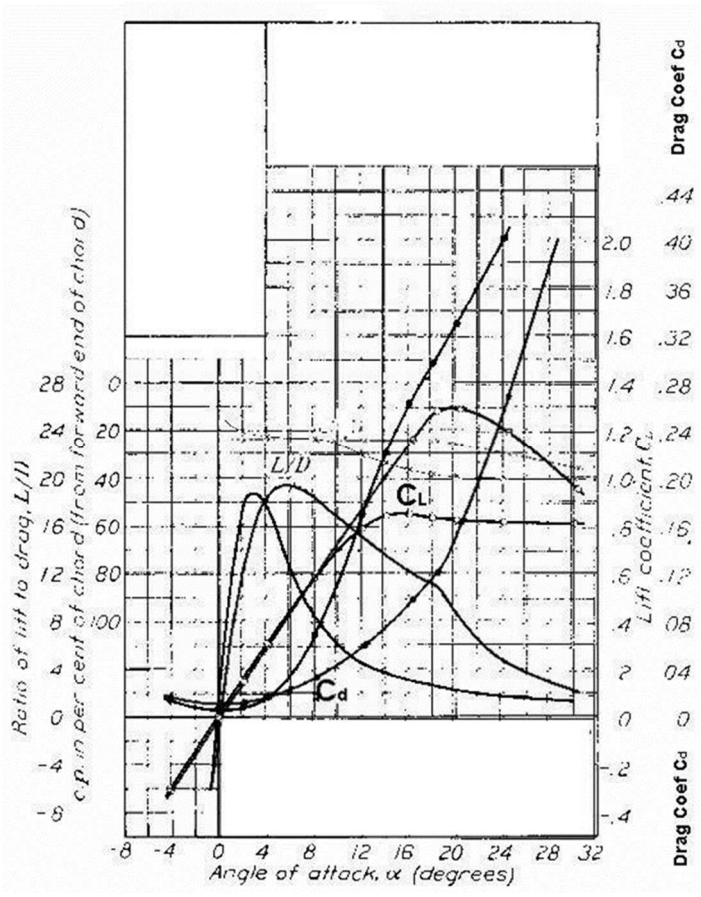

Figure 9-34: Trends for lift coefficient, drag coefficient and lift against drag ratio for NACA 0006 and NACA 0018 aerofoils obtained by NACA combined into one graph [NACA, 1985]

Considering the way in which the torque required to rotate the Wells turbine is produced, the lift against drag ratio (L/D) can be thought to follow the same pattern. The experimental results confirm the trend found in figure 9-30 showing the results of the varying blade profile on the torque coefficient, in that a thinner blade performs better at low angles of attack but is seen to stall earlier. Stall is where the lift force on the blades reduces rapidly, a component of which acts to provide the driving torque to the turbine. This results in a change in torque direction and a deceleration of the turbine. The thicker blade will not only stall later but also go on to achieve a higher lift against drag ratio (or torque) as the angle of attack is increased.

The thicker aerofoil is seen to provide both greater lift and drag coefficients at low angles of attack, the increased drag is more prominent than the increased lift and hence the lower lift to drag ratio in this region. The development of lift across an aerofoil was explained in section 7.7.1. For a given free-stream, the velocity values close to the thicker aerofoil (with a greater cross-sectional area) would be higher, as such, its lift and drag values are higher. Aside from the parasitic drag, the increased lift generates additional induced drag, and hence the total increases in drag are greater than the total increase in lift.

At higher angles of attack, the thinner aerofoil is seen to stall earlier, the drop in the lift against drag ratio is linked primarily to the more rapid rise in drag caused by flow separation. The resistance to stalling can be intuitively understood by considering that as the angle of attack is increased, the leading edge of a thicker aerofoil would cut into the airflow at a lesser angle. The postponing of flow separation is also observed over an aerofoil with a camber when compared to a purely symmetric aerofoil profile. Observations of how the varying blade profile affects heat transfer and the relationship to mass flow rate towards the generator are shown in figures 9-35 to 9-37 below.

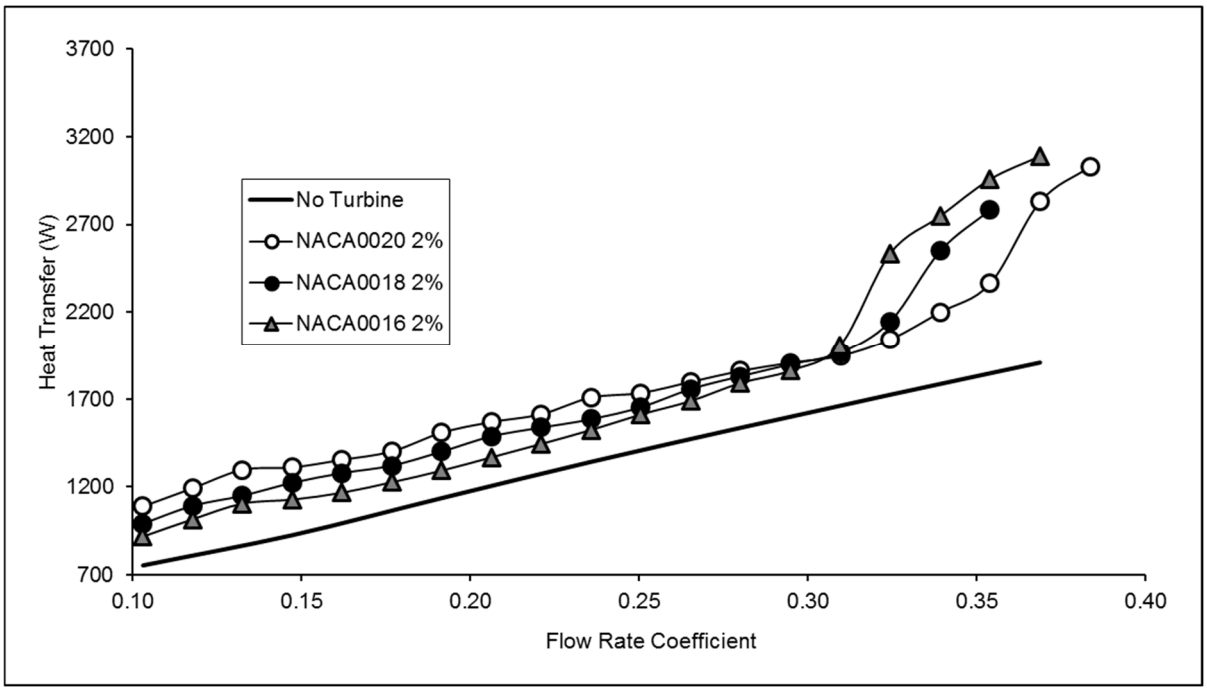

Figure 9-35: Total heat transfer against flow rate coefficient for varying turbine blade profiles

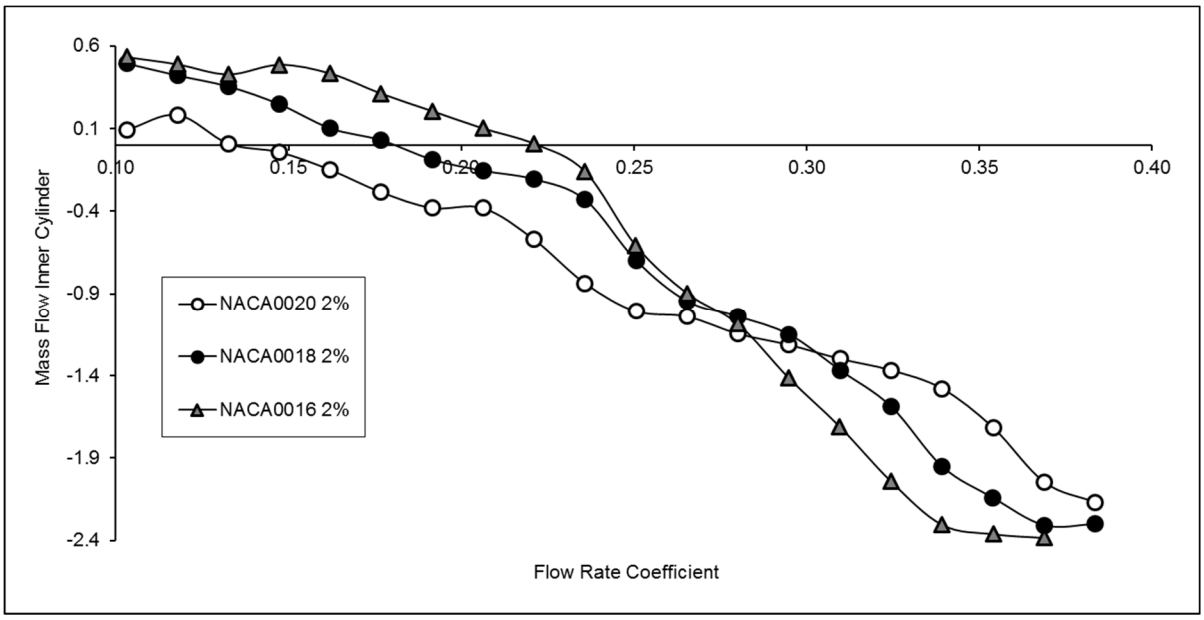

Figure 9-36: Mass flow rate towards generator at outer radius against flow rate coefficient for varying turbine blade profiles

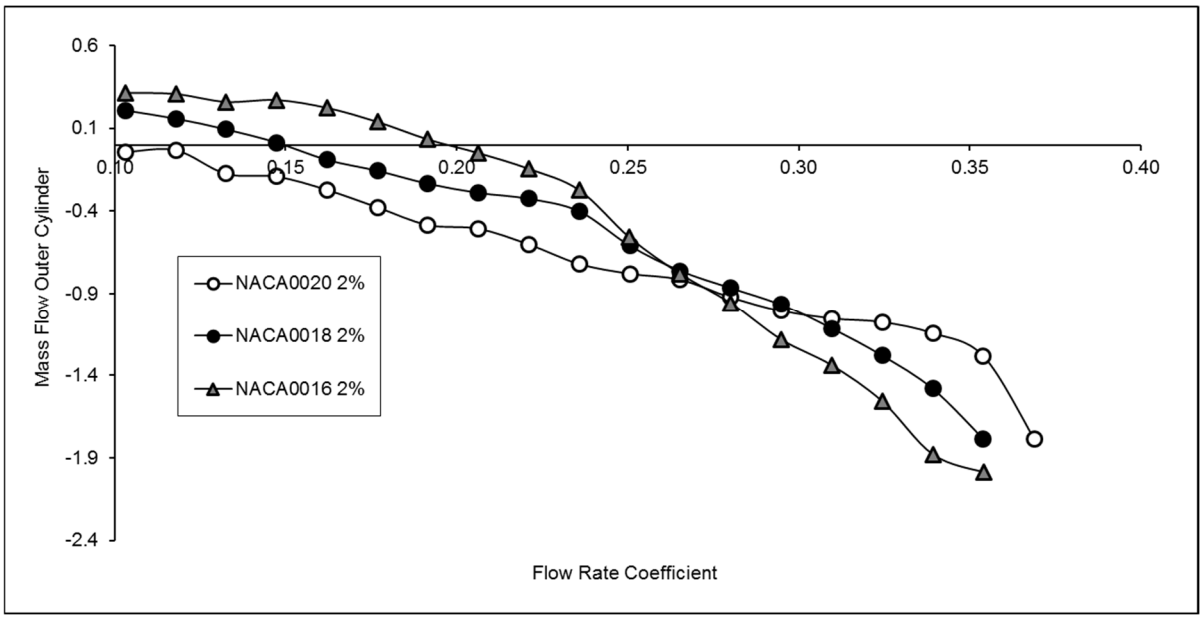

Figure 9-37: Mass flow rate towards generator at inner radius against flow rate coefficient for varying turbine blade profiles

Figure 9-35 demonstrates for a fixed turbine tip clearance, that reducing the thickness of the aerofoil consequently reduces the heat transfer from the generator in the pre-stall range, correlating with figures 9-36 and 9-37 which demonstrate that thicker aerofoils give greater mass flow rates towards the generator in the range of the equivalent flow coefficients. As mentioned previously, for a fixed incoming velocity value upstream of an aerofoil, a thicker profile would produce higher airflow velocities in the low pressure regions. As the thicker aerofoil takes up more volume, the flow past such a turbine will ultimately be faster, thus increasing the extent of airflow impingement towards the generator as well as the consequent heat transfer.

The earlier peaking in heat transfer is observed for thinner aerofoils corresponding to the earlier occurrence of aerofoil stall. In the stall regions, the reversal of the heat transfer trend is accompanied by a similar reversal of the mass flow rate trends. The use of thinner aerofoils may pose an advantage in that a generator may be cooled down extensively whenever the turbine reaches stall.

However, the choice of turbine thickness will ultimately depend on the range of predominant flow coefficients achieved during operation, and hence the occurrence of stalling would be made rare by design. Aside from this, within the operating range, the thickest (NACA 0020) aerofoil is deemed most appropriate as though a thinner aerofoil would produce higher torque (and therefore power) values, it would ultimately result in greater heat produced from within the generator, coupled with a reduced ability for heat transfer due to less airflow impingement this opposing choice would ultimately be detrimental to generator cooling.

9.5 The effects of increasing solidity

With the optimal designs for maximising the heat transfer having been established in terms of thickness and clearance, the next stage was to investigate the effect of turbine solidity. The previous turbine designs have all had the same solidity of 0.371, in that they are 3 bladed. To preserve the hub to tip ratio, a subsequent 5 bladed turbine with a profile of NACA 0020, tip clearance of 2% and solidity of 0.463, was simulated over the same range of flow coefficients, the results of which were contrasted with those in section 9.4. Comparisons of torque coefficient, and pressure drop coefficient and efficiency are shown in figures 9-38 to 9-40.

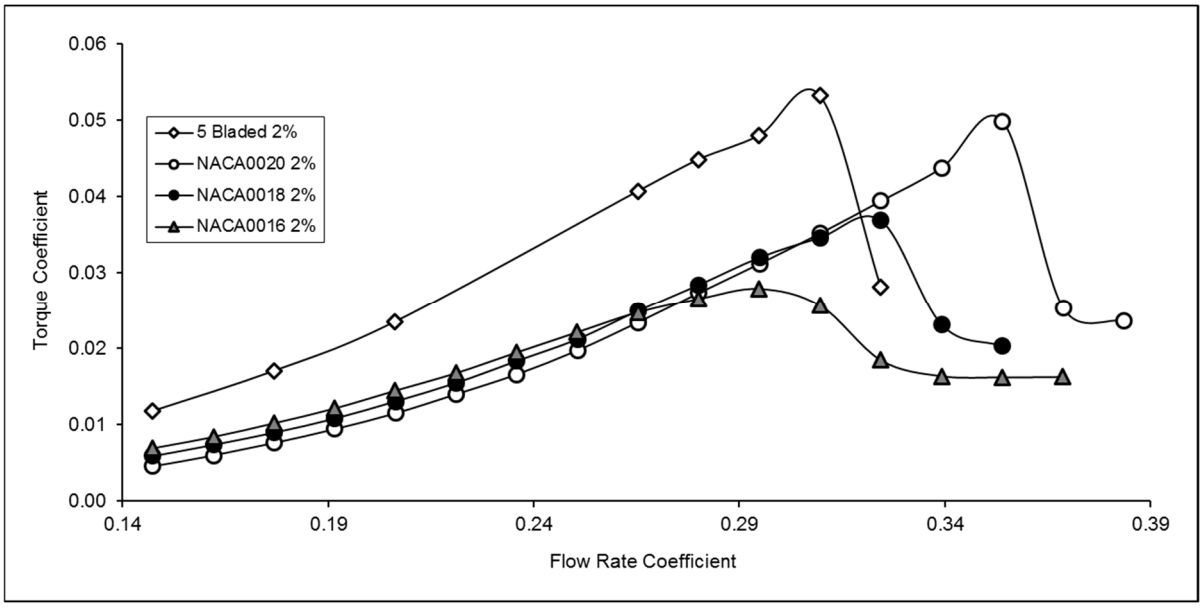

Figure 9-38: Torque coefficient against flow rate coefficient for varying turbine blade profiles and solidities

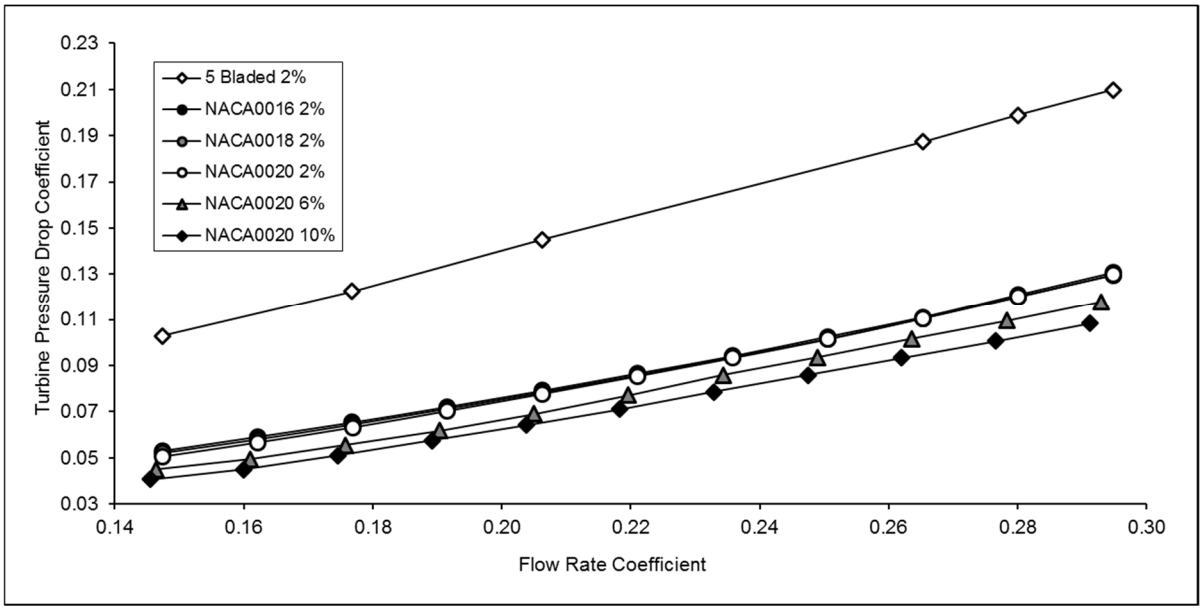

Figure 9-39: Turbine pressure drop coefficient against flow rate coefficient for all variations of turbine

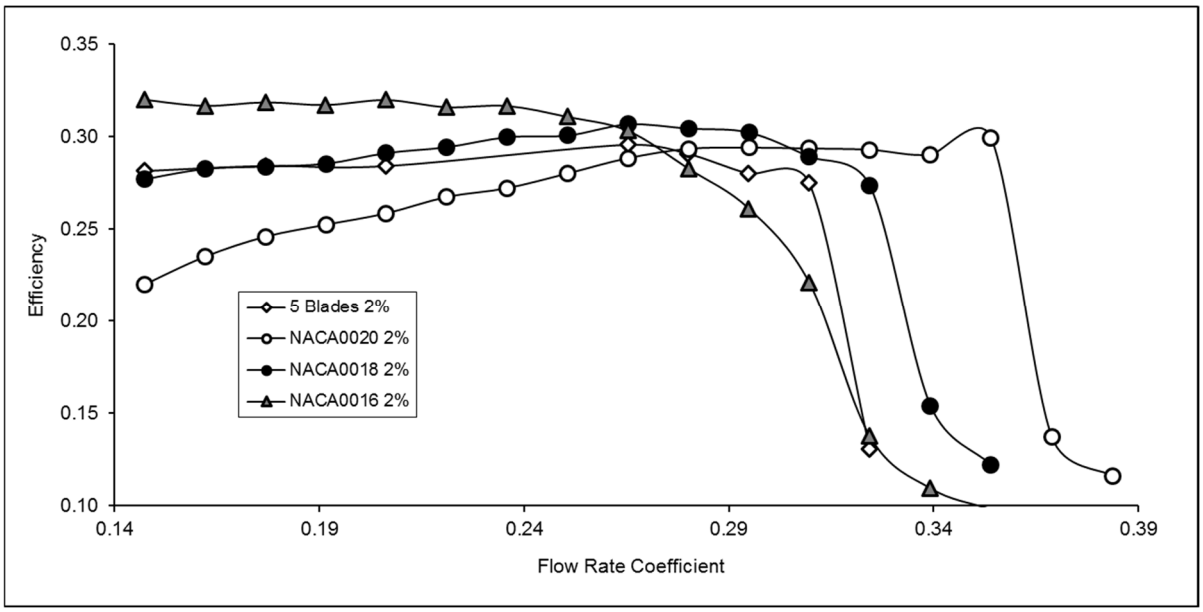

Figure 9-40: Efficiency against flow rate coefficient for varying turbine blade profiles and solidities

Such results demonstrate that in terms of design change, increasing the turbine solidity provides the greatest increase of torque over the equivalent range of flow coefficients. Similar to previous trends, such a design, though providing higher torque values, is seen to stall earlier. Predictably, the turbine pressure drop is also seen to greatly increase with a higher solidity as it creates a greater blockage to flow. Having already mentioned the makeup of the efficiency equation, the resulting efficiency values above are seen to be more in the range of previous designs.

In essence, increasing the turbine solidity, similar to using thinner blade profiles shifts the trends left, thus giving the best performance at lower flow coefficients. Though the shape of the torque results from the higher solidity turbine is near identical to that of the three bladed equivalent, given the higher gradient of the turbine pressure drop, the efficiency trend is observed to be flatter than the 3 bladed equivalent. Observations of how the varying of turbine solidity affects heat transfer and the relationship to mass flow rate towards the generator are shown below.

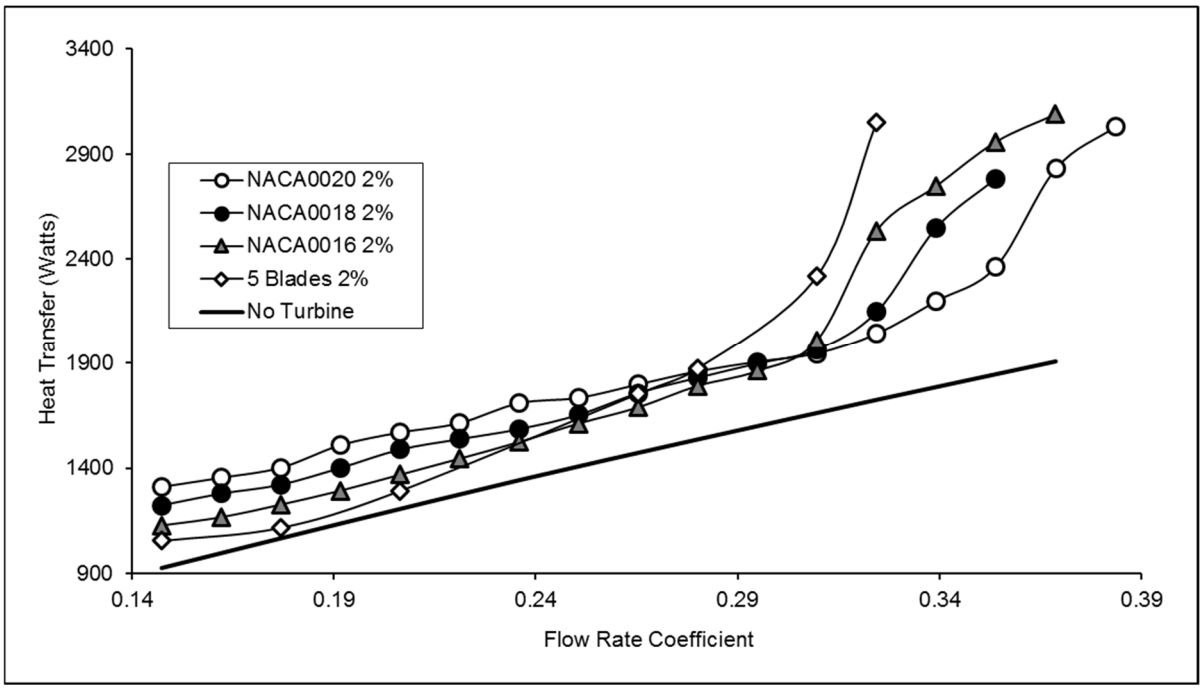

Figure 9-41: Total heat transfer against flow rate coefficient for varying turbine blade profiles and solidities

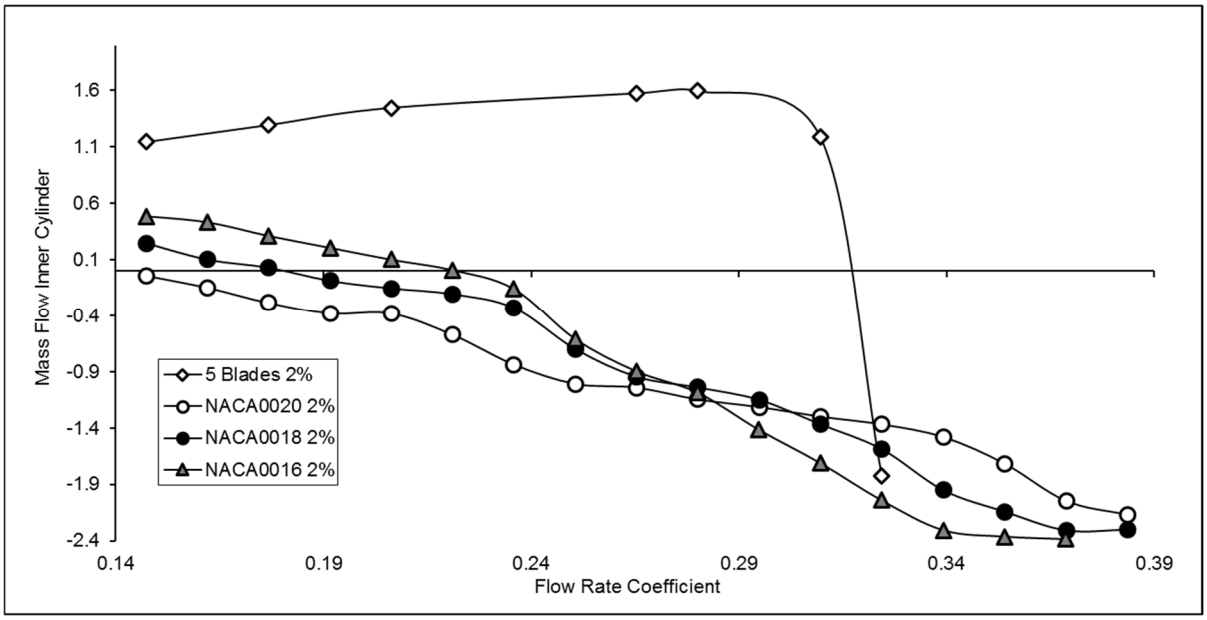

Figure 9-42: Mass flow rate towards generator at inner radius against flow rate coefficient for varying turbine blade profiles and solidities

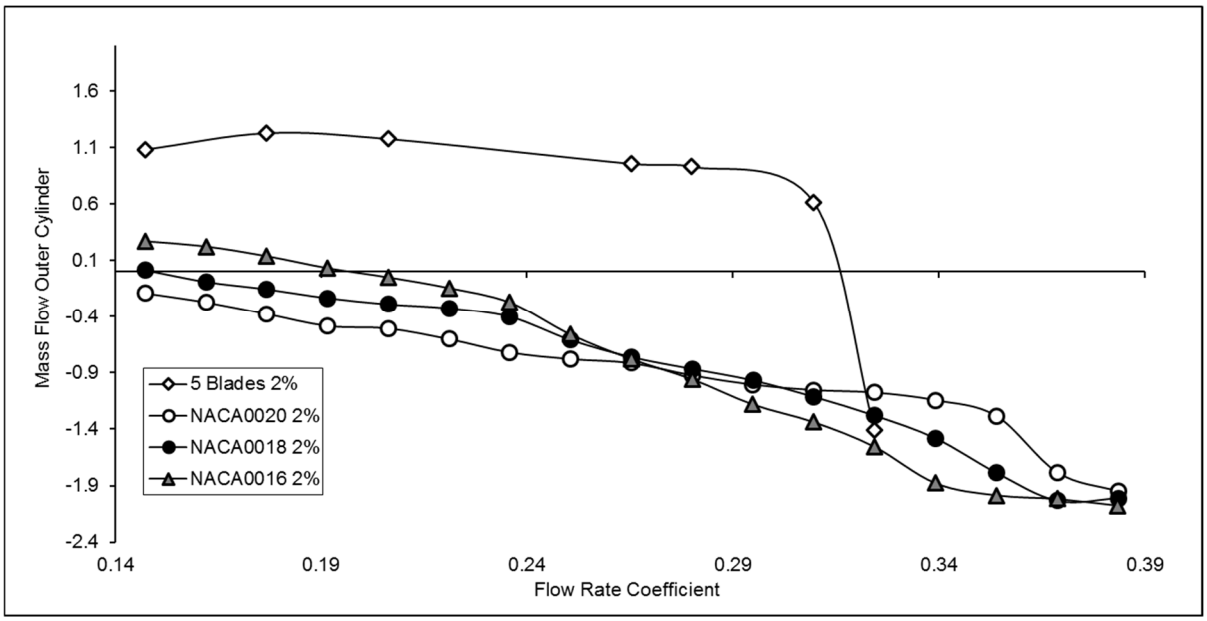

Figure 9-43: Mass flow rate towards generator at outer radius against flow rate coefficient for varying turbine blade profiles and solidities

Figure 9-41 demonstrates that for a given turbine tip clearance, blade profile and hub to tip ratio, an increase in the turbine solidity greatly reduces the heat transfer from the downstream generator. At low flow coefficients the heat transfer remains near constant, whilst at higher coefficients the gradient at which the heat transfer rises, is greater than any of the previous designs. Finally, given that the high solidity turbine has the earliest onset of stall, the peaking in heat transfer is the most prominent for this design.

The difference in the trends of heat transfer for the high solidity design can be understood when considering the mass flow rates towards the generator. In the case of the 5 bladed turbine, unlike the other designs, the overall direction of mass flow in the pre-stall region (as the values are positive) is observed to be outwards. Low flow coefficients are characterised by a low inlet velocity, coupled with a lack of impingement towards the generator this would be severely reduce the airflow velocity in the fin channels and consequently be most detrimental to the heat transfer.

The factors that determine the degree of heat transfer from the generator are understood firstly to be related to the incoming velocity of the airflow, then to the extent of impingement towards the generator and finally to the turbine pressure drop which results in the majority of airflow in the fin channels to be directed backwards towards the turbine.

In the case of the low solidity turbines, the airflow impingement towards the generator is seen to increase with incoming airflow velocity, thereby the heat transfer is observed to rise with the flow rate coefficient. Whilst for the 5-bladed design, at low flow rate coefficients, as seen in figures 9-42 and 9-43, the overall mass flow rate *towards* the generator is reducing despite increasing incoming airflow

velocities, these opposing factors are believed to result in the near constant heat transfer rate observed early on. The phenomena of airflow in the radial direction towards the turbine tips was also found to occur in the simulations conducted by Toressi.

The overall mass flow rate remains positive across the range of flow rate coefficients until the point of stall. Though after exceeding a flow rate coefficient of 0.19 the significant increasing slope of the mass flow rate is observed to cease. Consequently, the amount of heat transfer begins to rise with the increasing incoming airflow velocity. The rate at which the amount of heat transfer increases is certainly higher than any of the 3 bladed designs, this is understood to be due to the much larger turbine pressure drop which more greatly influences the airflow in the fin channels towards the suction (downstream) side of the blades.

With the occurrence of turbine stalling, the rate of heat transfer predictably begins to peak, and is related to an increased impingement of airflow towards the generator characterised by the mass flow rate which begins to rapidly reduce in this region, eventually becoming negative. As in the case of reducing the thickness of aerofoils, the higher solidity turbine shifts the range of highest performance to lower flow rate coefficients. However, the increase in solidity is seen to have a most detrimental impact on downstream generator heat transfer due to the high extent of radial flow towards the turbine tips (rather than towards the centre) as was also found for the high solidity turbine simulated by Torresi *et al.*

Despite the higher torque and therefore power attainable from such popular designs, the negative consequence to generator heat transfer negates the viability of long term high power generation from such a turbine. Such results opened up opportunities to investigate how the turbine simulated by Torresi would affect the heat transfer due to its different hub to tip ratio relative to a 3 bladed turbine of equivalent tip diameter. It would be worthwhile to investigate the independent effect of the hub to tip ratio on heat transfer between turbines of equal solidity. Such designs were indeed investigated across a lesser range of flow rate coefficients nearer the end of the PhD, the results of which will be discussed later in the thesis.

9.6 The effect of varying the rotational speed of the turbine

After establishing that both increasing the solidity and reducing the blade thickness of a turbine would be detrimental to generator performance, the 3 bladed NACA 0020 turbine at a 2% clearance was re-simulated across a shorter range of flow rates comparing results when setting the rotational speed of the turbine at 1500 RPM and 2500 RPM. The results of torque coefficient, turbine pressure drop and efficiency are initially shown in figures 9-44 to 9-46. Subsequently, the results of torque and turbine pressure drop alone are shown for clarification.

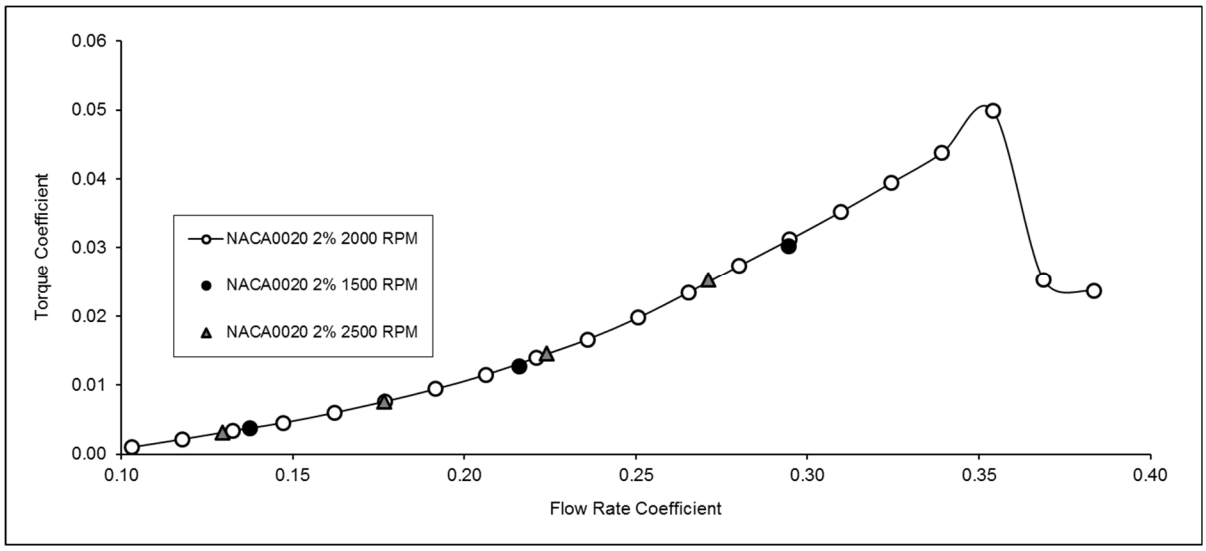

Figure 9-44: Torque coefficient against flow rate coefficient for varying turbine rotational speed

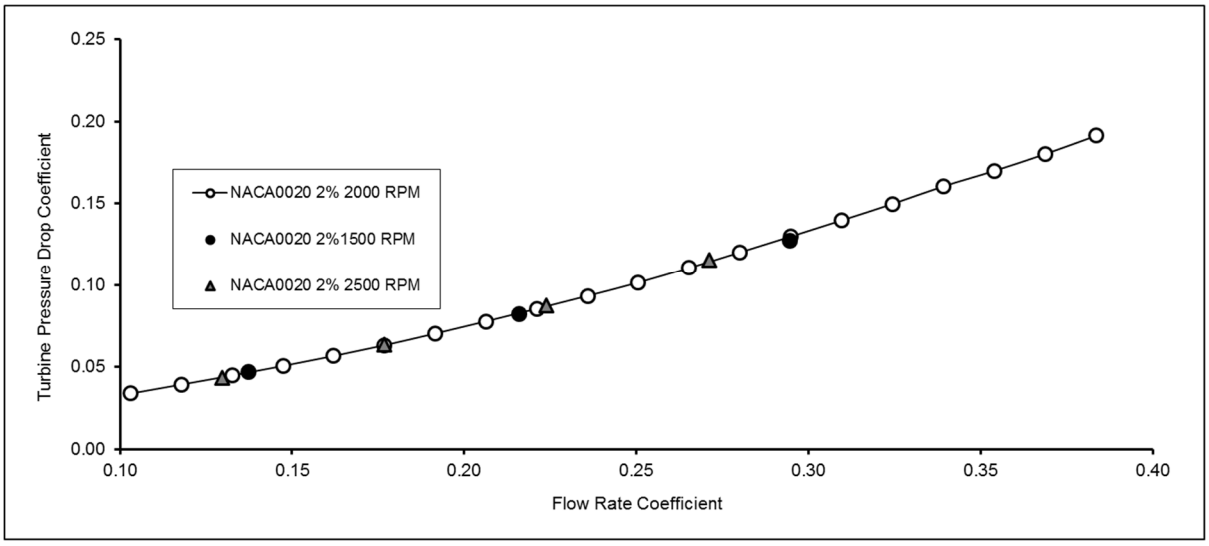

Figure 9-45: Turbine pressure drop coefficient against flow rate coefficient for varying turbine rotational speed

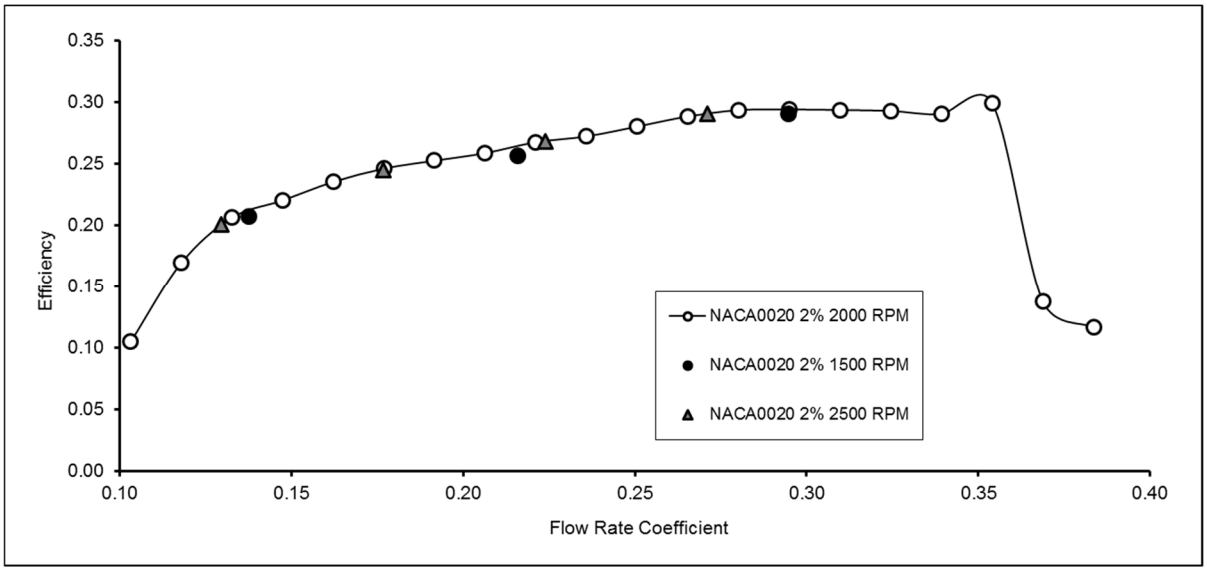

Figure 9-46: Efficiency against flow rate coefficient for varying turbine rotational speed

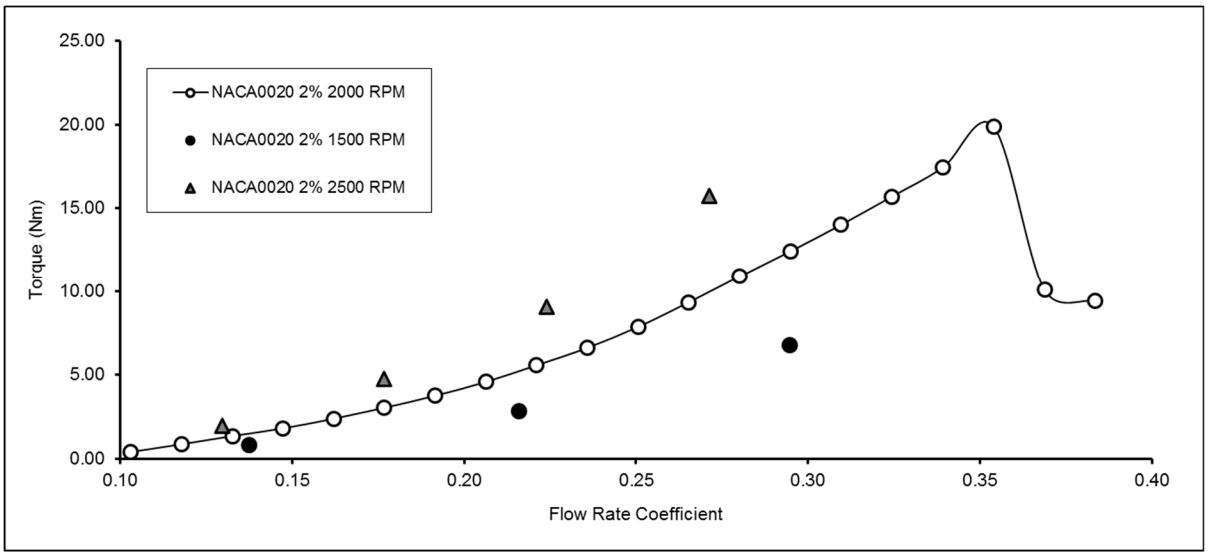

Figure 9-47: Torque against flow rate coefficient for varying turbine rotational speed

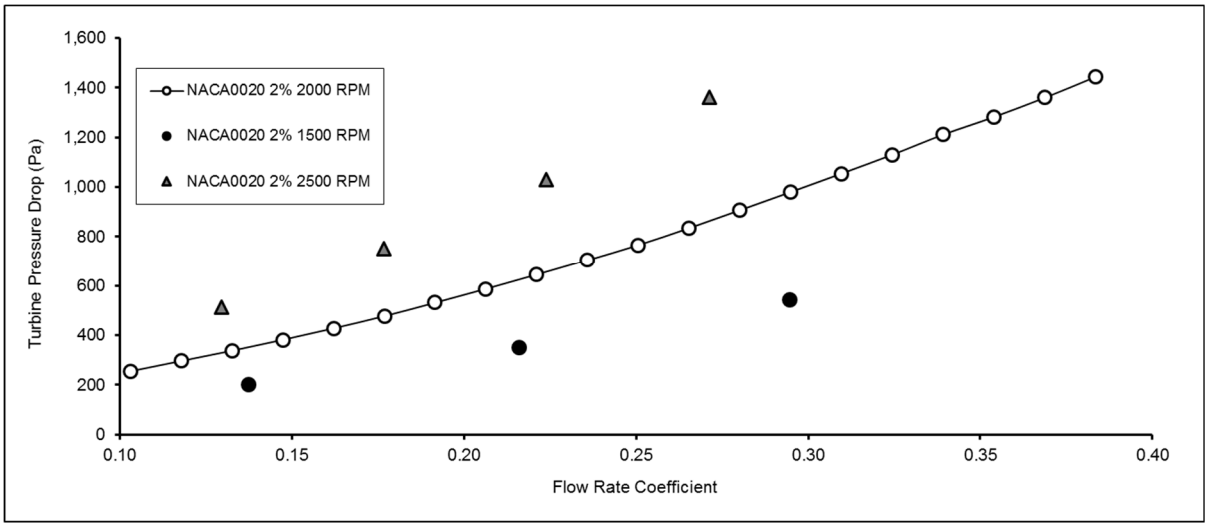

Figure 9-48: Turbine pressure drop against flow rate coefficient for varying turbine rotational speed

The results across varying flow rate coefficients were observed to remain on the same trend line, as is expected given that the equations for the torque and pressure drop coefficients take into account the rotational speed. The actual torque and turbine pressure drop are seen to increase with angular velocity as seen in figures 9-47 and 9-48, whilst to maintain the flow rate coefficient, the flow rate (Q) must increase with angular velocity. As these four variables constitute the efficiency equation, they ultimately balance each other out such that the efficiency trend remain consistent. Observations of how the varying the angular speed of the turbine affects the heat transfer and the relationship to mass flow rate towards the generator are shown figures 9-49 and 9-50 below.

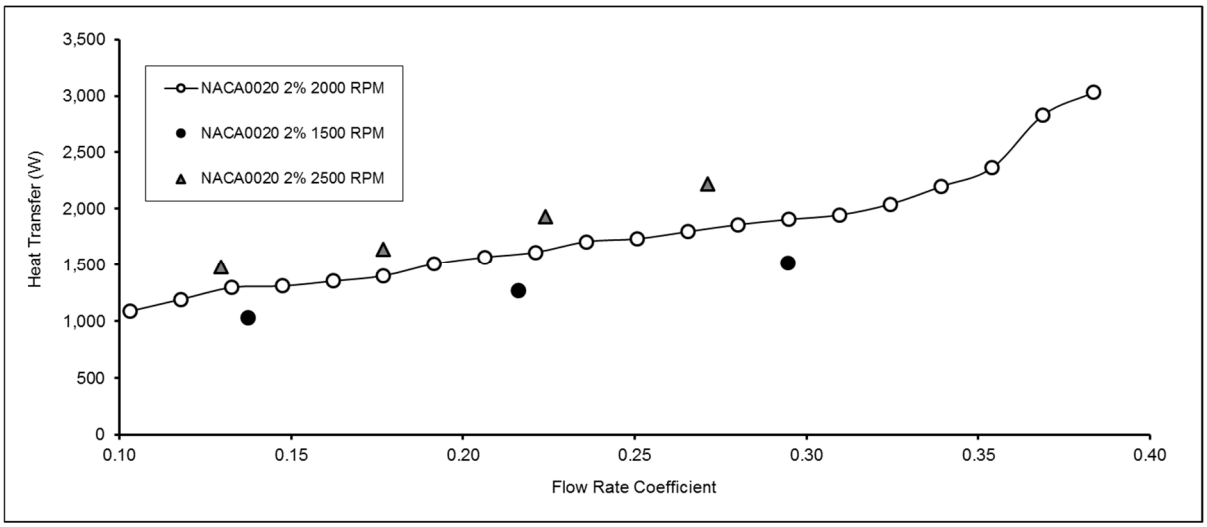

Figure 9-49: Total heat transfer against flow rate coefficient for varying turbine rotational speed

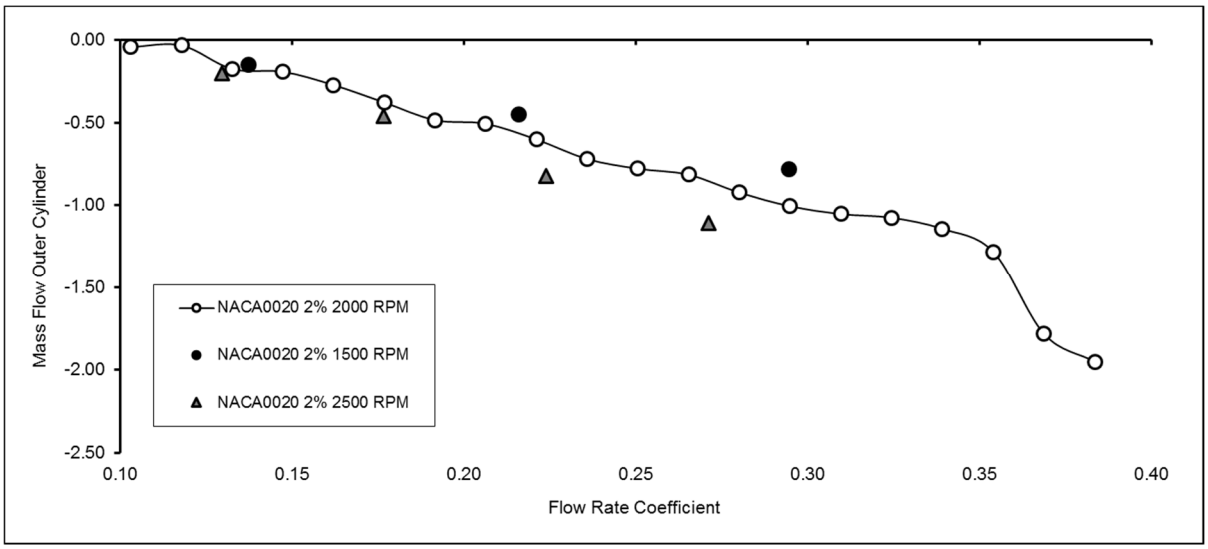

Figure 9-50: Mass flow rate towards generator at outer radius against flow rate coefficient for varying turbine rotational speed

At equivalent flow rate coefficients the extent of heat transfer from the downstream generator is greater for a turbine rotating at a higher angular velocity. The trend of flow rates towards the generator is seen to correlate with such results. Previous heat transfer results were observed against the presumption of purely axial flow past the finned generator. However, such a result assumes a fixed rotational speed of 2000 RPM for all results. As such, to compare heat transfer results from a generator cooling under purely axial flow against one that is cooling via airflow impingement due to an upstream turbine at varying angular velocities, the x-axis can be defined by the value of incoming velocity as seen in figure 9-51 below.

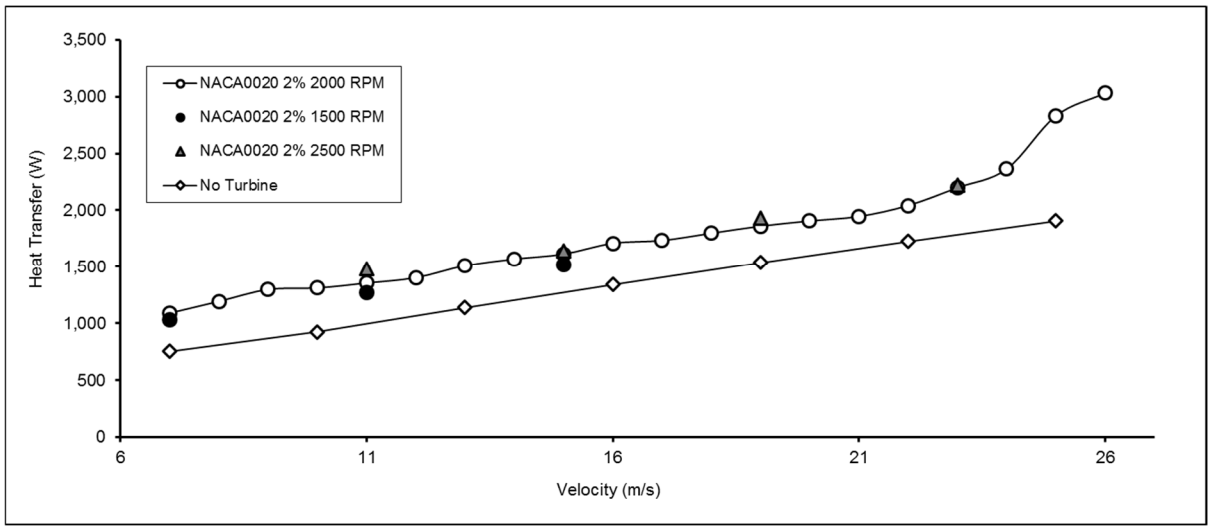

Figure 9-51: Total heat transfer against incoming air velocities for varying turbine rotational speed

As both variables affect the heat transfer independently, thus the same heat transfer rate of 1500 W is seen to be maintained when increasing the flow velocity by simultaneously decreasing the blade tip speed. The variation of turbine angular velocity at 1500 RPM, 2000 RPM and 2500 RPM gives turbine tip speeds of 58.82 m/s, 78.5 m/s and 98.12 m/s respectively.

From figure 9-51 it is clear that the incoming flow velocity has a far greater effect on the extent of heat transfer than does the angular velocity of the turbine. By the combination of these variables each aerofoil blade can be understood as experiencing a resultant airflow velocity at a given angle of attack. The flow rate coefficient is ultimately the inverse of the angle of attack experienced by a turbine blade. The variation of the incoming airflow velocity acts to increase to angle of attack up to the point of stall, but has a far lesser influence on the resultant velocity, which increases from 78.81m/s to 82.69 m/s when the turbine is rotating at 2000 RPM.

The above results may suggest that for a given design and scale, the heat transfer from the generator is in fact only dependent on the two variables of effective freestream (resultant) velocity and angle of attack (flow rate coefficient). The equations in section 7.2 demonstrated that the heat transfer and frictional coefficients over a flat plate were ultimately functions of the Reynolds and Prandtl numbers. This opens an opportunity to investigate the same geometry at different scales at the same angle of attack, observing whether Reynolds number (comprising of the resultant velocity and a characteristic length of the turbine) can be related to the Nusselt number (comprising of the heat transfer coefficient and characteristic length of the generator).

10.0 CONCLUSIONS AND FURTHER WORK

10.1 Contribution to knowledge

This PhD has been driven by gaps in knowledge regarding the cooling of electrical machines that operate in the turbo generation section of an oscillating water column. The generators used in such wave power devices are often purchased "off-the-shelf" without considerations for the planned OWC environment. Such generators are designed to be cooled by air which flows axially through the fin channels, often due to an in-built fan which is driven by rotor motion, and is the basis for the defined power rating.

The consequences of airflow impingement on the cooling of the generator are not known and therefore not taken into account by today's designers of OWCs wave energy devices. Downstream of the Wells turbine, air does not necessarily flow axially past the generator. Instead, this work has shown that the presence of the turbine may result in airflow impingement around the generator. The design of the Wells turbine in terms of tip clearance, profile and solidity, would normally be chosen with a primary focus on aerodynamic efficiency in the given operating environment of the OWC.

This PhD work has shown that certain Wells turbine designs may improve the total extent of cooling, thereby allowing for a greater potential power output without overheating the generator. Whilst other designs, though advantageous for turbine efficiency, could be detrimental to the heat transfer, reducing the lifetime of the generator. Consideration of the findings from this work by designers of OWC wave power devices would therefore be beneficial to maximise power generation, as well as reduce maintenance costs.

Finally, the Wells turbine used in the LIMPET OWC was 2.6m in diameter, whilst the turbine in this work was 0.75m in diameter, and was based on the dimensions of the experimental test-rig used for investigating prototype equipment. Hence results using these dimensions would certainly be of significance, given that they were considered sufficient to test prototype equipment.

10.2 Main findings of this PhD

This PhD involved computation fluid dynamic simulations of finned generators cooling under forced convection in an oscillating water column environment. Various design changes to the upstream Wells turbine and its effect on the consequent cooling of the generator were investigated. Analytical correlations for the heat transfer coefficient across flat plates and within fin channels due to forced convection under laminar and turbulent flow conditions could also be used to validate the CFD results for given freestream velocities.

Prior to the CFD modelling, an analytical model was created to compare the average heat flux and total heat transfer across smooth and finned generators for increasing airflow velocities. The diameter and

fin dimensions of the generators used in the analytical models were based on an 18.5kW prototype induction generator undergoing experimental testing in the turbo generation section of the LIMPET Oscillating Water Column device.

Though the heat equations assume turbulent flow through the fin channels, in the case of flat housings an assumption can be made as to whether a turbulent boundary layer develops from an initial laminar boundary layer, or the flow is purely turbulent across the entire generator, providing greater heat transfer. Comparing heat values between a finned generator and that of a smooth generator under purely turbulent flow, the level of heat transfer from the finned generator is seen to prevail, so long as the flow velocity within the fin channels of the generator remains higher than 33% of the free-stream velocity. The analytical model also demonstrated that increasing the fin height was found to raise the heat flux whilst reducing the fin spacing led to a reduction.

Initial CFD simulations of the finned generator were performed to determine the effect of upstream and downstream attenuators. The addition of such attenuators, were found to increase the heat transfer by allowing the airflow to enter the fin channels purely axially, with a minimal of leakage flow. The average axial velocity through the fin channels from the CFD simulations was used to calculate analytically the average heat transfer coefficient within the fin channels. The deviation in the average heat flux was 2.86%, whilst the deviation in the total heat transfer was 6.9%. The reasoning for the deviations of heat flux and heat transfer were understood as follows. The velocity is seen to have a slight outward radial (leakage) component, especially after entry into the fin channels, whereas the heat equations assume a constant axial velocity. Heat transfer from the fin tips are considered in the CFD simulations, whereas the analytical equations only account for the fin channels. Despite the leakage flow, the axial velocity of airflow within the fin channels was not seen to fall below 65% of the free-stream velocity, ensuring the viability of the finned design.

The analytical model demonstrated that for a given velocity within the fin channels, the heat flux increases with fin height, reaching a maximum and then reducing. This means that although the addition of fins raises heat transfer due to the increase in surface area, the fin dimensions are also important in that there is an optimal fin height to maximise heat flux, independent of surface area. For constant dimensions, the maximum heat flux was seen to reduce with increasing channel velocity. For a free-stream value of 10 m/s, the optimal fin height is 21mm, sufficiently close to the specified value of the generator.

Having established the best layout of the generator for heat transfer in cases of convention axial flow, further CFD modelling was performed to investigate the effect of an upstream Wells turbine, and the consequent impinging airflow. The clearance between of the turbine tips and outer shroud was set at 10% of the blade cord-length. The results for the smooth housing revealed very high values of heat flux where the impingement was greatest, whilst the presence of fins was found to force air to flow axially

in the channels immediately, the additional degree of freedom over the smooth housing allowed for a larger heat dissipation area and higher heat flux values therein.

Comparing the four scenarios, of axial against impinging airflow, for both smooth and finned generators. The generator with a smooth housing experienced a greater net improvement in heat transfer when encountering impinging flow, however overall, the generator with a finned housing outperformed the smooth in both scenarios of airflow.

Focussing on the finned generator, during impingement, the magnitude of airflow velocities are higher than in the cases of no turbine, along the majority of the generator length, especially in the top fin channel. However despite airflow impingement providing better cooling, it results in a greater difference between the highest and lowest values of heat flux across the generator casing. Such low values of heat flux are more prominent on the generator undergoing impingement and can lead to greater instances of hotspots in the stator windings, which is a consequence of the presence of the rotating turbine. The emphasises the importance of understanding the operational environment when designing a generator for a wave energy convertor.

Having established the increased cooling effect of an upstream Wells turbine as well as the preference of a finned generator, the remainder of CFD simulations investigated changes to the Wells turbine design. The effect of reducing tip clearance was investigated and found to increase the turbine torque, pressure drop and efficiency. The heat transfer from the generator also increased as a greater mass flow rate of air flowed radially towards the generator.

The torque results were compared with CFD simulations of a high solidity Wells turbine conducted by Toressi *et al* (2008), in which a very fine mesh was used with the Spalart-Almaras turbulence model, such work was an update to earlier work by Toressi (2004) in which the K-Omega SST turbulence model was used but with a much coarser mesh. The current PhD work also used the K-Omega SST turbulence model, and results by Toressi revealed a similar over-prediction of peak torque just prior to turbine stall.

The torque values obtained by Toressi *et al* (2008) for the 1% clearance, validated against the results from Curran and Gato, were reproduced with the equivalent mesh and turbulence model used in this PhD work. Should the results obtained be similar to the published results, it would stand to reason that the results of this PhD, modelling the flow downstream of a Wells turbine, would also be viable. The K-Omega SST turbulence model results matched very well with the results of Curran and Gato, suggesting the accuracy of the results by Toressi *et al* were due to the refinement of the mesh, rather than the choice of turbulence models.

Having established the viability of the mesh and turbulence model used in this PhD work, the effect of varying the turbine blade thickness was investigated. The result was an increase in turbine torque and

efficiency, whilst the heat transfer from the generator was observed to reduce. The profile changes had a negligible effect on turbine pressure drop, and though there was an increase in performance, the turbine was seen to stall earlier, such findings were corroborated with experimental results obtained by NACA for thick and thin symmetrical aerofoils. Upon turbine stalling, the heat transfer from the generator was seen to peak, both the overall reduction and peaking in heat transfer were observed to correlate with reducing and increasing rates of airflow, directed radially towards the generator.

The final design change to be investigated was the solidity of the turbine. The original 3 bladed design had a solidity of 0.371, by reducing the cord-length, the number of blades was increased to 5, resulting in a solidity of 0.463. The blade profile was maintained at NACA0020. The result was an increase in turbine torque and pressure drop, and the rise in turbine efficiency approached that achieved by the NACA0018 turbine, but the stall point was slightly earlier. Under the high solidity design, the heat transfer from the generator was observed to be the lowest. The results revealed a net radial flow of air toward the turbine tips rather than the generator, a phenomenon also noted by Toressi *et al.*

After establishing that both increasing the solidity and reducing the blade thickness of a turbine would be detrimental to generator performance, the 3 bladed NACA20 turbine at a 2% clearance was re-simulated across a shorter range of flow rate coefficients, at a higher and lower turbine rotational speed of 1500 RPM and 2500 RPM respectively. The results in terms of the coefficients of turbine torque, pressure drop and consequent efficiency were consistent with the previous results obtained for a rotational speed of 2000 RPM. However the absolute values of turbine torque and pressure drop, were found to be higher and lower, at equivalent flow rate coefficients, for increasing and reducing turbine rotational speed.

The rate of heat transfer from the generator varies in a similar fashion with changes to the turbine rotational speed. As expected, the increases in heat transfer, were seen to correlate with increased rates of mass flow towards to the generator. However, altering the x-axis to the inlet velocity, revealed that the changes in heat transfer due to the turbine rotational speed were very minor as compared to the effects of increasing incoming airflow.

Finally, the investigations into the effects of various turbine designs on the cooling of the downstream generator revealed trends such that, by increasing the thickness of the blade profile from NACA0016 to NACA0020, reducing the turbine tip clearance from 10% to 2% of blade cord length, and even reducing the solidity of the turbine from 5 blades to 3 blades, in each case, the generator can safely be pushed to generate more power, beyond its original rating, to where it produces, on average, 33% extra heat losses.

10.3 Recommendations for further work

After this PhD, there still remain areas of further work, which could not be completed due to time and computational restrictions. In terms of design changes to the Wells turbine, the effect of the hub to tip ratio was not investigated, indeed, the effect of higher solidity was investigated without changing the hub to tip ratio. Higher solidity turbines were shown to be more suited to lower flow rate coefficients, and the hub to tip ratio is generally reduced to incorporate further blades. Given that a higher solidity was found to reduce airflow impingement, it would prove important to investigate the effect of changing the hub to tip ratio, both independently, as well as due to a change in solidity.

In the case of this PhD work, to incorporate more blades into the turbine, the cord-length was reduced, however, the clearance of the turbine tip was maintained at 2% of the original blade cord-length. The difference was minor, the true tip clearance in the case of the high solidity turbine was effectively 2.67% of the cord-length. Additional work may investigate the significance of this difference.

It was found that for a given turbine design, the heat transfer from a downstream generator was influenced by both the incoming velocity as well as the turbine rotational speed, and unlike the turbine performance, could not be characterised purely by the flow rate coefficient. Instead it appeared that the heat transfer may be a combined function of a resultant velocity and angle of attack.

Further work would need to be done in taking a dimension of the turbine as a characteristic length, and investigating at different scales, to reveal whether the heat transfer can indeed be defined as a function of a Reynolds number and angle of attack. It terms of understanding the scalability of the entire OWC, as opposed to only the turbo generation section, due to the effects of gravity and air compressibility in the capture chamber, this would require much more in-depth work in terms of the Froude number as well as the Reynolds number, and is beyond the scope of this thesis.

Additional work could also be done in investigating the extent to which the effects of reversed flow propagate upstream from the pressure outlet boundary. In subsequent simulations, the outlet boundary could be positioned further downstream to determine how much impact, if any, the occurrence of reversed flow at the outlet had on the rate of heat transfer from the generator.

All the simulations conducted in this PhD work were performed using RANS turbulence modelling due to limitations in the available computing power. As access to high performance computing clusters becomes more feasible, further work may be done in simulating the turbo generation section of the oscillating water column, without the use of turbulence modelling. The improved accuracy of these results could be compared with those achieved with the “industrial standard” turbulence models. With the ability to perform highly accurate unsteady simulations, a final goal would therefore be to simulate the generator cooling over time, with a sinusoidal velocity inlet condition, and compare the trends of heat transfer against those achieved in this thesis. Additionally, using a heat flux boundary condition on

the inside wall of the generator casing, a temperature distribution across the generator casing could be obtained.

BIBLIOGRAPHY

Alberti, L. & Bianchi, N., (2008), "A coupled thermal-electromagnetic analysis for a rapid and accurate prediction of IM performance," *IEEE Transactions on Industrial Electronics*, 55 (10), p3575-3582

Alternative Energy Tutorials, (2015), "Wave Profile Devices". [image], Available: http://www.alternative-energy-tutorials.com/wave-energy/wave-energy-devices.html, Accessed December 2015

Anderson, J. D., (2011), "Fundamentals of Aerodynamics SI Paperback", New York: McGraw-Hill Higher Education

Avstop, (2015), "Momentum Influences Airflow Over an Airfoil". [image], Available: http://avstop.com/ac/flighttrainghandbook/lowpressureabove.html, Accessed December 2015

Baer, W., (2015), "Circulation". [image], Available: http://www.woseba.de/02_subsonic_stream_&_lift.html, Accessed December 2015

Benecke, W., (1966), "Temperature field and heat flow in case of small surface cooled three-phase motors with squirrel cage rotor", *ETZ (A)*, 87, (13)

Blasius, H., (1908), "The Boundary Layers in Fluids with Little Friction (in German)" *Z. Math. Phys*., 56 (1), p1–37;

Boglietti, A., (2009), "Evolution and Modern Approaches for Thermal Analysis of Electrical Machines", *IEEE Transactions on Industrial Electronics*, 56 (3), p871-882

Bryden, I., (2009), P02884 [Lecture notes], "Introduction to Wave Energy", Marine Energy 5, Institute for Energy Systems, University of Edinburgh

Burchell, J. (2009), "CFD modelling of an induction generator in an oscillating water column wave energy device to assess heat transfer", Dissertation, (MSc), University of Edinburgh, UK

Burdekin, M.; Crossland, B., (2007), "Alan Arthur Wells. 1 May 1924 -- 8 November 2005: Elected FRS 1977". *Biographical Memoirs of Fellows of the Royal Society,* 53 (365)

Carbon Trust, (2005), "Variability of UK marine resources", Environmental Change Institute, University of Oxford, Available: http://www.marinerenewables.ca/wp-content/uploads/2012/11/Variability-of-UK-marine-resources.pdf, Accessed December 2015

CD-Adapco, (2011), "User Guide STAR-CCM+ Version 6.04.014", Melville, New York

Cengel, Y.A. & Ghajar, A. J., (2011), "Heat and Mass Transfer (in SI Units) Paperback", New York: McGraw-Hill Higher Education

CFD-Online, (2011), “Img lawOfTheWall whiteBG”. [image], Available: http://www.cfd-online.com/Wiki/File:Img_lawOfTheWall_whiteBG.png, Accessed December 2015

Chong, Y., (2015), “Thermal Analysis and Airflow Modelling of Electrical Machines”, Thesis, (PhD), University of Edinburgh, UK

Commutant, (2011), “PDE 2 | Three fundamental examples”. [video], Available: https://www.youtube.com/watch?v=DDPO-19FyJM, Accessed December 2015

Connor, P., (2013), “Computational Fluid Dynamics Modelling of a Synchronous Electric Generator”, Thesis, (PhD), University of Nottingham, UK

Crown Estate, (2012), “UK Wave and Tidal Key Resource Areas Project Summary Report, Technical report”, Available: http://www.thecrownestate.co.uk/media/5476/uk-wave-and-tidal-key-resource-areas-project.pdf, Accessed December 2015

Curran, R. & Gato, L. M. C., (1997), “The energy conversion performance of several types of Wells turbine designs”, *Journal of Power and Energy*, 211 (2), p133–145

Department for Business, Energy & Industrial Strategy (BEIS), (2017), “Digest of UK Energy Statistics”, Available: https://www.gov.uk/government/statistics/energy-chapter-1-digest-of-united-kingdom-energy-statistics-dukes, Accessed November 2017

Department of Trade and Industry (now BERR), (2001), “The UK wind resource, Wind Energy Fact Sheet 8”, Available: http://www.berr.gov.uk/files/file17789.pdf, Accessed December 2015

Department of Trade and Industry, (2002), “Islay Limpet Project Monitoring Final Report”, Available: http://www.wavegen.co.uk/pdf/art.1707.pdf

Department for Trade and Industry, (2004), “Atlas of UK Marine Energy Renewable Resources”, Available: http://www.dti.gov.uk/renewables/publications/pdfs/annualmeanwavepower.pdf, Accessed December 2015

Dhanasekaran, T. S. & Govardhan, M., (2005), “Computational analysis of performance and flow investigation on wells turbine for wave energy conversion”, *Renewable Energy,* 30, p2129-2147

Dipprey, D. F. & Sabersky, D. H., (1963), “Heat and Momentum Transfer in Smooth and Rough Tubes at Various Prandtl Numbers”, *International Journal of Heat Mass Transfer,* 6 (5), p329–353

Dorrell, D. G.; Staton, D. A.; Hahout, J.; Hawkins, D.; McGilp, M. I., (2006) “Linked Electromagnetic and Thermal Modelling of a Permanent Magnet Motor”, *IEEE PEMD, Dublin, Ireland,*p536-540, Available: http://www.motor-design.com/cmsAdmin/uploads/pemd_2006_servo_motor_thermal_analysis.pdf, Accessed December 2015

Evans, W., (2016), “UK Energy Statistics”, Available: https://www.gov.uk/government/uploads/system/uploads/attachment_data/file/642716/Chapter_1.pdf, Accessed November 2017

Federal Ministry for the Environment, Nature Conservation and Nuclear Safety, Germany, (2006), “Renewable Energy: Employment Effects”, Available: http://www.bmu.de/files/pdfs/allgemein/application/pdf/employment_effects_061211.pdf

Fitzpatrick, R., (2012), “Boundary Layer Separation”. [image], Available: http://farside.ph.utexas.edu/teaching/336L/Fluidhtml/node90.html, Accessed December 2015

Folley, M.; Curran, R.; Whittaker, T., (2006), “Comparison of LIMPET contra-rotating wells turbine with theoretical and model test predictions”, *Ocean Engineering*, 33 (8-9), p1056–1069

Heiles, F., (1952), “Design and Arrangement of Cooling Fins”, *Elecktrotecknik und Maschinenbay*. 69 (14), p42-48.

Hodgins, N. (2009), “High Speed Electrical Power Takeoff for Oscillating Water Columns”, Thesis, (PhD), University of Edinburgh, UK

IEA, (2017), “Renewables 2017”, Available: https://www.iea.org/publications/renewables2017, Accessed November 2017.

Jacobs, E. N.; Ward, K. E.; Pinkerton, R, M., (1935), “The Characteristics of 78 Related Airfoil Sections from Tests in the Variable-Density Wind Tunnel”, *National Advisory Committee for Aeronautics (NACA)*, Report No. 460

Kim, T. H.; Setoguchi, T.; Kaneko, K.; Raghunathan, S., (2002), “Numerical investigation on the effect of blade sweep on the performance of Wells turbine”, *Renewable Energy*, 25 (2), p235-248

Kinoue, Y.; Setoguchi, T.; Kim, T. H.; Kaneko, K., (2003), “Mechanism of Hysteretic Characteristics of Wells Turbine for Wave Power Conversion”, *Journal of Fluids Engineering*, 125, p302-307

Knowles, E., (1997), “Introductory Oceanography, Chapter 10 – Ocean Waves”, North Carolina State University, Available: http://www4.ncsu.edu~ceknowle/Envisions/chapter10copy/index.html, Acessed December 2015

Kovalev, E.B.; Burkovski, A.N.; Tokarenko, A.T., (1965), “Heat transfer in channels between frame-ribbing of enclosed asynchronous motors”, *Elektrotechnika*, 11

Kuczaj, A.K.; Komen, E.M.J.; Loginov, M.S., (2010), “Large-Eddy Simulation Study of Turbulent Mixing in a T-Junction”, *Nuclear Engineering and Design*, 240 (9), p2116–2122

Lampard, D.; Mugglestone, J.; Pickering, S.J., (1997), "Effects of end winding porosity upon the flow field and ventilation losses in the end region of TEFC induction motors", *Eighth International Conference on Electrical Machines and Drives, (Conf. Publ. No. 444)*, Available: http://ieeexplore.ieee.org/xpl/articleDetails.jsp?reload=true&arnumber=676935, Accessed December 2015

Lewis, D. (2017), "Salt, silicon or graphite: energy storage goes beyond lithium ion batteries" *The Guardian*, 6 April, [Online], Available: https://www.theguardian.com/sustainable-business/2017/apr/06/salt-silicon-or-graphite-energy-storage-goes-beyond-lithium-ion-batteries, Accessed: February 2018

Liao, C.; Chen, C.L.; Katcher, T., (1999), "Thermal Management of AC Induction Motors Using Computational Fluid Dynamics Modelling", *Institute of Electrical and Electronics Engineers, (IEEE)*, p189-191

Liptak, B., (2007), "Ocean wave energy collection design. Courtesy of World Energy Council – WEC". [image], Available: http://www.controlglobal.com/articles/2007/195, Accessed December 2015

Liu, Z.; Winter, T.; Schier, M., (2015), "Comparison of Thermal Performance between Direct Coil Cooling and Water Jacket Cooling for Electric Traction Motor based on Lumped Parameter Thermal Network and Experimentation" *International Electric Vehicle Symposium and Exhibition (EVS28),* Kintex, Korea

Mamun, M., (2006), "The Study on the Hysteretic Characteristics of the Wells Turbine in a Deep Stall Condition", Thesis, (PhD), Saga University, Japan

Maughan, J. R. & Incropera, F. P.,(1990), "Mixed Convection Heat Transfer With Longitudinal Fins in a Horizontal Parallel Plate Channel: Part II—Experimental Results", *Journal of Heat Transfer*, 112 (3), p619-624

Metservice, (2015), "Statistical Wave Distribution". [image], Available: http://blog.metservice.com/wp-content/uploads/2015/03/Fig-6.png, Accessed December 2015

MH-Aerotools, (2004), "Pressure force distribution the surface of the Eppler E 64 airfoil at 2 degrees angle of attack". [image], Available: http://www.mh-aerotools.de/airfoils/velocitydistributions.htm, Accessed December 2015

Micallef, C.; Pickering, S. J.; Simmons, K. A.; Bradley, K. J., (2008), "Improved cooling in the end region of a strip-wound totally enclosed fan-cooled induction electric machine", Transactions on Industrial Electronics, 55 (10), p3517-3524

Mills, A. F., (1999), “Heat Transfer”, New Jersey: Prentice-Hall

Nathan, P., (2011), “Airfoil starting vortex”. [video], Available: https://www.youtube.com/watch?v=B-tcx5hTf_A, Accessed December 2015

Nptelhrd, (2012), “Mod-06 Lec-35 Derivation of the Reynolds -averaged Navier-Stokes equations”. [video], Available: https://www.youtube.com/watch?v=4vSxxSzIuNU, Accessed December 2015

OWCwaveenergy, (2010), “Wells Turbine Demonstration”. [image], Available: http://owcwaveenergy.weebly.com/our-demonstrations.html, Accessed December 2015

Petukhov, B. S., (1970), “Heat Transfer and Friction in Turbulent Pipe Flow with Variable Physical Properties”, *Advances in Heat Transfer*, 6, p503-564

Pickering, S. J.; Lampard, D.; Shanel, M., (2001), “Modelling ventilation and cooling of the rotors of salient pole machines,” *IEEE International Electric Machines & Drives Conference (IEMDC),* Cambridge, MA, p806-808

Queens University Belfast, (2002), “Islay LIMPET wave power plant”, Available: http://www.wavegen.co.uk/pdf/LIMPET%20publishable%20report.pdf

Raghunathan, S. & Ombaka, O. O., (1984), “The Wells turbine in an oscillating air flow”, *Advanced energy systems - Their role in our future; Proceedings of the Nineteenth Intersociety Energy Conversion Engineering Conference (IECEC)*, San Francisco, CA, 1, p7-12

Raghunathan, S. & Ombaka, O.O., (1985), “Effect of frequency of air flow on the performance of the Wells turbine”, *International Journal of Heat and Fluid Flow*, 6 (2), p127-132

Raghunathan, S., (1995). “The Wells Air Turbine for Wave Energy Conversion”, *Progress in Aerospace Sciences*, 31 (4), p335-386

Raghunathan, S. & Watterson, J. K., (1996), “Investigation of Wells Turbine Performance using 3-D CFD”, *IEEE Xplore, Proceeding of the 31st Intersociety, Energy Conversion Engineering Conference*, Washington, DC, p1777-1782

Renewable Energy Policy Multi-Stakeholder Network (REN21), (2017), “Renewables 2017 Global Status Report”, Available: http://www.ren21.net/status-of-renewables/global-status-report, Accessed November 2017

Roache, P.J., (1998), “Verification and Validation in Computational Science and Engineering”, Albuquerque: Hermosa Publishers

Sahin, B. & Demir, A., (2008). “Performance Analysis of a Heat Exchanger Having Perforated Square Fins”, *Applied Thermal Engineering*, 28 (5-6), p621-632

Schmitt, F.G., (2007), "About Boussinesq's turbulent viscosity hypothesis: historical remarks and a direct evaluation of its validity", *Comptes Rendus Mécanique,* 335 (9–10), p617–627

See,Y.; Hahn, S.; Kauh, S., (2000), "Thermal analysis of induction motor with forced cooling channels", *IEEE Transactions on Magnetics*, 36 (4), p1398-1402

Shaeri, M.R. & Yaghoubi, M., (2009), "Numerical Analysis of Turbulent Convection Heat Transfer from an Array of Perforated Fins", *International Journal of Heat and Fluid Flow*, 30 (2), p218-228

Shengtai, Li. & Hui, Li., (2006), "Parallel AMR Code for Compressible MHD or HD Equations". [image], Available: http://math.lanl.gov/Research/Highlights/amrmhd.shtml, Accessed November 2017.

Sparrow, E.M. & Kadle, D.S., (1986), "Numerical and Experimental Study of Turbulent Heat Transfer and Fluid Flow in Longitudinal Fin Arrays". *Journal of Heat Transfer*, 108 (1), p16-24.

Spiegel, M. R.; Lipschutz, S.; Spellman, D., (2009), "Vector Analysis. Schaum's Outlines", New York: McGraw-Hill Higher Education

Staton, D.; Boglietti, A; Cavagnino, A., (2005), "Solving the more difficult aspects of electric motor thermal analysis in small and medium size industrial induction motors", *IEEE Trans. Energy Convers*, 20 (3), p620-628

Staton, D. & Cavagnino, A., (2008), "Convection heat transfer and flow calculations suitable for electric machines thermal models", *IEEE Transactions on Industrial Electronics*, 55 (10), p3509-3516

Sustainable Energy Ireland, (2002), "Options for the Development of Wave Energy in Ireland: A Public Consultation Document", Available: http://www.sei.ie/uploadedfiles/InfoCentre/wave.pdf, Accessed December 2015

Tapered Channel Wave Energy, (2010), "TAPCHAN. Photo courtesy of Boyle, 1996". [image], Available: http://taperedchannelwaveenergy.weebly.com/, Accessed December 2015

Tease, W. K., (2003), "Dynamic Response of a Variable Pitch Wells Turbine", Available: http://s3.amazonaws.com/zanran_storage/www.wavegen.co.uk/ContentPages/17726650.pdf, Accessed December 2015

Thombre, S.B. & Sukhatme, S.P., (1995), "Turbulent Flow Heat Transfer and Friction Factor Characteristics of Shrouded Fin Arrays with Uninterrupted Fins", *Experimental Thermal and Fluid Science*, 10 (3), p388-396

Torresi, M.; Camporeale, S. M.; Pascazio, G.; Fortunato, B., (2004), "Fluid dynamic analysis of a low solidity Wells turbine", *Conference: Atti del 59° Congresso Annuale ATI*, Genova, Italy

Torresi, M.; Camporeale, S.; Strippoli, P.; Pascazio, G., (2008), "Accurate Numerical Simulation of a High Solidity Wells Turbine", *Renewable Energy*, 33 (4), p735–747

Toshi, F., (2012), "Wave farm". [image], Available: http://toshichile.blogspot.co.uk/2012/06/combination-of-renewable-energy-and.html, Accessed December 2015

Trigeol, J. F.; Bertin, Y.; Lagonotte, P., (2006), "Thermal modelling of an induction machine through the association of two numerical approaches", *IEEE Transactions on Energy Conversion*, 21, (2), p314-323

Waveplam, (2009), "Non-technological Barriers to Wave Energy Implementation", Available: http://www.waveplam.eu/files/downloads/Waveplam_Del_2-2_Non-technological-barriers.pdf, Accessed December 2015

Wilcox, D.C., (1988), "Re-assessment of the scale-determining equation for advanced turbulence models", *AIAA Journal*, 26 (11), p1299-1310.

World Economic Forum, (2016), "Renewable Infrastructure Investment Handbook: A Guide for Institutional Investors", Available: http://www3.weforum.org/docs/WEF_Renewable_Infrastructure_Investment_Handbook.pdf, Accessed March 2018

Young, I. R., (1999), "Wind Generated Ocean Waves", London: Elsevier

Zuckerman, N. & Lior, N., (2006). "Jet Impingement Heat Transfer: Physics, Correlations, and Numerical Modelling", *Advances in Heat Transfer*, 39, p565-631

APPENDIX A - The Mathematical Rules Required for Reynolds Averaging

Averaging a Sum of Two Vectors

$$\overline{(f+g)} = \int (f+g)\,dt = \int f\,dt + \int g\,dt = \bar{f} + \bar{g}$$

Averaging a Scaler Multiple of a Vector

$$\overline{sf} = s\bar{f}$$

Averaging a Product of Two Vectors

$$\overline{fg} = \int fg\,dt = \int (\bar{f} + f')(\bar{g} + g')\,dt$$

$$= \int \bar{f}\bar{g}\,dt + \int \bar{f}g'\,dt + \int \bar{g}f'\,dt + \int f'g'\,dt$$

$$= \int \bar{f}\bar{g}\,dt + 0 + 0 + \int f'g'\,dt$$

$$= \bar{f}\bar{g} + f'g'$$

Averaging a Spatial Vector Derivative

$$\overline{\frac{\partial f}{\partial x}} = \int \frac{\partial f}{\partial x}dt = \frac{\partial}{\partial x}\int f dt = \frac{\partial \bar{f}}{\partial x}$$

Averaging a Temporal Vector Derivative

$$\overline{\frac{\partial f}{\partial t}} = \int \left(\frac{\partial \bar{f}}{\partial t} + \frac{\partial f'}{\partial t}\right)dt = \frac{\partial \bar{f}}{\partial t}$$

APPENDIX B - The Standard (Wilcox) *k*–ω Turbulence Model

Turbulence Kinetic Energy

$$\frac{\partial k}{\partial t} + U_j \frac{\partial k}{\partial x_j} = \tau_{ij} \frac{\partial U_i}{\partial x_j} - \beta^* k\omega + \frac{\partial}{\partial x_j}\left[(v + \sigma^* v_T)\frac{\partial k}{\partial x_j}\right]$$

Specific Dissipation Rate

$$\frac{\partial \omega}{\partial t} + U_j \frac{\partial \omega}{\partial x_j} = \alpha \frac{\omega}{k} \tau_{ij} \frac{\partial U_i}{\partial x_j} - \beta \omega^2 + \frac{\partial}{\partial x_j}\left[(v + \sigma v_T)\frac{\partial \omega}{\partial x_j}\right]$$

Kinematic Eddy Viscosity

$$v_T = \frac{k}{\omega}$$

Closure Coefficients and Auxiliary Relations

$$\alpha = \frac{5}{9}$$

$$\beta = \frac{3}{40}$$

$$\beta^* = \frac{9}{100}$$

$$\sigma = \frac{1}{2}$$

$$\sigma^* = \frac{1}{2}$$

$$\varepsilon = \beta^* \omega k$$

APPENDIX C – The *k*–ω SST (Menter's Shear Stress Transport) Turbulence Model

Turbulence Kinetic Energy

$$\frac{\partial(\rho k)}{\partial t}+\frac{\partial\left(\rho u_j k\right)}{\partial x_j}=P-\beta^*\rho\omega k+\frac{\partial}{\partial x_j}\left[(\mu+\sigma_k\mu_t)\frac{\partial k}{\partial x_j}\right]$$

Specific Dissipation Rate

$$\frac{\partial(\rho\omega)}{\partial t}+\frac{\partial\left(\rho u_j \omega\right)}{\partial x_j}+\frac{\gamma}{v_t}P-\beta\rho\omega^2+\frac{\partial}{\partial x_j}\left[(\mu+\sigma_\omega\mu_t)\frac{\partial\omega}{\partial x_j}\right]+2(1-F_1)\frac{\rho\sigma_{\omega 2}}{\omega}\frac{\partial k}{\partial x_j}\frac{\partial\omega}{\partial x_j}$$

Variable Definitions

$$P=\tau_{ij}\frac{\partial u_i}{\partial x_j}$$

$$\tau_{ij}=\mu_t\left(2S_{ij}-\frac{2}{3}\frac{\partial u_k}{\partial x_k}\delta_{ij}\right)-\frac{2}{3}\rho k\delta_{ij}$$

$$S_{ij}=\frac{1}{2}\left(\frac{\partial u_i}{\partial x_j}+\frac{\partial u_j}{\partial x_i}\right)$$

$$v_t=\frac{\rho a_1 k}{max(a_1\omega,\Omega F_2)}$$

$$\emptyset=F_1\emptyset_1+(1-F_1)\emptyset_2$$

$$F_1=tanh(arg_1^4)$$

$$arg_1=min\left[max\left(\frac{\sqrt{k}}{\beta^*\omega d},\frac{500v}{d^2\omega}\right),\frac{4\rho\sigma_{\omega 2}k}{CD_{k\omega}d^2}\right]$$

$$CD_{k\omega}=max\left(2\rho\sigma_{\omega 2}\frac{1}{\omega}\frac{\partial k}{\partial x_j}\frac{\partial\omega}{\partial x_j},10^{-20}\right)$$

$$F_2=tanh(arg_2^2)$$

$$arg_2=max\left(2\frac{\sqrt{k}}{\beta^*\omega d},\frac{500v}{d^2\omega}\right)$$

Closure Coefficients

$\sigma_{k1} = 0.85, \quad \sigma_{\omega 1} = 0.65, \quad \beta_1 = 0.075$

$\sigma_{k2} = 1.00, \quad \sigma_{\omega 2} = 0.856, \quad \beta_2 = 0.0828$

$\beta^* = 0.09 a_1 = 0.31$

Boundary Conditions and Far Field Conditions

$$\omega_{\text{wall}} = 10 \frac{6v}{\beta_1 (\Delta d_1)^2}$$

$$k_{\text{wall}} = 0$$

$$\frac{U_\infty}{L} < \omega_{\text{farfield}} < 10 \frac{U_\infty}{L}$$

$$\frac{10^{-5} U_\infty^2}{Re_L} < k_{\text{farfield}} < \frac{0.1 U_\infty^2}{Re_L}$$